Measurements of the W Boson mass from $e^+e^- \rightarrow W^+W^- \rightarrow \ell\bar{\nu}q\bar{q}$ events with the ALEPH Detector

Evelyn Jean Thomson

A thesis submitted for the degree of
Doctor of Philosophy
of the University of Glasgow

Department of Physics and Astronomy
December 1998

Abstract

The W boson mass is measured directly from the reconstructed invariant mass distribution of the decay products in $e^+e^-\to W^+W^-\to e\bar{\nu}q\bar{q}$ and $e^+e^-\to W^+W^-\to \mu\bar{\nu}q\bar{q}$ events, recorded by the ALEPH detector at the LEP collider at centre-of-mass energies of $\sqrt{s} = 172$ GeV during 1996 and $\sqrt{s} = 183$ GeV during 1997. An efficient, pure selection and a new kinematic fit to treat the undetected neutrino correctly are developed. The W boson mass is measured by a direct comparison of the data invariant mass distribution with simulated distributions for various W mass values, which are obtained by using the CC03 matrix element to reweight a large sample fully simulated at one value for the W mass.

The result for the W boson mass from the direct reconstruction of 34 $e\bar{\nu}q\bar{q}$ and $\mu\bar{\nu}q\bar{q}$ candidates at $\sqrt{s} = 172$ GeV is:

$$M_W = 80.54 \pm 0.47(stat.) \pm 0.11(syst.)\ \mathrm{GeV/c^2}$$

With the higher statistics at $\sqrt{s} = 183$ GeV, the $e\bar{\nu}q\bar{q}$ and $\mu\bar{\nu}q\bar{q}$ channels are studied separately and the results for the W boson mass from the direct reconstruction of 94 $e\bar{\nu}q\bar{q}$ and 78 $\mu\bar{\nu}q\bar{q}$ candidates are:

$$M_W^{e\bar{\nu}q\bar{q}} = 80.428 \pm 0.269(stat.) \pm 0.043(syst.)\ \mathrm{GeV/c^2}$$
$$M_W^{\mu\bar{\nu}q\bar{q}} = 80.370 \pm 0.287(stat.) \pm 0.039(syst.)\ \mathrm{GeV/c^2}$$

The combination of results at $\sqrt{s} = 172$ GeV and $\sqrt{s} = 183$ GeV is:

$$M_W = 80.422 \pm 0.181(stat.) \pm 0.040(syst.)\ \mathrm{GeV/c^2}$$

This is compared to other measurements and the Standard Model prediction for the W boson mass of 80.365 ± 0.030 GeV/c^2.

Preface

The W boson mass is a fundamental parameter of the Standard Model of particle physics. The interpretation of other experimental measurements in the context of the Standard Model gives a prediction for the W boson mass with a precision of 0.030 GeV/c^2. This is three times smaller than the current experimental error from the direct determination by experiments at the Tevatron. A more precise, direct measurement of the W boson mass empowers a new, crucial test of the consistency of the Standard Model that is also sensitive to the mass of the Higgs boson.

This thesis presents the first measurements of the W boson mass by direct reconstruction of the W decay products in the $e^+e^-\to W^+W^-\to e\bar{\nu}q\bar{q}$ and $e^+e^-\to W^+W^-\to \mu\bar{\nu}q\bar{q}$ channels, using data collected in 1996 and 1997 by the ALEPH detector at the LEP collider. Chapter 1 introduces the theoretical and experimental context in which to interpret a more precise measurement of the W boson mass from LEP. Chapter 2 describes the LEP collider and the ALEPH detector. This analysis develops an efficient selection, described in Chapter 3; a kinematic fit specific to the $\ell\bar{\nu}q\bar{q}$ channel that treats the unmeasured neutrino correctly, described in Chapter 4; an unbiased method to extract the W boson mass from the data distribution, described in Chapter 5; and stability and systematic checks, described in Chapters 6 and 7. The combination of results from this thesis, which are also the official ALEPH results, with other W mass measurements is discussed and interpreted as a test of the consistency of the Standard Model in Chapter 8. Conclusions are drawn in Chapter 9.

Author's Declaration

The work of the ALEPH collaboration depends on the participation of many people over a long period of time. The author's contribution to the experiment includes taking shifts to monitor the data quality of the ALEPH detector, helping to align and maintain the ALEPH TPC laser calibration system and being partly responsible for the safe operation and data quality of the ALEPH TPC.

As part of a small group, the author developed the selection for the $\sqrt{s} = 172$ GeV and $\sqrt{s} = 183$ GeV data and a new kinematic fit for the $\sqrt{s} = 183$ GeV data in order to solve the problems associated with the existing kinematic fit. The author helped to adapt the mass fit technique to the semileptonic channel, checked the reproducibility and stability of the results and evaluated the systematic uncertainties at $\sqrt{s} = 183$ GeV from calorimeter calibrations and jet corrections. No portion of the author's work described in this thesis has been submitted in support of an application for another degree or qualification in this, or any other, institute of learning.

Acknowledgements

I would like to thank The Carnegie Trust for the Universities of Scotland for financial support in the form of a Caledonian Research Foundation Scholarship and Carnegie Grants. I would also like to thank the University of Glasgow and Rutherford Appleton Laboratory for additional support whilst at CERN. I thank the Physics and Astronomy department at the University of Glasgow for giving me the opportunity to do this research.

I am infinitely grateful to Jason Ward and Rob Edgecock, without whom none of this would have been possible, for their help, encouragement and many comments! Many thanks to Helenka "The τ Task Force" Przysiezniak too for all her help and friendship. I would also like to thank Pedro Teixeira-Dias, Ian Knowles, Paolo Azzurri, Selvam Dhamotharan, Andrea Valassi, Eric Lançon and Alain Blondel for useful discussions and the ALEPH WW Working Group for their advice and interest. Thanks to Stephen, Allan, Simon, Fiona, Lee, Matt, David, Barbara, John and Giulio for being such friendly and entertaining office-mates. Thanks also to Jim, Stan and Peter and especially to Catherine for taking care of all those forms and her kind help. Thanks to Christine, Fiona, Johanna, Stephen and Craig for being super flat-mates and, of course, Gavin for providing me with such a handy room by going away to DESY for seven months! A big thank-you to Fred, for always listening patiently to kinematic fit woes, and to Smita, for being my rôle model in the writing of this thesis. I would like to thank Christine and Irene for being such great friends and to apologise to everyone whom I have neglected these past months.

Finally, I would like to thank my Mum, Dad, Stephen and Owen for their love and support. This thesis is dedicated to them.

Contents

List of Figures

List of Tables

Chapter 1

Introduction.

This chapter introduces the theoretical and experimental context in which to interpret a precision measurement of the W boson mass. The interactions of three of the four known fundamental forces in the universe are successfully explained by Quantum Field Theory. Section 1.1 briefly describes the key features of this Standard Model and emphasises the rôle of the W boson. A more detailed description can be found in [1, 2, 3, 4, 5]. Section 1.2 explores the experimental opportunities for the determination of the W boson mass. Section 1.3 discusses how a more precise measurement of the W boson mass can test the Standard Model further - there is no known experimental deviation from the Standard Model at this time.

1.1 The Standard Model.

1.1.1 Fundamental forces and particles.

The universe appears to be governed by only four fundamental forces: strong, electromagnetic, weak and gravitational. The strong force acts only at short distances (less than 10^{-15}m) and binds quarks together to make nucleons (protons and neutrons) and binds nucleons together to make nuclei. The electromagnetic force has infinite range and provides the attractions between electrons and nuclei that build atoms and molecules. The short-range weak force lies behind processes like beta decay, which allows protons to transmute into neutrons, and is vital for the fusion power cycle of stars. Gravity, the weakest force by far, has infinite range and is important for large composite bodies, but is negligible in the context of nuclear and sub-nuclear interactions.

The application of quantum mechanics by Dirac in 1927 [6] to Maxwell's electromagnetic field led to the foundations for the original quantum field theory of Quantum Electrodynamics, or QED. In QED, the interactions of electrically charged particles are mediated by a massless spin-1 particle, the photon, which is the quantum of the electromagnetic field. These interactions can be represented by Feynman diagrams, like those shown in Figure 1.1.

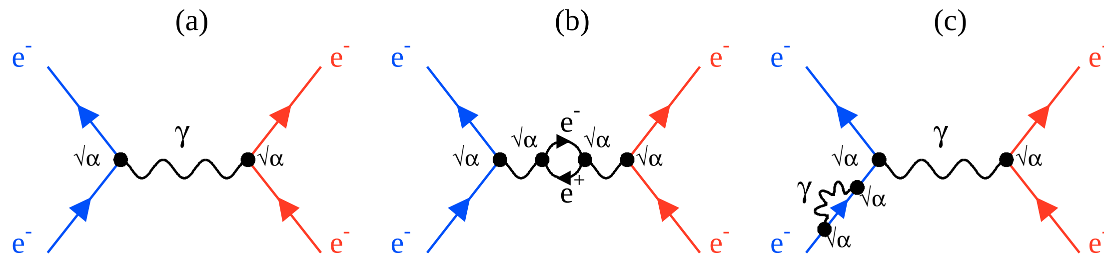

Figure 1.1: Three Feynman diagrams that contribute to the Coulomb repulsion between two electrons.

The Feynman rules can be used to calculate the amplitude, $\mathcal{M}$, of any such diagram, from which the cross section for the interaction can be derived. A factor of $\sqrt{\alpha}$ is introduced into $\mathcal{M}$ at every vertex where a charged particle interacts with a photon. α is called the electromagnetic coupling constant.

The contribution to the cross section from diagrams like 1.1a, which are of the lowest order in terms of α, can be calculated exactly. The presence of an extra factor of α in the contribution from higher-order diagrams like 1.1b and c suggests that all the Feynman diagrams, which have to be summed to give the total amplitude for the interaction, can be arranged to form a power series in α. If α is less than 1, as in QED, then each power of α is smaller than the preceding one and each higher-order term can be considered as a small correction to the series up to that point - the basis of perturbation theory.

However, the contribution from some of the higher-order diagrams, like 1.1b and c, is infinite! The problem of how to extract concrete numerical predictions from a theory plagued with infinities was finally solved by Tomonaga [7], Schwinger [8] and Feynman [9] in 1949. They showed that the contribution from diagrams like 1.1b and c could be split into a finite part and an infinite part. The miracle is that the infinite parts appear only as corrections to the coupling constant α and the masses of the particles. So the troublesome infinities can be absorbed into redefinitions of the coupling constant and the masses. The finite parts cause the effective coupling constant and masses to depend on the energy of the process considered. Since Nature sums all the diagrams automatically, these renormalised parameters are the correct ones to compare with the experimental measurements.

The success of QED, which has now been experimentally tested to within one part in 10^8, encouraged the development of quantum field theories for the other three forces. Progress was slow until 1971, when 't Hooft [10] proved that Yang-Mills gauge theory, a generalisation of the Maxwell theory of light but with a larger symmetry group, was renormalisable[1]. Solid numerical predictions could then be made from various gauge theories and checked against the experimental data.

The strong interaction is well described by the SU(3) colour symmetry group of Quantum Chromodynamics, or QCD. Particles that experience the strong force are said to have colour charge, of which there are three types. The interactions of colour charged particles are mediated by eight massless spin-1 gluons, which are the quanta of the eight gauge fields of the SU(3) group. The gluons also carry colour charge and can therefore interact with each other, unlike the electrically neutral photon. As a result, the effective strong coupling constant, α_s, decreases with increasing energy, which leads to asymptotic freedom ("free" coloured particles) at high energies and confinement (only colourless combinations of particles) at low energies. Since α_s exceeds unity at low energies, exact calculations by perturbation theory are no longer possible and phenomenological models [11] have to be used instead to describe the confinement of coloured quarks to colourless hadrons, a process which is called hadronisation or fragmentation.

The weak and electromagnetic forces are combined in an electroweak theory, based on the SU(2)xU(1) symmetry group, by Glashow [12], Salam [13] and Weinberg [14]. The remarkable Higgs mechanism [15] spontaneously breaks the symmetry and gives masses to the spin-1 $W^{\pm}$ and Z^0 mediators while leaving the spin-1 photon massless and retaining renormalisability. The need to produce a heavy $W^{\pm}$ or Z^0 causes the apparent weakness of the weak force at low energies - a universe with massless mediators for the weak force would be a very different place [16]. The Higgs mechanism requires the existence of at

[1] The renormalisability of QED can be traced to the fact that it is a *local gauge theory* and is invariant under arbitrary phase, or gauge, $e^{i\theta(x)}$ transformations. The phase factors $e^{i\theta(x)}$ belong to the symmetry group U(1) of unitary 1x1 matrices.

least one spin-0 Higgs particle, the search for which continues apace [17]. The electroweak theory is discussed in more detail in the next section.

Although the gravitational force was the first of the four fundamental forces to be investigated classically, a consistent quantum field theory of gravity does not yet exist. The long-range attractive nature of the force does imply that the mediators are massless and have an even spin of at least two [18].

The combination of QCD and the electroweak theory forms a first approximation, known as the Standard Model, to the ultimate theory of particle interactions. The fundamental particles of this Standard Model are the spin-1 bosons that mediate the fundamental forces, the spin-0 Higgs boson from the mechanism for electroweak symmetry breaking and spin-$\frac{1}{2}$ fermions, which make up matter.

The fermions are shown in Table 1.1 and sub-divide into two groups: quarks, which have colour charge and interact via the strong force, and leptons, which do not. Both groups undergo electroweak interactions. The confinement of the strong force means that only colourless combinations of three quarks (baryons) or of a quark and an anti-quark (mesons) are observed experimentally. The up and down quarks are the building blocks of the familiar proton (uud) and neutron (udd), which combine with electrons to make up atoms. The ghostly electron neutrino interacts only via the weak force. These four fermions form a generation of particles. Two further generations exist, identical except for heavier masses and different flavours.

In principle, the Higgs boson can also be used to give masses to the quarks and leptons. The quark mass eigenstates are not the same as the quark weak eigenstates, so the down-type quarks (d, s, b) are said to mix to give the weak eigenstates (d′, s′, b′). This mixing is described by the Cabibbo-Kobayashi-Maskawa (CKM) matrix [20]:

$$\begin{pmatrix} d' \\ s' \\ b' \end{pmatrix} = \begin{pmatrix} V_{ud} & V_{us} & V_{ub} \\ V_{cd} & V_{cs} & V_{cb} \\ V_{td} & V_{ts} & V_{tb} \end{pmatrix} \begin{pmatrix} d \\ s \\ b \end{pmatrix}$$

The Standard Model cannot predict the values of the fermion masses, the coupling constants, the four independent parameters of the CKM matrix, the mass of the Higgs boson or even the number of generations of particles. All of these quantities have to be experimentally determined. The predictions of the Standard Model, with the experimental values as input, can then be tested against further experimental measurements. At this

	Particle	Symbol	Charge (e)	Mass (GeV/c^2)
First generation				
Quarks	up	u	$+\frac{2}{3}$	0.0015-0.0050
	down	d	$-\frac{1}{3}$	0.0030-0.0090
Leptons	electron	e	-1	0.0005
	electron neutrino	ν_e	0	0Γ
Second generation				
Quarks	charm	c	$+\frac{2}{3}$	1.1-1.4
	strange	s	$-\frac{1}{3}$	0.06-0.170
Leptons	muon	μ	-1	0.106
	muon neutrino	ν_μ	0	0Γ
Third generation				
Quarks	top	t	$+\frac{2}{3}$	173.8 ± 5.2
	bottom	b	$-\frac{1}{3}$	4.1-4.4
Leptons	tau	τ	-1	1.7
	tau neutrino	ν_τ	0	0Γ

Table 1.1: The fundamental fermions of the Standard Model [19]. Each particle has an anti-matter equivalent, with the same mass but with opposite quantum numbers.

time, the predictions have been tested to the 0.1% level and no unexplainable discrepancy has been found [21]. The Standard Model is a far cry from an ultimate theory with at most one undetermined coupling constant, so it is important to test its predictions even more carefully in order to find the correct direction towards the ultimate theory.

1.1.2 The electroweak model and the W boson mass.

The electroweak model of Glashow, Salam and Weinberg is based on the symmetry group $\mathrm{SU(2)_L xU(1)_Y}$. The underlying gauge fields are W_i^μ ($i = 1, 2, 3$) for the $\mathrm{SU(2)_L}$ group and B^μ for the $\mathrm{U(1)_Y}$ group, with respective coupling constants g and g'. The subscript L indicates that the $\mathrm{SU(2)_L}$ fields couple only to left-handed fermions, which transform as weak isospin doublets L, with a weak isospin quantum number of $T = \frac{1}{2}$. The right-handed fermions transform as weak isospin singlets R, with $T = 0$. The subscript Y denotes weak hypercharge, which is defined such that the electric charge $Q = T_3 + \frac{Y}{2}$, where T_3 is the third component of weak isospin. For example, for the first generation:

$$L = \begin{pmatrix} \nu_e \\ e^- \end{pmatrix}_L , \begin{pmatrix} u \\ d' \end{pmatrix}_L \quad \text{with } T = \tfrac{1}{2},\ T_3 = \begin{cases} +\frac{1}{2} \\ -\frac{1}{2} \end{cases}$$
$$R = \ e^-_R, u_R, d'_R \qquad \text{with } T = 0$$

The first piece of the electroweak Lagrangian results from imposing $\mathrm{SU(2)_L xU(1)_Y}$ invariance and has the form:

$$\begin{aligned} \mathcal{L}_1 \;=\; & \bar{L}\gamma^\mu(i\partial_\mu - g\tfrac{1}{2}\tau.\mathbf{W}_\mu - g'\tfrac{Y}{2}B_\mu)L \;+\; \bar{R}\gamma^\mu(i\partial_\mu - g'\tfrac{Y}{2}B_\mu)R \\ & - \tfrac{1}{4}\mathbf{W}_{\mu\nu}.\mathbf{W}^{\mu\nu} - \tfrac{1}{4}B_{\mu\nu}B^{\mu\nu} \end{aligned} \tag{1.1}$$

where the τ matrices are the Pauli spin matrices. The first line represents the lepton and quark kinetic energies and their interactions with the W^μ and B^μ fields. The second line represents the kinetic energies and self-interactions of the W^μ and B^μ fields themselves. The direct insertion of a mass term for the gauge fields would destroy the invariance of the Lagrangian.

In order to keep $\mathrm{SU(2)_L xU(1)_Y}$ invariance and introduce masses for three of the gauge fields, the subtlety of the Higgs mechanism is required. This adds a term:

$$\mathcal{L}_2 \;=\; \left|(i\partial_\mu - g\tfrac{1}{2}\tau.\mathbf{W}_\mu - g'\tfrac{Y}{2}B_\mu)\phi\right|^2 \;-\; V(\phi) \tag{1.2}$$

to the electroweak Lagrangian, where the fields ϕ must also belong to a $\mathrm{SU(2)_L xU(1)_Y}$ multiplet and $|x|^2 = x^\dagger x$. The minimal choice for ϕ is to arrange four real scalar fields ϕ_j in a weak isospin doublet with weak hypercharge $Y = +1$:

$$\phi \;=\; \begin{pmatrix} \phi^+ \\ \phi^0 \end{pmatrix} \quad \text{with} \quad \begin{aligned} \phi^+ &= (\phi_1 + i\phi_2)/\sqrt{2} \\ \phi^0 &= (\phi_3 + i\phi_4)/\sqrt{2} \end{aligned}$$

The minimal choice for the Higgs potential is:

$$V(\phi) = \mu^2\phi^\dagger\phi + \lambda(\phi^\dagger\phi)^2 \tag{1.3}$$

where $\mu^2 < 0$ and $\lambda > 0$. This has a minimum at

$$|\phi|^2 = -\frac{\mu^2}{2\lambda} \neq 0 \tag{1.4}$$

and this is the ground state of ϕ. The ground state is degenerate - it has no preferred direction in weak isospin space as a consequence of the $\mathrm{SU}(2)_\mathrm{L}$ symmetry. Since the physics cannot depend on the direction, or phase, of ϕ, the ground state can be chosen to be:

$$\phi_0 = \frac{1}{\sqrt{2}} \begin{pmatrix} 0 \\ \nu \end{pmatrix} \tag{1.5}$$

where this choice deliberately leaves the $\mathrm{U}(1)_\mathrm{em}$ symmetry unbroken. That is, $Q\phi_0 = 0$ and the gauge boson of the electromagnetic force, the photon, remains massless. After expanding about the ground state ϕ_0 and applying a suitable gauge transformation, ϕ can be written in terms of one remaining field - the Higgs field, H:

$$\phi = \frac{1}{\sqrt{2}} \begin{pmatrix} 0 \\ \nu \ + \ H \end{pmatrix} \tag{1.6}$$

The substitution of this expression for ϕ into $\mathcal{L}_2$ generates mass terms for the gauge bosons that do *not* break the invariance:

$$(\frac{1}{2}\nu g)^2 W_\mu^+ W_\mu^- \ + \ \frac{1}{8}\nu^2 \left(W_\mu^3,\ B_\mu\right) \begin{pmatrix} g^2 & -gg' \\ -gg' & g'^2 \end{pmatrix} \begin{pmatrix} W_\mu^3 \\ B_\mu \end{pmatrix} \tag{1.7}$$

where $W^\pm = \frac{1}{\sqrt{2}}(W^1 \mp iW^2)$. The W boson mass is easily identified by comparison of the first term with the expected mass term for a charged boson, $M_W^2 W^+ W^-$:

$$M_W \ = \ \frac{1}{2}\nu g \tag{1.8}$$

The second term is off-diagonal in the $(W_\mu^3,\ B_\mu)$ basis. Diagonalisation of the 2×2 mass matrix yields:

$$0\left(g'W_\mu^3 + gB_\mu\right)^2 \ + \ \frac{1}{8}\nu^2\left(gW_\mu^3 - g'B_\mu\right)^2 \tag{1.9}$$

which are the two physical fields, A_μ and Z_μ, with masses M_A and M_Z identified by comparison with the expected mass terms for neutral bosons, $\frac{1}{2}M_A^2 A^2 + \frac{1}{2}M_Z^2 Z^2$:

$$\begin{aligned} A_\mu &= \frac{g'W_\mu^3 + gB_\mu}{\sqrt{g^2 + g'^2}} & M_A &= 0 \\ Z_\mu &= \frac{gW_\mu^3 - g'B_\mu}{\sqrt{g^2 + g'^2}} & M_Z &= \tfrac{1}{2}\nu\sqrt{g^2 + g'^2} \end{aligned} \tag{1.10}$$

Rewriting this in terms of the mixing angle between the W_μ^3 and B_μ fields, $\theta_W = \tan^{-1}(g'/g)$, gives:

$$\begin{aligned} A_\mu &= \cos\theta_W B_\mu + \sin\theta_W W_\mu^3 \\ Z_\mu &= -\sin\theta_W B_\mu + \cos\theta_W W_\mu^3 \end{aligned} \tag{1.11}$$

and:

$$M_W = M_Z \cos\theta_W \tag{1.12}$$

The inequality $M_W \neq M_Z$ is due to the mixing between the W_μ^3 and B_μ fields. The choice of ϕ and its groundstate automatically generates a massless photon A_μ and a massive Z_μ field with $M_Z > M_W$. The relation between M_W and M_Z depends on the structure of the Higgs sector and thus forms an indirect probe of whether the assumed minimal scenario is correct.

Rewriting $\mathcal{L}_1$ in terms of the physical fields, Z_μ and A_μ, and comparing the result with the QED Lagrangian of:

$$\mathcal{L}_{\mathrm{QED}} = \bar{\psi}\gamma\mu\left(i\partial_\mu - eQA_\mu\right)\psi - \tfrac{1}{4}F_{\mu\nu}F^{\mu\nu} \tag{1.13}$$

allows the identification of the coupling constants g and g' with the electric charge $e = \sqrt{4\pi\alpha}$ and the mixing angle θ_W:

$$e = g\sin\theta_W = g'\cos\theta_W \tag{1.14}$$

This relationship is a direct consequence of the $\mathrm{SU(2)_L}$ symmetry of the electroweak model.

1.1.3 Radiative corrections.

The values of the three fundamental parameters of the electroweak theory, g, g' and ν, are not predicted. The three related quantities that are experimentally determined with high precision are [22]:

- The fine structure constant:

$$\alpha(0) = \frac{e^2}{4\pi} = 1/137.035\ 989\ 5(61)$$

- The muon decay (Fermi) constant:

$$G_\mu = \frac{g^2}{4\sqrt{2}M_W^2} = \frac{1}{\sqrt{2}\nu^2} = 1.166\ 39(1) \times 10^{-5}\ \mathrm{GeV}^{-2}$$

- The Z^0 boson mass:

$$M_Z = \frac{g\nu}{\cos\theta_W} = 91.187(7)\ \mathrm{GeV/c^2}$$

where the relations are valid at lowest order only. Here the relationship between the W and Z^0 boson masses can be written as:

$$M_W^2 \ = \ \frac{\pi\alpha}{\sqrt{2}G_\mu \sin^2\theta_W} \quad \text{where} \quad \sin^2\theta_W = 1 - \frac{M_W^2}{M_Z^2} \tag{1.15}$$

Therefore, a direct measurement of the W boson mass over-constrains the model. The prediction for the W boson mass can be compared with the direct experimental measurement in order to test the consistency of the Standard Model.

However, current measurements are sufficiently precise that radiative corrections from higher-order diagrams, like those in Figure 1.2, are required. The comparison of the electroweak prediction and the direct measurement is then sensitive to the masses and couplings of the particles propagating in the loops. Information on these particles can thus be obtained well below the energy threshold for their direct production.

The relationship between the W and Z^0 boson masses becomes:

$$M_W^2 \ = \ \frac{\pi\alpha}{\sqrt{2}G_\mu \sin^2\theta_W(1-\Delta r)} \tag{1.16}$$

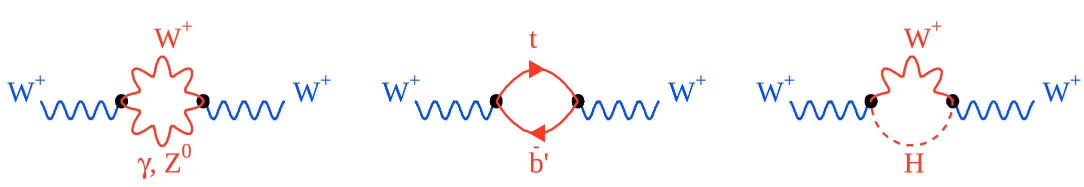

Figure 1.2: Three Feynman diagrams that represent some of the radiative corrections to the W boson mass.

where Δr represents the radiative corrections. The largest contribution to Δr is from the effect of running the coupling constant α to the W mass scale ($\alpha(M_W^2) = 1/128$). Δr also depends quadratically on the top quark mass and logarithmically on the Higgs boson mass [23].

1.2 Experimental measurements of M_W.

In 1983, the $W^{\pm}$ and Z^0 bosons were observed directly for the first time in $p\bar{p}$ collisions at the Super Proton Synchrotron at CERN [24, 25, 26, 27]. The masses of the $W^{\pm}$ and Z^0 bosons were measured by the UA2 collaboration [28] to be $M_W = 80.8 \pm 0.9$ GeV/c^2 and $M_Z = 91.7 \pm 1.0$ GeV/c^2, in excellent agreement with the Standard Model.

Precision measurements of the Z^0 boson mass now allow the mass of the W boson to be predicted with a precision of around 0.030 GeV/c^2 [21]. A major goal of current experimental programmes is to match this precision by direct measurement and thus provide a new test of the Standard Model, which is also sensitive to the mass of the Higgs boson. This section describes the experimental opportunities for the determination of the W boson mass.

1.2.1 Opportunities at LEP.

The Large Electron Positron (LEP) collider at CERN was constructed to study the properties of the Z^0 and $W^{\pm}$ bosons in detail and to test the Standard Model to very high precision. The operation of the LEP collider is divided into two phases:

- LEP1 (1989-1995), designed for the study of the Z^0 boson, with a centre-of-mass energy around 91 GeV.

- LEP2 (1996-2000), designed for the study of $W^{\pm}$ pairs, with a centre-of-mass energy increasing in steps from threshold at 161 GeV to about 200 GeV in 1999.

The analysis presented here uses the LEP2 data collected by the ALEPH detector during 1996 at $\sqrt{s} = 172$ GeV and during 1997 at $\sqrt{s} = 183$ GeV. More information on the LEP collider and the ALEPH detector can be found in Chapter 2

W^+W^- pair production proceeds through s-channel Z/γ and t-channel neutrino exchange at lowest order. These three charged current (CC03) diagrams are shown in

Figure 1.3.

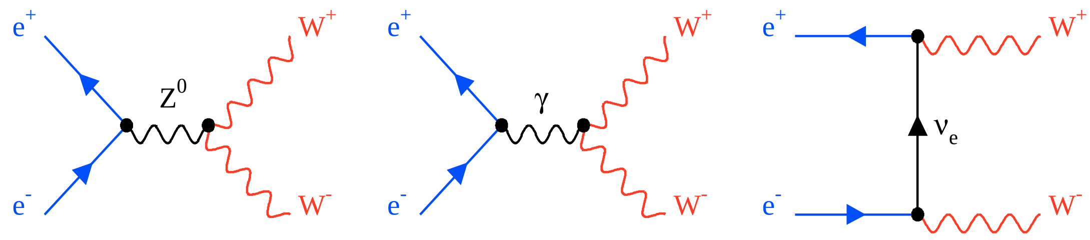

Figure 1.3: The three lowest-order (CC03) Feynman diagrams through which W^+W^- pair production proceeds.

Each W^- swiftly decays into one of $\bar{u}d'$, $\bar{c}s'$, $e^-\bar{\nu}_e$, $\mu^-\bar{\nu}_\mu$, $\tau^-\bar{\nu}_\tau$ and each W^+ into one of $u\bar{d}'$, $c\bar{s}'$, $e^+\nu_e$, $\mu^+\nu_\mu$, $\tau^+\nu_\tau$. This results in three characteristic final states:

- Fully hadronic ($q\bar{q}q\bar{q}$), where both W bosons decay to quarks.
- Semileptonic ($\ell\bar{\nu}q\bar{q}$), where one W boson decays to leptons and one W boson decays to quarks.
- Fully leptonic ($\ell\nu\ell\nu$), where both W bosons decay to leptons.

The Standard Model branching ratios for $W^+W^-\rightarrow q\bar{q}q\bar{q}$, $W^+W^- \rightarrow \ell\bar{\nu}q\bar{q}$ and $W^+W^-\rightarrow\ell\nu\ell\nu$ are 46%, 44% and 10% respectively. More information on the production and decay of W bosons at LEP2 can be found elsewhere [29].

Precise measurements of the W boson mass are possible at LEP2 by using either the sensitivity of the W^+W^- cross section to the W boson mass near threshold or by directly reconstructing the invariant mass distribution of the W decay products above threshold. The shape of the lepton energy spectrum can also be used, albeit with less precision.

Figure 1.4 shows the measurements of the W^+W^- cross section at LEP. Selections are developed for all three characteristic final states. The W mass follows from a comparison of the observed cross section with the theoretical prediction as a function of $\mathrm{M_W}$ [30]. The combined result of all four LEP experiments, which collected about 10 pb^{-1} each at $\sqrt{s}$ = 161 GeV [31], for the W boson mass is:

$$M_W = 80.40 \pm 0.22\ \mathrm{GeV/c^2}$$

where the error is statistically limited.

At higher LEP energies, the cross section is much less sensitive to the W mass and the better technique is to reconstruct the W mass directly from the invariant mass of the decay products. Only the $q\bar{q}q\bar{q}$ and $\ell\bar{\nu}q\bar{q}$ final states can be used as there is not enough kinematic information in the $\ell\nu\ell\nu$ channel due to the presence of two neutrinos. Kinematic fit techniques, imposing overall energy and momentum conservation and equality of the two W masses in each selected event, can be used to improve the mass resolution by a factor of four.

The association of the experimentally observed jets of hadrons to the correct parent W boson in the $q\bar{q}q\bar{q}$ final state is ambiguous as there are three ways of assigning four jets to two W bosons. This channel may also be affected by hadronic final state interactions, since the two W bosons typically decay so close together that their decay products could interact. The phenomena of colour reconnection, in which coloured partons from different W's can connect, and Bose-Einstein correlations, in which coherence effects may

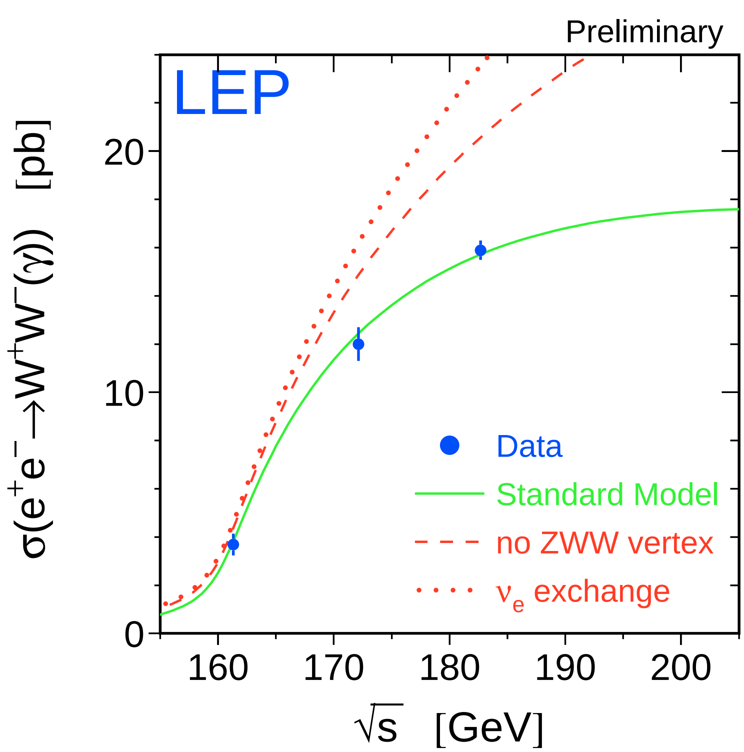

Figure 1.4: The W^+W^- cross section as a function of the centre-of-mass energy of the LEP collider. The data points are the LEP averages. Also shown is the Standard Model prediction and for comparison the cross section if the ZWW coupling did not exist, or if only the t-channel ν_e exchange diagram existed [31].

occur between identical low-momentum bosons from different W's, are not completely understood theoretically. The uncertainty in the modelling of these phenomena could bias the W mass result from the $q\bar{q}q\bar{q}$ channel by up to 100 MeV/c^2 [32, 33].

The $\ell\bar{\nu}q\bar{q}$ final state, which is studied in this thesis where ℓ=e or μ, is not liable to such complications. A comparison of the W mass result from this channel with that from the fully hadronic channel could investigate the magnitude of the effects from such final state interactions. The semileptonic channel suffers from less kinematic information due to the unmeasured neutrino. The constraints from conservation of momentum have to be used to infer the neutrino momentum, which requires a kinematic fit specifically designed for the $\ell\bar{\nu}q\bar{q}$ channel.

The expected error on the W mass from four LEP experiments, with 500 pb^{-1} of data each, is shown in Table 1.2. If the effects from final state interactions are understood, then the results of equal precision from the $q\bar{q}q\bar{q}$ and $\ell\bar{\nu}q\bar{q}$ channels can be combined to give an error of 34 MeV/c^2 on the W mass.

Source	$W^+W^-\to q\bar{q}q\bar{q}$	$W^+W^-\to \ell\bar{\nu}q\bar{q}$	Combined
Statistical	36	36	25
Common systematic	25	23	23
Uncorrelated systematic	9	9	6
Total	45	44	34

Table 1.2: Estimated total error on the W boson mass, in MeV/c^2, by direct reconstruction, after combining four experiments each with an integrated luminosity of 500 pb^{-1} at $\sqrt{s}$=175 GeV. Colour reconnection and Bose-Einstein effects are not included in the systematic error [30].

1.2.2 Opportunities at the Tevatron.

The Tevatron at Fermilab collides 0.9 TeV beams of protons and anti-protons. W bosons are dominantly produced singly from $q\bar{q}'$ annihilation. The leptonic W decays, $W \to \ell\bar{\nu}$ with ℓ=e or μ, are used to defeat the enormous QCD background. The lepton momentum is measured and the transverse momentum of the neutrino is inferred from the missing momentum, which also contains contributions from the W recoil, multiple interactions at each beam crossing and the "pile-up" from the several beam crossings that occur during the readout of the detector. The longitudinal momentum of the W boson is not known.

Therefore, the W boson mass is extracted from the transverse mass distribution:

$$m_T = \sqrt{2 p_T^\ell p_T^\nu (1 - \cos\psi^{\ell\nu})}$$

where $\psi^{\ell\nu}$ is the angle between the lepton and the neutrino in the transverse plane. This distribution, which is shown in Figure 1.5, exhibits a Jacobian edge that is characteristic of two-body decays and contains most of the mass information.

The results from the D0 and CDF experiments, which accumulated about 110 pb^{-1} of data each during 1992-1995, are:

D0 [34]	$M_W = 80.43 \pm 0.11$ GeV/c^2	(preliminary)
CDF [35]	$M_W = 80.38 \pm 0.12$ GeV/c^2	(preliminary)

The dominant systematic errors are from the absolute energy scale of the calorimeters, the modelling of the effects from recoil and pile-up and the parton distribution functions for the proton.

The Tevatron collider is currently being upgraded in order to obtain much higher luminosities and is scheduled to restart in April 2000. The projected error on the W boson mass is about 40 MeV/c^2 per experiment for an integrated luminosity of 2 fb^{-1} [35].

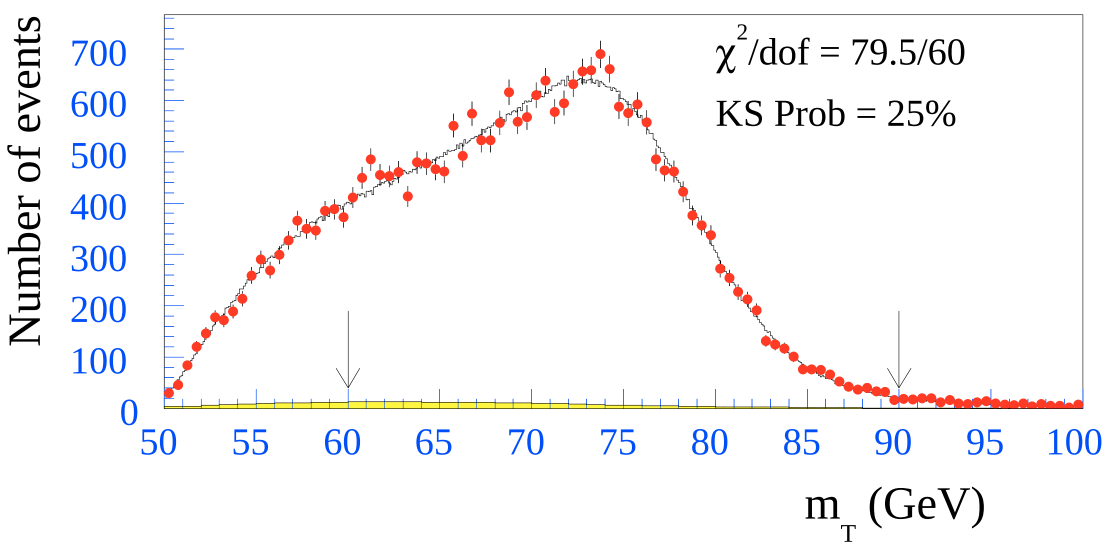

Figure 1.5: Transverse mass distribution from the DO experiment. The region used in the fit for the W mass is indicated by the arrows [34].

1.2.3 Opportunities at future colliders.

The Large Hadron Collider (LHC) is expected to begin colliding 7 TeV beams of protons in 2005. The two LHC experiments should be able to achieve a precision of 30 MeV/c^2 or better on the W mass, with 10 fb^{-1} of data in the first year at low luminosity, using similar techniques to those of the Tevatron experiments [36].

Experiments at a proposed linear e^+e^- collider, designed to reach a centre-of-mass energy of $\sqrt{s}$=500 GeV with an integrated luminosity of 50 fb^{-1} per year, could directly reconstruct the W boson mass from the W decay products in a similar way to those at LEP. The estimated statistical error on the W boson mass with one year's data is 0.020 GeV/c^2 [37].

A $\mu^+\mu^-$ circular collider could use the threshold stratagem to measure the W boson mass even more precisely to 0.006 GeV/c^2 [38]. The advantage of a muon collider is that the larger muon mass reduces the beam energy spread from synchrotron radiation and beamsstrahlung. However, there are some considerable technical disadvantages from the need to produce large numbers of muons and to accelerate them swiftly to high energies before they decay (the mean lifetime of a muon at rest is τ_μ=2.2μs). Muon decays in the collider itself result in high detector backgrounds and heating in superconducting bending magnets, so the design of a muon collider is a very challenging task [39].

1.3 The W boson mass as a test of the Standard Model.

The Standard Model of strong and electroweak interactions has been extremely successful at providing the theoretical framework for the description of a very rich phenomenology spanning a wide range of energies, from the atomic scale up to the Z boson mass. It is being tested at the level of 0.1% and correctly predicts the range of the top quark mass from radiative corrections. However, the Standard Model has a number of shortcomings. In particular, it does not explain the origin of mass, the observed hierarchical pattern of fermion masses and why there are three generations of quarks and leptons. It is widely believed that at high energies, or in very high precision measurements that are sensitive to radiative corrections, deviations from the Standard Model will appear, signalling the presence of new physics.

The W boson mass is a fundamental parameter of the Standard Model. The interpretation of other experimental measurements in the context of the Standard Model gives a prediction for the W boson mass with a precision of 0.030 GeV/c^2 [21]. This is three times smaller than the current experimental error from the direct determination of the W boson mass by experiments at the Tevatron. Experiments at both LEP and the Tevatron have the capability to make such a precise measurement over the next few years. The combination of these measurements will reduce the world average error even further as the systematic uncertainties are very different.

A more precise, direct measurement of the W boson mass empowers a new, crucial test of the consistency of the Standard Model: the comparision of the indirect prediction with the direct measurement. Furthermore, this comparison is sensitive to the radiative corrections of the Standard Model and thus to the top quark mass and the Higgs boson mass. Comparison of the indirect predictions for the top quark mass and the W boson mass with the direct measurements yields another test of the Standard Model and a loose constraint on the mass of the Higgs boson.

Extensions to the Standard Model, such as the Minimal Supersymmetric Standard Model (MSSM), have many theoretical advantages, but are not yet required to explain experimental results. New particles may contribute to the radiative corrections to the W boson mass and so the comparison of the direct measurement with the indirect predictions of the MSSM can also constrain the allowed parameter space of such models.

The current status of these tests will be discussed, including the results from this thesis, in chapter 8.

Chapter 2

The ALEPH detector at LEP.

The analysis presented in this thesis was carried out at CERN, the European Laboratory for Particle Physics, using the data produced by the LEP collider and collected by the ALEPH detector during the years 1996-1997. This chapter gives an overview of the LEP collider and the ALEPH detector. Emphasis is placed on the three most relevant points for the direct reconstruction of the W boson mass from $e^+e^-\rightarrow W^+W^-\rightarrow e\bar{\nu}q\bar{q}$ and $e^+e^-\rightarrow W^+W^-\rightarrow \mu\bar{\nu}q\bar{q}$ events:

- The measurement of the LEP beam energy.
- The energy and angular reconstruction capabilities of ALEPH.
- The identification of electrons and muons in ALEPH.

2.1 The LEP collider.

The Large Electron Positron (LEP) collider [40] is a large circular ring, or more precisely an octagonal polygon with eight straight sections, which are about 500 m long and contain accelerating cavities, and eight circular arcs, which have a radius of curvature of 3300 m and contain bending magnets. The ring has a circumference of 26.67 km and is in a tunnel 50-150 m underground, as illustrated in Figure 2.1. During construction from 1983 to 1988, LEP was the largest civil engineering project in Europe and was completed on time with a precision of better than 1 cm in 26.67 km.

Synchrotron radiation is the reason for the large scale, since a charged particle moving along a curved path radiates photons. The energy loss per turn is proportional to $\frac{E^4}{m^4\rho}$,

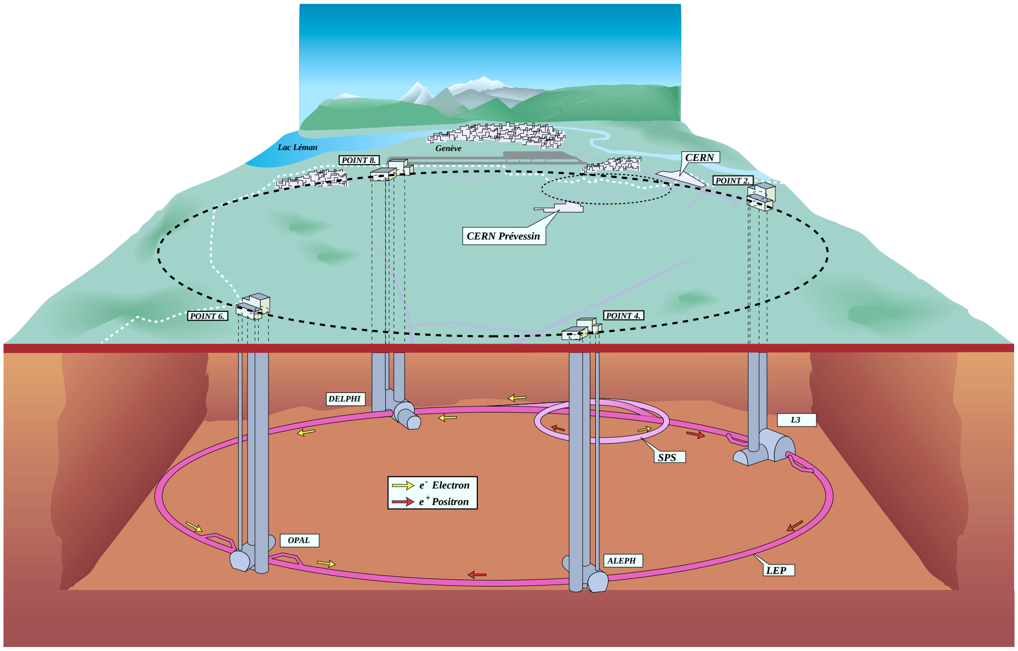

Figure 2.1: Schematic view of LEP and the surrounding area.

where E is the energy, m is the mass of the particle and ρ is the bending radius. Each 100 GeV electron at LEP loses approximately 3 GeV of energy per turn, which must be replenished by the acceleration system. The maximum energy for electrons at LEP is about 100 GeV as above this the power required to operate the acceleration system and remove the heat dissipated rapidly exceeds that affordable.

The stages by which electrons and positrons are injected into LEP are shown in Figure 2.2. Electrons from a high-intensity electron gun accelerate to 200 MeV in a linear accelerator, or LINAC, after which some of them pass through a tungsten converter to produce positrons. Both electrons and positrons then accelerate to 600 MeV in a second LINAC. The leptons accumulate into bunches in the Electron Positron Accumulator (EPA) before injection into the Proton Synchrotron (PS), where they accelerate to 3.5 GeV. Then the bunches move to the Super Proton Synchrotron (SPS) and accelerate to 22 GeV prior to injection into LEP and acceleration to the appropriate energy.

The beams of electrons and positrons in LEP circulate at a frequency of 11,246 Hz and have a typical lifetime of eight hours. The beams are grouped into bunches that are about 1500 μm long, 250 μm wide in the horizontal direction and 10 μm wide in the vertical

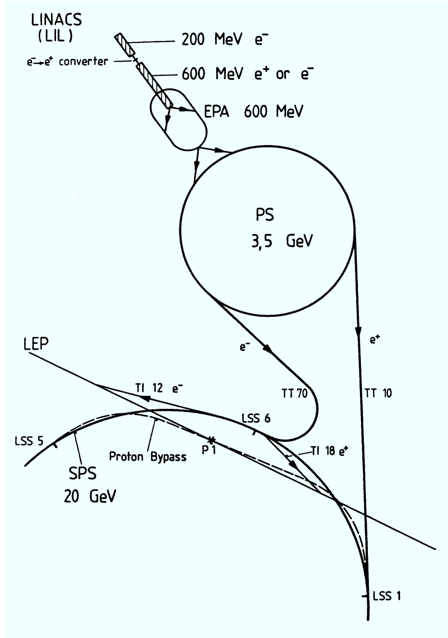

Figure 2.2: The LEP injection system.

direction of the plane transverse to the beam direction. In 1996 and 1997, four equally spaced bunches per beam collide every 22 μs at the interaction points around the LEP ring surrounded by the four LEP experiments, of which ALEPH is one. The maximum current per bunch is 0.65 mA, which corresponds to about 3.6×10^{11} particles. The instantaneous rate of events from colliding beams is given by:

$$\frac{dN}{dt} = \sigma \mathcal{L} \tag{2.1}$$

where σ is the cross section of the process of interest and $\mathcal{L}$ is the luminosity, which at LEP is given by:

$$\mathcal{L} = \frac{N_+ N_- k f}{4\pi\sigma_x\sigma_y} \tag{2.2}$$

where N_i are the number of electrons and positron in the colliding bunches, k is the number of bunches, f is the revolution frequency and σ_x and σ_y are the transverse dimensions of the beam. The maximum luminosity from 1997 is 4.9×10^{31} cm^{-2}s^{-1} [41]. The integrated luminosity delivered by LEP during 1996 at $\sqrt{s} = 172$ GeV is 11.5 pb^{-1} and during 1997 at $\sqrt{s} = 183$ GeV is 63.5 pb^{-1}.

2.2 The measurement of the LEP energy.

The LEP beam energy sets the absolute energy scale for the measurement of the W boson mass, resulting in a relative uncertainty of $\Delta M_W/M_W \approx \Delta E_{beam}/E_{beam}$. The statistical uncertainty on the W boson mass with the full LEP2 data sample is expected to be around 25 MeV/c^2, so ΔE_{beam} should be less than about 15 MeV to avoid a significant contribution to the total error on the W boson mass.

At LEP1 the average beam energy was measured directly at the physics energy with a precision better than 1 MeV by resonant depolarisation [42]. Unfortunately, this technique cannot be used at LEP2 since it is difficult to obtain a useful level of polarisation with a beam energy above 55 GeV. Instead, the resonant depolarisation measurements are extrapolated to higher energies by the use of NMR probes, which continuously measure the main dipole field seen by the circulating beams [43]. The probes are precisely calibrated using resonant depolarisation at several beam energies between 41 and 55 GeV. The calibrations are then applied to the probe readings taken during physics in order to obtain the average beam energy.

Time dependent effects extensively studied at LEP1, like the stretching of the LEP ring by the movement of the moon and leakage currents from the passage of the TGV on a nearby railway line, are taken into account in the calibration of the NMR probes and in deriving the centre-of-mass energy as a function of time. The final correction necessary to find the exact beam energy at each interaction point is to account for the variation of the beam energy around the LEP ring, which is due to the loss of energy by synchrotron radiation in the arcs and the gain of energy in the straight sections with accelerating cavities.

The worry is that the NMR probes sample the magnetic field in only 16 out of 3200 LEP dipoles, whilst the beam energy is proportional to the integrated vertical magnetic field along the entire beam trajectory. The validity of the extrapolation is therefore tested by flux loop experiments [44], where the flux loop measures 97% of the total bending field of LEP. The uncertainties on the LEP beam energy (± 30 MeV for the $\sqrt{s} = 172$ GeV data and ± 24 MeV for the $\sqrt{s} = 183$ GeV data) are dominated by the scatter between the flux loop measurements and the extrapolation using the NMR probes.

The construction of a spectrometer to measure the LEP energy directly and the determination of the LEP energy by the LEP experiments themselves should help to check the extrapolation and reduce the error on the LEP beam energy in future. The spectrometer will measure the bend angle of the LEP beams before and after a special LEP dipole, whose bending field has been surveyed to high precision [45]. With high statistics, the LEP experiments can use radiative return $e^+e^- \to Z^0\gamma \to f\bar{f}\gamma$ events, where the Z boson is on-shell, and the precisely known Z boson mass from LEP1 to reconstruct the LEP energy [46].

2.3 The ALEPH detector.

The ALEPH (Apparatus for LEp PHysics) detector is designed to study all types of Standard Model processes at LEP and to search for new phenomena. To meet these goals, ALEPH is designed to be hermetic and highly granular in order to gather as much information as possible from each e^+e^- interaction. The sub-detectors that comprise ALEPH are shown in the cut-away view in Figure 2.3 and are:

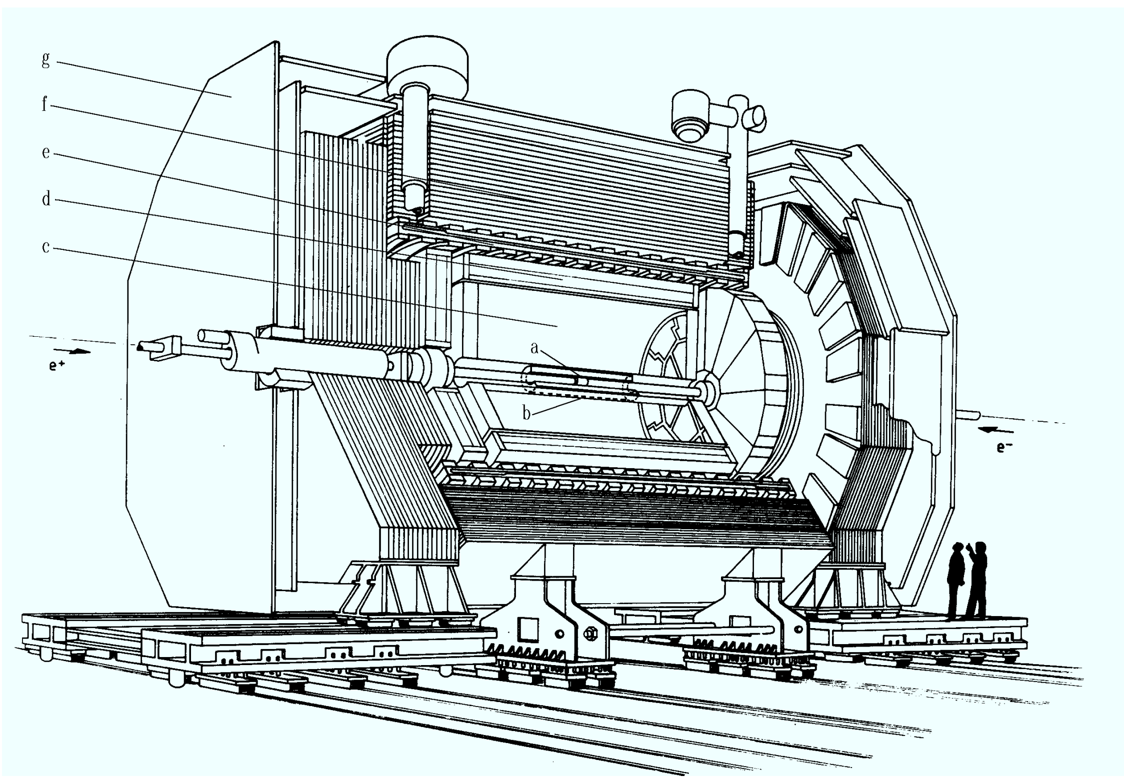

Figure 2.3: A cut-away view of the ALEPH detector with two people for scale. The following sub-detectors are indicated: (a) Vertex Detector, (b) Inner Tracking Chamber, (c) Time Projection Chamber, (d) Electromagnetic Calorimeter, (e) Superconducting Solenoid, (f) Hadron Calorimeter, (g) Muon Chambers.

- A Vertex Detector (VDET) to measure high precision coordinates for charged particles very close to the interaction point.
- An Inner Tracking Chamber (ITC) to perform fast tracking for trigger information.
- A Time Projection Chamber (TPC) to provide accurate three-dimensional tracking of charged particles and ionisation information for particle identification.
- A finely-grained Electromagnetic Calorimeter (ECAL) to identify and measure the energies of electrons and photons.
- A Superconducting Solenoid to produce a uniform magnetic field of 1.5 T that is essential for the measurement of particle momenta.
- A Hadron Calorimeter (HCAL) to determine the energies of hadrons and identify muons.
- Muon Chambers to assist in muon identification.
- Several luminosity calorimeters (LCAL, SICAL and BCAL) to measure the luminosity delivered by LEP.

The entire detector is about 11 m long, 10 m in diameter and weighs about 2800 tonnes. The conventional coordinate system used by ALEPH is defined with the origin at the nominal interaction point. The z-axis points along the direction of travel of the electron beam, the x-axis towards the centre of the LEP ring and the y-axis points almost vertically upwards.

The following sections briefly describe the principles and performance of the sub-detectors. More details may be found in [47, 48, 49, 50].

2.4 Tracking detectors.

Charged particles can interact electromagnetically with atoms in their path. If atomic electrons are released, then the application of an electric field can pull the electrons and ions apart towards electrodes and create an electrical signal. Further information can be deduced from the size and arrival time of the signal. This technique of observing the ionisation produced by charged particles in matter is used by gas detectors and solid-state detectors.

Gas detectors rely on avalanche amplification, which occurs when the electric field is so strong that the electrons (ions are typically too heavy) are accelerated to high enough velocities to create further electron-ion pairs through ionisation. The new electrons are also accelerated by the electric field, with the result that more and more atoms are ionised and an avalanche of electrons and ions develops. The charge created can be much greater than (by a factor of 10^6) but is still proportional to the original charge. This leads to the classic design for a gas detector - a gas-filled cylinder whose surface forms the cathode and with a central sense wire to form the anode. Note that most of the multiplication takes place in the regions of high electric field near the anode wire. A refinement is the multiwire chamber, where many anode wires are sandwiched between two cathode plates to form a flat chamber or cathode wires are arranged around each anode wire. In these configurations, the position of the charged particle is known from the position of the wire on which the signal pulse is detected.

Solid-state detectors are essentially reverse biased p-n silicon diodes and are capable of extremely good position resolution. The large number of electron-hole pairs from ionisation drift apart in the strong, internal electric field and produce a detectable current.

Once the trajectory of a charged particle is measured, the momentum can be deduced if the tracking detectors are inside a magnetic field. A charged particle moving in a magnetic field describes a helix whose radius is proportional to the component of the momentum perpendicular to the magnetic field and inversely proportional to the particle's charge. Since all the charged particles that are directly detectable with ALEPH have charge of magnitude 1, the size and sign of the radius of curvature is sufficient for the determination of the transverse momentum and charge of the particle.

The measurement of the direction and momentum of charged particles is performed in ALEPH by three different sub-detectors: the large-volume TPC, the fast ITC and the very precise solid-state VDET. These detectors are inside the superconducting solenoid, which provides a 1.5 T magnetic field parallel to the beam axis. The longitudinal component of this field has been measured to be uniform to within 0.2% in the tracking volume.

2.4.1 The Time Projection Chamber.

The TPC, shown in Figure 2.4, is the main tracking detector in ALEPH and provides three-dimensional tracking and good momentum resolution for charged particles. The axis of the chamber, which is 4.7 m long, is parallel to the magnetic field. The inner and outer radii are 0.31 m and 1.8 m, respectively, in order to obtain good momentum resolution at the highest energies. The chamber is filled with a mixture of argon (91%), which has desirable ionisation properties, and methane (9%), which prevents the avalanches from getting out of control, and is held at a slight over-pressure to prevent any contamination from the atmosphere. The electric drift field extends from each end-plate towards the central membrane that divides the chamber in half and is held at a potential of -27 kV. This membrane and a set of annular electrodes, situated on the inner and outer cylinder walls, create an extremely uniform electric field of 11 kV/m. Electrons from ionisation drift in tight spirals to the end-plates where multiwire chambers measure their arrival positions and times.

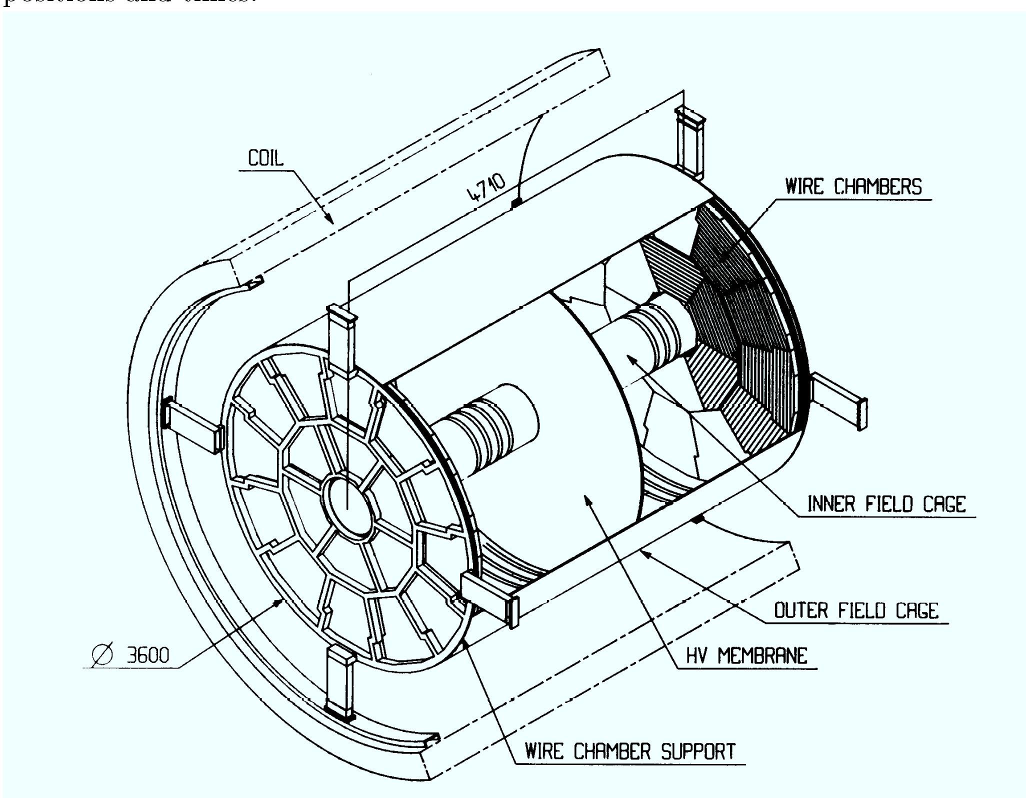

Figure 2.4: A cut-away view of the Time Projection Chamber, with the wire chambers on each end indicated, as well as the inner and outer field cages and the central membrane. The feet that attach the TPC to the Solenoid are also shown.

The structure of the multiwire chambers is shown in Figure 2.5. Cathode wires at 0 V form the boundary of the drift volume and the anode sense wires at +1250 V collect electrons from avalanches initiated nearby by the ionisation electrons. Cathode pads underneath the sense wires collect an induced signal and an accurate measurement of the $r\phi$ coordinate of the track is achieved by interpolation between the signal on different pads. The z coordinate is deduced from the arrival time of the pulse and the known electron drift velocity. With 21 concentric rings of pads, the TPC can provide up to 21 three-dimensional coordinates for charged particles.

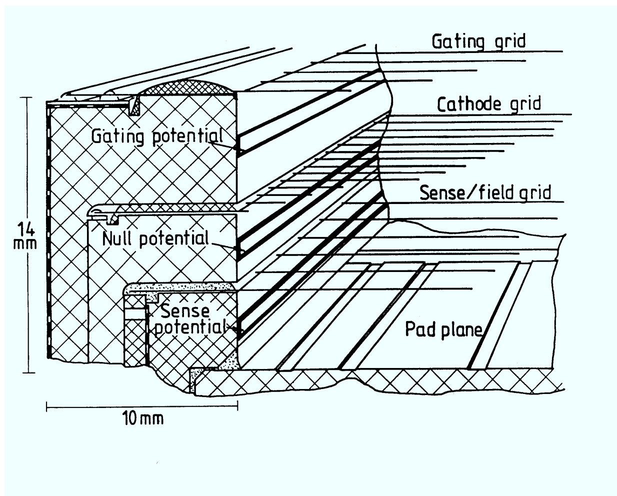

Figure 2.5: A section through a TPC sector edge, showing the pad plane, the wire grids and the potential strips.

The $r\phi$ coordinate resolution depends on the drift length and the angle of the track segment with respect to both the wires and the pads. The resolution on the z coordinate depends on the polar angle. For isolated leptons from leptonic Z^0 decays, the resolutions are $\sigma_{r\phi}$=173 μm and σ_z=740 μm for tracks at angles greater than 80° with respect to the beam axis. The measured dependence of the resolution has been parameterised and is used to calculate coordinate errors in the track helix fit.

The purpose of the plane of gating wires is to prevent the positive ions, which are produced in the avalanches close to the sense wires, from entering the main chamber and distorting the electric drift field. In the 'open' state, a potential of $V_g \approx -67$ V is placed on the gate wires so that the gate is transparent to the passage of charged particles. In the 'closed' state, the potentials $V_g \pm \Delta V_g \approx -67 \pm 100$ V are placed on alternate wires of the grid, so that the resulting dipole fields render the gate opaque to the passage of charged particles. The gate is opened 2 μs before a beam crossing is due and if a collision produced an interesting event (positive first level trigger after 5 μs - see Section 2.8) then the gate is held open for 45 μs to allow all the ionisation electrons to drift in and the TPC information to be collected. Otherwise, the gate is closed until the next beam crossing is due.

The TPC is equipped with a laser calibration system, shown in Figure 2.6. One Nd-YAG laser serves each half of the TPC, the output being divided into three equidistant beams in ϕ and then five beams in θ. The straight tracks of ionisation produced by the beams can be used to correct inhomogeneities in the electric and magnetic fields and to monitor the drift velocity.

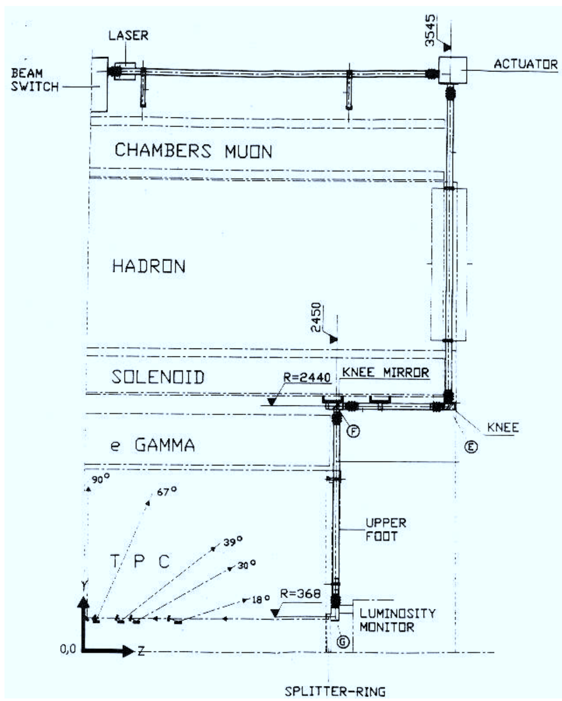

Figure 2.6: The TPC laser beam transport system.

The TPC can also separate particle species according to measurements of the energy loss by ionisation per unit distance, dE/dx, as the magnitude of the signals on the sense wires (up to 338 per track) is proportional to this quantity. Since the dE/dx depends only on the particle velocity for a given material, a combination of dE/dx and momentum information allows the mass and thus the identity of the charged particle to be deduced. Figure 2.7 shows the measured dE/dx for tracks from hadronic Z^0 decays.

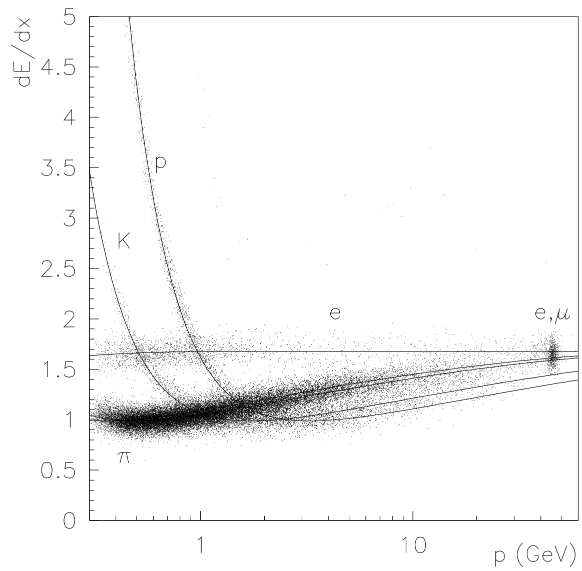

Figure 2.7: The measured dE/dx of tracks from hadronic Z^0 decays, with the fitted Bethe-Bloch curve for the different mass hypotheses overlaid.

2.4.2 The Inner Tracking Chamber.

The ITC provides the only tracking information that is used by the first level trigger (see Section 2.8) and up to 8 accurate coordinates in the $r\phi$ plane. The ITC lies inside the TPC and is a cylindrical, multiwire drift chamber that is 2 m long and has inner and outer radii of 13 cm and 29 cm respectively. The chamber is filled with a gas mixture of argon (80%), carbon dioxide (20%), which performs the same function as methane in the TPC, and a small amount of alcohol which has been found to retard the ageing process of the chamber.

The ITC contains 960 sense wires, which run parallel to the beam direction. The sense wires are held at a potential of about 1.8 kV and are surrounded by six earthed wires to form a hexagonal drift cell, as shown in Figure 2.8. The cells are arranged in eight layers, the inner four contain 96 cells each and the outer four contain 144 cells each. The time taken for the ionisation electrons to drift to the sense wire gives the $r\phi$ coordinate, with an average precision of 150 μm. The z coordinate is measured with an accuracy of about 5 cm by measuring the difference between the arrival times of pulses at the two ends of each sense wire.

For the first level trigger, the ITC has two associated processors that find charged

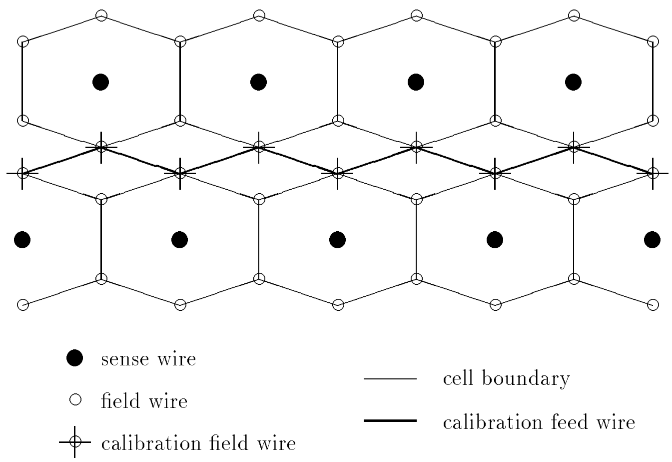

Figure 2.8: Schematic diagram of ITC drift cells showing the arrangement of the wires.

particle trajectories in two dimensions (the $r\phi$ projection) and three dimensions. The result from the 2D trigger is available within 1 μs and that from the 3D trigger within 3 μs of the beam crossing.

2.4.3 The Silicon Vertex Detector.

The VDET provides high precision measurements of charged particle trajectories close to the interaction point, so that long-lived particles can be identified by the displaced vertices of their decay products. A new VDET, shown in Figure 2.9, was installed at the end of 1995 and consists of two concentric layers, at radii of 6.3 cm and 11.0 cm, of silicon wafers with double-sided readout. The new detector extends the angular coverage, halves the passive material and is more radiation hard than the previous detector [51].

The inner and outer layers contain 9 and 15 faces respectively, each of which lies parallel to the beam axis and consists of six 6.5 cm long, 300 μm thick silicon wafers joined together. The angular acceptance is $|\cos\theta| \leq 0.95$ for tracks required to pass through at least one VDET layer. The wafers are divided into strips with a pitch of 25 μm and every strip acts like a reverse-biased p-n diode for detecting the passage of charged particles. The motion of the electron-hole pairs produced by the charged particle induces signals over several strips by capacitative coupling. Therefore, only every second strip is equipped with readout electronics and the coordinate for the particle track is obtained by interpolation with negligible loss in precision.

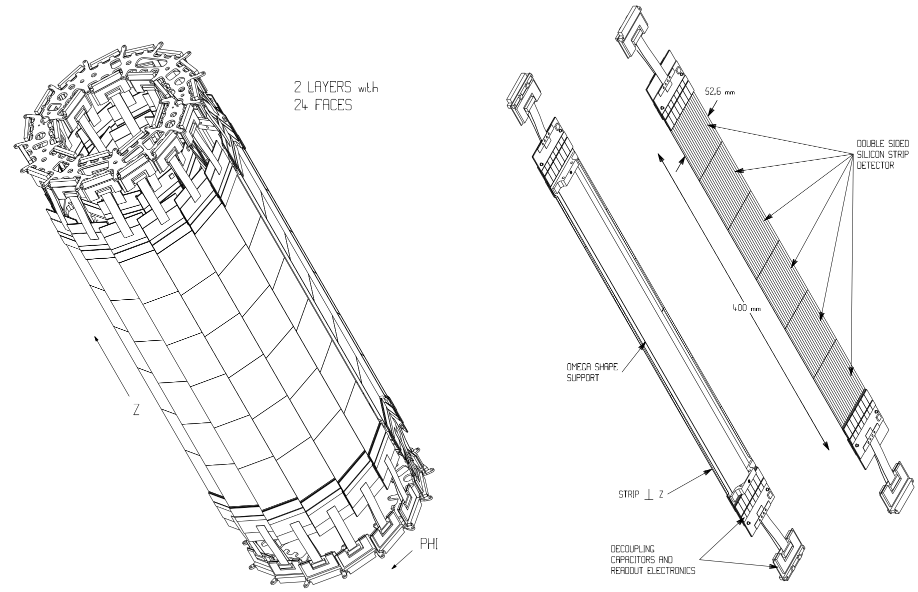

Figure 2.9: The Silicon Vertex Detector.

The strips lie parallel to the beam-axis on one side of the face, which provides a ϕ coordinate, and perpendicular on the other side, which provides a z coordinate. The known radius of the face provides the r coordinate. The coordinate resolutions measured from data are $\sigma_{r\phi}$=8 μm over the angular acceptance of the detector and σ_z=10 μm for tracks at angles greater than 80° to the beam axis [52].

2.4.4 Track reconstruction and momentum determination.

Using a combination of these three sub-detectors, the trajectory of each charged particle can be traced by a string of up to 31 three-dimensional coordinates. Nearby points in the TPC are connected by requiring that they are consistent with a helix hypothesis, which is then extrapolated to the ITC and the VDET and fitted to the points measured there. Figure 2.10 shows the parameters used to define the track in the helix fit:

- $1/R$ is the inverse of the radius of curvature of the particle trajectory in the xy plane. It is positive if the track bends counter-clockwise.

- $\tan\lambda$ is the tangent of the angle of the particle trajectory with respect to the xy plane: λ=90°-θ.

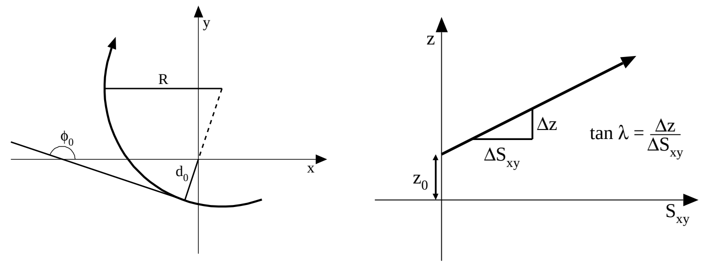

Figure 2.10: Definition of the helix parameters used to describe charged particle tracks. The quantity S_{xy} is the arc length traversed by the particle in the xy plane.

- d_0 is the distance of closest approach between the particle trajectory and the origin in the xy plane. It is signed according to the particle's angular momentum about the z axis at that point.
- ϕ_0 is the angle in xy plane that the particle trajectory makes with respect to the x axis at the point of closest approach.
- z_0 is the z coordinate at the point of closest approach.

The performance of the track reconstruction is studied using $Z^0 \to \mu^+\mu^-$ events, where at least 19 TPC, 6 ITC and 1 VDET coordinates are used in the track fit. With this sample, the transverse momentum resolution is measured to be [49]:

$$\sigma(p_T)/p_T = 0.6 \times 10^{-3} \times p_T/\mathrm{GeV/c}$$

The momentum resolution for the three tracking detectors is summarised in Table 2.1. At low momentum, multiple scattering adds a constant term of 0.005 to $\sigma(p_T)/p_T$. Since the error on the measurement of the polar angle is small, the relative error on the momentum coincides with the relative error on the transverse momentum.

Detector	$\sigma(p_T)/p_T^2$ (GeV/c)$^{-1}$
TPC	1.2×10^{-3}
TPC+ITC	0.8×10^{-3}
TPC+ITC+VDET	0.6×10^{-3}

Table 2.1: Momentum resolution of the ALEPH tracking detectors [49].

2.5 Calorimeters.

A calorimeter is a block of matter that is of sufficient thickness to cause the primary particle to interact and deposit all of its energy in a subsequent ‘shower’ of increasingly lower-energy particles. Calorimeters can measure the energy of photons, electrons, positrons and hadrons, but not neutrinos, which interact via the weak force only, or muons, which are too heavy to rapidly lose sufficient energy by radiation.

A high energy photon can interact with matter and convert to an e^+e^- pair, each of which can then radiate Bremsstrahlung photons, which may themselves convert into e^+e^- pairs and so on, rapidly creating an electromagnetic shower of particles. This process obviously occurs for incident electrons and positrons as well. The radiation length of a material, X_0, is the amount of material that reduces the mean energy of an electron by a factor of e and is given approximately in cm by $\frac{180A}{\rho Z^2}$, where A is the atomic weight, Z is the atomic number and ρ is the density of the material in gm/cm^3. To contain 98% of the energy of a 50 GeV electron requires 19 X_0 of material. Therefore, high-Z, dense materials, like lead with X_0=0.56 cm, are normally used to make a compact electromagnetic calorimeter that stops photons, electrons and positrons. The transverse size of the electromagnetic shower is narrow and roughly 95% of the shower is contained in a cylinder with radius 3 cm in lead. In order to extract a signal, the material creating the electromagnetic shower can be interspersed with detectors that measure the ionisation from the charged particles in the shower, which is proportional to the energy of the incident particle.

Hadrons can interact via the strong force with matter to produce more hadrons, mainly pions, protons and neutrons. These may themselves interact to produce yet more hadrons or if the hadron in question is a π^0 decay to two photons and create an electromagnetic shower. The characteristic distance of hadronic showers is the nuclear interaction length, λ_{int}, which is the mean distance between nuclear interactions and is given approximately in cm by $35A^{\frac{1}{3}}/\rho$. To contain 98% of the energy of a 50 GeV proton requires 8 λ_{int}. Since iron and lead both have λ_{int}=17 cm, iron is typically used to lessen the mechanical stress from supporting the weight of the large hadronic calorimeter. The transverse size of the hadronic shower is large and roughly 95% of the shower is contained in a cylinder with radius 17 cm in iron. Again, the material creating the hadronic shower can be interspersed with detectors that measure the ionisation from the charged particles in the shower, though the resolution on the incident hadron energy is worse due to fluctuations in the type of particles (pions, neutrons, protons, muons, neutrinos) in the hadronic shower and energy losses of the order of 20% from nuclear binding effects.

The sampling of the energy deposited by a shower in a calorimeter is a statistical process and the number of samples is proportional to energy, E, of the incident particle, which implies that the energy resolution is proportional to $\sqrt{E}$. Therefore, the relative energy resolution improves as the square root of the energy of the incident particle. This is to be contrasted with the relative momentum resolution from tracking detectors, which worsens as the first power of the momentum of the charged particle.

The ALEPH calorimeters are located in a barrel around the TPC and in two end-caps, as shown in Figure 2.11. The electromagnetic calorimeter is designed to stop photons, electrons and positrons but not hadrons, which are stopped by the hadronic calorimeter. The superconducting solenoid, which is 1.6 X_0 and 0.4 λ_{int} thick, lies between the electromagnetic and the hadronic calorimeters.

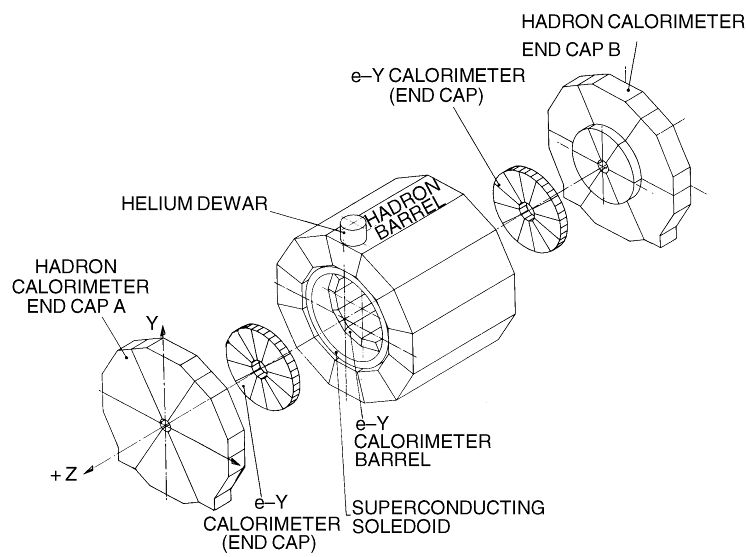

Figure 2.11: The Electromagnetic Calorimeter surrounded by the Superconducting Solenoid and the Hadron Calorimeter.

2.5.1 The Electromagnetic Calorimeter.

The ECAL is a sampling calorimeter that is 22 X_0 thick and comprises 45 layers of lead and gas-filled proportional chambers. The barrel is a 4.8 m long cylinder with inner and outer radii of 1.85 m and 2.25 m respectively. The end-caps complete the solid angle coverage of 3.9π. The barrel and each end-cap consist of 12 modules, each subtending 30° in azimuth. The end-cap modules are offset by 15° in ϕ with respect to the barrel and all modules are rotated by 1.9° in ϕ with respect to the hadron calorimeter in order to minimise the overlap of cracks, which represent 2% of the inner surface of the barrel and 6% of the end-cap surface.

The structure of one ECAL layer is shown in Figure 2.12. The proportional wire chambers contain a gas mixture of xenon (80%) and carbon dioxide (20%). The charged particles in the electromagnetic shower cause ionisation avalanches around the proportional wire chambers. The total charge collected is proportional to the energy of the incident particle. The signals from the anode sense wires are used for triggering whilst energy and position information is taken from the signals induced on pads, into which one cathode plane of each wire chamber is segmented. Pads from consecutive layers are connected into towers that point towards the interaction point, each with an angular coverage of about $0.9^\circ \times 0.9^\circ$. Every tower is divided into three storeys in depth that cover four, nine and nine radiation lengths each.

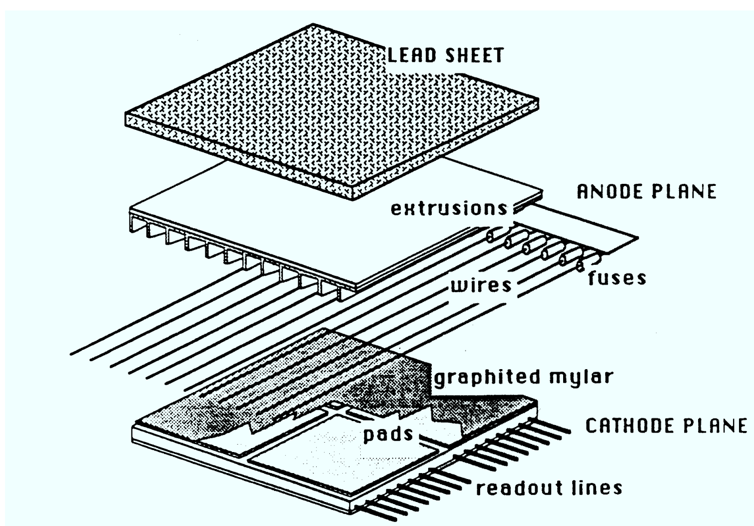

Figure 2.12: Schematic of an ECAL layer.

The fine granularity of ECAL, which is very important for the identification of electrons, photons and neutral pions, allows an angular resolution of [49]:

$$\sigma_\phi = \frac{\sigma_\theta}{\sin\theta} = \left(0.25 + \frac{2.5}{\sqrt{E/GeV}}\right) \text{ mrad.}$$

The electron energy resolution is estimated by comparing the measured energy to the track momentum, in $e^+e^-\rightarrow Z^0 \rightarrow e^+e^-$events, and is parameterised as [49]:

$$\frac{\sigma_E}{E} = 0.009 + \frac{0.18}{\sqrt{E/\mathrm{GeV}}}$$

2.5.2 The Hadronic Calorimeter and the Muon Chambers.

The HCAL is also a sampling calorimeter that is 7.2 λ_{int} thick and comprises 23 layers of iron and gas-filled streamer tubes. The barrel section, which is 7.3 m long with inner and outer radii of 3 m and 4.7 m respectively, is outside the Superconducting Solenoid. The iron thus provides a return path for the lines of magnetic flux as well as forming a passive filter for muons. The barrel is made of 12 modules and the end-caps of 6 modules each.

The streamer tubes are similar to proportional wire chambers, but operate at a higher voltage, which means that the size of the signal is independent of the particle energy. Therefore, the total charge collected is proportional to the number of charged particles in the hadronic shower. Each streamer tube consists of eight 0.9×0.9 cm^2 cells that are 700 cm long in the barrel section. An anode wire runs along the middle of each cell and operates at a potenial of 4250 V. The streamer tubes contain a gas mixture of argon (13%), carbon dioxide (57%) and butane (30%). As with ECAL, cathode pads are connected into projective towers that point towards the interaction point, each with an angular coverage of about $3.7^\circ\times 3.7^\circ$. The energy resolution for pions at normal incidence is [49]:

$$\frac{\sigma_E}{E} = \frac{0.85}{\sqrt{E/\mathrm{GeV}}}$$

On the cathode plane opposite to the pads, a 4 mm wide strip runs parallel to each wire and provides a digital signal if a streamer tube has fired at least once. This gives a two-dimensional picture in the $r\phi$ plane of the development of the shower and is useful for identifying muons, which pass through the HCAL leaving only an ionisation trail.

Muon identification is completed by the muon chambers, which are two planes of double-layer streamer tubes, one of which is shown in Figure 2.13, beyond the last layer of iron in HCAL and separated by 40-50 cm. The chambers do not provide an energy measurement but give x and y coordinates for tracks by means of strips on the two cathode planes. The typical accuracy on the muon exit angle is 10 mrad.

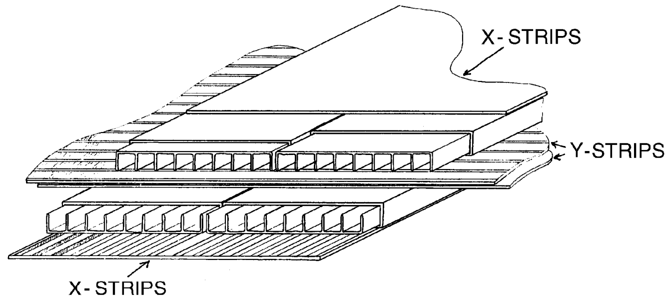

Figure 2.13: A Muon Chamber double layer.

2.6 Lepton identification.

2.6.1 Electron identification.

Electron identification is performed using two independent and complementary measurements: the dE/dx measurement from the TPC and the energy deposition in the ECAL, compared to the track momentum and the expected shape of the shower. Note that the dE/dx information is more discriminant at low momentum and the shape of the showers in the ECAL at high momentum. The basic information is expressed in normally distributed estimators, which are described here. The approach chosen to select electrons in $e\bar{\nu}q\bar{q}$ events is discussed in Section 3.1.4.

The dE/dx estimator is:

$$R_I = \frac{I - <I>}{\sigma_I}$$

where I is the measured dE/dx, $<I>$ is the expected dE/dx for an electron and σ_I is the resolution on dE/dx. Tracks are required to have at least 50 measurements of dE/dx in order to ensure a reliable calculation of R_I.

The R_T estimator exploits the compactness of the electromagnetic energy deposition transverse to the particle direction. R_T is defined using the four towers in ECAL closest to the extrapolated track in each storey:

$$R_T = \frac{E_4/p - <E_4/p>}{\sigma_{E_4/p}}$$

where E_4 is the total energy deposited in the selected towers, p is the momentum of the charged track measured by the tracking detectors, $<E_4/p>$ is the mean energy fraction deposited by an electron in the four central towers and $\sigma_{E_4/p}$ is the resolution expected for this ratio.

The R_L estimator measures the degree to which the observed longitudinal shower profile matches that expected for an electron. R_L is based on the inverse of the mean position of the longitudinal energy deposition in the shower:

$$X_L = \frac{E_4}{\sum_{i=1}^{4}\sum_{j=1}^{3} E_j^i S_j}$$

where E_j^i is the energy deposited in selected tower i of storey j in depth of the calorimeter and S_j is the mean depth of energy deposition in that storey. The estimator R_L is then defined by:

$$R_L = \frac{X_L - < X_L >}{\sigma_{X_L}}$$

Figure 2.14 shows the distribution of R_T versus R_L for a sample of tracks enriched in photon conversions. The electron and hadron contributions are clearly separated.

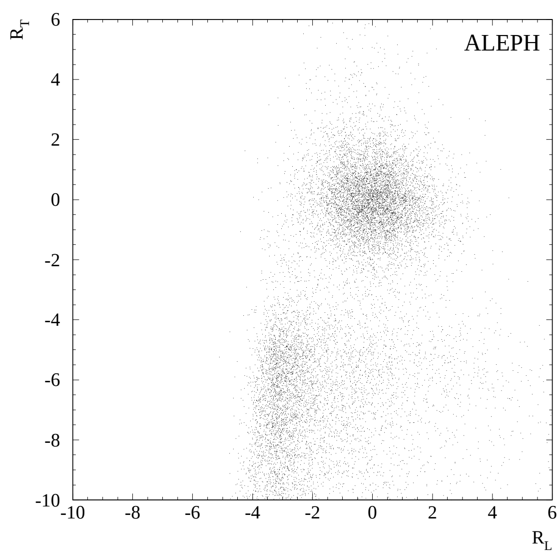

Figure 2.14: Distribution of the electron estimators R_T and R_L for a sample of tracks enriched in photon conversions. The electron contribution is the upper concentration and the hadron contribution is the lower concentration.

2.6.2 Muon identification.

Muon identification is performed using the tracking capabilities of the hadron calorimeter and the information from the muon chambers, which are described here. The approach chosen to select muons in $\mu\bar{\nu}q\bar{q}$ events is discussed in Section 3.1.4.

Charged particle tracks are extrapolated (as if they were a muon) through the calorimeter material taking into account a detailed magnetic field map and estimated energy losses. A 'road' is opened around the extrapolated track, with a width of three times the estimated extrapolation uncertainty due to multiple scattering. A calorimeter plane is said to be expected to fire if the extrapolated track intersects it within an active region and the plane is said to have fired if a digital hit lies within the multiple scattering road. For a hit to be counted, the number of adjacent firing tubes must not be greater than three.

The cuts used to define a penetrating track are $N_{fire}/N_{exp} \geq 0.4$, $N_{exp} \geq 10$ and $N_{10} > 4$, where N_{fire}, N_{exp} and N_{10} are, respectively, the number of actually firing planes, the number of expected planes and the number of firing planes within the last ten expected for the track. Figure 2.15 shows the distributions of the above quantities for isolated muons from $Z^0 \rightarrow \mu^+\mu^-$ events and pions from τ decays. The variable X_{mult}, which represents the average hit multiplicity per fired plane, enhances the discrimination for muons in hadronic jets and must be less than 1.5.

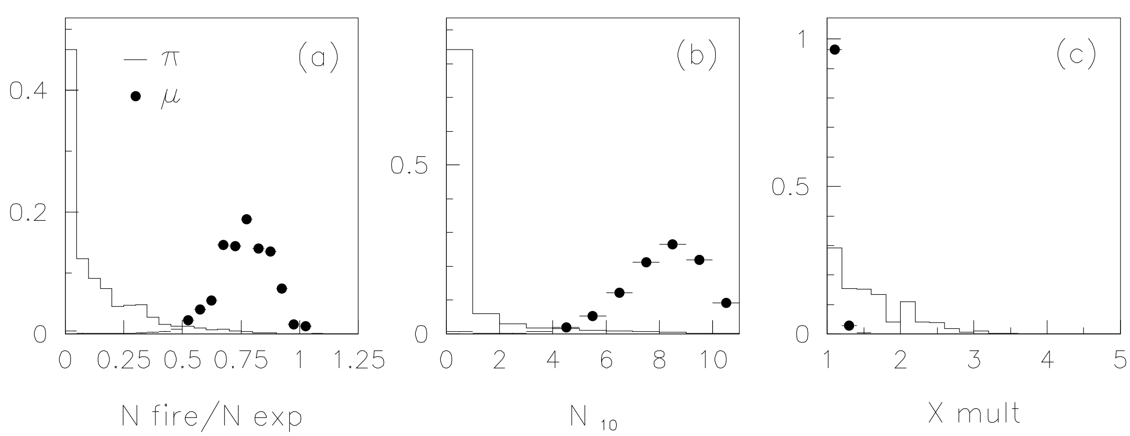

Figure 2.15: Distribution of (a) N_{fire}/N_{exp}, (b) N_{10} and (c) X_{mult}, for muons (dots) and pions (solid line), with N_{exp} greater than 10. The plots have been normalised to equal areas and the vertical scale is arbitrary.

In addition to the above, each muon chamber measures two orthogonal coordinates for a penetrating track. The track is said to hit a muon chamber if the distance between the muon chamber coordinate and the extrapolated track is less than four times the estimated standard deviation from multiple scattering.

2.7 Luminosity determination.

The luminosity is determined using elastic e^+e^- scattering at small angles (Bhabha scattering) since the cross section is known theoretically to high precision. The rate of Bhabha scattering is measured by the simultaneous detection of the e^+ and the e^- on opposite sides of the detector. The luminosity is given by the ratio of the measured rate to the cross section.

ALEPH has three luminosity calorimeters, which are situated close to the beam-pipe at each end of the detector. The most accurate is a silicon tungsten calorimeter, SICAL, with a polar angle acceptance of 25-58 mrad. However, at LEP2 part of this acceptance is obscured by a tungsten shield, which protects ALEPH from the increased level of background from synchrotron radiation. Therefore the luminosity measurements at LEP2 are provided by LCAL, which is a lead/proportional wire chamber device similar in design and operation to the ECAL. This detector lies behind SICAL at a distance of 2.62 m from the interaction point and has a polar angle acceptance of 45-190 mrad. The angular resolution of LCAL is worse than that of SICAL, which affects the luminosity measurement since the Bhabha cross section is strongly dependent on the polar angle. The luminosity precision at LEP2 is thus $\sim$0.4% instead of $\sim$0.1%.

The third luminosity calorimeter, BCAL++, is situated about 7.7 m on either side of ALEPH beyond the LEP magnetic quadrupoles and covers a range in polar angle where the rate from Bhabha scattering is roughly twenty times higher than that for LCAL and SICAL. The polar angles of the electrons and positrons are not precisely known since the field of the quadrupoles changes during LEP operation. Therefore, BCAL++ is calibrated relative to LCAL and uses the higher rate of Bhabha scattering to provide online monitoring of the relative LEP luminosity during data-taking.

2.8 Data collection and reconstruction.

In order to make use of the ALEPH detector, information from all of the sub-detectors must be collected, stored and then combined to make a complete picture of each event. Timing constraints dictate that not every collision can be recorded, so a trigger system is necessary to select the most interesting events.

The trigger design is influenced by two time scales: the interval between LEP bunch crossings (22 μs) and the time taken to read out the detector (45 μs), which is the time taken for ionisation electrons in the TPC to drift from the centre to the end-plates. It is important to keep the trigger rate from background (noise, cosmic rays and beam-gas interactions) low both to minimise the dead time during which a new event cannot be recorded, because the detector is already being read out, and the time that the TPC gate is open, for the effective operation of the TPC.

The ALEPH trigger is designed to operate on three levels to accept any genuine e^+e^- annihilation event and to reduce the rate of recorded background events to a manageable level of 1-2 Hz. At LEP2, the sub-detector thresholds are set low enough to trigger on the interesting events but only cause first level triggers at a rate below 2 Hz. Therefore, the second and third level triggers only reject a small fraction of events.

The first level trigger is based on information from the ITC, ECAL and HCAL sub-detectors and is available within 5 μs of the bunch crossing so that a first-level rejection does not introduce any dead time. Acceptance at first-level prevents the TPC gate from closing so the ionisation electrons already drifting towards it still pass freely. Semileptonic WW decays, studied by the analysis presented in this thesis, are selected with an efficiency close to 100% by one or more of the following triggers:

- Total-energy trigger: energy deposits in ECAL greater than $\sim$6 GeV in the barrel, $\sim$3 GeV in either end-cap or $\sim$1.5 GeV in both end-caps.
- Electron-track trigger: track segments in the ITC in coincidence with an energy deposit in the module of ECAL to which the track is pointing.
- Muon-track trigger: track segments in the ITC in coincidence with an energy deposit in the module of HCAL to which the track is pointing.

The second level trigger replaces the ITC track information with that from the TPC, analysing the signals during the drift time so that a decision is made within 50 μs of the bunch crossing. If the event is rejected, the detector is reset and ready to accept data two bunch crossings after the one that passed the first level trigger. If the event is accepted, then full readout of the detector is initiated.

The ALEPH data acquisition system is designed to make each sub-detector autonomous during development and data-taking. A hierarchical structure means that information flows downstream or upstream from each readout component without communication between components at the same level. This system means that while a given stage is analysing data from one event, the component downstream can readout the next event and the component upstream can finish processing the previous event. The data from the sub-detector electronics flows to a sub-detector Event Builder and then to the Main Event Builder, or MEB. Each sub-detector reads out at a different speed, so the MEB has to synchronise the information for each event and to check that it is complete. The data is then passed to the third level trigger, which checks the decision made at second level and performs data reduction, and finally to the main computer, where it is stored on magnetic tape and held available for online analysis and monitoring of the detector performance.

The raw information collected by the data acquisition system has to be processed to provide a picture of the tracks and energy depositions in each event. This task is performed on a dedicated computer system with the JULIA (Job to Understand Lep Interactions in ALEPH) program, which:

- Reconstructs charged tracks.
- Calculates their dE/dx from the TPC wire information.
- Reconstructs the primary vertex and V^0 candidates.
- Clusters calorimeter energy deposits and performs an energy flow analysis.
- Identifies electrons, muons and photons.

This event reconstruction takes place within a few hours of the time the event occurred in the ALEPH detector.

2.9 Energy flow calculation.

The aim of energy flow is to combine measurements of track momenta, calorimeter energy deposits and particle identification to improve the resolution on the visible energy from hadronic Z^0 decays at LEP1. The energy flow algorithm builds a list of 'energy flow objects' (electrons, muons, photons, charged and neutral hadrons), which should closely resemble the stable particles actually produced in an e^+e^-collision, in a number of steps summarised below. A more detailed description of the algorithm and its performance at LEP1 can be found in [49].

The first step rejects badly reconstructed charged tracks and calorimeter noise, before extrapolating the good quality charged particle tracks to the calorimeters in order to group topologically connected tracks and calorimeter energy deposits together into 'calorimeter objects'. These objects are classified in the following steps:

- The charged particle tracks identified as electrons [49] and the associated energy deposit in ECAL are removed from the calorimeter object list. If the difference between the calorimeter energy and the track momentum is three times larger than the expected resolution, the excess is assumed to come from a Bremsstrahlung photon and is counted as neutral electromagnetic energy.

- The charged particle tracks identified as muons [49], a maximum of 1 GeV from the closest associated energy deposit in ECAL (if any) and a maximum of 0.4 GeV per fired plane around the extrapolated muon track from the corresponding HCAL energy deposit are removed from the calorimeter object list.

- Identified photons and π^0's [49] are counted as neutral electromagnetic energy and removed from the calorimeter object list.

- The only particles left in the calorimeter object list should be charged and neutral hadrons. Charged hadrons are easily identified with the remaining particle tracks, where the pion mass is assumed. Neutral hadrons are identified as a significant excess of calorimetric energy. The sum of the energy remaining in the calorimeters, after first scaling the ECAL contribution by the ratio of the response to electrons and pions (1.0:1.3:1.6 in the first, second and third storeys in order to account for unidentified low-energy photons), is compared to the energy of the remaining charged particle tracks. Any excess that is both larger than the expected calorimeter resolution and 0.5 GeV is then counted as neutral hadronic energy.

2.10 Monte Carlo simulation.

The production of simulated Monte Carlo events is necessary for many analyses, including the one presented in this thesis. A brief description of the ALEPH simulation procedure is given here.

Firstly, the physics process is generated using a specific program (see Section 3.1.1), which includes the production and decays of the short-lived particles involved. For instance, the various simulation stages are shown for a semileptonic WW decay in Figure 2.16:

I represents the pair production of two resonant W bosons and their subsequent decay to quarks and leptons. This stage is well described by the electroweak theory.

II represents the radiation of gluons by the quarks and is described by QCD.

III represents the confinement of coloured quarks and gluons to colourless hadrons. Since α_s exceeds unity here, exact calculations by perturbation theory are no longer possible and phenomenological models like JETSET [11] or HERWIG [53] have to be used instead.

IV represents the decay of unstable hadrons created during the fragmentation process into the more stable hadrons that will actually be seen in the detector.

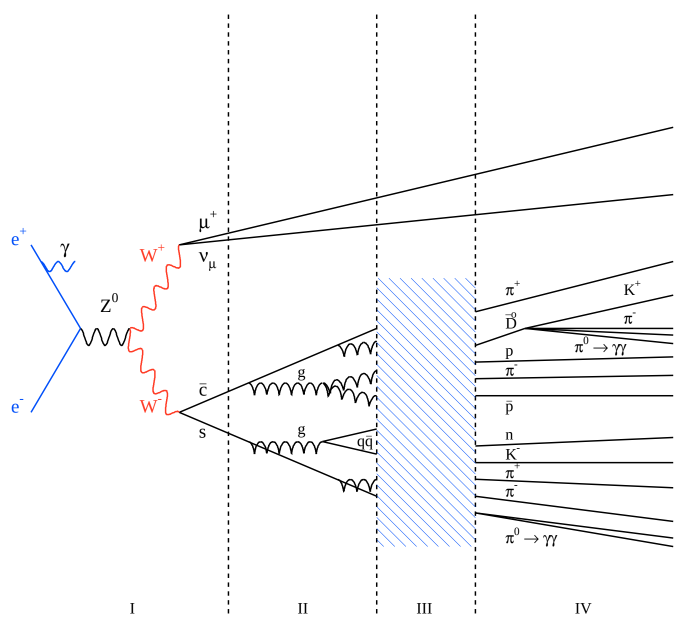

Figure 2.16: Different stages of the simulation of the process $e^+e^- \rightarrow W^+W^- \rightarrow \mu\bar{\nu}q\bar{q}$.

Secondly, the response of the detector to these particles is simulated using the GALEPH program, which is based on the GEANT package [54]. GALEPH simulates the interactions of the particles with the detector material and accounts for the effects of detector geometries and magnetic fields. The output from GALEPH has exactly the same formal structure as that from the ALEPH detector for data events, so that simulated events can be reconstructed in exactly the same way as the data. The responses and efficiencies of the different sub-detectors are carefully tuned to match the data. Since the LEP centre-of-mass energy and features of the detector change from year to year, new Monte Carlo is produced each year.

2.11 Summary.

The LEP collider is designed to produce the electroweak bosons, $W^{\pm}$ and Z^0, and ALEPH is one of four experiments at LEP constructed to study the properties of these bosons. The ALEPH data analysed in this thesis is collected at centre-of-mass energies of 172 GeV and 183 GeV, where W bosons are pair-produced. The current precision on the LEP beam energy, which is vital to the W mass measurement, is $\sim$24 MeV.

The ALEPH detector is designed to study e^+e^- collisions up to centre-of-mass energies of 200 GeV. The main features are the accurate momentum and vertex resolution of the tracking chambers and the hermeticity and fine granularity of the calorimeters. The tracking system includes the world's largest time projection system and the first double-sided silicon vertex detector. The analysis presented in this thesis uses the excellent tracking system and the good calorimetry to directly reconstruct the W decay products in semileptonic WW events. The lepton identification information from the TPC, the calorimeters and the muon chambers is used in the selection of semileptonic WW events.

Chapter 3

Semileptonic event selection.

This chapter covers the development of a selection for $e^+e^-\rightarrow W^+W^-\rightarrow e\bar{\nu}q\bar{q}$ and $e^+e^- \rightarrow W^+W^- \rightarrow \mu\bar{\nu}q\bar{q}$ events, which are referred to as semileptonic WW events throughout this thesis unless specifically stated otherwise, at $\sqrt{s} = 172$ GeV and the subsequent evolution of the selection to $\sqrt{s} = 183$ GeV.

3.1 Semileptonic event selection at $\sqrt{s} = 172$ GeV.

The characteristic features of $e^+e^-\rightarrow W^+W^- \rightarrow e\bar{\nu}q\bar{q}$ and $e^+e^- \rightarrow W^+W^- \rightarrow \mu\bar{\nu}q\bar{q}$ events are a high energy, isolated lepton, two or more jets and a large amount of missing energy due to the neutrino, as shown in Figure 3.1. The branching ratio for semileptonic WW decays is 29%, which implies that the cross section is approximately 3.6 pb. This is over thirty times smaller than that for the main background process of $e^+e^-\rightarrow Z/\gamma\rightarrow q\bar{q}(\gamma)$. Therefore, a highly discriminant selection is required to obtain a pure sample of semileptonic WW decays with a good efficiency.

The Monte Carlo and data samples are described briefly in the next section. The selection, which consists of a number of stages, is then discussed in the following sections.

3.1.1 Monte Carlo and data samples.

The KORALW, version 1.21 [55], event generator is used to produce the four-fermion (4-f) final states that can come from WW production and decay at a number of values for the W mass. The 4-f diagrams are computed by the GRACE [56] package with fixed W and Z widths. This program includes multi-photon initial state radiation (ISR) with finite

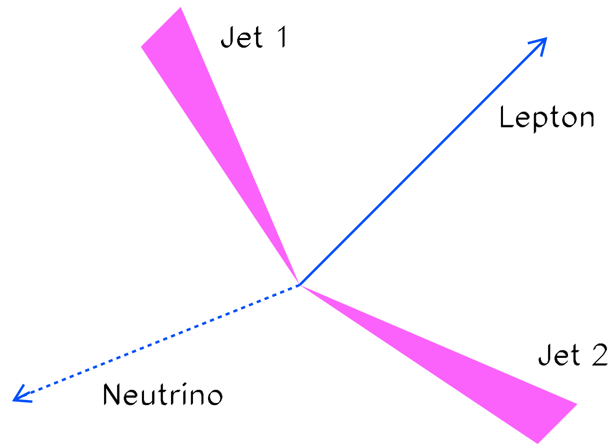

Figure 3.1: Schematic of the topology of semileptonic WW decays.

photon transverse momentum via Yennie-Frautschi-Suura exponentiation [57], final state radiation (FSR) via PHOTOS [58] and the effect of the Coulomb attraction between the W bosons [59]. The JETSET [11] package takes care of gluon radiation and hadronisation. Colour flow reconnection is not included. Loose cuts are applied at the generation level on the outgoing electron angle or the fermion-antifermion pair invariant masses to avoid regions of phase space with poles in the cross section. Events produced in these regions would in any case be rejected by the selection cuts. The KORALW program can be restricted to the lowest-order CC03 processes and is used in this form to generate a sample of events from which the selection efficiency is determined, thus eliminating the dependence on the particular generator cuts used for the 4-f simulation.

Monte Carlo samples, with integrated luminosities corresponding to at least twenty times that of the data, are fully simulated for all background reactions. Annihilations into quark pairs, $e^+e^-\rightarrow Z/\gamma\rightarrow q\bar{q}(\gamma)$, are simulated with PYTHIA [11]. KORALZ [60] and UNIBAB [61] are used for dilepton final states. PYTHIA is also used to simulate the $e^+e^-\rightarrow ZZ$, Ze^+e^- and $We\nu_e$ processes, all of which lead to four fermions in the final state. Events with a flavour content that could originate from WW production are specifically rejected from the ZZ sample. Two-photon ($\gamma\gamma$) reactions into leptons and hadrons are simulated with the PHOT02 [62] and PYTHIA generators. The minimum invariant mass is 3.5 GeV/c^2 and the minimum lepton transverse momentum is 0.15 GeV/c for leptonic final states. The minimum invariant mass is 30 GeV/c^2 for hadronic final states. The cross sections and number of events simulated for all of the processes are given in Table 3.1.

Process	Cross section (pb)	Number of events
$e^+e^- \to W^+W^-$		
4-f M_W= 79.25 GeV/c^2	13.27	120,000
4-f M_W= 79.75 GeV/c^2	12.97	10,000
4-f M_W= 80.00 GeV/c^2	12.81	10,000
4-f M_W= 80.25 GeV/c^2	12.63	120,000
4-f M_W= 80.50 GeV/c^2	12.46	10,000
4-f M_W= 80.75 GeV/c^2	12.24	10,000
4-f M_W= 81.25 GeV/c^2	11.80	120,000
CC03 M_W= 80.25 GeV/c^2	12.38	10,000
$e^+e^- \to Z/\gamma \to q\bar{q}(\gamma)$	121.1	75,000
$e^+e^- \to Z/\gamma \to \tau^+\tau^-(\gamma)$	10.8	5,000
$e^+e^- \to Z/\gamma \to \mu^+\mu^-(\gamma)$	11.1	5,000
$e^+e^- \to e^+e^-(\gamma)$	1186.	300,000
$e^+e^- \to ZZ$	3.066	3,000
$e^+e^- \to Ze^+e^-$	6.520	7,000
$e^+e^- \to We\nu_e$	0.483	1,000
$\gamma\gamma \to e^+e^-$	1810.	300,000
$\gamma\gamma \to \mu^+\mu^-$	1810.	300,000
$\gamma\gamma \to \tau^+\tau^-$	1810.	100,000
$\gamma\gamma \to q\bar{q}$	1600.	200,000

Table 3.1: Generated cross sections and number of events for all signal and background processes considered.

The integrated luminosity of 10.65 ± 0.08 pb^{-1} was collected by the ALEPH detector at LEP in 1997 at a mean centre-of-mass energy of 172.09 ± 0.06 GeV, with 1.11 pb^{-1} at 170.28 GeV and 9.54 pb^{-1} at 172.30 GeV. The VDET, ITC, TPC, ECAL and HCAL detectors and the luminosity monitors must all be operational for this data set. Any events with data acquisition errors are also excluded.

3.1.2 Preselection.

The aim of the preselection is to reject as much background as possible and to retain more than 99% of the signal semileptonic WW decays. This aim is achieved in two stages.

The first stage is to require at least five charged tracks reconstructed in the TPC that satisfy the following requirements:[1]

- The fit to the track helix must use at least four three-dimensional points in the TPC. This eliminates most fake or badly-fitted tracks.

- The track helix must pass through a cylinder centred around the fitted average interaction point, with a radius of 2 cm and a length of 20 cm. This rejects badly fitted tracks, particles originating far from the interaction point and cosmic ray background.

- The angle between the track and the beam axis must satisfy $|\cos\theta| < 0.95$. This ensures that at least six of the TPC pad rows are traversed by the track.

In addition, the total energy of all the good charged tracks should be more than 10% of the LEP energy. This removes two-photon events and beam-gas interactions. The number of good charged tracks and their total energy is shown in Figure 3.2 after the above criteria have been satisfied.

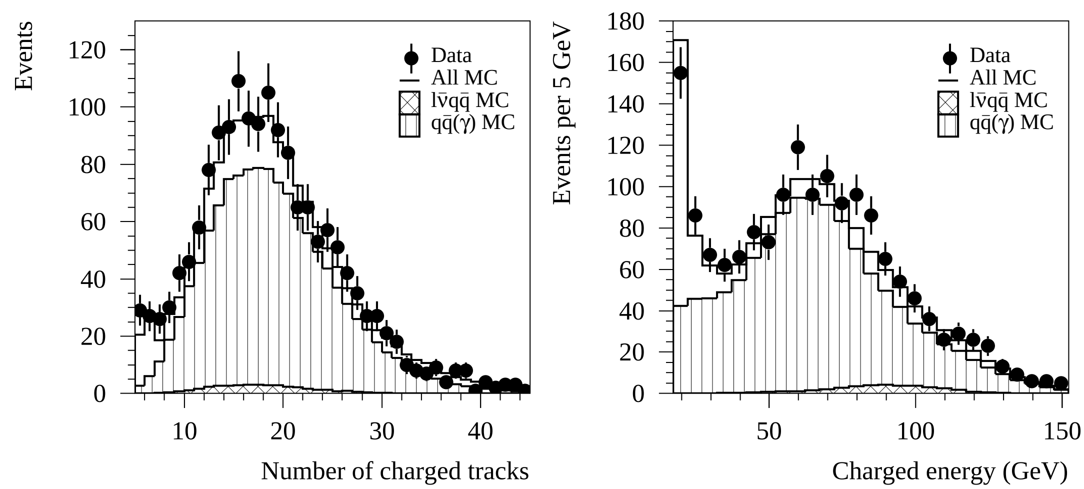

Figure 3.2: Number of good charged tracks and their total charged energy.

The second stage uses the missing momentum and the missing energy to discriminate between signal and background events. The missing momentum, $\not{p}$, is defined as the vector equal and opposite to the sum of the momenta of all the energy flow objects in each event. Likewise, the missing energy, $\not{E}$, is defined as the LEP energy minus the sum of the

[1]The tracks that meet these requirements will be called good charged tracks throughout this thesis.

energies of all the objects in each event. Figure 3.3 shows the missing energy, the missing momentum and the missing momentum components transverse and parallel to the beam axis.

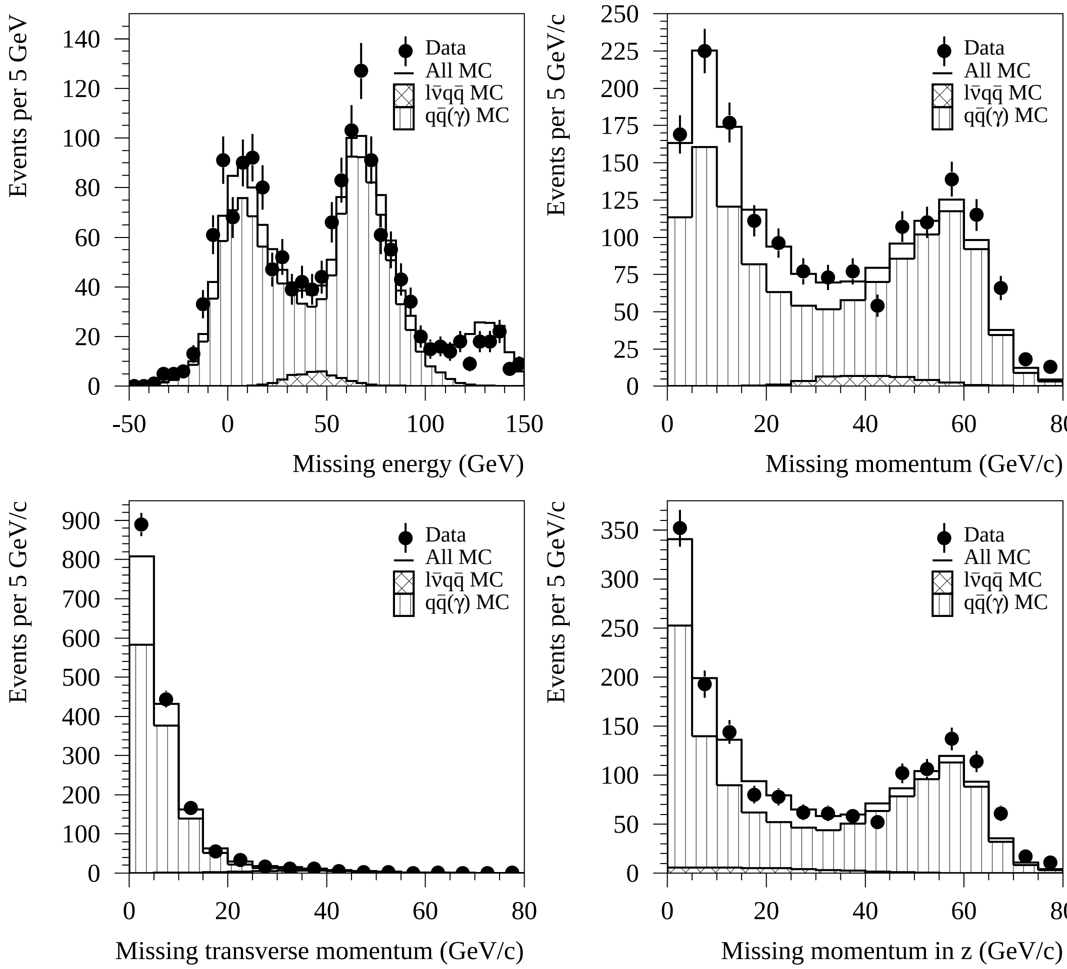

Figure 3.3: Missing energy, missing momentum, and the missing momentum components transverse and parallel to the beam axis.

In semileptonic WW decays, the neutrino has an energy in the range 20-70 GeV and is distributed almost isotropically in the detector. Therefore the missing energy is large and the missing momentum has no preferred direction as shown in Figure 3.3. This Figure also shows that the background $e^+e^-\rightarrow Z/\gamma\rightarrow q\bar{q}(\gamma)$ process has two distinct topologies, corresponding to the two peaks in the missing energy and momentum distributions, which results from the sharp drop in the cross section away from the Z resonance. This favours the radiation of energetic photons that boost the effective e^+e^- centre-of-mass energy back to the Z mass. In order for such a radiative return to occur at $\sqrt{s} = 172$ GeV, the photon has to carry off an energy of approximately 62 GeV. Most radiative return photons, which are preferentially emitted at a small angle with respect to the beam direction, miss the detector. This results in large values for both the missing energy and the missing momentum component parallel to the beam axis, which produces one peak in Figure 3.3. Non-radiative events and events that are completely within the detector acceptance should essentially have no missing energy or momentum and thus produce the second peak.

The kinematics of radiative return events can be used to design a cut on the longitudinal momentum that scales automatically to higher LEP energies [63]. Assuming the radiative return photon is collinear with the beam-axis, the four-vectors of the radiative return photon can be written as $(0, 0, p_{3\gamma}, E_\gamma)$, the Z boson as $(0, 0, p_{3Z}, E_Z)$ and the original e^+e^- state as $(0, 0, 0, \sqrt{s})$. Then, by energy and momentum conservation:

$$p_{3Z}^2 = p_{3\gamma}^2 = E_\gamma^2 = (\sqrt{s} - E_Z)^2 \tag{3.1}$$

Using this to substitute for p_{3Z} in:

$$E_Z^2 = p_{3Z}^2 + m_Z^2 \tag{3.2}$$

and solving for E_Z gives the expected values for E_Z and E_γ in a radiative return event:

$$E_Z = \frac{\sqrt{s}}{2}(1 + \frac{m_Z^2}{s}) \tag{3.3}$$
$$E_\gamma = \frac{\sqrt{s}}{2}(1 - \frac{m_Z^2}{s}) \tag{3.4}$$

The measured value for the missing energy, $\not{E}$, can be used as an approximation for E_γ and the measured value for the longitudinal missing momentum, $\not{p}_3$, likewise for $p_{3\gamma}$. Note that the $q\bar{q}$ system is strongly boosted in the opposite direction to the radiative return photon. So if the measurement of the $q\bar{q}$ system energy is an underestimate, then $\not{E}$ is an overestimate for E_γ. However, as the missing momentum is just the vector equal and opposite to the visible momentum of the $q\bar{q}$ system, $\not{p}_3$ is an underestimate for p_γ. This can be expressed in the form:

$$\not{p}_3 = p_{3\gamma} - (\not{E} - E_\gamma) \tag{3.5}$$

Both E_γ and $p_{3\gamma}$ can be replaced using equation 3.4 to give a relation between $\not{p}_3$ and $\not{E}$:

$$\not{p}_3 = \sqrt{s}(1 - \frac{m_Z^2}{s}) - \not{E} \tag{3.6}$$

In the more general case of non-zero transverse missing momentum, $\not{p}_T$, equation 3.6 becomes:

$$\not{p}_3 = \sqrt{s}(1 - \frac{m_Z^2}{s}) - \sqrt{|\not{E}^2 - \not{p}_T^2|} \tag{3.7}$$

Recall that $\not{p}_T$ is negligible for radiative return events, but is large for semileptonic WW decays. So the value calculated for $\not{p}_3$ from equation 3.7, using the measured values for $\not{E}$ and $\not{p}_T$, is low for radiative return events and high for semileptonic WW decays. This means that equation 3.7 can be interpreted as an event-by-event upper bound for $\not{p}_3$ and used to discriminate between semileptonic WW decays and radiative return events.

From a Monte Carlo study [63], the criteria to select semileptonic WW decays are:

$$\not{p}_3 < \text{maximum} \begin{pmatrix} \sqrt{s}(1 - \frac{m_Z^2}{s}) - \sqrt{|\not{E}^2 - \not{p}_T^2|} - 6.0 \\ \frac{\sqrt{s}}{2}(1 - \frac{m_Z^2}{s}) - 27.5 \end{pmatrix} \tag{3.8}$$

where the second equation comes simply from the expression for the photon energy in equation 3.4. And in order to reduce the background from non-radiative events and events that are completely contained within the detector:

$$\begin{aligned} \not{E} &> 0.0 \\ \not{p} &> 0.0 \\ \not{p} &> 35.0 - \not{E} \end{aligned} \tag{3.9}$$

Figure 3.4 illustrates the effects of the missing momentum cuts on signal semileptonic WW decays and on the $Z/\gamma \rightarrow q\bar{q}(\gamma)$ background process.

Table 3.2 lists the efficiencies of the various cuts for all the processes considered. In subsequent tables of efficiencies, only background processes with an expectation of at least 0.5 events for the 10.65 pb^{-1} of data collected at $\sqrt{s} = 172$ GeV are shown.

3.1.3 Lepton track selection.

The high energy lepton in semileptonic WW decays is selected by taking advantage of the large angle between the lepton and the neutrino. At LEP energies just above the threshold

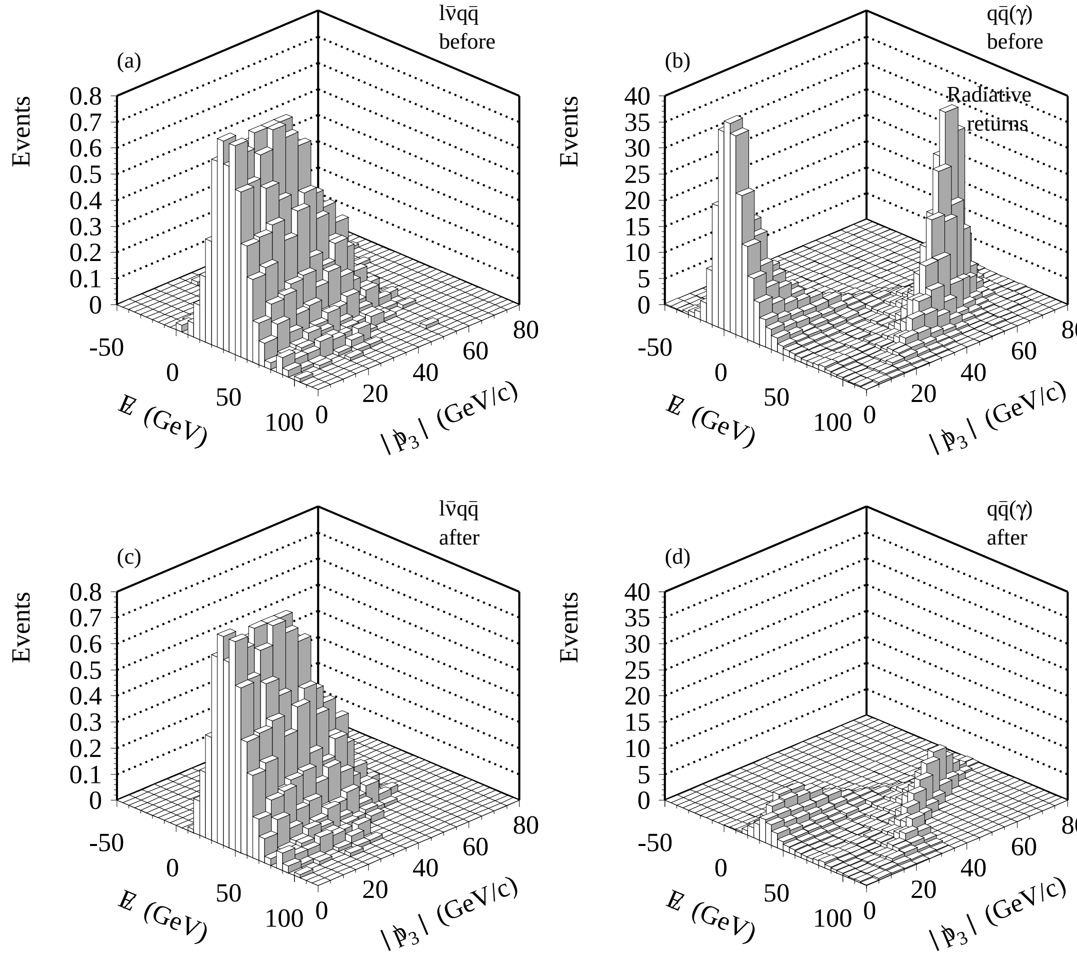

Figure 3.4: Illustration of the effects of the missing momentum cuts on the signal ($W^+W^-\rightarrow\ell\bar{\nu}q\bar{q}$) and the main background ($Z/\gamma\rightarrow q\bar{q}(\gamma)$) processes. The number of events is normalised to the data luminosity.

for WW pair production, the W bosons have a small boost. A consequence of this is that the two fermions from each W decay are emitted almost back-to-back. Therefore, the lepton can be selected by first assuming that the neutrino direction is approximated by the missing momentum direction and then finding the good charged track with the highest momentum component anti-parallel to this [64]. At $\sqrt{s} = 172$ GeV, this technique is 92% efficient in the $e\bar{\nu}q\bar{q}$ channel and 97% efficient in the $\mu\bar{\nu}q\bar{q}$ channel, considering only the 95% of semileptonic WW events where the lepton is within the tracking acceptance of $|\cos\theta| < 0.95$. This method does not work for the $\tau\bar{\nu}q\bar{q}$ channel due to the presence of a second energetic neutrino from the τ decay, which means that the missing momentum direction is no longer a good approximation for the direction of the neutrino from the W

Process	Efficiency (%)		
	N_{ch} and E_{ch}	$\not{E}$ and $\not{p}$	$\not{p}_3$
$e^+e^-\to W^+W^-\to e\bar{\nu}q\bar{q}$	99.9	99.1	98.8
$e^+e^-\to W^+W^-\to \mu\bar{\nu}q\bar{q}$	99.9	99.3	99.1
$e^+e^-\to W^+W^-\to \tau\bar{\nu}q\bar{q}$	99.6	99.4	98.6
$e^+e^-\to W^+W^-\to q\bar{q}q\bar{q}$	100.0	10.8	10.8
$e^+e^-\to W^+W^-\to \ell\nu\ell\nu$	1.1	1.1	0.9
$e^+e^-\to Z/\gamma\to q\bar{q}(\gamma)$	91.7	60.5	30.3
$e^+e^-\to Z/\gamma\to \tau^+\tau^-(\gamma)$	25.9	20.2	14.3
$e^+e^-\to Z/\gamma\to \mu^+\mu^-(\gamma)$	0.02	0.00	0.00
$e^+e^-\to e^+e^-(\gamma)$	0.05	0.01	0.01
$e^+e^-\to ZZ$	61.4	34.6	29.9
$e^+e^-\to Ze^+e^-$	33.2	29.1	15.3
$e^+e^-\to We\nu_e$	64.4	64.1	53.1
$\gamma\gamma\to e^+e^-$	0.00	0.00	0.00
$\gamma\gamma\to \mu^+\mu^-$	0.00	0.00	0.00
$\gamma\gamma\to \tau^+\tau^-$	0.08	0.08	0.05
$\gamma\gamma\to q\bar{q}$	1.00	1.00	0.91
Efficiency (%)	99.9	99.2	98.9
Purity (%)	2.5	3.6	5.9
Predicted events	1569	1090	659
Observed events	1640	1095	607

Table 3.2: Preselection efficiencies for all signal and background processes. The symbol ℓ in $\ell\nu\ell\nu$ represents an electron, muon or tau.

decay, and the lower energy of the charged particle(s) from the τ decay.

At higher LEP energies, the boost of the W bosons increases and the angle between the lepton and the neutrino, $\theta_{\ell\nu}$, decreases. Table 3.3 shows that the efficiency of this technique at finding the lepton from the semileptonic W decay drops slowly as the LEP energy rises. However, even at $\sqrt{s} = 192$ GeV, the technique is still very efficient.

The difference of 5% between the efficiency for the $e\bar{\nu}q\bar{q}$ and the $\mu\bar{\nu}q\bar{q}$ channels is due to the emission of Bremsstrahlung photons from the electron as it passes through the detector and also to the increased incidence of final state radiation (FSR) from the $W \to e\bar{\nu}$ decay due to the lighter electron mass. Both of these processes distort the electron momentum and thus reduce the efficiency.

The advantage of only using kinematic information to select the lepton is the track

$\sqrt{s}$	β (c^{-1})	$<\theta_{\ell\nu}>$ ($^\circ$)	$e\bar{\nu}q\bar{q}$ Eff. (%)	$\mu\bar{\nu}q\bar{q}$ Eff. (%)
161	0.05	157	92.3	97.3
172	0.36	146	91.7	97.0
184	0.49	135	89.1	95.1
192	0.55	129	87.0	92.3

Table 3.3: The W boost, the mean lepton-neutrino angle and the lepton track identification efficiency (corrected for the detector acceptance) for several LEP energies.

chosen in background events tends to be a low energy track within a jet. Typically, this track is a pion (62%), a kaon (20%) or a proton (10%) for the $Z/\gamma \rightarrow q\bar{q}(\gamma)$ background process. Therefore, energy, isolation and lepton identification variables discriminate between signal and background events very powerfully. The alternative technique of choosing the identified lepton with the highest energy [65] would find energetic electrons or muons in background events, for example from heavy flavour decays in $Z/\gamma \rightarrow q\bar{q}(\gamma)$ decays. This would make the discrimination necessary to obtain a pure sample of semileptonic WW decays with high efficiency more difficult.

3.1.4 Lepton identification.

Loose lepton identification criteria [66] are applied to the selected track in order to separate the $e\bar{\nu}q\bar{q}$ and $\mu\bar{\nu}q\bar{q}$ channels. The aim is to retain a very high efficiency for semileptonic WW decays whilst reducing the background further. The lepton identification estimators are shown in figure 3.5 and the criteria for electron identification are:

- The momentum of the track must exceed 2 GeV/c. This ensures that there is a reasonable energy deposit in the ECAL detector on which to base the calculation of the electromagnetic shower shape.

- The allowed values for the R_T, R_L and R_I estimators, where the calculations must have converged with at least 50 independent values of dE/dx for R_I, depend on the ECAL geometry:

    In a good region, then $R_T > -3$ and R_L converged.

    In an overlap region, then $\{R_T > -5$ and R_L converged$\}$ or $\{R_I > -0.5\}$.

    In a crack region, then $\{R_T > -7$ and R_L converged$\}$ or $\{R_I > -0.5\}$.

The criteria for muon identification are:

- The momentum of the track must exceed 3 GeV/c. This ensures a muon would penetrate through the ECAL and HCAL detectors to the muon chambers.
- The QMUID0 [49] routine is used to analyse the response of the HCAL detector and the muon chambers. The track is identified as a muon if the identification flag is positive, which occurs if the hit pattern in HCAL is inconsistent with that from a hadron or if there is at least one hit in the muon chambers.

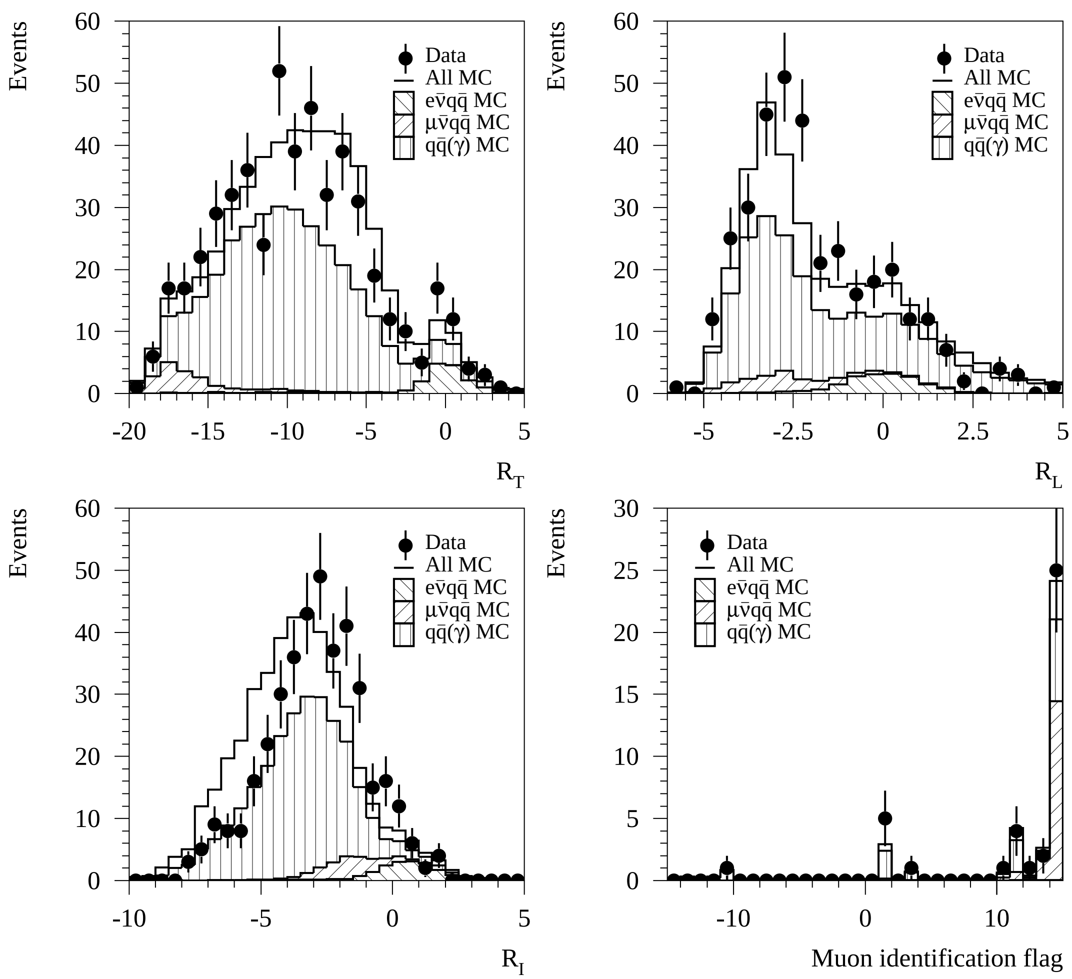

Figure 3.5: The electron identification estimators and the muon identification flag.

The identification efficiency is nearly 100% for the electrons and muons from semileptonic WW decays that are correctly selected by the missing momentum technique. Note that in those semileptonic WW decay events where the lepton is not selected, the track chosen usually fails the lepton identification criteria. The selection efficiencies for signal and background after lepton identification are shown in Table 3.4. Due to the loose electron identification, 2% of the identified leptons satisfy both sets of criteria. In this case, the track is taken to be a muon as the likelihood of a real electron penetrating the HCAL is very small.

Process	Efficiency (%)	
	$e\bar{\nu}q\bar{q}$ channel	$\mu\bar{\nu}q\bar{q}$ channel
$e^+e^-\to W^+W^-\to e\bar{\nu}q\bar{q}$	87.8	0.5
$e^+e^-\to W^+W^-\to \mu\bar{\nu}q\bar{q}$	0.2	91.4
$e^+e^-\to W^+W^-\to \tau\bar{\nu}q\bar{q}$	8.8	8.4
$e^+e^-\to W^+W^-\to q\bar{q}q\bar{q}$	0.2	0.3
$e^+e^-\to W^+W^-\to \ell\nu\ell\nu$	0.2	0.1
$e^+e^-\to Z/\gamma\to q\bar{q}(\gamma)$	1.7	1.1
$e^+e^-\to Z/\gamma\to \tau^+\tau^-(\gamma)$	1.3	0.4
$e^+e^-\to e^+e^-(\gamma)$	0.01	0.00
$e^+e^-\to ZZ$	2.7	2.0
$e^+e^-\to Ze^+e^-$	2.5	0.6
$e^+e^-\to We\nu_e$	3.4	1.3
$\gamma\gamma\to\tau^+\tau^-$	0.01	0.00
$\gamma\gamma\to q\bar{q}$	0.04	0.01
Efficiency (%)	87.8	91.4
Purity (%)	30.8	48.3
Predicted events	56.4	36.9
Observed events	53	39

Table 3.4: Efficiencies after lepton identification for signal and background processes.

3.1.5 Energy correction for Bremsstrahlung.

The electron energy is an important quantity for both the determination of the W boson mass and the discrimination between signal and background processes. However, in 40% of $e\bar{\nu}q\bar{q}$ events the electron radiates a Bremsstrahlung photon with an energy of at least 0.5 GeV. This degrades the resolution on the original electron energy as shown in Figure 3.6 and distorts the electron energy spectrum to lower energies as shown in Figure 3.7.

The Bremsstrahlung photons are radiated when the electron interacts with material in the detector. Most of the Bremsstrahlung photons are produced at radii of 12 cm and

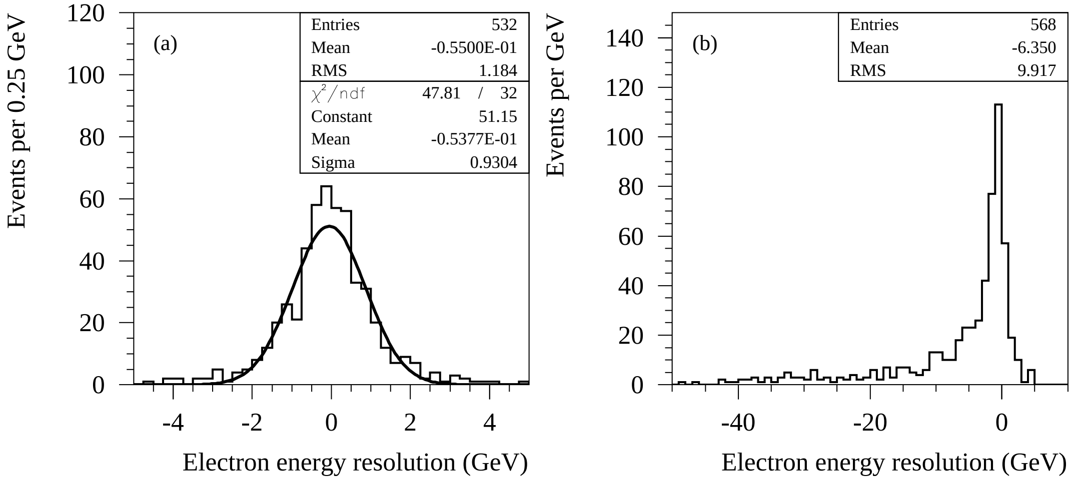

Figure 3.6: The resolution on the electron energy in (a) events without any Bremsstrahlung or FSR and (b) events with Bremsstrahlung only.

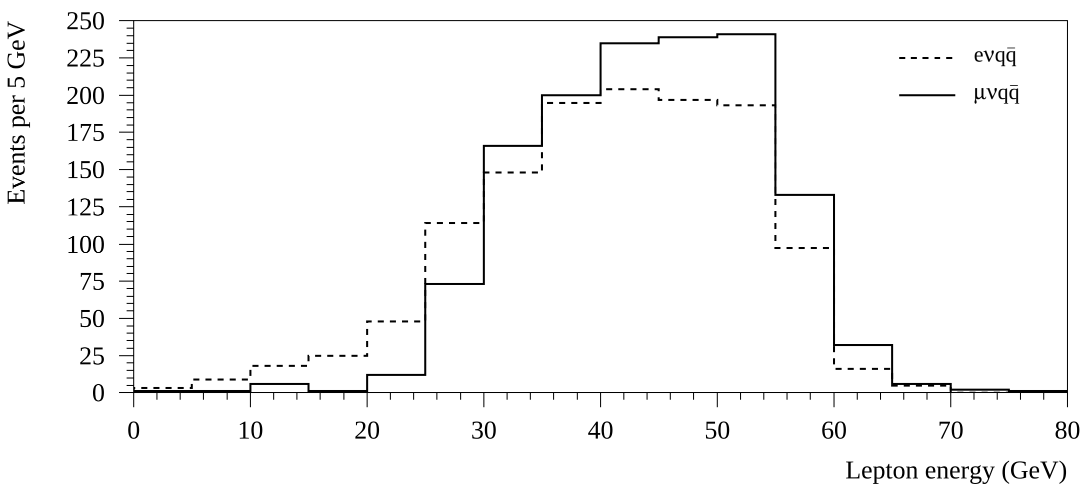

Figure 3.7: Comparison of the electron and muon energy spectra, for correctly identified leptons from simulated $W^+W^-\to\ell\bar{\nu}q\bar{q}$ decays.

31 cm, which correspond to the concentrations of material found at the VDET/ITC and ITC/TPC boundaries. The accuracy of the simulation of the material at these radii has recently been checked by a study of photon conversions [67]. The reasonable description of the amount of detector material is improved for the $\sqrt{s} = 183$ GeV simulation.

In order to recover some of the lost resolution, a search is made for energy deposits in a region nearby to the electron impact point on the ECAL [64, 68]. Figure 3.8 shows that this region is defined by:

- A cone of 2° around the impact point on ECAL of the electron track.

- An ellipse that joins cones of 2° around the impact points on ECAL of two hypothetical photons, radiated from the electron at the VDET/ITC and ITC/TPC boundaries respectively.

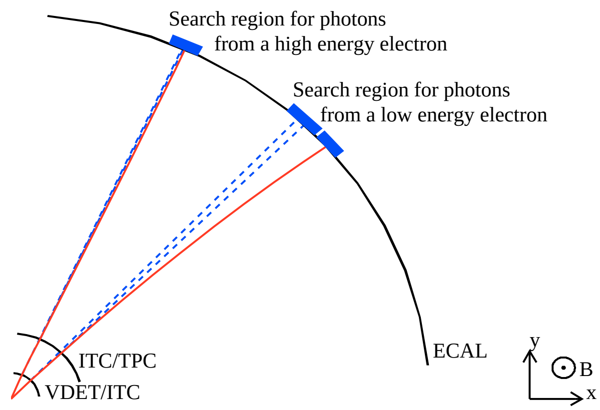

Figure 3.8: Schematic of the region of ECAL that is checked for energy deposits.

Any energy deposits, with an energy greater than 0.5 GeV, found in this region are then combined in one of the following two ways with the measurement of the electron track momentum.

If less energy is found in any overlap region between the cone and the ellipse than in the rest of the ellipse, then the electron and Bremsstrahlung photon electromagnetic showers are separable. The photon energy is estimated by weighting the energy in the overlap region by:

$$\frac{E_{ellipse\ only}}{E_{ellipse\ only} + E_{cone\ only}} \tag{3.10}$$

and adding that amount to the energy found only in the ellipse. The electron four-vector from the tracking and the estimate for the photon four-vector are then simply added.

However, for electrons with energies greater than about 6 GeV, the electron and Bremsstrahlung photon electromagnetic showers in the ECAL are not usually separable. In this case, the total energy deposit in the ECAL and the electron track energy are combined using weights w_{track} and w_{cal} to give a corrected energy and momentum:

$$\begin{aligned} E_{corr} &= w_{track}E_{track} + w_{cal}E_{cal} \\ \mathbf{p}_{corr} &= w_{track}\mathbf{p}_{track} + w_{cal}\mathbf{p}_{cal} \end{aligned} \tag{3.11}$$

The weights are based on the significance, x, of the difference between the calorimeter and the tracking estimates for the electron energy:

$$x = \frac{E_{cal} - E_{track}}{\sqrt{\sigma_{cal}^2 + \sigma_{track}^2}} \tag{3.12}$$

The calorimeter and tracking energy resolutions, σ_{cal} and σ_{track}, are shown in Figure 3.9, where it is assumed that the track helix fit uses at least 19 TPC, 6 ITC and 1 VDET coordinates [49]:

$$\begin{aligned} \sigma_{cal} &= 0.01E_{cal} + 0.18\sqrt{E_{cal}} \\ \sigma_{track} &= 0.6 \times 10^{-3}E_{track}^2 \end{aligned} \tag{3.13}$$

An estimator $\mathcal{R} \in [0,1]$ is constructed using the error function:

$$\mathcal{R} = 0.5(1 + erf\ (1.5 - x)) \quad \text{where} \quad erf\ (1.5 - x) = \frac{2}{\sqrt{\pi}} \int_0^{1.5-x} e^{-t^2} dt \tag{3.14}$$

and then the weights are defined as:

$$w_{cal} = \frac{1 - \mathcal{R}}{\sigma_{cal}^2} \quad \text{and} \quad w_{track} = \frac{\mathcal{R}}{\sigma_{track}^2} \tag{3.15}$$

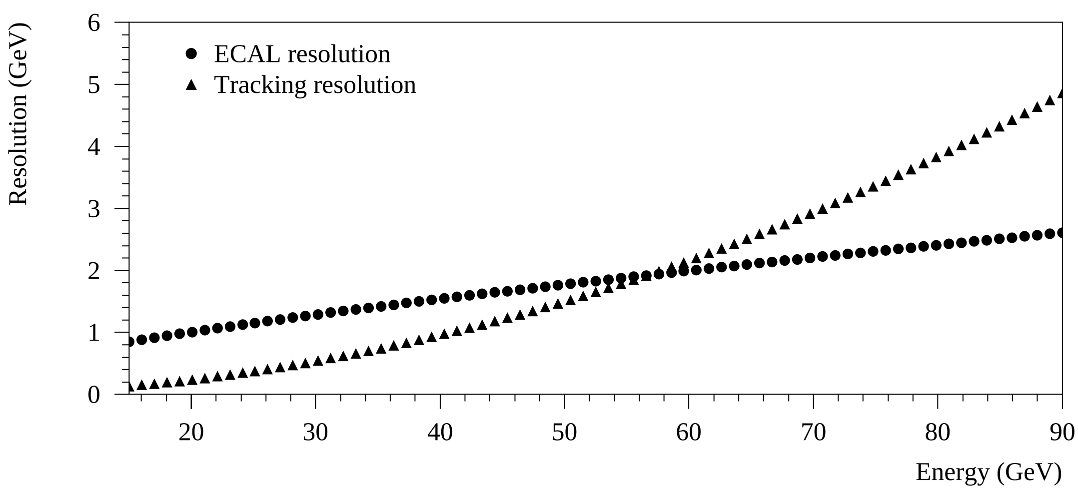

Figure 3.9: Energy resolutions from tracking and the ECAL as a function of energy.

such that if the calorimeter energy is more than three standard deviations above the tracking energy, then the corrected energy is essentially the calorimeter energy as illustrated by Figure 3.10.

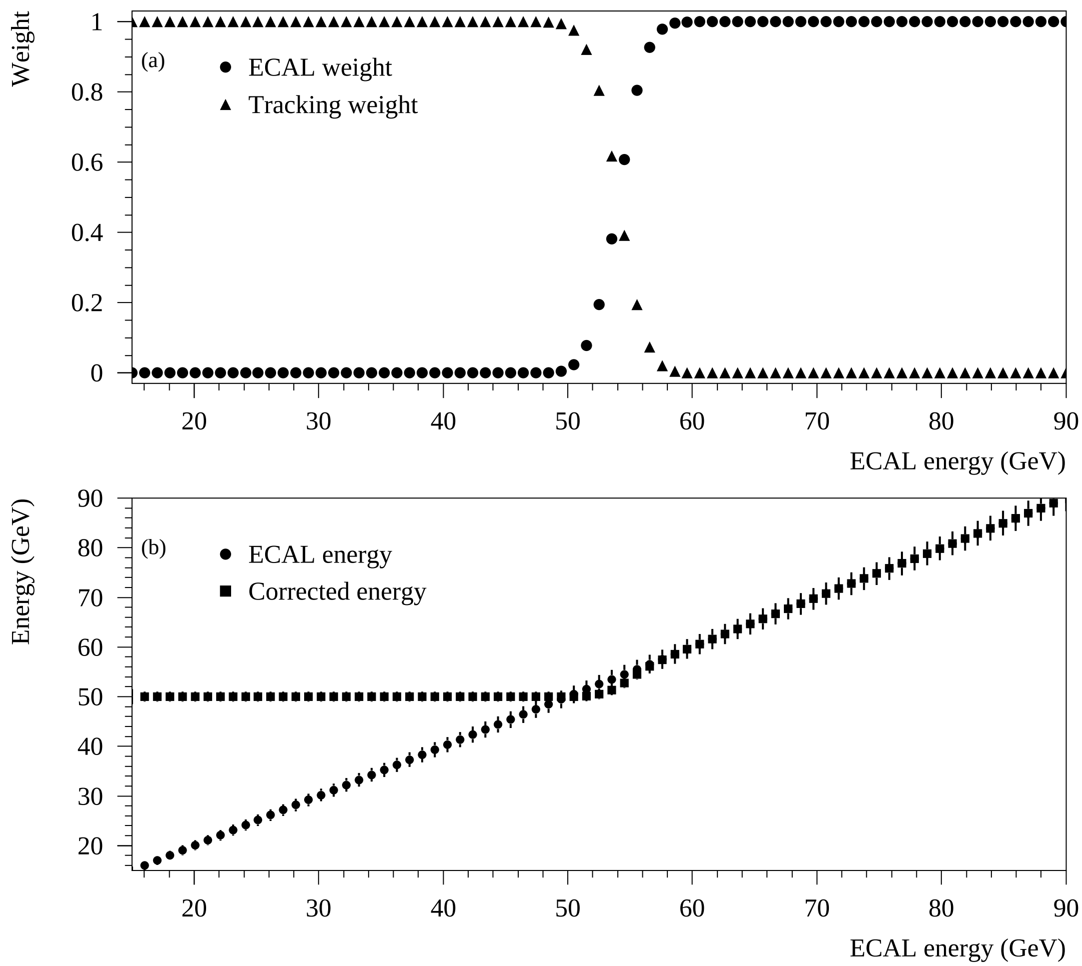

Figure 3.10: The weights for a track with a momentum of 50 GeV are shown as a function of the calorimeter energy in (a). The value for the corrected energy is shown in (b) as a function of the calorimeter energy.

In order to avoid introducing noise, the tracking measurement is kept if the correction is less than 0.3 GeV [69]. The improved electron energy resolution is shown in Figure 3.11 and the energy added by the correction in Figure 3.12. Table 3.5 lists the mean energy added to the electron and the percentage of selected events to which the correction is applied for $W^+W^-\to e\bar{\nu}q\bar{q}$ decays and the main background of $Z/\gamma\to q\bar{q}(\gamma)$ decays. The correction is applied to a large percentage of the background events because the track is normally in a jet and so energy deposits from nearby particles are also added.

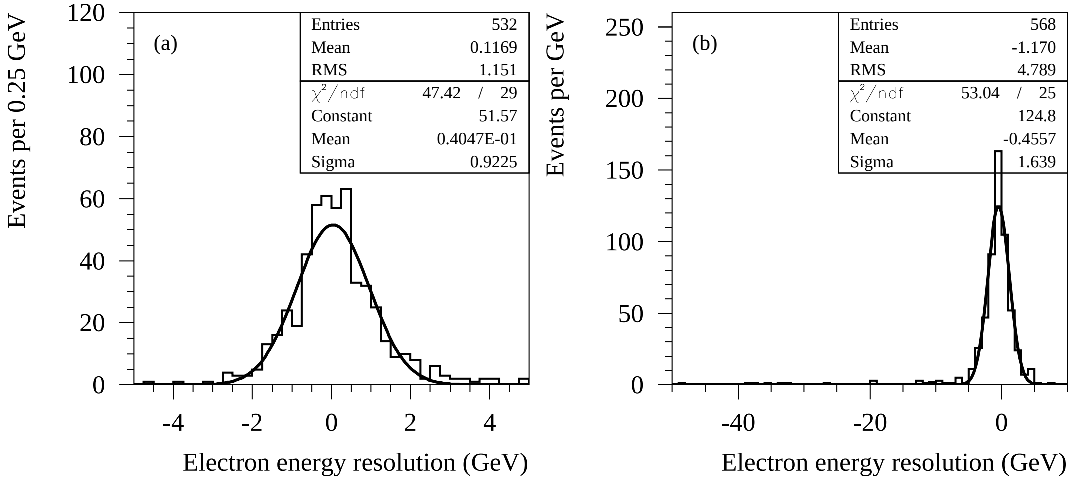

Figure 3.11: The resolution on the electron energy after the Bremsstrahlung correction for (a) events without any Bremsstrahlung or FSR and (b) events with Bremsstrahlung.

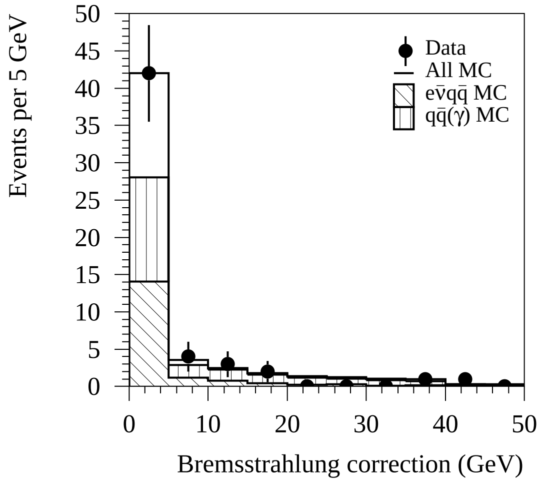

Figure 3.12: The energy added by the Bremsstrahlung correction to electrons in simulation and data.

3.1.6 Lepton energy.

The energy distribution of the lepton, shown in Figure 3.13, affords powerful discrimination between signal and background. Imposing the requirement that the lepton energy should be over 15 GeV keeps over 99% of the signal and rejects 50% and 75% of the $Z/\gamma\rightarrow q\bar{q}(\gamma)$ background for the $e\bar{\nu}q\bar{q}$ and $\mu\bar{\nu}q\bar{q}$ channels respectively. The lower rejection power for the $e\bar{\nu}q\bar{q}$ channel is a result of the Bremsstrahlung correction, which can increase the energy of the selected track in background events. Table 3.6 lists the efficiencies for all the signal

Process	Composition	Percentage with energy added	Mean energy added (GeV)
$e^+e^-\to W^+W^-\to e\bar{\nu}q\bar{q}$	100	37	9.3
No Brem. or FSR	40	14	1.6
Brem. only	43	49	10.7
E_{Brem} >5 GeV	16	86	15.4
FSR only	9	50	9.3
E_{FSR} >5 GeV	4	76	13.5
$e^+e^-\to Z/\gamma\to q\bar{q}(\gamma)$	100	46	16.9

Table 3.5: Mean energy added by the Bremsstrahlung correction to fully simulated, selected $W^+W^-\to e\bar{\nu}q\bar{q}$ and $e^+e^-\to Z/\gamma\to q\bar{q}(\gamma)$ events. The second column breaks the sample down into various components and the third column gives the percentage of that component to which energy is added.

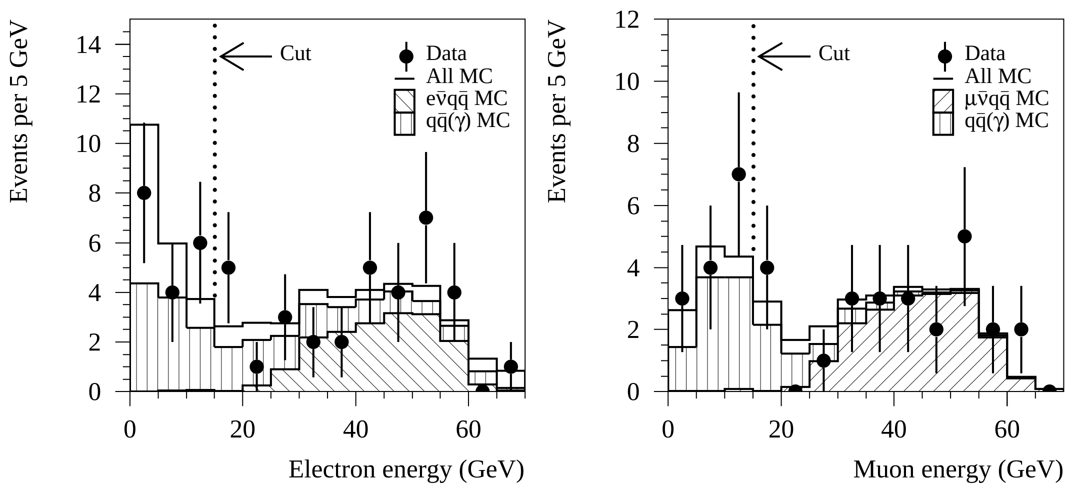

Figure 3.13: The lepton energy distribution for the $e\bar{\nu}q\bar{q}$ and $\mu\bar{\nu}q\bar{q}$ channels.

and background processes.

3.1.7 Jet clustering.

The hadronic W decay produces two or more jets of collimated particles. Two jets are reconstructed by the DURHAM [70, 71, 72] clustering algorithm. This is applied to all the energy flow objects that are not used to construct the lepton, *ie* the energy flow copy of the lepton charged track and the energy flow object based on any ECAL energy deposit associated to the electron by the Bremsstrahlung correction are excluded.

Process	Efficiency (%)	
	$e\bar{\nu}q\bar{q}$ channel	$\mu\bar{\nu}q\bar{q}$ channel
$e^+e^-\to W^+W^-\to e\bar{\nu}q\bar{q}$	87.1	0.2
$e^+e^-\to W^+W^-\to \mu\bar{\nu}q\bar{q}$	0.1	90.8
$e^+e^-\to W^+W^-\to \tau\bar{\nu}q\bar{q}$	6.7	7.0
$e^+e^-\to W^+W^-\to q\bar{q}q\bar{q}$	0.1	0.1
$e^+e^-\to W^+W^-\to \ell\nu\ell\nu$	0.2	0.1
$e^+e^-\to Z/\gamma\to q\bar{q}(\gamma)$	0.9	0.4
$e^+e^-\to Z/\gamma\to \tau^+\tau^-(\gamma)$	1.1	0.4
$e^+e^-\to ZZ$	1.7	1.3
$e^+e^-\to Ze^+e^-$	1.9	0.2
$e^+e^-\to We\nu_e$	2.6	0.5
Efficiency (%)	87.1	90.8
Purity (%)	51.4	70.2
Predicted events	33.5	25.2
Observed events	35	25

Table 3.6: Efficiencies after requiring that the lepton energy should be greater than 15 GeV.

The DURHAM algorithm defines the jet resolution variable y as:

$$y = 2 \times \min[E_1^2, E_2^2](1 - \cos\theta_{12}) \tag{3.16}$$

where E_1 and E_2 are the energies of two particles that are separated by an angle θ_{12}. This variable is calculated for every pair of energy flow objects. The pair with the smallest value for y are combined together into a new pseudo-particle, with four-momentum p_{12} defined according to the massless P scheme described below. This procedure is repeated until there are exactly two objects left, which are called jets.

In the P scheme, the momentum of the pseudo-particle (12) is the vector sum of the momenta of particles 1 and 2. The energy of the pseudo-particle (12) is rescaled so that it has zero invariant mass:

$$\begin{aligned} \mathbf{p}_{12} &= \mathbf{p}_1 + \mathbf{p}_2 \\ E_{12} &= |\mathbf{p}_1 + \mathbf{p}_2| \end{aligned} \tag{3.17}$$

Monte Carlo studies show that this scheme gives the best energy and angular resolutions for the jets relative to the original quarks [73]. However, the studies also show that this massless combination biases the invariant mass of the two jets away from the hadronic W mass. Therefore, after the energy flow objects have been assigned to a jet by the P scheme, the four-vectors of all the energy flow objects belonging to each jet are simply added, since this is found to give the smallest bias between the reconstructed and the generated W masses. The energy and angular resolutions on the jets are shown in Figure 3.14.

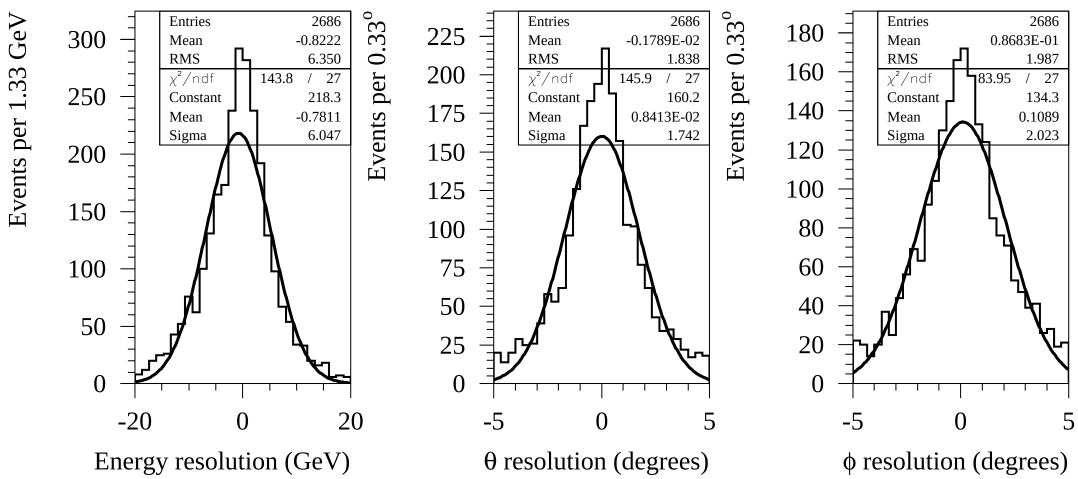

Figure 3.14: The energy and angular resolutions for jets from simulated semileptonic WW decays.

3.1.8 Multidimensional discrimination.

In order to improve the purity of the selection without destroying the high efficiency, a statistical test is constructed from three discriminating variables. This takes advantage of correlations between the variables and thus uses more information than a technique considering each variable separately. The three variables chosen are shown in Figure 3.15 and are [64]:

- The corrected energy of the lepton, E_ℓ.
- The missing transverse momentum, $\not{p}_T$.
- The isolation of the lepton, Iso_ℓ, which is defined as:

$$Iso_\ell = \log(\tan(\alpha_{jet}/2)) + \log(\tan(\alpha_{ch}/2)) \tag{3.18}$$

where α_{jet} is the angle between the lepton and the closest jet and α_{ch} is the angle between the lepton and the nearest good charged track[2] above 0.2 GeV/c.

[2]The polar angle requirement is relaxed to $|\cos\theta| \leq 0.975$ here.

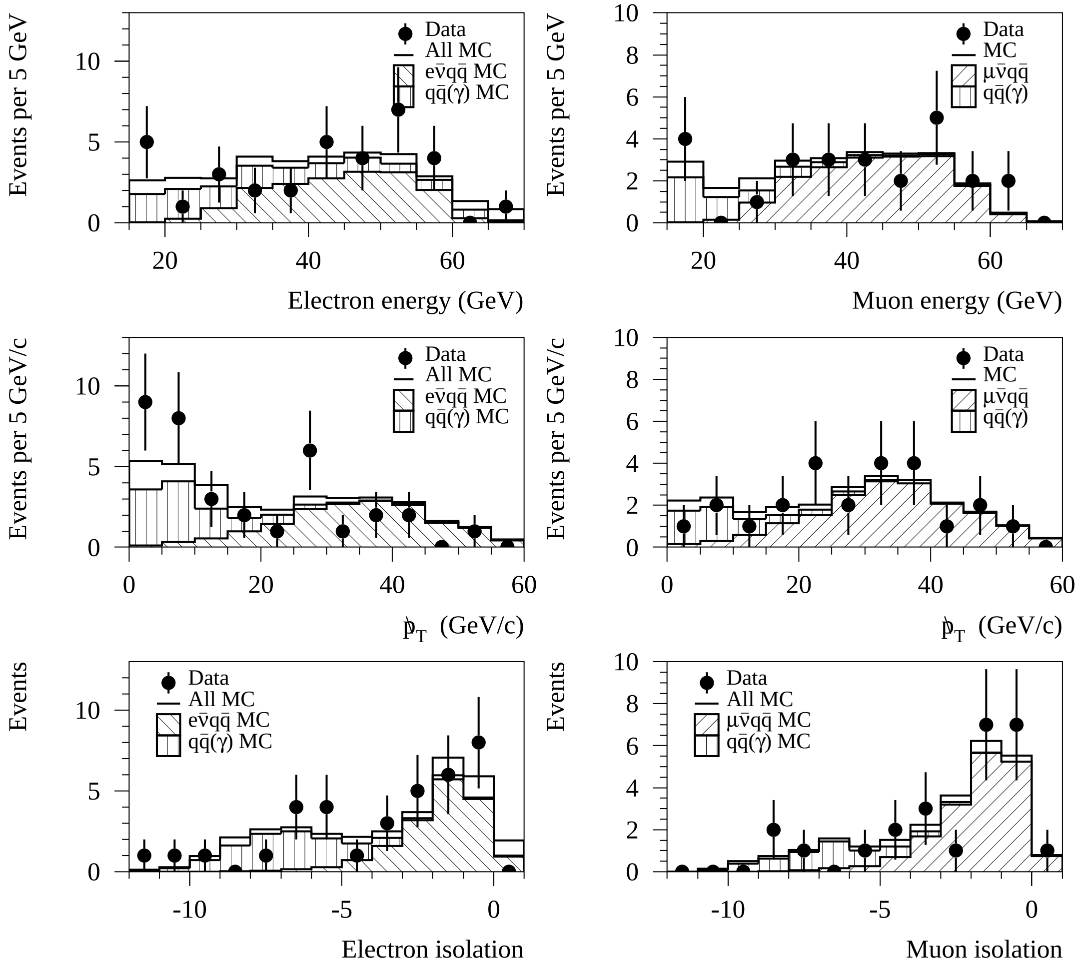

Figure 3.15: The lepton energy, the missing transverse momentum and the isolation of the lepton for the $e\bar{\nu}q\bar{q}$ and $\mu\bar{\nu}q\bar{q}$ channels.

A three-dimensional space, constructed from the above variables, is populated with events from simulation. Probability density functions (pdfs), represented by multiquadric radial basis functions [74], are evaluated separately for signal and background in both the $e\bar{\nu}q\bar{q}$ and $\mu\bar{\nu}q\bar{q}$ channels [75].

In the $e\bar{\nu}q\bar{q}$ channel, the pdf $g(E_e, \not{p}_T, iso_e \mid e\bar{\nu}q\bar{q})$ represents the hypothesis that an event is from the $W^+W^-\rightarrow e\bar{\nu}q\bar{q}$ process and the pdf $g(E_e, \not{p}_T, iso_e \mid bkg)$ the hypothesis that the event is from background processes. Then the probability that an event with observed values of E_e, $\not{p}_T$ and iso_e is from the $W^+W^-\rightarrow e\bar{\nu}q\bar{q}$ process can be obtained from the pdfs using Bayes' Theorem [76]:

$$P(e\bar{\nu}q\bar{q} \mid E_e, \not{p}_T, iso_e) \;=\; \frac{\frac{\sigma_{e\bar{\nu}q\bar{q}}}{\sigma_{total}}\; g(E_e, \not{p}_T, iso_e \mid e\bar{\nu}q\bar{q})}{\frac{\sigma_{e\bar{\nu}q\bar{q}}}{\sigma_{total}}\; g(E_e, \not{p}_T, iso_e \mid e\bar{\nu}q\bar{q}) \;+\; \frac{\sigma_{bkg}}{\sigma_{total}}\; g(E_e, \not{p}_T, iso_e \mid bkg)} \tag{3.19}$$

where $\frac{\sigma_{e\bar{\nu}q\bar{q}}}{\sigma_{total}}$ and $\frac{\sigma_{bkg}}{\sigma_{total}}$ are the prior probabilities for the hypotheses $e\bar{\nu}q\bar{q}$ and background. The total selected cross section, σ_{total}, is the sum of the cross sections for the signal, $\sigma_{e\bar{\nu}q\bar{q}}$, and background, σ_{bkg}, processes. The probability that an event is from the $W^+W^-\to\mu\bar{\nu}q\bar{q}$ process is calculated in a similar way.

Figure 3.16 shows the probabilities and the variation of the efficiency, purity and quality factor (defined as the square root of the product of the efficiency and the purity) with a lower bound on the probability for the $e\bar{\nu}q\bar{q}$ and the $\mu\bar{\nu}q\bar{q}$ channels. The optimum lower bound is defined to be that which maximises the quality factor, which leads to the smallest statistical error on the cross section. The values for the lower bounds are:

$$\begin{aligned} P(e\bar{\nu}q\bar{q} \mid E_e, \not{p}_T, iso_e) &\geq 0.36 \\ P(\mu\bar{\nu}q\bar{q} \mid E_\mu, \not{p}_T, iso_\mu) &\geq 0.70 \end{aligned} \tag{3.20}$$

The efficiencies after these requirements are shown in Table 3.7

Process	Efficiency (%)	
	$e\bar{\nu}q\bar{q}$ channel	$\mu\bar{\nu}q\bar{q}$ channel
$e^+e^-\to W^+W^-\to e\bar{\nu}q\bar{q}$	83.1	0.1
$e^+e^-\to W^+W^-\to \mu\bar{\nu}q\bar{q}$	0.1	88.8
$e^+e^-\to W^+W^-\to \tau\bar{\nu}q\bar{q}$	4.8	5.1
$e^+e^-\to W^+W^-\to q\bar{q}q\bar{q}$	0.0	0.0
$e^+e^-\to W^+W^-\to \ell\nu\ell\nu$	0.2	0.0
$e^+e^-\to Z/\gamma\to q\bar{q}(\gamma)$	0.01	0.01
$e^+e^-\to Z/\gamma\to \tau^+\tau^-(\gamma)$	0.10	0.02
$e^+e^-\to ZZ$	0.27	0.30
$e^+e^-\to Ze^+e^-$	0.23	0.00
$e^+e^-\to We\nu_e$	1.60	0.20
Efficiency (%)	83.1	88.8
Purity (%)	91.4	93.4
Predicted events	18.0	18.5
Observed events	14	20

Table 3.7: Efficiencies with the lower bounds on the probabilities.

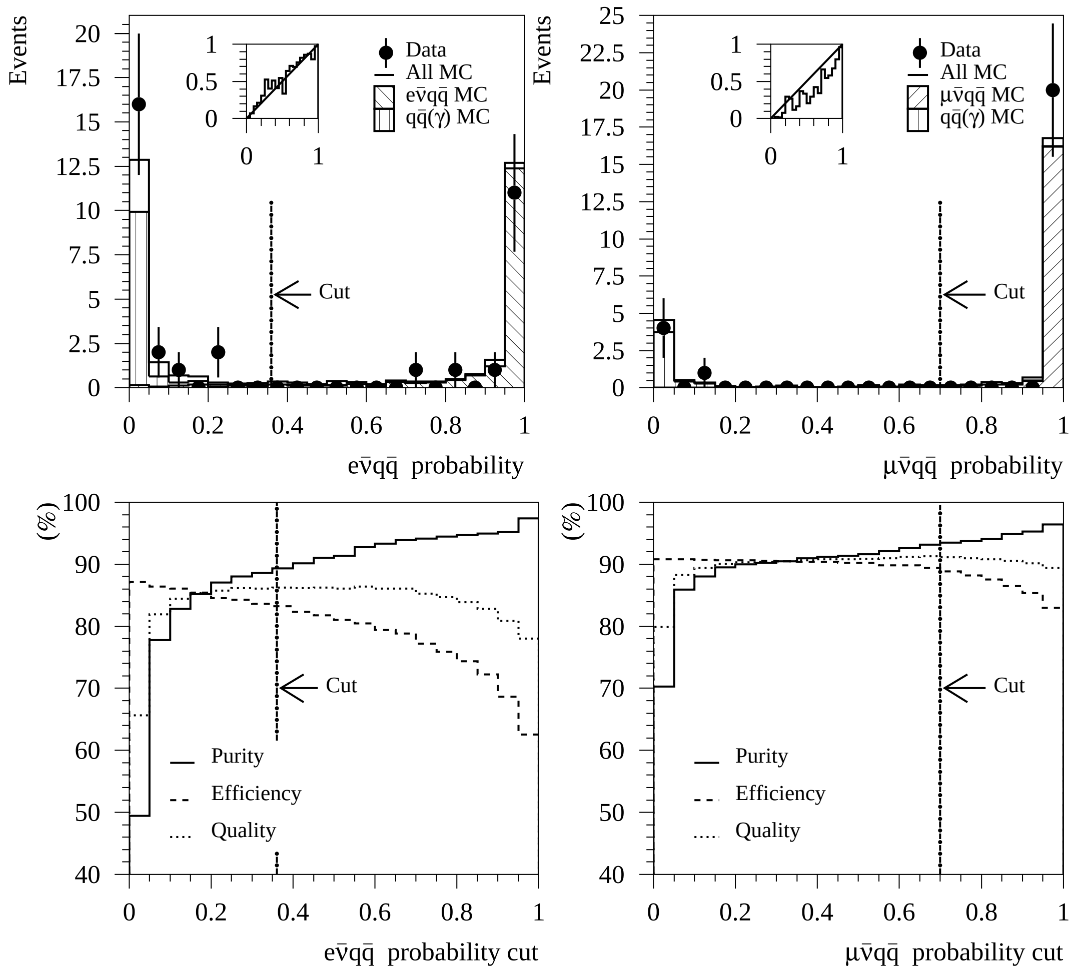

Figure 3.16: The $e\bar{\nu}q\bar{q}$ and $\mu\bar{\nu}q\bar{q}$ probabilities are shown in the upper plots, where the inset graphs show the $e\bar{\nu}q\bar{q}$ or $\mu\bar{\nu}q\bar{q}$ fraction versus the $e\bar{\nu}q\bar{q}$ or $\mu\bar{\nu}q\bar{q}$ probability. The variation of the efficiency, purity and quality factor with a lower bound on the probability is shown in the lower plots.

3.1.9 Summary.

The overall efficiency and purity of the selection are high at 83.1% and 91.4% for the $e\bar{\nu}q\bar{q}$ channel and 88.8% and 93.4% for the $\mu\bar{\nu}q\bar{q}$ channel. The expected and observed number of events from the 10.65 pb^{-1} of data collected at $\sqrt{s} = 172$ GeV are in good agreement.

Figure 3.17 shows a display of a data event that is selected as an $e\bar{\nu}q\bar{q}$ candidate and Figure 3.18 shows a data event that is selected as an $\mu\bar{\nu}q\bar{q}$ candidate. Note the large ECAL energy deposit for the electron in the $e\bar{\nu}q\bar{q}$ candidate and the hits in the muon chambers for the muon in the $\mu\bar{\nu}q\bar{q}$ candidate. The line that traverses the detector indicates the direction of the missing momentum vector.

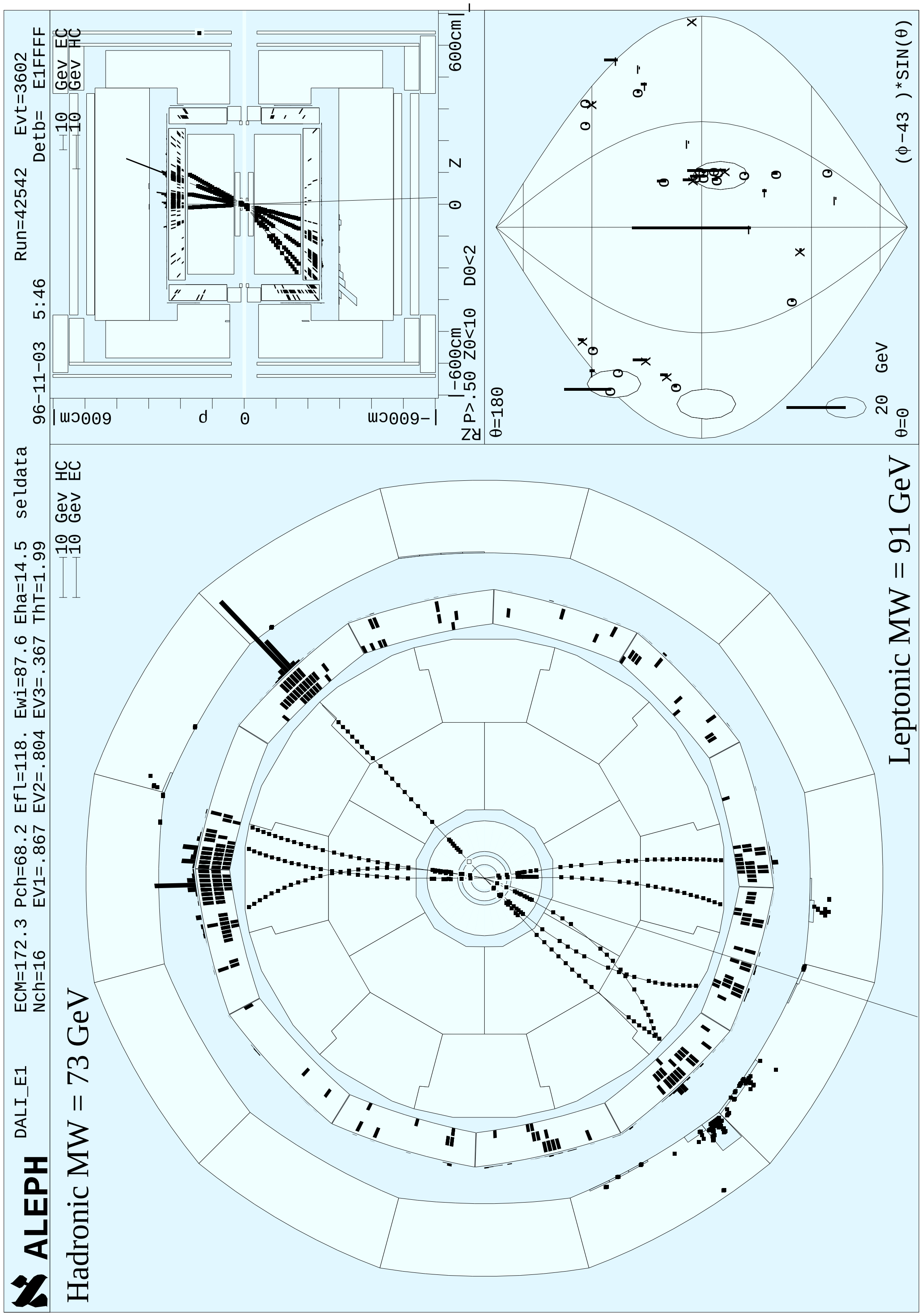

Figure 3.17: An event display of a data event that is selected as an $e\bar{\nu}q\bar{q}$ candidate.

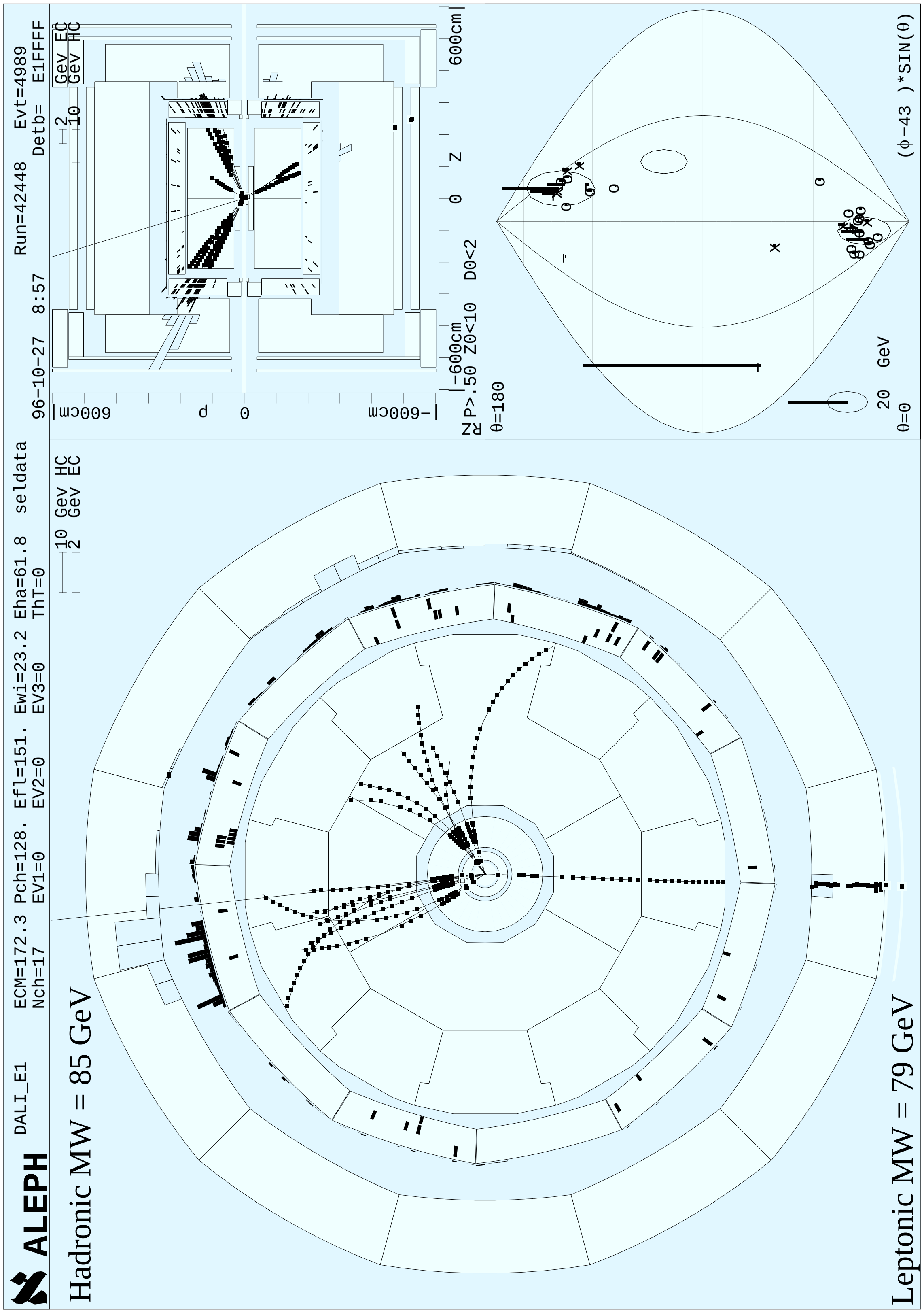

Figure 3.18: An event display of a data event that is selected as an $\mu\bar{\nu}q\bar{q}$ candidate.

3.2 Semileptonic event selection at $\sqrt{s} = 183$ GeV.

At $\sqrt{s} = 183$ GeV, the cross section for $e^+e^- \to W^+W^- \to e\bar{\nu}q\bar{q}$ and $e^+e^- \to W^+W^- \to \mu\bar{\nu}q\bar{q}$ events increases by 1 pb to 4.6 pb. The philosophy of the selection is the same as that for $\sqrt{s} = 172$ GeV. This section concentrates on improvements to the reconstruction of the lepton energy and comparisons of simulation with data for the selection variables. Several improvements to the simulation are discussed briefly below. In addition, the reconstruction of charged particles in the tracking detectors is improved by a new program [77].

3.2.1 Simulation improvements.

Several problems with the simulation of the detector response have been resolved, including:

- An error from 1996 in a VDET database, which shifted the alignment of the VDET in simulation by 8 μm in both the z and the rϕ planes. The z shift simply moves the position of the primary vertex. The effect in rϕ, which is a translation in the plane of each VDET wafer, causes a change in the distance of closest approach of a track to the primary vertex and a shift in the momentum for positive and negative tracks in opposite senses. The magnitude of the shift is $\pm$ 2 GeV/c for a 90 GeV/c track and $\pm$ 0.1 GeV/c for a 20 GeV/c track, so it is a bias of approximately $0.5\sigma_{track}$ [78]. This has a detrimental effect on the high-energy leptons from semileptonic WW decays. The $\mathrm{R_T}$ estimator, which compares the momentum of the track with the energy deposit in ECAL, is also shifted and broadened in a momentum-dependent way from the normal distribution [79].

- The electronic readout system for the ECAL was replaced in 1994. As a result, the electronic noise in the barrel decreased by a factor of two. In the simulation, it was incorrectly assumed that this was also true in the endcap region [80]. Note that electronic channels with readings consistently above the noise threshold are not used in the reconstruction of energy deposits in the ECAL, which causes the simulation to underestimate the ECAL energy.

- The previously poor simulation of the HCAL response to single pions is much improved. This reverses the sign of the discrepancy in the HCAL energy between data and simulation in $Z/\gamma\to q\bar{q}(\gamma)$ events [81]. Improvements to the geometrical description and modelling of the response of the HCAL will further reduce this discrepancy in future [82].

The ECAL problem is the main source of a large discrepancy between the simulated jet energy and the measured jet energy in data discussed in 7.1.3. The new simulation at $\sqrt{s}$ = 183 GeV was made available in May 1998 and is used throughout the $\sqrt{s}$ = 183 GeV analysis.

3.2.2 Monte Carlo and data samples.

As at $\sqrt{s}$ = 172 GeV, the KORALW, version 1.21, generator is used to simulate WW processes. Monte Carlo samples, with integrated luminosities corresponding to at least eighty times that of the data, are fully simulated for all background reactions. The cross section for the $e^+e^-\to Ze^+e^-$ process is much higher as the minimum invariant mass of the e^+e^- system is now 0.2 GeV/c^2 instead of 12 GeV/c^2. For two-photon reactions, the minimum invariant mass is 2.5 GeV/c^2 and the minimum lepton transverse momentum is 0.15 GeV/c for leptonic final states. The minimum invariant mass is 40 GeV/c^2 for hadronic final states. The cross sections and number of events simulated for all of the processes are given in Table 3.8.

The integrated luminosity of 56.81 $\pm$ 0.11 pb^{-1} was collected by the ALEPH detector at LEP in 1997 at a mean centre-of-mass energy of 182.655 $\pm$ 0.048 GeV, with 0.17 pb^{-1} at 180.83 GeV, 3.92 pb^{-1} at 181.72 GeV, 50.79 pb^{-1} at 182.69 GeV and 1.93 pb^{-1} at 183.81 GeV. The final alignment obtained in October 1998 for the $\sqrt{s}$ = 183 GeV data is used in this analysis. The previous alignment suffered from a deformation to the geometry of the VDET, due to an incorrect database entry from the 1997 alignment. This shifted the momentum of positive and negative tracks in opposite senses by over half the momentum resolution - the difference is 3 GeV/c for tracks with a nominal momentum 90 GeV/c. The overall VDET resolution in the rϕ plane improves from 10 to 8 μm on the realignment of the undeformed VDET and the momentum resolution also improves significantly. The alignment of the $\sqrt{s}$ = 183 GeV data was especially problematic due to field distortions in the TPC, caused by the build-up of charge on the TPC laser mirrors after a beam loss occurred in ALEPH [83].

Process	Cross section (pb)	Number of events
$e^+e^-\to W^+W^-$		
4-f M_W= 79.85 GeV/c^2	16.04	50,000
4-f M_W= 80.10 GeV/c^2	16.01	50,000
4-f M_W= 80.35 GeV/c^2	16.01	400,000
4-f M_W= 80.60 GeV/c^2	15.97	50,000
4-f M_W= 80.85 GeV/c^2	15.69	50,000
CC03 M_W= 80.25 GeV/c^2	15.71	400,000
$e^+e^-\to Z/\gamma\to q\bar{q}(\gamma)$	107.6	500,000
$e^+e^-\to Z/\gamma\to \tau^+\tau^-(\gamma)$	8.3	350,000
$e^+e^-\to Z/\gamma\to \mu^+\mu^-(\gamma)$	8.9	600,000
$e^+e^-\to e^+e^-(\gamma)$	1025.	300,000
$e^+e^-\to ZZ$	2.545	30,000
$e^+e^-\to Ze^+e^-$	97.	60,000
$e^+e^-\to We\nu_e$	0.672	6,000
$\gamma\gamma\to e^+e^-$	3760.	250,000
$\gamma\gamma\to \mu^+\mu^-$	3420.	293,000
$\gamma\gamma\to \tau^+\tau^-$	421.	389,000
$\gamma\gamma\to q\bar{q}$	1100.	200,000

Table 3.8: Generated cross sections and number of events for all signal and background processes considered.

3.2.3 Preselection and lepton identification.

The preselection scales automatically to higher LEP energies and is still over 99% efficient for signal semileptonic decays whilst rejecting 71% of the $Z/\gamma\to q\bar{q}(\gamma)$ process. Figure 3.19 shows the number of good charged tracks and the charged energy and Figure 3.20 shows the missing energy, missing momentum and the missing momentum component parallel to the beam axis. The apparent discrepancy between data and simulation, which appears for example at the low end of the charged energy distribution, is due to the too high value for the invariant mass cut in the simulation of hadronic final states from two-photon reactions. The efficiencies are shown in Table 3.9.

The lepton track is identified as the good charged track with the highest momentum component anti-parallel to the missing momentum. The efficiency for identifying the lepton is 89% in the $e\bar{\nu}q\bar{q}$ channel and 95% in the $\mu\bar{\nu}q\bar{q}$ channel, considering only the 95%

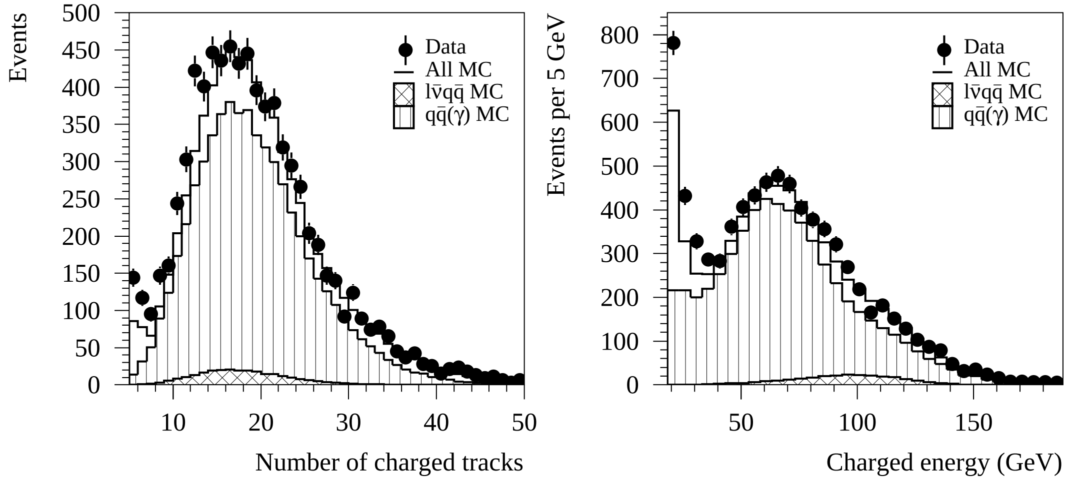

Figure 3.19: Number of good charged tracks and their total charged energy.

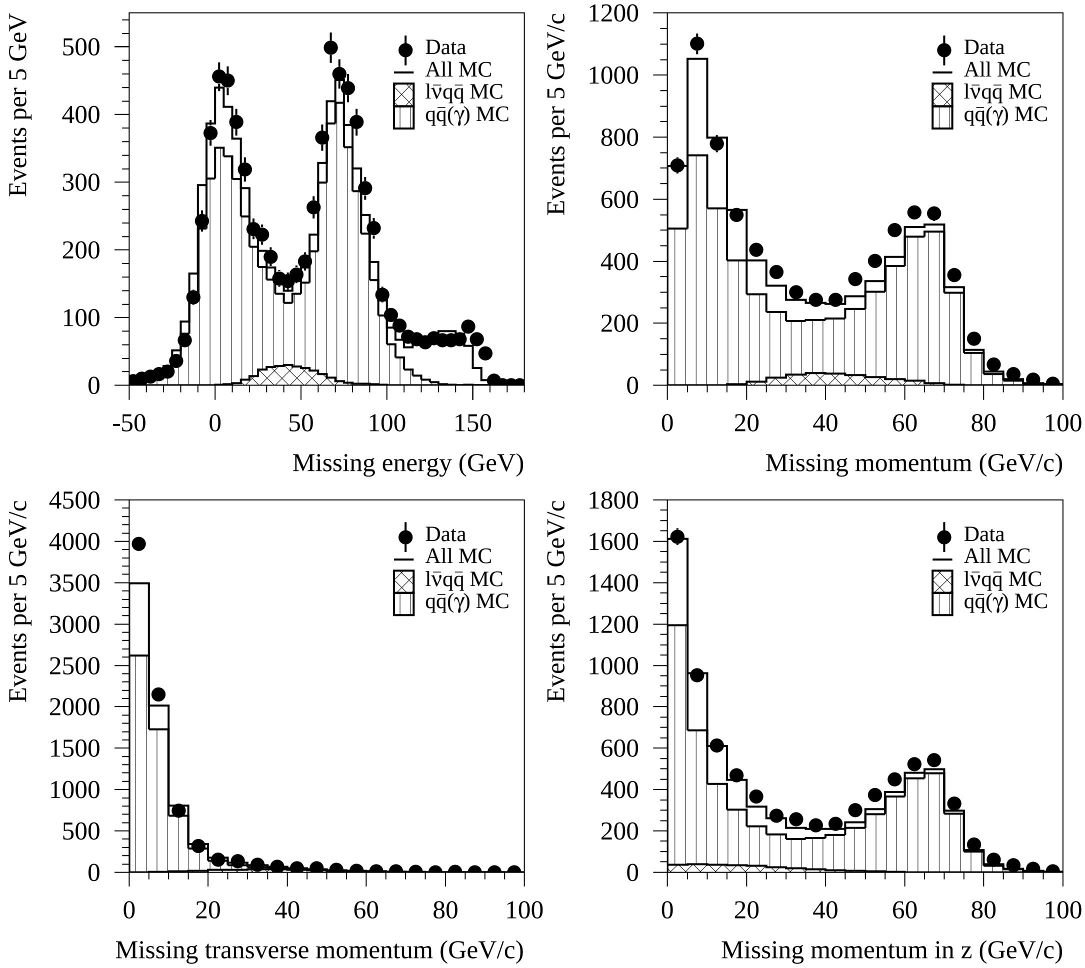

Figure 3.20: Missing energy, missing momentum and the component of the missing momentum parallel to the beam axis.

Process	Efficiency (%)		
	N_{ch} and E_{ch}	$\not{E}$ and $\not{p}$	$\not{p}_3$
$e^+e^-\to W^+W^-\to e\bar{\nu}q\bar{q}$	99.8	98.3	98.3
$e^+e^-\to W^+W^-\to \mu\bar{\nu}q\bar{q}$	99.6	98.4	98.2
$e^+e^-\to W^+W^-\to \tau\bar{\nu}q\bar{q}$	99.6	99.1	98.8
$e^+e^-\to W^+W^-\to q\bar{q}q\bar{q}$	100.0	11.4	11.4
$e^+e^-\to W^+W^-\to \ell\nu\ell\nu$	1.2	1.2	1.1
$e^+e^-\to Z/\gamma\to q\bar{q}(\gamma)$	90.0	56.7	29.4
$e^+e^-\to Z/\gamma\to \tau^+\tau^-(\gamma)$	5.4	4.8	3.8
$e^+e^-\to Z/\gamma\to \mu^+\mu^-(\gamma)$	0.00	0.00	0.00
$e^+e^-\to e^+e^-(\gamma)$	0.11	0.02	0.01
$e^+e^-\to ZZ$	62.3	33.5	30.1
$e^+e^-\to Ze^+e^-$	2.5	2.2	1.1
$e^+e^-\to We\nu_e$	64.7	64.6	57.5
$\gamma\gamma\to e^+e^-$	0.00	0.00	0.00
$\gamma\gamma\to \mu^+\mu^-$	0.00	0.00	0.00
$\gamma\gamma\to \tau^+\tau^-$	0.06	0.06	0.04
$\gamma\gamma\to q\bar{q}$	0.93	0.93	0.87
Efficiency (%)	99.7	98.4	98.2
Purity (%)	3.6	5.4	8.7
Predicted events	7243	4721	2939
Observed events	7799	5280	3166

Table 3.9: Preselection efficiencies for all signal and background processes. The symbol ℓ in $\ell\nu\ell\nu$ represents an electron, muon or tau.

of semileptonic WW events where the lepton is within the tracking acceptance of $|\cos\theta|<$ 0.95. The drop of about 3% in efficiency from $\sqrt{s}$ = 172 GeV is due to the higher boost of the W decay products, as discussed in Section 3.1.3.

The lepton identification criteria are the same as at $\sqrt{s}$ = 172 GeV and the estimators are shown in Figure 3.21. The selection efficiencies for signal and background after lepton identification are given in Table 3.10.

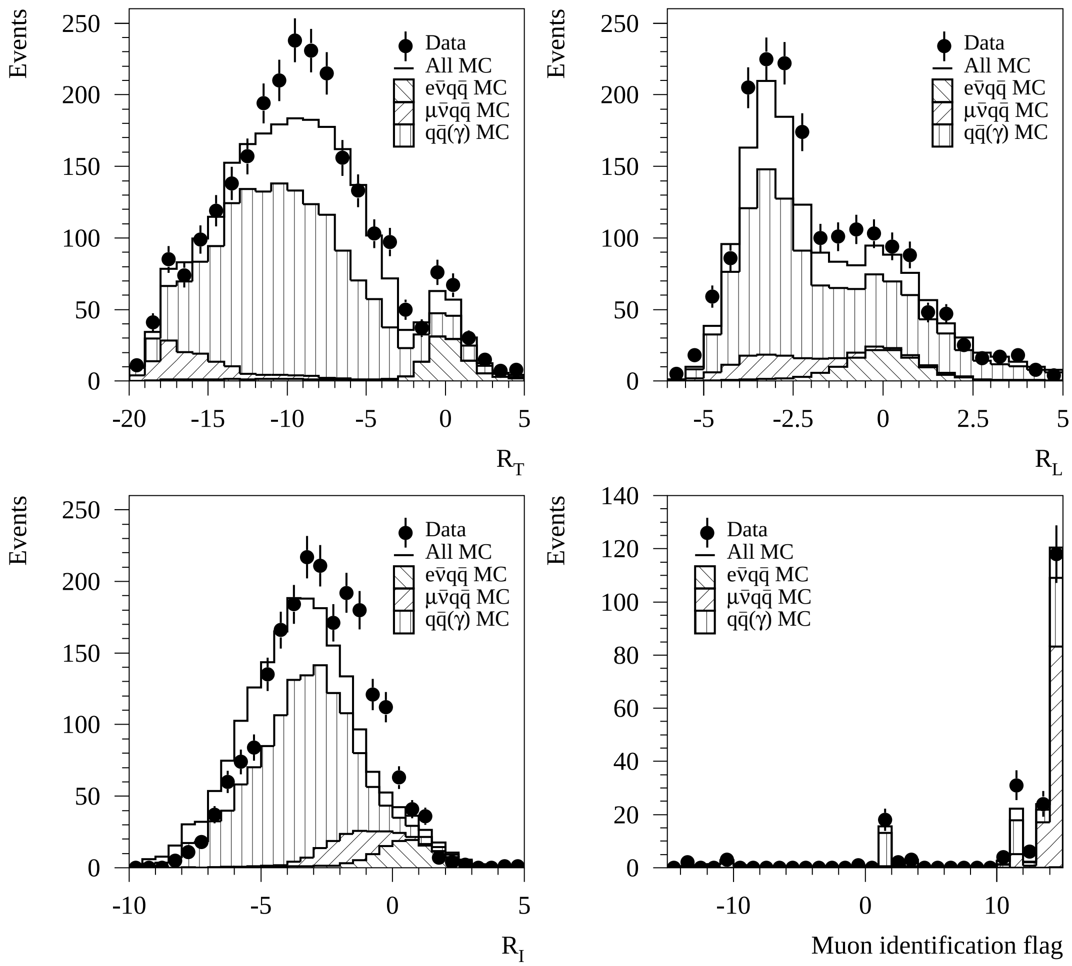

Figure 3.21: The electron identification estimators and the muon identification flag.

Process	Efficiency (%)	
	$e\bar{\nu}q\bar{q}$ channel	$\mu\bar{\nu}q\bar{q}$ channel
$e^+e^-\rightarrow W^+W^-\rightarrow e\bar{\nu}q\bar{q}$	85.3	0.3
$e^+e^-\rightarrow W^+W^-\rightarrow \mu\bar{\nu}q\bar{q}$	0.47	86.5
$e^+e^-\rightarrow W^+W^-\rightarrow \tau\bar{\nu}q\bar{q}$	7.7	6.6
$e^+e^-\rightarrow W^+W^-\rightarrow q\bar{q}q\bar{q}$	0.35	0.27
$e^+e^-\rightarrow W^+W^-\rightarrow \ell\nu\ell\nu$	0.26	0.17
$e^+e^-\rightarrow Z/\gamma\rightarrow q\bar{q}(\gamma)$	1.7	1.0
$e^+e^-\rightarrow Z/\gamma\rightarrow \tau^+\tau^-(\gamma)$	0.56	0.12
$e^+e^-\rightarrow e^+e^-(\gamma)$	0.01	0.00
$e^+e^-\rightarrow ZZ$	2.5	2.0
$e^+e^-\rightarrow Ze^+e^-$	0.24	0.02
$e^+e^-\rightarrow We\nu_e$	4.0	1.4
$\gamma\gamma\rightarrow\tau^+\tau^-$	0.01	0.00
$\gamma\gamma\rightarrow q\bar{q}$	0.05	0.01
Efficiency (%)	85.3	86.5
Purity (%)	38.9	57.2
Predicted events	286	197
Observed events	330	213

Table 3.10: Efficiencies after lepton identification for signal and background processes.

3.2.4 Energy correction for Bremsstrahlung.

At $\sqrt{s} = 172$ GeV, the search for energy deposits from Bremsstrahlung photons uses a cone, with an opening angle of 2°, around the electron impact point on ECAL. No check is made on the isolation of the electron, with the result that a lot of energy is added to the electron candidate track in background events.

In order to investigate whether an opening angle of 2° is the optimal choice, the bias and resolution on the electron energy are studied for several opening angles. Figure 3.22 shows the bias and resolution, which are defined to be the mean and RMS of the distribution of the reconstructed electron energy minus the true electron energy, known from simulation. Only events in which the electron in $e\bar{\nu}q\bar{q}$ events is correctly identified by the missing momentum technique are studied here. The results are separated into four classes:

- $e\bar{\nu}q\bar{q}$ events with neither Bremsstrahlung nor Final State Radiation (FSR) from the electron.
- $e\bar{\nu}q\bar{q}$ events with Bremsstrahlung but without FSR from the electron.
- $e\bar{\nu}q\bar{q}$ events without Bremsstrahlung but with FSR from the electron.
- $e\bar{\nu}q\bar{q}$ events with Bremsstrahlung and with FSR from the electron (not shown).

With no correction at all, *ie* an opening angle of 0°, the electron energy is underestimated by over 5 GeV on average for events with Bremsstrahlung and the resolution on the electron energy is 9 GeV instead of 1.6 GeV. As the opening angle is increased, the average bias goes down to -0.7 GeV and the resolution improves to just under 3 GeV. The optimal choice for the opening angle is in the range 2°- 3°. In order to improve the resolution slightly for events with FSR, the opening angle is chosen to be 2.5°.

In order to reduce the amount of energy added to the electron candidate track in background events, the amount of charged energy within 6° of the electron track is required to be less than 5 GeV. This is designed to keep the Bremsstrahlung correction for 99% of the signal $W^+W^-{\rightarrow}e\bar{\nu}q\bar{q}$ events and to reduce the percentage of $Z/\gamma{\rightarrow}q\bar{q}(\gamma)$ events to which the correction is applied, in this case to 53%.

During the development of the $\sqrt{s} = 183$ GeV analysis, the simple weighting of the tracking and calorimeter estimates for the electron four-vector was found to bias the direction of the electron. The tracking actually gives the best estimate for the original

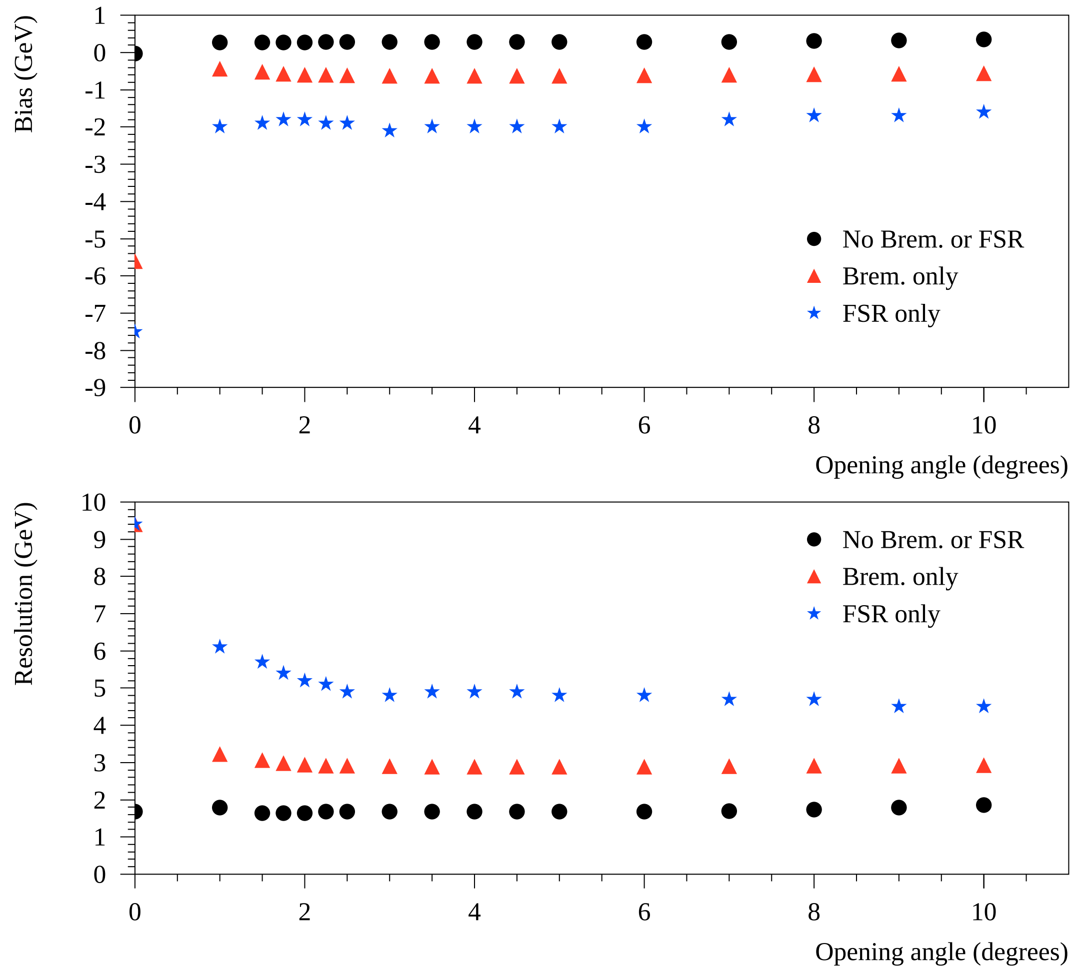

Figure 3.22: The variation of the bias (top) and resolution (bottom) on the electron energy for several values of the opening angle.

electron direction due to the importance of the high precision coordinates from the VDET in the track helix fit. As the majority of the Bremsstrahlung radiation occurs after the electron has passed through the VDET, the VDET coordinates are on the original trajectory of the electron. Therefore, the electron energy is corrected as before, but the tracking estimate for the direction is kept and the electron track momentum is simply scaled in order to set the electron mass:

$$\begin{aligned} E_{corr} &= w_{track} E_{track} + w_{cal} E_{cal} \\ \mathbf{p}_{corr} &= \frac{\sqrt{E_{corr}^2 - m_e^2}}{|\mathbf{p}_{track}|} \mathbf{p}_{track} \end{aligned} \tag{3.21}$$

3.2.5 Search for Final State Radiation.

Final State Radiation occurs as a result of the acceleration of a charge during the decay of the W boson. In the KORALW program, FSR is modelled by PHOTOS [58]. FSR, of up to two photons, happens in 18% of all simulated $W \rightarrow e\bar{\nu}$ decays and 10% of all simulated $W \rightarrow \mu\bar{\nu}$ decays, with a mean photon energy of 8 GeV. The photons may be radiated at large angles with respect to the lepton, though 90% are within 30° of the lepton. Some of the photons are recovered by the Bremsstrahlung correction, but the remainder are mistakenly included in the jet clustering. This can seriously bias the jet direction and energy and can give an equal mass constraint kinematic fit severe problems.

In order to improve the event reconstruction, a search is made for FSR [84]. Figure 3.23 shows a display of a simulated $\mu\bar{\nu}q\bar{q}$ event with FSR. The energy deposit in ECAL from the photon is clearly visible and is easily identified as a photon by the GAMPEX program [85]. Therefore, the closest GAMPEX photon to the lepton that meets the following criteria is considered as an FSR candidate:

- Energy greater than 0.5 GeV.
- Inconsistent with a $\pi^0 \rightarrow \gamma\gamma$ hypothesis from QPI0DO [86].
- Not associated to any object found by the Bremsstrahlung correction.

In order to avoid photons that are from the hadronic jets or from ISR, the following three requirements, illustrated in Figure 3.24, must be satisfied:

- The photon must be more than 40° away from the nearest good charged track that is not the lepton. In simulated events, 95% of the photons from the hadronic jets are within 40° of a good charged track that is not the lepton.
- The photon must be closer to the lepton than to the beam axis. In simulated events, 70% of all ISR photons are within 20° of the beam axis. Note also that photon identification extends down to 12° from the beam axis and that the lepton must be at least 18° away from the beam axis.
- The photon must be closer to the lepton than to any other charged track.

The four-vector of the FSR candidate is then added to the tracking estimate of the lepton four-vector. This is different to the Bremsstrahlung case as FSR occurs essentially at the

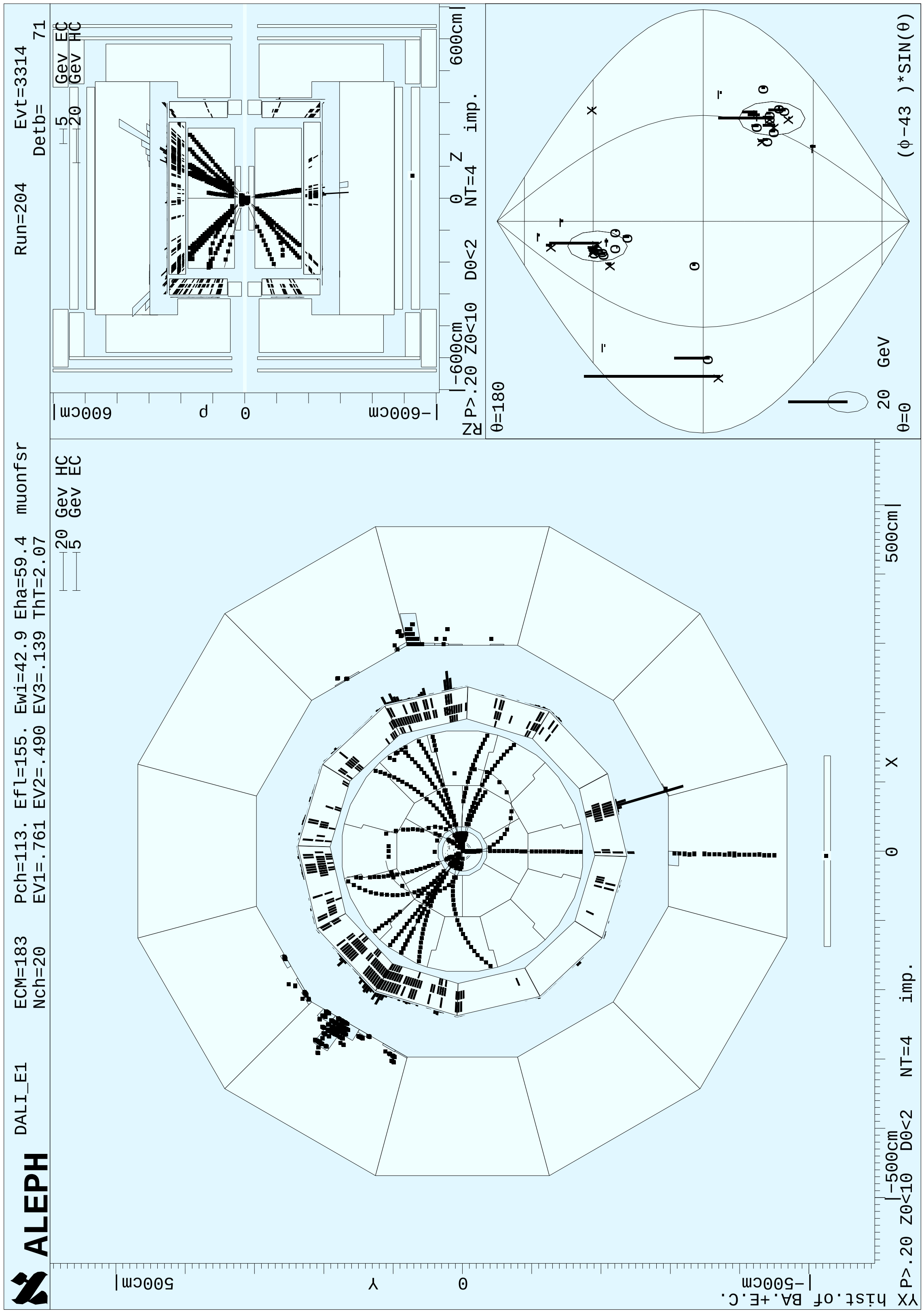

Figure 3.23: Event display for a simulated $e^+e^- \to W^+W^- \to \mu\bar{\nu}q\bar{q}$ decay with FSR from the muon

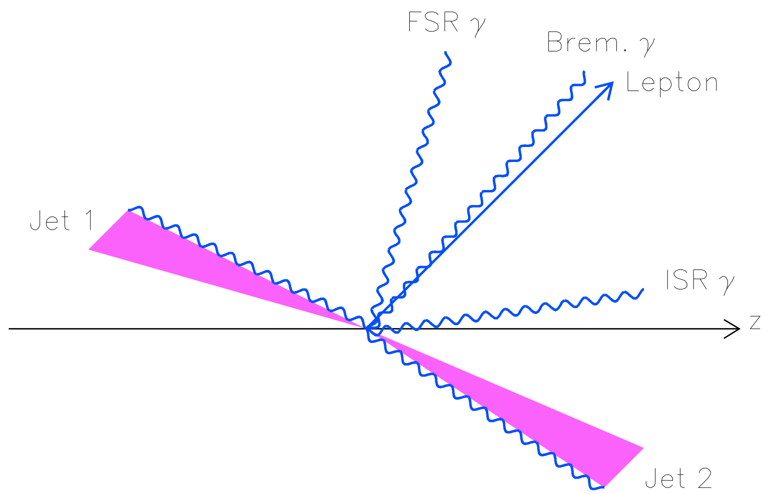

Figure 3.24: Schematic of photons in a $W^+W^-\rightarrow e\bar{\nu}q\bar{q}$ decay.

interaction point and may subtend a wide angle with respect to the lepton. Therefore, the tracking estimate of the lepton direction does not, in general, closely correspond to the original lepton direction.

As photons are not identified close to charged tracks with high efficiency, any energy deposit over 2 GeV that is found in the Bremsstrahlung region is added to the muon track energy in order to improve the reconstruction of the muon energy. The isolation check described in the previous section is also made for the muon.

The performance of the combined Bremsstrahlung correction and FSR search is shown in Table 3.11. The correction is applied to 39% and 9% of simulated $e\bar{\nu}q\bar{q}$ and $\mu\bar{\nu}q\bar{q}$ events, respectively. After subtracting the percentage of events without any photon radiation but to which the correction is mistakenly applied, about 45% of all FSR photons are recovered, increasing to 60% for FSR photon energies above 5 GeV. Around 32% of the Bremsstrahlung photons are found, which increases to 71% for Bremsstrahlung photon energies over 5 GeV. Energy is mistakenly added to the lepton in 18% and 4% of $e\bar{\nu}q\bar{q}$ and $\mu\bar{\nu}q\bar{q}$ events, respectively, but the average energy added is much less at 2 GeV. The correction is applied to 18% of the simulated $Z/\gamma\rightarrow q\bar{q}(\gamma)$ events selected in the $e\bar{\nu}q\bar{q}$ channel and only 9% of those selected in the $\mu\bar{\nu}q\bar{q}$ channel.

Figures 3.25 and 3.26 show the resolution on the lepton energy before and after the Bremsstrahlung correction and FSR search for leptons with and without energy lost to photon radiation. The resolution on the lepton energy, in those events that do not have any

Process	Composition	Percentage with energy added	Mean energy added (GeV)
$e^+e^- \to W^+W^- \to e\bar{\nu}q\bar{q}$	100	39	9.4
No Brem. or FSR	40	18	1.6
Brem. only	44	50	10.8
E_{Brem} >5 GeV	14	89	16.8
FSR only	9	59	10.8
E_{FSR} >5 GeV	4	78	17.1
$e^+e^- \to Z/\gamma \to q\bar{q}(\gamma)$	100	18	15.7
$e^+e^- \to W^+W^- \to \mu\bar{\nu}q\bar{q}$	100	8	5.1
No FSR	91	4	2.3
FSR	9	54	7.1
E_{FSR} >5 GeV	3	65	13.6
$e^+e^- \to Z/\gamma \to q\bar{q}(\gamma)$	100	9	10.6

Table 3.11: Mean energy added by the combined Bremsstrahlung correction and FSR search to fully simulated, selected $W^+W^- \to e\bar{\nu}q\bar{q}$ and $e^+e^- \to Z/\gamma \to q\bar{q}(\gamma)$ events. The second column breaks the sample down into various components and the third column gives the percentage of that component to which energy is added.

energy lost to photon radiation, is not significantly worsened by the corrections, although the energy is biased upwards by 0.2 GeV on average for electrons. The overall resolution on the electron energy improves to 4.2 GeV from 8.7 GeV and the bias decreases to -0.8 GeV from -4.3 GeV. The overall resolution on the muon energy also improves to 3.1 GeV from 3.8 GeV and the bias decreases to -0.2 GeV from -0.6 GeV. The energy added by the Bremsstrahlung correction and FSR search is shown in Figure 3.27 for data and simulation. The agreement between them is good.

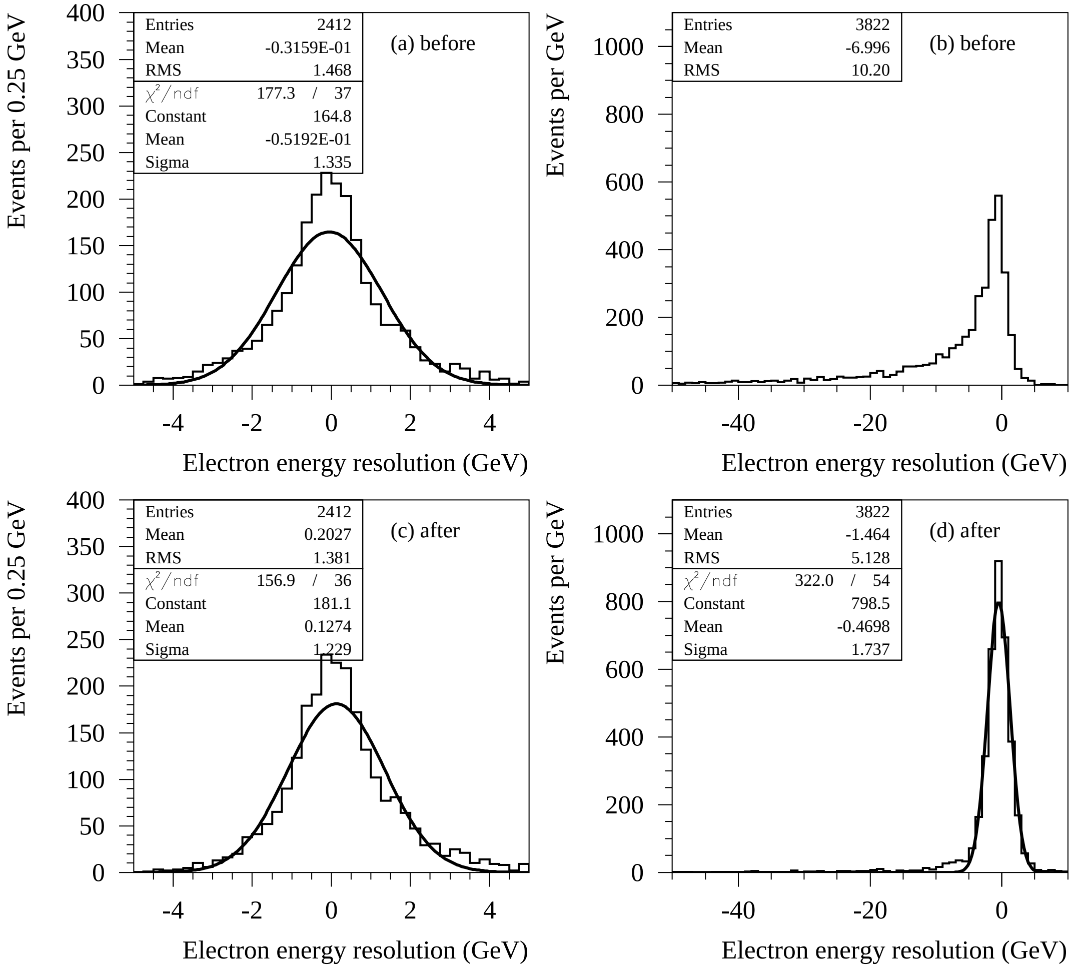

Figure 3.25: The resolution on the electron energy, in fully simulated and selected $e\bar{\nu}q\bar{q}$ events, before the Bremsstrahlung correction and FSR search for (a) events without any energy lost to photon radiation and (b) events with some energy lost to photon radiation. The corresponding resolutions after the Bremsstrahlung correction and FSR search are shown in (c) and (d).

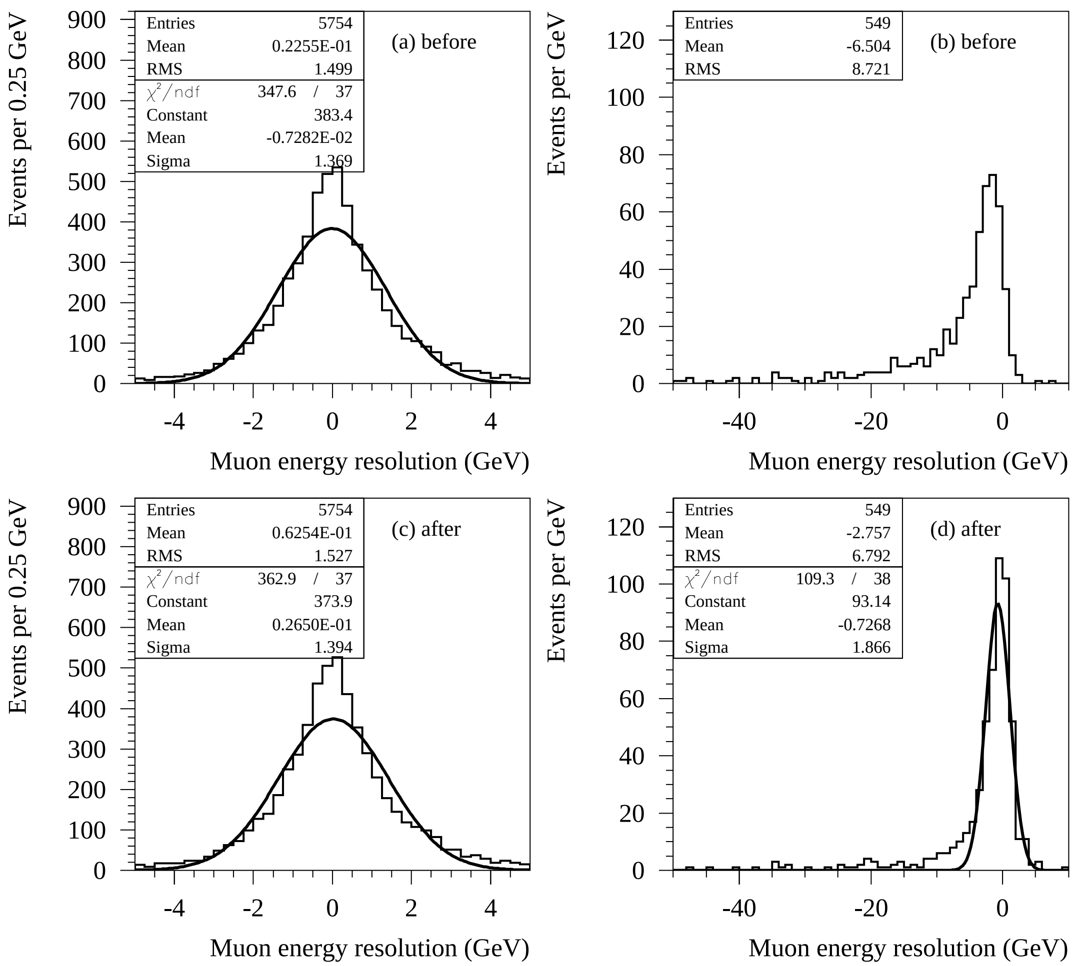

Figure 3.26: The resolution on the muon energy, in fully simulated and selected $\mu\bar{\nu}q\bar{q}$ events, before the FSR search for (a) events without any energy lost to photon radiation and (b) events with some energy lost to photon radiation. The corresponding resolutions after the FSR search are shown in (c) and (d).

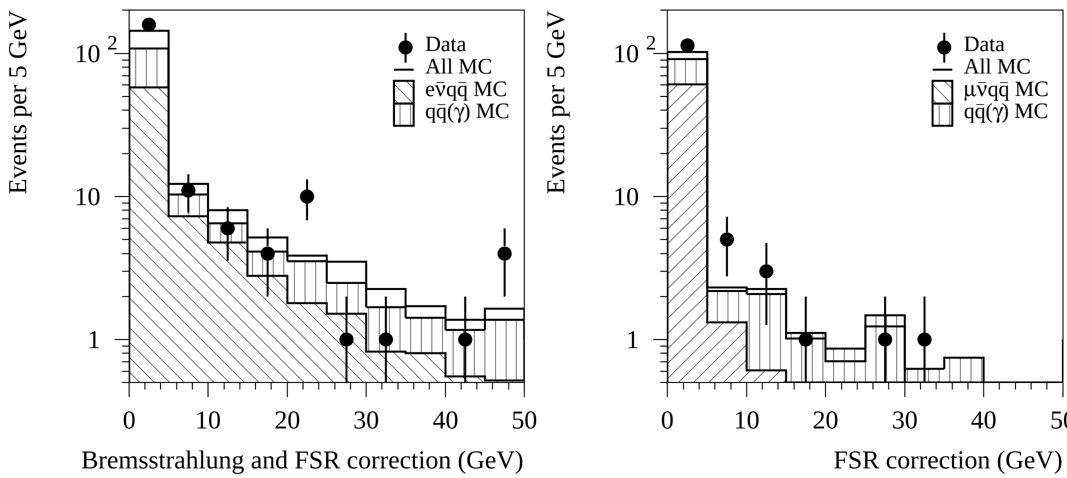

Figure 3.27: The energy added by the Bremsstrahlung correction and FSR search to (left) electrons and (right) muons for simulation and data.

3.2.6 Lepton energy.

The discriminating power between signal and background that is obtained from the lepton energy distribution, which is shown in Figure 3.28, is maximised by requiring the lepton energy to be at least 21 GeV. This keeps 99% of the signal semileptonic WW decays and rejects 73% of the $Z/\gamma \to q\bar{q}(\gamma)$ background in both the $e\bar{\nu}q\bar{q}$ and $\mu\bar{\nu}q\bar{q}$ channels. The increased rejection power for the $e\bar{\nu}q\bar{q}$ channel with respect to the $\sqrt{s} = 172$ GeV analysis is due to the requirement that the electron should be isolated for the Bremsstrahlung correction to be applied. Table 3.12 lists the efficiencies for all the signal and background processes.

3.2.7 Association of energy flow objects to the lepton.

In order to correctly reconstruct the two jets from the hadronic W decay, all objects associated to the lepton must be identified and removed from the list of energy flow objects used by the jet clustering algorithm. At $\sqrt{s} = 172$ GeV, the lepton charged track and any ECAL energy deposit associated by the Bremsstrahlung correction are excluded. However, the electron energy deposit may be partially in the HCAL, which creates a different kind of energy flow object, or the muon may deposit more energy in the calorimeters than expected, which creates an additional energy flow object. These energy flow objects should also be excluded.

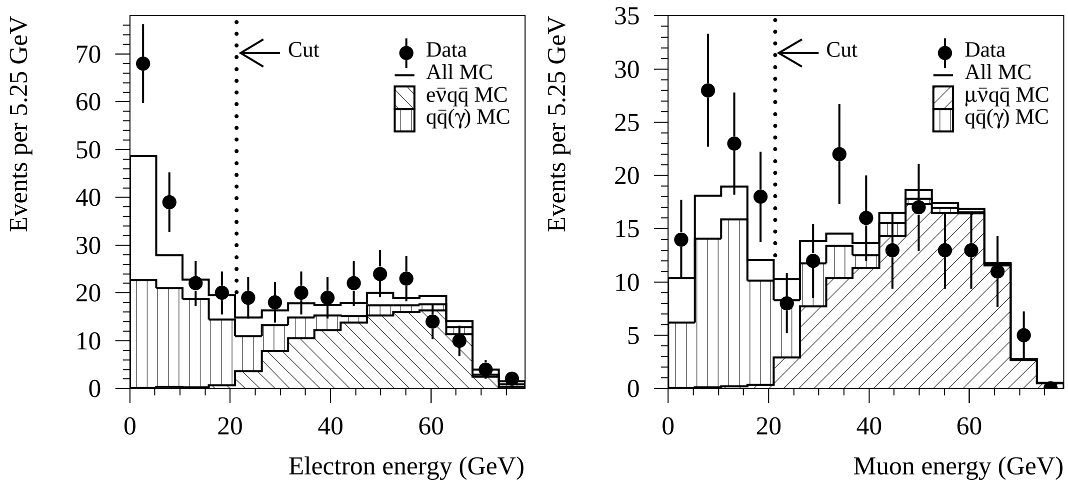

Figure 3.28: The lepton energy distribution for the $e\bar{\nu}q\bar{q}$ and $\mu\bar{\nu}q\bar{q}$ channels.

Process	Efficiency (%)	
	$e\bar{\nu}q\bar{q}$ channel	$\mu\bar{\nu}q\bar{q}$ channel
$e^+e^-\to W^+W^-\to e\bar{\nu}q\bar{q}$	84.2	0.07
$e^+e^-\to W^+W^-\to \mu\bar{\nu}q\bar{q}$	0.18	86.0
$e^+e^-\to W^+W^-\to \tau\bar{\nu}q\bar{q}$	4.3	4.1
$e^+e^-\to W^+W^-\to q\bar{q}q\bar{q}$	0.08	0.07
$e^+e^-\to W^+W^-\to \ell\nu\ell\nu$	0.24	0.17
$e^+e^-\to Z/\gamma\to q\bar{q}(\gamma)$	0.48	0.26
$e^+e^-\to Z/\gamma\to \tau^+\tau^-(\gamma)$	0.35	0.09
$e^+e^-\to e^+e^-(\gamma)$	0.00	0.00
$e^+e^-\to ZZ$	1.23	1.04
$e^+e^-\to Ze^+e^-$	0.17	0.02
$e^+e^-\to We\nu_e$	1.95	0.30
$\gamma\gamma\to\tau^+\tau^-$	0.00	0.00
$\gamma\gamma\to q\bar{q}$	0.00	0.00
Efficiency (%)	84.2	86.0
Purity (%)	68.4	81.6
Predicted events	161	137
Observed events	181	130

Table 3.12: Efficiencies after requiring that the lepton energy should be greater than 21 GeV.

Therefore, the lepton charged track, any energy deposits in ECAL or HCAL associated to the lepton by the Bremsstrahlung routine and any FSR photons associated to the lepton are all identified and removed from the energy flow list. Any remaining energy deposits in ECAL within 1.5° or in HCAL within 2.0° of the lepton track, after extrapolation to the relevant calorimeter, are also removed [87], provided that the lepton track passes the isolation check. The remaining energy flow objects are then clustered into jets using the same algorithm as at $\sqrt{s} = 172$ GeV.

3.2.8 Multidimensional discrimination.

The probability density functions, which describe the three-dimensional space formed by the lepton energy, the missing transverse momentum and the lepton isolation variables shown in Figure 3.29, are re-parameterised at $\sqrt{s} = 183$ GeV and used to calculate the

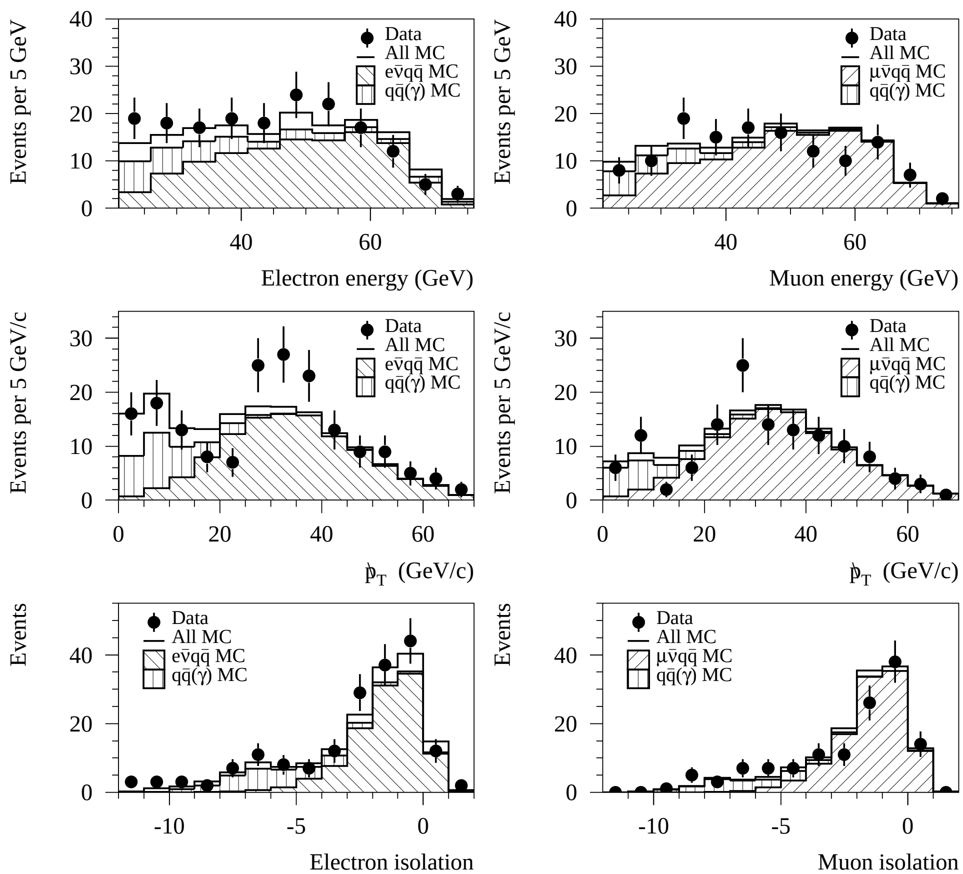

Figure 3.29: The lepton energy, the missing transverse momentum and the isolation of the lepton for the $e\bar{\nu}q\bar{q}$ and $\mu\bar{\nu}q\bar{q}$ channels.

probabilities as before. Figure 3.30 shows the probabilities and the variation of the efficiency, purity and quality factor with a lower bound on the probability for the $e\bar{\nu}q\bar{q}$ and the $\mu\bar{\nu}q\bar{q}$ channels. The optimum values for the lower bounds are:

$$\begin{aligned} P(e\bar{\nu}q\bar{q} \mid E_e, \not{p}_T, iso_e) &\geq 0.40 \\ P(\mu\bar{\nu}q\bar{q} \mid E_\mu, \not{p}_T, iso_\mu) &\geq 0.40 \end{aligned} \tag{3.22}$$

The efficiencies after these requirements are shown in Table 3.13

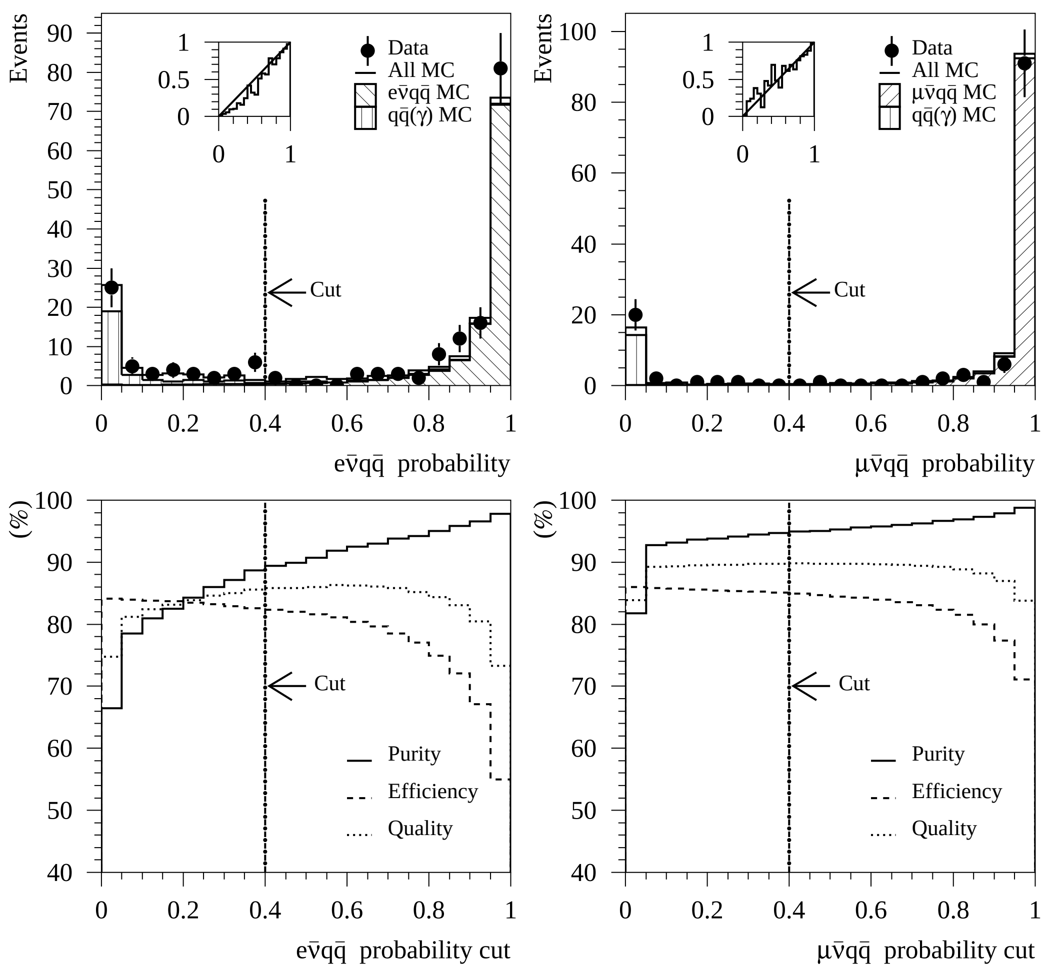

Figure 3.30: The $e\bar{\nu}q\bar{q}$ and $\mu\bar{\nu}q\bar{q}$ probabilities are shown in the upper plots, where the inset graphs show the $e\bar{\nu}q\bar{q}$ or $\mu\bar{\nu}q\bar{q}$ fraction versus the $e\bar{\nu}q\bar{q}$ or $\mu\bar{\nu}q\bar{q}$ probability. The variation of the efficiency, purity and quality factor with a lower bound on the probability is shown in the right-hand plots.

Process	Efficiency (%)	
	$e\bar{\nu}q\bar{q}$ channel	$\mu\bar{\nu}q\bar{q}$ channel
$e^+e^-\to W^+W^-\to e\bar{\nu}q\bar{q}$	82.4	0.05
$e^+e^-\to W^+W^-\to \mu\bar{\nu}q\bar{q}$	0.15	84.9
$e^+e^-\to W^+W^-\to \tau\bar{\nu}q\bar{q}$	3.1	3.2
$e^+e^-\to W^+W^-\to q\bar{q}q\bar{q}$	0.01	0.01
$e^+e^-\to W^+W^-\to \ell\nu\ell\nu$	0.17	0.11
$e^+e^-\to Z/\gamma\to q\bar{q}(\gamma)$	0.04	0.01
$e^+e^-\to Z/\gamma\to \tau^+\tau^-(\gamma)$	0.11	0.05
$e^+e^-\to ZZ$	0.37	0.46
$e^+e^-\to Ze^+e^-$	0.06	0.00
$e^+e^-\to We\nu_e$	1.53	0.10
Efficiency (%)	82.4	84.9
Purity (%)	89.8	94.9
Predicted events	119.6	116.4
Observed events	130	105

Table 3.13: Efficiencies with the lower bounds on the probabilities.

3.2.9 Summary.

The overall efficiency and purity of the selection are high at 82.4% and 89.9% for the $e\bar{\nu}q\bar{q}$ channel and 84.9% and 95.0% for the $\mu\bar{\nu}q\bar{q}$ channel. The expected and observed number of events from the 56.81 pb^{-1} of data collected at $\sqrt{s} = 183$ GeV are in good agreement.

Chapter 4

Kinematic fitting.

> "It is a capital mistake to theorise before one has data. Insensibly one begins to twist facts to suit theories, instead of theories to suit facts", said Sherlock Holmes in *A Scandal in Bohemia* by Sir Arthur Conan Doyle.

The reconstruction of the energies and directions of the two jets and the lepton can be enhanced in order to build a more sensitive estimator for the W mass. The first step is to correct the measurements for any biases introduced by the finite detector acceptance. The second step is to vary the corrected measurements in order to satisfy:

- Conservation of momentum (3 constraints)
- Conservation of energy (1 constraint)
- Hadronic W mass = Leptonic W mass (1 constraint)

This gives values for the energies and directions that are more accurate than those from the measurements alone and which are also physically consistent with the conservation equations.

The most effective way to use all the information from the measurements and the constraints is a kinematic fit. Here, the corrected measurements are allowed to vary, according to their experimental resolutions, until a solution is found that both satisfies the constraints and minimises the difference between the fitted and corrected quantities.

The problems posed by the kinematic fit strategy adopted for the $\sqrt{s} = 172$ GeV analysis are discussed in Section 4.1. In order to solve these problems, a new kinematic fit is developed for the $\sqrt{s} = 183$ GeV analysis and this is described in detail in Section 4.2.

4.1 First kinematic fit at $\sqrt{s} = 172$ GeV.

The kinematic fit for semileptonic WW decays at $\sqrt{s} = 172$ GeV is adapted from that for the fully hadronic WW decay channel [65]. A discussion of the minimisation strategy, parameterisation, performance and problems of this approach follow. In order to decide whether to use the equal mass constraint, a study of the relative precision of estimators defined with or without this constraint is performed.

4.1.1 Minimisation strategy.

The kinematic fit package MATHKINE [88] performs a least squares minimisation and uses Lagrange multipliers [89] to impose constraints. The function to be minimised is:

$$\mathcal{S} = (y - y^0)^T V^{-1}(y - y^0) + 2\lambda f(y) \tag{4.1}$$

where y is the vector of fitted correction factors;
y^0 is the vector of expected correction factors;
V is the error matrix;
λ is the vector of Lagrange multipliers;
$f(y)$ is the vector of constraint functions.

Note well that a diagonal approximation for the error matrix is used, so all correlations between the variables are neglected.

The conditions that must be satisfied for $\mathcal{S}$ to be a minimum are that the derivative of $\mathcal{S}$ with respect to all the variables and the Lagrange multipliers must be zero:

$$\begin{array}{rclcl} \frac{\partial \mathcal{S}}{\partial y} & = & 2V^{-1}(y - y^0) + 2\lambda \frac{\partial f(y)}{\partial y} & = & 0 \\ \frac{\partial \mathcal{S}}{\partial \lambda} & = & 2f(y) & = & 0 \end{array} \tag{4.2}$$

The starting values for y are the expected correction factors, y^0, which are calculated from the measured momenta and corrected for detector effects as discussed in the next section. In general, the starting values do not satisfy the constraint conditions. An improved set of values, y^{l+1} with $l = 0, 1, 2, \ldots$, can be calculated by performing a Taylor series expansion on $f(y^{l+1})$:

$$f(y^{l+1}) \approx f(y^l) + \left.\frac{\partial f(y)}{\partial y}\right|_{y=y^l} (y^{l+1} - y^l) \tag{4.3}$$

Note that the constraint equations are actually non-linear in y, so it is necessary to assume that the correct solution is close enough for a Taylor series expansion to be applicable. On replacing $\left.\frac{\partial f(y)}{\partial y}\right|_{y=y^l}$ with a matrix B and manipulating 4.2, the conditions become:

$$\begin{array}{lclclclcl} V^{-1}y^{l+1} & & & - & V^{-1}y^0 & + & B^T\lambda & = & 0 \\ By^{l+1} & - & By^l + f(y^l) & & & & & = & 0 \end{array} \tag{4.4}$$

and can be written more neatly in matrix form as:

$$\begin{pmatrix} V^{-1} & B^T \\ B & 0 \end{pmatrix} \begin{pmatrix} y^{l+1} \\ \lambda \end{pmatrix} = \begin{pmatrix} V^{-1}y^0 \\ By^l - f(y^l) \end{pmatrix} \tag{4.5}$$

This matrix equation can be solved for y^{l+1} by multiplying through by the inverse of $\begin{pmatrix} V^{-1} & B^T \\ B & 0 \end{pmatrix}$. The recursive relation obtained is:

$$y^{l+1} = y^0 + VB^T(BVB^T)^{-1}\left[B(y^l - y^0) - f(y^l)\right] \tag{4.6}$$

which is used to find better approximations for y, until the change in $\mathcal{S}$ with each iteration falls below some minimum value.

4.1.2 Parameterisation of jet and lepton corrections.

As in [65, 88], the variables are three correction factors, (a_i, b_i, c_i), for each of the two jets, lepton and neutrino. The correction factors transform the measured momenta, $\mathbf{p}_i^{meas}$, into the fitted momenta, $\mathbf{p}_i^{fit}$, as:

$$\mathbf{p}_i^{fit} = a_i\mathbf{p}_i^{meas} + b_i\mathbf{u}_i^{\theta} + c_i\mathbf{u}_i^{\phi} \tag{4.7}$$

where a_i are scale factors applied to the measured momenta;

b_i are scale factors applied to the transverse momentum component in the θ direction, *ie* in the plane defined by the measured momentum and the beam axis;

c_i are scale factors applied to the transverse momentum component in the ϕ direction, *ie* in the plane perpendicular to that containing the measured momentum and the beam axis.

The ratio of the momentum to the energy of the jet, *ie* the jet velocity, is usually very well measured as systematic effects due to particle mis-assignment or loss tend to cancel in the ratio. Therefore, the jet velocity is assumed to be perfectly measured and the fitted jet energy is defined as:

$$E_i^{fit} = E_i^{meas} \frac{\left|\mathbf{p}_i^{fit}\right|}{\left|\mathbf{p}_i^{meas}\right|} \tag{4.8}$$

The expected values and expected resolutions for the correction factors are parameterised from simulation as functions of the measured energy and polar angle for each type of particle [65]. When the variables y are distributed as Gaussians with mean $y^0(E^{meas}, \cos\theta^{meas})$ and variance $\sigma^2_{y^0}(E^{meas}, \cos\theta^{meas})$, then the value of $\mathcal{S}$ at the minimum is distributed as a χ^2. A χ^2 distribution is characterised by the number of degrees of freedom, ν, which is defined as the number of measured quantities minus the number of independent fitted parameters.

Here the number of measured quantities is twelve (the expected correction factors for the jets, lepton and neutrino), the number of fitted parameters is twelve (the fitted correction factors for the jets, lepton and neutrino) and the number of constraints is five. This leaves seven independent fitted parameters and implies that the fit has five degrees of freedom. However, even ALEPH cannot measure neutrinos so the real number of measured quantities is nine and the number of degrees of freedom is two. If the optional equal mass constraint is not used, then the number of degrees of freedom decreases to one. The problem of how to deal with an unmeasured particle in a kinematic fit will be discussed further in Section 4.1.4.

4.1.3 Performance of MATHKINE.

The W mass distributions for selected, simulated semileptonic WW decays before and after a kinematic fit with only the energy and momentum conservation constraints ($\nu = 1$) or with the additional equal mass constraint ($\nu = 2$) are shown in Figure 4.1. The resonance is much sharper for the fit with the equal mass constraint. Rescaling the hadronic and leptonic masses by $\frac{E_{beam}}{E_{had}}$ and $\frac{E_{beam}}{E_{lept}}$, respectively, is similar to an equal mass constraint.

The resolutions on the W mass before and after kinematic fits with $\nu = 1$, $\nu = 1$ with rescaling and $\nu = 2$ are shown in Figure 4.2. After a kinematic fit with $\nu = 2$, the event-by-event bias between the fitted mass and the generated mass is over 0.650 GeV/c^2 for

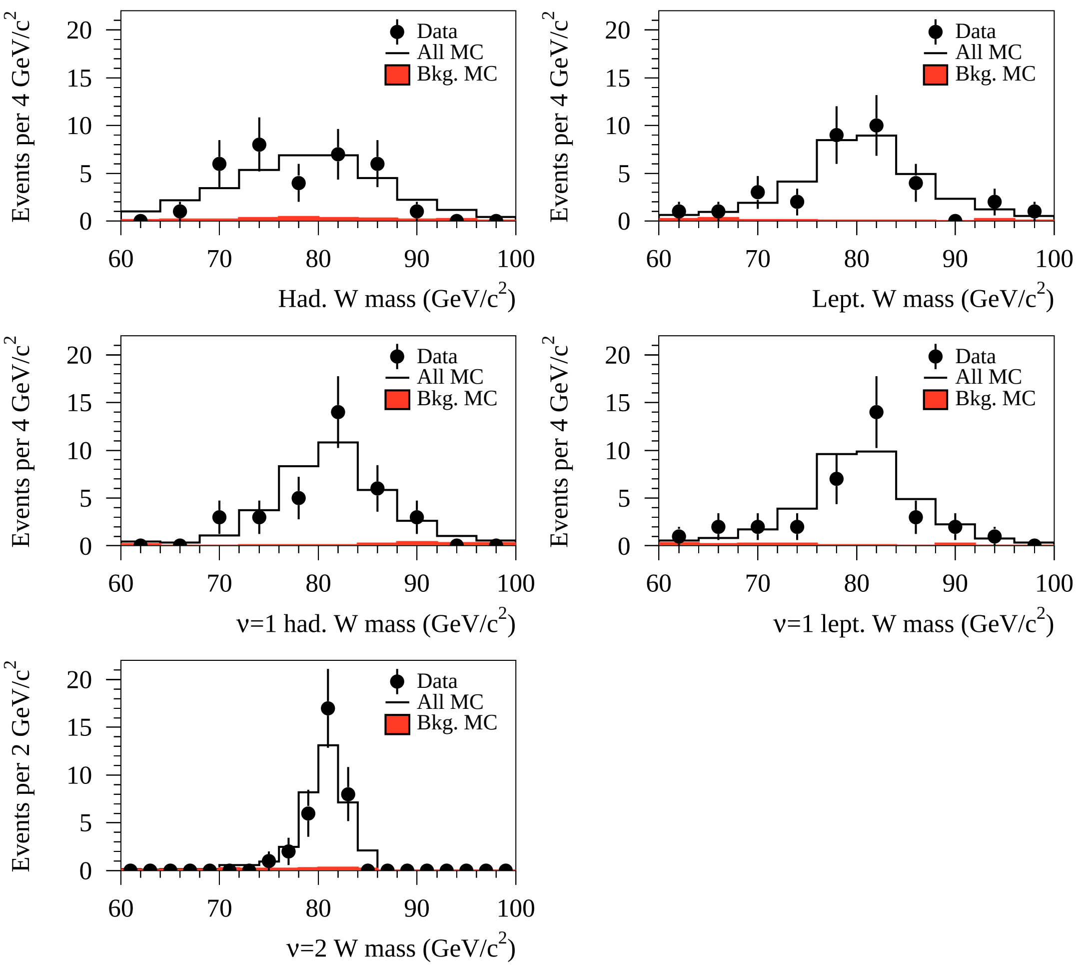

Figure 4.1: W mass distributions before and after a MATHKINE fit with 1 or 2 degrees of freedom.

all semileptonic WW events, 0.280 GeV/c^2 of which is due to events with over 0.5 GeV of energy lost to ISR. The positive shift from ISR can be easily understood as the radiation of an energetic ISR photon lowers the effective centre-of-mass energy for WW production. However, the conservation of energy constraint ignores the energy lost to the ISR photon and scales the energy of the jets, lepton and neutrino so that the sum is equal to the full LEP energy. As $M_W \approx \sqrt{2E_1E_2(1-\cos\theta_{12})}$, this biases the fitted W mass upwards. The remainder of the bias arises from the effects discussed in the next section.

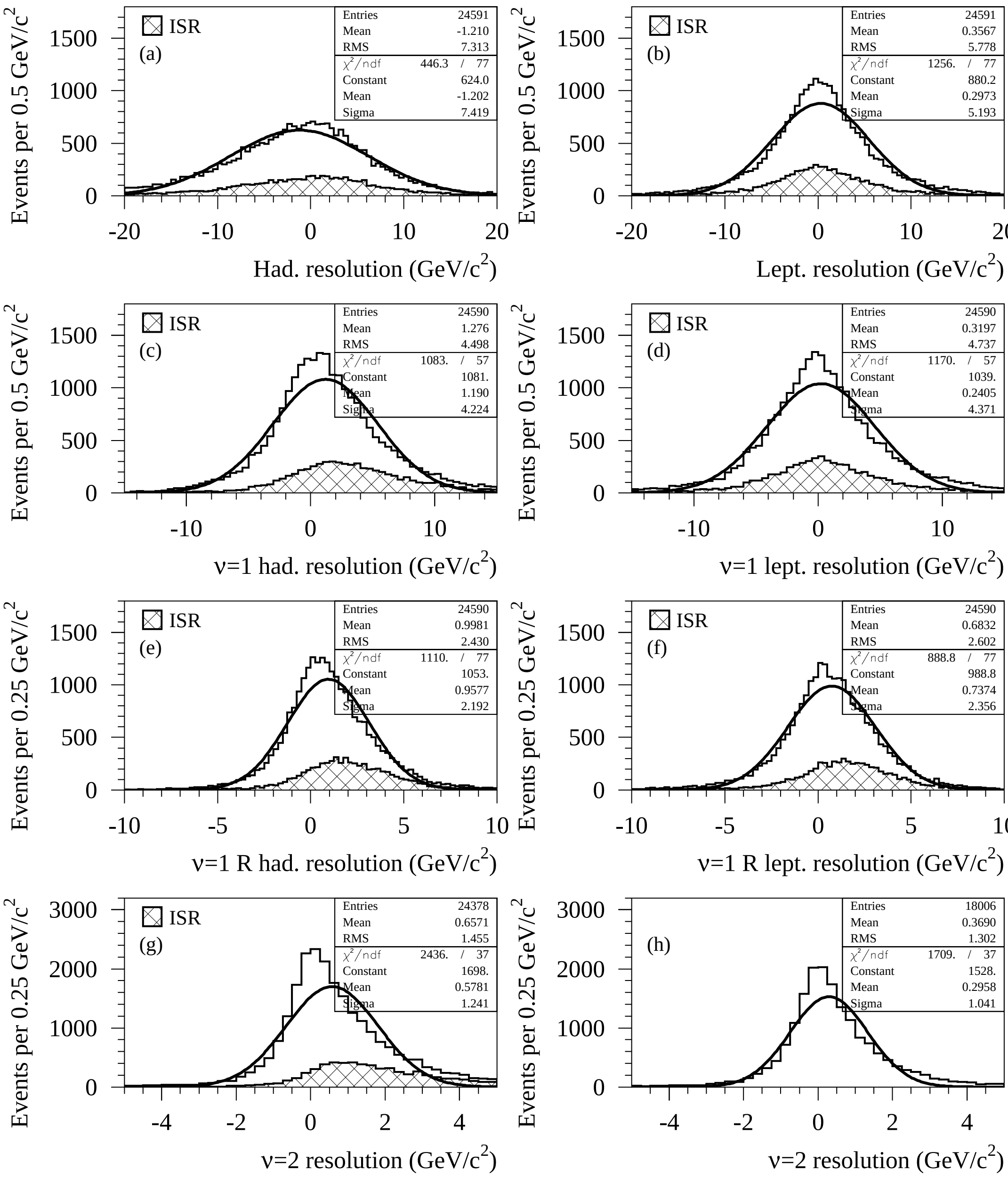

Figure 4.2: Resolution on the hadronic and leptonic W masses for fully simulated and selected semileptonic WW events: (a) hadronic and (b) leptonic resolution before kinematic fit; (c) hadronic and (d) leptonic resolution with $\nu = 1$ kinematic fit; (e) hadronic and (f) leptonic resolution with $\nu = 1$ kinematic fit and rescaling (labelled R); (g) including and (h) excluding events with more than 0.5 GeV of energy lost to ISR using a $\nu = 2$ kinematic fit, where the true W mass is taken to be the average of the two generated W masses.

4.1.4 Problems.

There are several problems associated with applying a kinematic fit developed for the fully hadronic channel directly to the semileptonic channel.

The first problem is obvious and serious - the strategy described above assumes that all of the fitted variables that appear in the constraint equations $f(y)$ are independently measured. However, this is not true as the neutrino is not detected by ALEPH and the three constraints from conservation of momentum have to be used to infer the neutrino momentum from the measured momenta of the jets and the lepton. This implies that the neutrino variables are completely anti-correlated with those for the jets and the lepton.

Therefore, the neutrino variables should only appear in the constraint equations and not in the vector of fitted variables [89, 90]. If one still insists on fitting for the neutrino variables, then the error matrix must contain off-diagonal elements in order to account for the anti-correlation and to properly reduce the number of degrees of freedom to two or one. The approximation used is to parameterise the expected correction factors and resolutions for the neutrino as a function of those for the jets and the lepton [91].

The second problem is that the parameterisation for the jet correction factors is taken directly from that for the fully hadronic WW decay channel [65]. In the fully hadronic channel, there are four jets in the final state and a jet from one W can be close to a jet from the other W. This promotes mixing and degrades the energy and angular resolution of the jets with respect to the original fermions from the W decays [92]. In the semileptonic channel, there are only two jets in the final state and the absence of the second di-jet suppresses the mixing effect. The application of the jet correction factors from the fully hadronic channel to the semileptonic channel results in an over-estimate of the jet measurement errors by a factor of 1.3 and a concomitant reduction in the sensitivity of the fit.

The third problem is that the correction factor parameterisation is identical for electrons and muons and is only a function of polar angle. The loss of energy in the form of Bremsstrahlung radiation from the electron and the use of the calorimeter energy measurement by the Bremsstrahlung correction creates differences between the reconstruction of electrons and muons. The correction factors should depend on momentum as well, since the momentum resolution from the tracking detectors for a charged particle is directly proportional to the momentum of the particle.

The effect of these approximations is shown in Figure 4.3, where the $\mathcal{S}_{min}$ distribution is compared to a true χ^2 with two degrees of freedom. The agreement is only reasonable below 4, even when discounting those events with ISR photons above 0.5 GeV. As a consequence, the $P(\chi^2 > \mathcal{S}_{min})$ distribution is only flat when the probability to obtain a worse kinematic fit result exceeds 20%. The lack of uniformity implies that the assumed correction factors and resolutions are incorrect for over a quarter of semileptonic WW events without ISR.

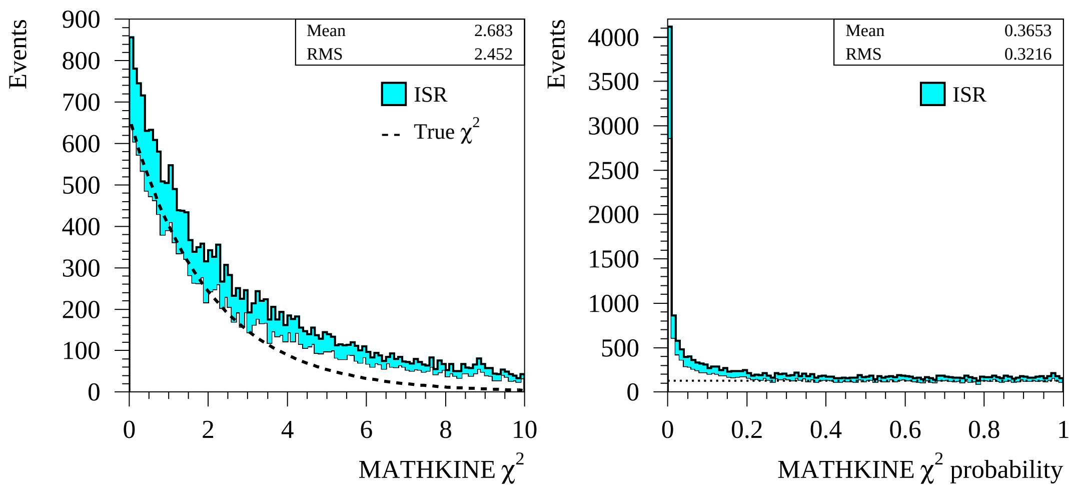

Figure 4.3: The MATHKINE $\mathcal{S}_{min}$ distribution, which is compared to a true χ^2 distribution with two degrees of freedom, and the MATHKINE $P(\chi^2 > \mathcal{S}_{min})$ distribution for fully simulated and selected semileptonic WW events.

The fourth problem is more subtle and concerns both the parameterisation and the fit strategies. The parameterisations for the expected correction factors, y^0, are functions of the measured energy and measured polar angle. However, the underlying true energy spectrum (prior to the simulation of the detector response) is not uniform and is in fact completely contained within the allowed kinematic region, as shown in Figure 4.4. The result is correction factors that depend strongly on the measured energy: the jet energy is reduced when above average and increased when below average.

As a case in point, consider an event that contains a jet with a measured energy of 60 GeV and a measured $\cos\theta$ of 0.9. The parameterisation for the correction factor a, shown in Figure 4.5 (a) and derived for the relevant bin from Figure 4.4 (b), corrects the jet energy down to 57 GeV. However, the low polar angle of the jet suggests that several particles in the jet may be nearly collinear with the beam axis and thus go undetected. This

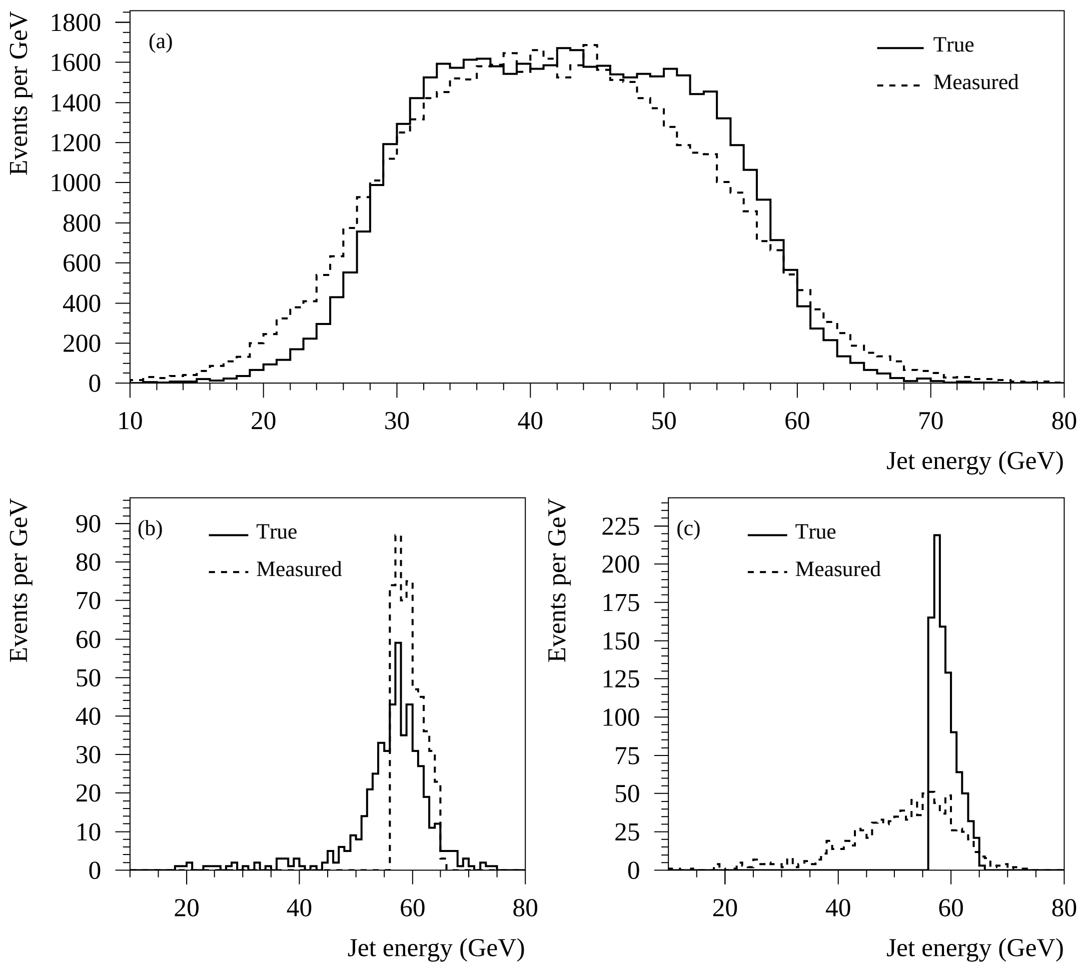

Figure 4.4: The measured and true energy spectra for (a) all jets, (b) jets where the measured energy is in the range [56.25,65.25) and the measured $|\cos\theta|$ is in the range [0.8,1.0] and (c) jets where instead the true energy and true $|\cos\theta|$ are in the above ranges, for fully simulated and selected semileptonic WW decays.

implies that the jet energy should be corrected up and not down, as shown by Figure 4.4 (c).

The correction factors are supposed to correct for non-Gaussian detector effects. If the correction factors are parameterised in terms of the measured energy and measured polar angle, then the particle momenta are altered over and above the real effects from detector acceptance and resolution. This is most evident in the regions where the underlying energy spectrum changes rapidly. The effect is to make any event look more like a WW decay. In light of the fact that the fit strategy assumes that the starting point (*ie* the set of expected correction factors) is good enough for a Taylor series expansion of the constraint functions

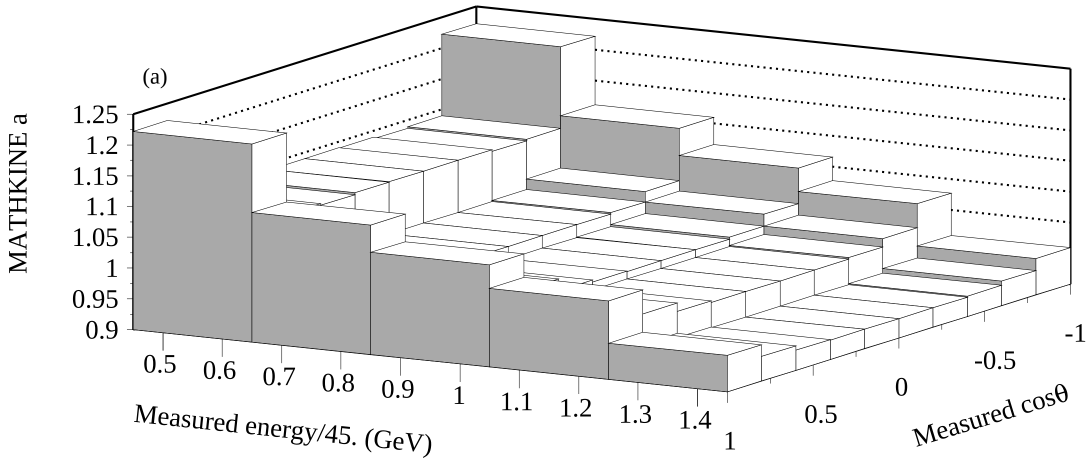

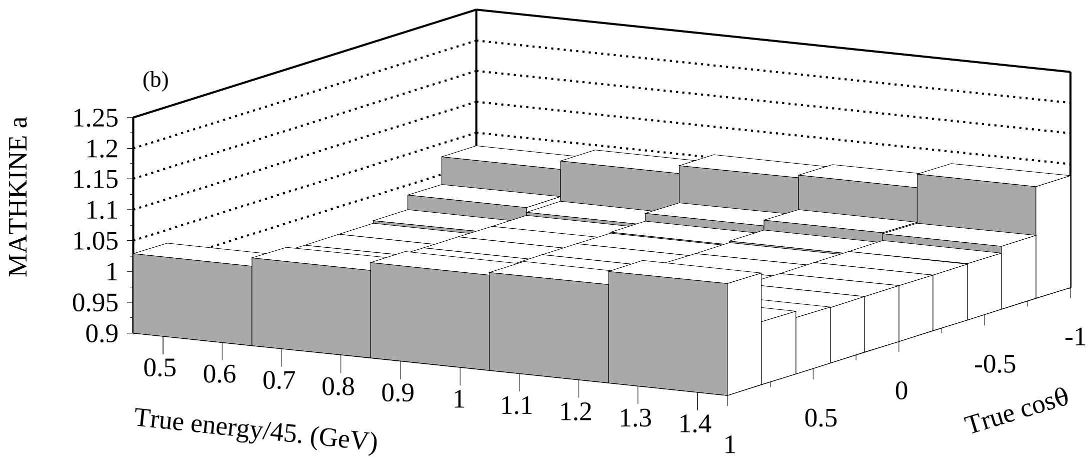

Figure 4.5: The parameterisation for the MATHKINE correction factor a for jets in simulated semileptonic WW decays when (a) the measured jet energy and measured polar angle are used to define the binning and (b) the true jet energy and true polar angle are used to define the binning.

to be applicable, then perhaps it is not too surprising to find that the convergence rate is over 99% for events from both WW and background processes.

In addition, the sensitivity of the correction factors to the underlying energy spectrum implies an extremely undesirable dependency on the W mass and LEP beam energy assumed by the simulation. In principle the correction factors should be re-evaluated for each W mass and each LEP beam energy. Note that the two jets found by the clustering algorithm are ordered by momentum and thus have different measured energy spectra. Therefore the jet corrections also have to be calculated separately for the first and second jet.

The solution to this problem is to parameterise the correction factors in terms of the true polar energy and true polar angle, which are known from simulation. Figure 4.5 (b) illustrates this approach for the correction factor a. It is obvious that all jets with $|\cos\theta| > 0.8$ are corrected up in energy by between 3 and 8%.

Consequently, the fit strategy must be rewritten so that the probability that a given set of fitted parameters yields the measurements is maximised and not vice versa. This is equivalent to evaluating the expected correction factors and the error matrix at each iteration of the fit. The best estimates for the true energy and true polar angle are taken to be the fitted energies and fitted polar angles from the previous iteration.

These problems were not realised immediately and were not solved for MATHKINE in time for the $\sqrt{s} = 172$ GeV and $\sqrt{s} = 183$ GeV W mass measurements. A new kinematic fit, described in Section 4.2, is developed to eliminate these problems for the $\sqrt{s} = 183$ GeV measurement. Due to the low statistics at $\sqrt{s} = 172$ GeV, this measurement contributes negligibly to a weighted average of the two measurements.

4.1.5 Number of constraints.

A kinematic fit using the equal mass constraint ($\nu = 2$) gives one W mass estimator per event, whereas only using the conservation of energy and momentum constraints ($\nu = 1$) and then rescaling by $\frac{E_{beam}}{E_W}$ would give two W mass estimators per event. The equal mass constraint is somewhat unphysical due to the finite width of the W boson, $\Gamma_W \approx$ 2 GeV/c^2. However, this effect is mostly obscured as the experimental resolution on the W mass is about 6 GeV/c^2 and only improves to 4 GeV/c^2 with the use of the constraints from conservation of energy and momentum.

To investigate which option gives the smallest statistical error on the W mass measurement, approximately 140 independent samples from simulation are fitted using the mass extraction technique described in Section 5.1. The fitted values for the mean rescaled hadronic and leptonic masses are combined, taking into account the 71% correlation between the subsamples. Table 4.1 shows that the estimator from the combined rescaled hadronic and leptonic W masses gives the same precision as the estimator with the equal mass constraint. For simplicity, the estimator with the equal mass constraint is chosen.

Definition of W mass estimator	Mean mass (GeV/c^2)	RMS (GeV/c^2)	σ(RMS) (GeV/c^2)
$\nu = 1$ rescaled hadronic	80.202	0.418	0.036
$\nu = 1$ rescaled leptonic	80.248	0.487	0.042
$\nu = 1$ rescaled combined	80.214	0.409	0.040
$\nu = 2$	80.256	0.408	0.034

Table 4.1: Statistical precision on the W mass from an estimator with $\nu = 1$ and rescaling versus an estimator with $\nu = 2$. The W mass assumed in the simulation is 80.25 GeV/c^2 [93].

4.1.6 Summary.

The kinematic fit for semileptonic WW decays at $\sqrt{s} = 172$ GeV is adapted directly from that for the hadronic channel. The constraints of conservation of energy, conservation of momentum and equal W masses are used by the fit to improve the resolution on the W mass by a factor of four to 1.4 GeV/c^2. This fit is only a first approximation to a proper treatment of the semileptonic channel, which possesses an unmeasured neutrino and has superior jet resolution.

There is a serious problem with the definition of the correction factors for non-Gaussian detector effects, which affects the minimisation and the parameterisation strategies for all WW decay channels. The correction factors are parameterised in terms of the measured energies and angles. As the underlying jet energy spectrum is completely contained within the range of measured energies, the correction factors depend strongly on the measured energy and alter the particle momenta over and above the real effects from detector response. This implies an extremely undesirable dependence on the W mass and the LEP beam energy assumed in the simulation.

4.2 New kinematic fit at $\sqrt{s} = 183$ GeV.

This section describes the adaptation of a new kinematic fit to the semileptonic channel. This fit solves the problems that afflicted the fit used for the $\sqrt{s} = 172$ GeV measurement: the unmeasured neutrino is treated correctly; the jet corrections and resolutions are parameterised specifically for the semileptonic channel; the electron and muon corrections and resolutions are parameterised separately; and the parameterisation and fit strategy operate in terms of the fitted energies and angles rather than the measured energies and angles in order to avoid nasty dependencies on the measured energies and the assumed W mass and LEP beam energy in the simulation.

The KINFIT package was originally developed for the $e^+e^- \to W^+W^- \to q\bar{q}q\bar{q}$ channel [94]. The adaptation of the minimisation strategy to the semileptonic channel and the convergence problems, parameterisation and performance of the fit are discussed below.

4.2.1 Minimisation strategy.

The KINFIT minimisation strategy is outlined in Figure 4.6. KINFIT imposes constraints by switching to a smaller, independent set of variables. In order to fully describe a $e^+e^- \to W^+W^- \to \ell\bar{\nu}q\bar{q}$ event, sixteen parameters are required. These are simply the four-vectors of the four final state fermions. Constraints can be used to reduce the number of independent parameters to nine, which are chosen in the following way so that their physical limits are also independent.

A WW event can be viewed as three separate two-body decays:

1. e^+e^- system $\to W^+W^-$
2. $W^+ \to q\bar{q}$
3. $W^- \to \ell\bar{\nu}$

Each two-body decay is completely defined by eight parameters, which are the four-vectors of the two decay products. Consider the decay of the W^+ in the rest frame of the W^+ where the z-axis is parallel to the flight direction of the W^+ in the laboratory frame, as shown in Figure 4.7. The four-vectors of the W^+ and the two decay products are:

W^+: $(M_W, 0, 0, 0)$

q_1: $(E_1, p_{x1}, p_{y1}, p_{z1})$

$\bar{q}_2$: $(E_2, p_{x2}, p_{y2}, p_{z2})$

and the masses of the two decay products are m_1 and m_2. By momentum conservation $\mathbf{p}_2 = -\mathbf{p}_1$ and by energy conservation $E_2 = M_W - E_1$. This leaves four independent parameters $(E_1, p_{x1}, p_{y1}, p_{z1})$, but the physical bounds that the constraints of energy and

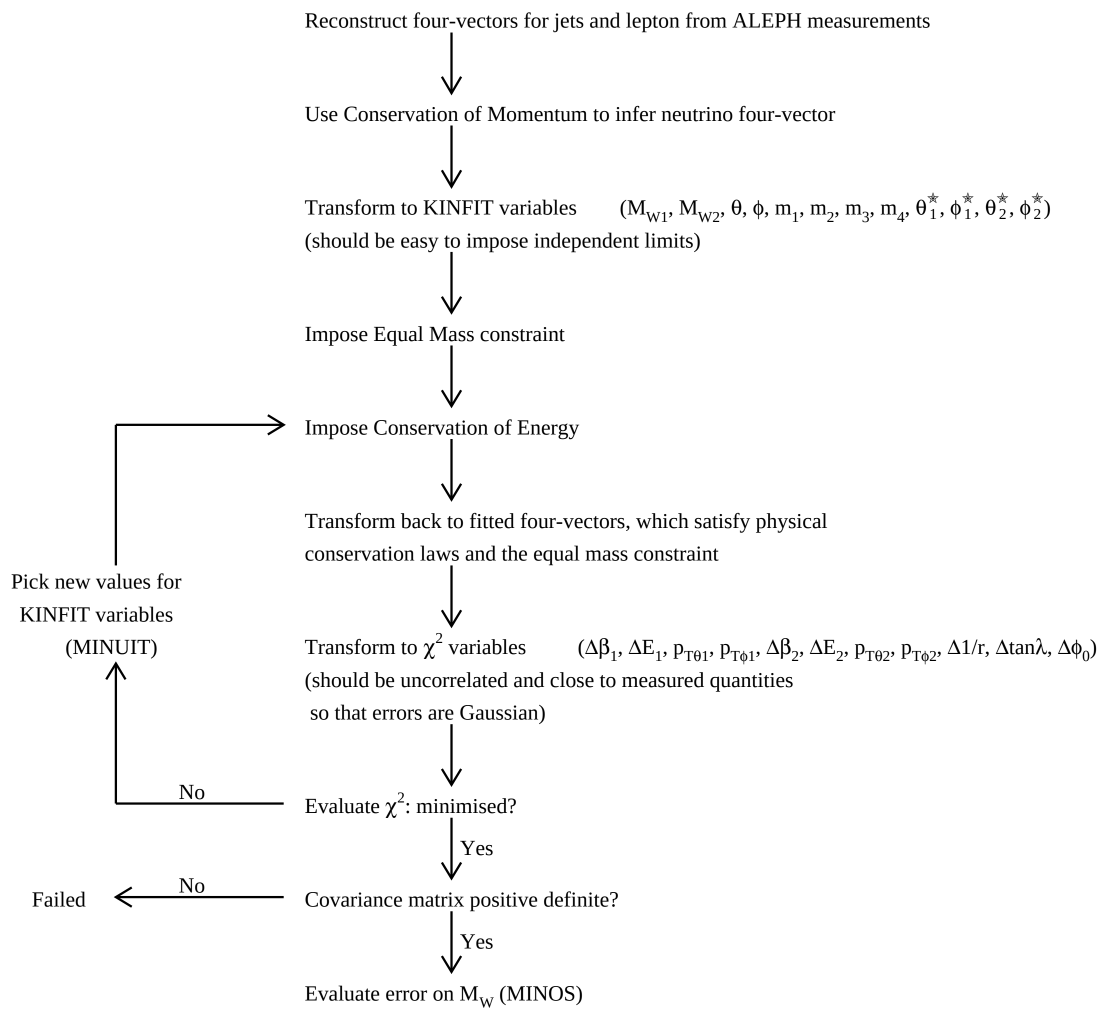

Figure 4.6: Schematic of the KINFIT minimisation strategy.

momentum conservation place on the range of values for these parameters cannot be defined independently. However, substituting for E_2 and p_2 in $E_2^2 - p_2^2 - m_2^2 = 0$ and then solving for E_1 gives:

$$E_1 = \frac{M_W^2 + m_1^2 - m_2^2}{2M_W} \tag{4.9}$$

and $\mathbf{p}_1$ can be written in spherical polar coordinates as $(p_1, \theta_1^\star, \phi_1^\star)$ where $p_1 = \sqrt{E_1^2 - m_1^2}$. The four independent parameters $(\frac{m_1+m_2}{M_W}, \frac{m_1-m_2}{m_1+m_2}, \theta_1^\star, \phi_1^\star)$ also describe the two-body decay completely, with the advantage that the physical bounds that the constraints of energy and momentum conservation place on the range of values can be defined independently and easily.

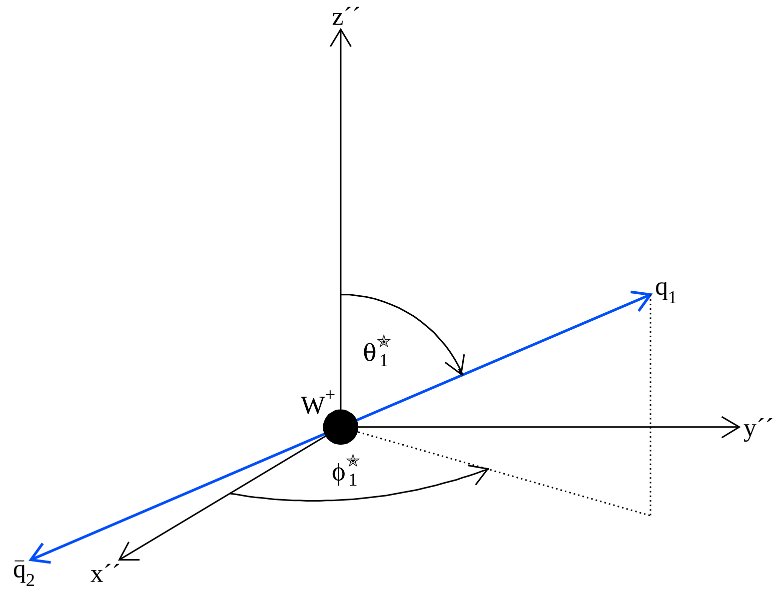

Figure 4.7: $W^+ \rightarrow q\bar{q}$ decay viewed in the rest frame of the W^+.

All three two-body decays can be described in this way by two masses and two angles, which are shown in Figure 4.8 and are listed below:

- M_{W1} and M_{W2}, the invariant masses of the W bosons. More generally, these are the invariant masses of the di-jet system and the lepton-missing momentum system.

- θ and ϕ, the polar and azimuthal production angles of W_1, *ie* the angles describing the flight direction of W_1, which is opposite to that of W_2, in the laboratory frame.

- m_1, m_2, m_3 and m_4, the masses of the two jets, the lepton and the neutrino.

- $\theta_1^\star$ and $\phi_1^\star$, the polar and azimuthal angles of a jet from the decay of W_1, in the rest frame of W_1 and with respect to the direction of flight of W_1 in the laboratory frame.

- $\theta_2^\star$ and $\phi_2^\star$, the polar and azimuthal angles of the lepton from the decay of W_2, in the rest frame of W_2 and with respect to the direction of flight of W_2 in the laboratory frame.

Since the lepton mass is fixed to the electron or muon mass and the neutrino is assumed to be massless, the number of independent parameters decreases to ten. The equal mass

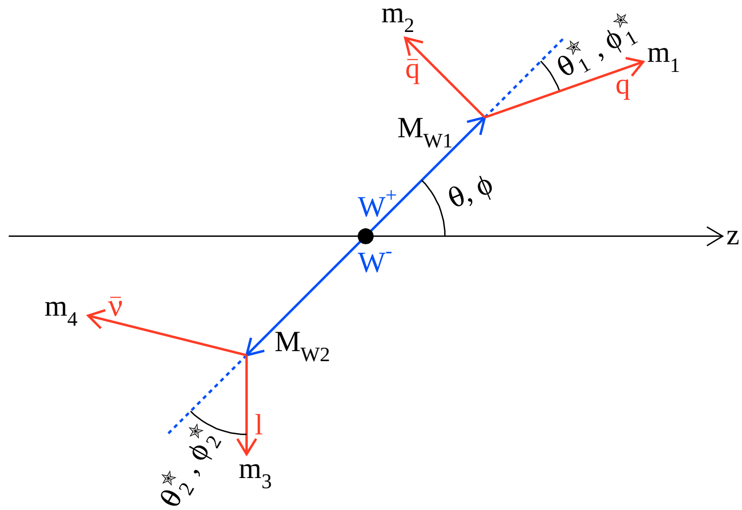

Figure 4.8: Schematic of the twelve parameters used by KINFIT to describe a $e^+e^- \rightarrow W^+W^- \rightarrow \ell\bar{\nu}q\bar{q}$ decay.

constraint is easily imposed by setting $M_{W1} - M_{W2}$ to zero, which reduces the number to nine.

Eleven quantities are measured in a semileptonic WW decay. These are the energies and momenta of the two jets and the momentum of the lepton. Therefore a fit that only uses the constraints of energy and momentum conservation has 11-10=1 degree of freedom. The addition of the equal mass constraint increases the number of degrees of freedom to 11-9=2.

To calculate initial values for the masses and angles, the constraints from conservation of momentum and zero neutrino mass are used to give a four-vector for the neutrino from the measured quantities. The four-vectors for the measured jets, lepton and the inferred neutrino are then transformed into the masses and angles according to the relativistic kinematics detailed in Appendix A.

The remaining constraints of equal W masses and energy conservation are imposed by setting $\frac{M_{W1}-M_{W2}}{M_{W1}+M_{W2}}$ to zero and defining the W momentum to be:

$$p_W = \frac{1}{2\sqrt{s}}\sqrt{s^2 + M_{W1}^4 + M_{W2}^4 - 2sM_{W1}^2 - 2sM_{W2}^2 - 2M_{W1}^2M_{W2}^2} \tag{4.10}$$

This value for the W momentum is used to transform the masses and angles back to the laboratory frame in order to find the initial fitted four-vectors for the jets and the lepton that satisfy all the constraints. The fitted four-vectors determine the value of a χ^2 function (described in 4.2.3), which measures the distance between the fitted and measured four-vectors.

The MIGRAD program from the MINUIT package [95] is used to minimise this χ^2 function. At each iteration of the minimisation, new values are chosen for the masses and angles, which are transformed into an improved set of fitted four-vectors, *ie* a set that still satisfies all the constraints but is closer to the measured four-vectors. The minimisation stops when the change in the value for the χ^2 function falls below 0.0001.

At each iteration, the MIGRAD program uses its current estimate of the covariance matrix to determine the current search direction for the minimum, as this is the optimal strategy for quadratic functions and "physical" functions should be quadratic in the neighbourhood of the minimum. If and only if the covariance matrix is positive-definite is the search direction guaranteed to be towards the minimum. If MIGRAD reports that it has found a non-positive definite covariance matrix, the error matrix is unreliable and the minimum is suspicious. Therefore, in this analysis, the minimisation is defined to have converged successfully only if the covariance matrix from MIGRAD is positive-definite at the minimum.

Note that the occurrence of a non-positive definite covariance matrix may actually indicate that either the starting point is too far away from the minimum for a quadratic approximation to be appropriate or that the problem is ill-defined due to high correlations between the fitted parameters.

The original parameterisation for KINFIT, as described above, creates severe problems for the semileptonic channel. Extremely large numbers of χ^2 evaluations (circa 15,000) are necessary to obtain convergence rates of around 80%. This makes the kinematic fit so computer intensive as to be impractical. Even when the fit does converge, the correct minimum is not necessarily the one found.

The asymmetric nature of a reconstructed $e^+e^-\to W^+W^-\to\ell\bar{\nu}q\bar{q}$ decay is the source of these problems. On average, the lepton energy is measured four times more precisely than the jets and the typical resolution on the lepton energy from the tracking detectors is 1.5 GeV. Five ($M_{W1}+M_{W2}$, θ, ϕ, $\theta_2^\star$ and $\phi_2^\star$) of the nine variable parameters are required to define the lepton momentum. So any changes to any of these parameters results in a change to the tightly constrained lepton momentum and therefore to a large increase in the χ^2 value. The minimisation program quickly learns that changes must be applied to these five parameters in a correlated manner. The high correlations severely degrade the performance of the minimisation program as many iterations are then needed to find the correct error matrix and search direction. The other two decay channels, $e^+e^-\to W^+W^-\to\tau\bar{\nu}q\bar{q}$ and $e^+e^-\to W^+W^-\to q\bar{q}q\bar{q}$, do not have such high correlations as the individual jets and the tau lepton are measured with similar resolutions.

The solution is to replace the variables θ, ϕ, $\theta_2^\star$ and $\phi_2^\star$ with the momentum components of the lepton (p_{x3}, p_{y3}, p_{z3}) and an angle α, which is defined in Figure 4.9 as the azimuthal angle that the component of the W momentum perpendicular to the lepton makes with respect to the $\hat{\theta}$ direction of the lepton. The high correlations disappear as the lepton momentum is now varied explicitly by MIGRAD. The number of χ^2 evaluations required to obtain a successful minimisation is now drastically lower at around 200 and the correct minimum is generally found.

This KINFIT parameterisation allows the lepton momentum, the best known quantity in the event, to be fixed to the measured value while the constraints are imposed and the χ^2 is minimised with respect to the other measurements. This simplifies the minimisation as the number of variable parameters is then reduced to six in a fit with two degrees of freedom. Subsequently, the lepton momentum is also allowed to vary and the initial minimisation is improved upon.

At this point, the kinematic fit is accomplished. However, to obtain an error on the fitted W mass, a few further steps are necessary. The $M_{W1} + M_{W2}$ and $\frac{M_{W1}-M_{W2}}{M_{W1}+M_{W2}}$ parameters are replaced by M_{W1} and M_{W2}. Then the error(s) on the W mass(es) can be found directly by the MINOS program from MINUIT. It is important to note that the error parameterisation for the measured quantities in the χ^2 function should be as good as possible so that the error on the W mass is reliable. This is because an error parameterisation that overestimates the errors on the measurements will result in an error on the fitted W mass that is itself an overestimate.

4.2.2 Convergence problems.

Although changing the KINFIT parameterisation to include the lepton momentum both speeds up the fit and vastly improves the resolution on the W mass, the convergence rate is low at 78%. Several reasons for this have been found and are discussed in this section.

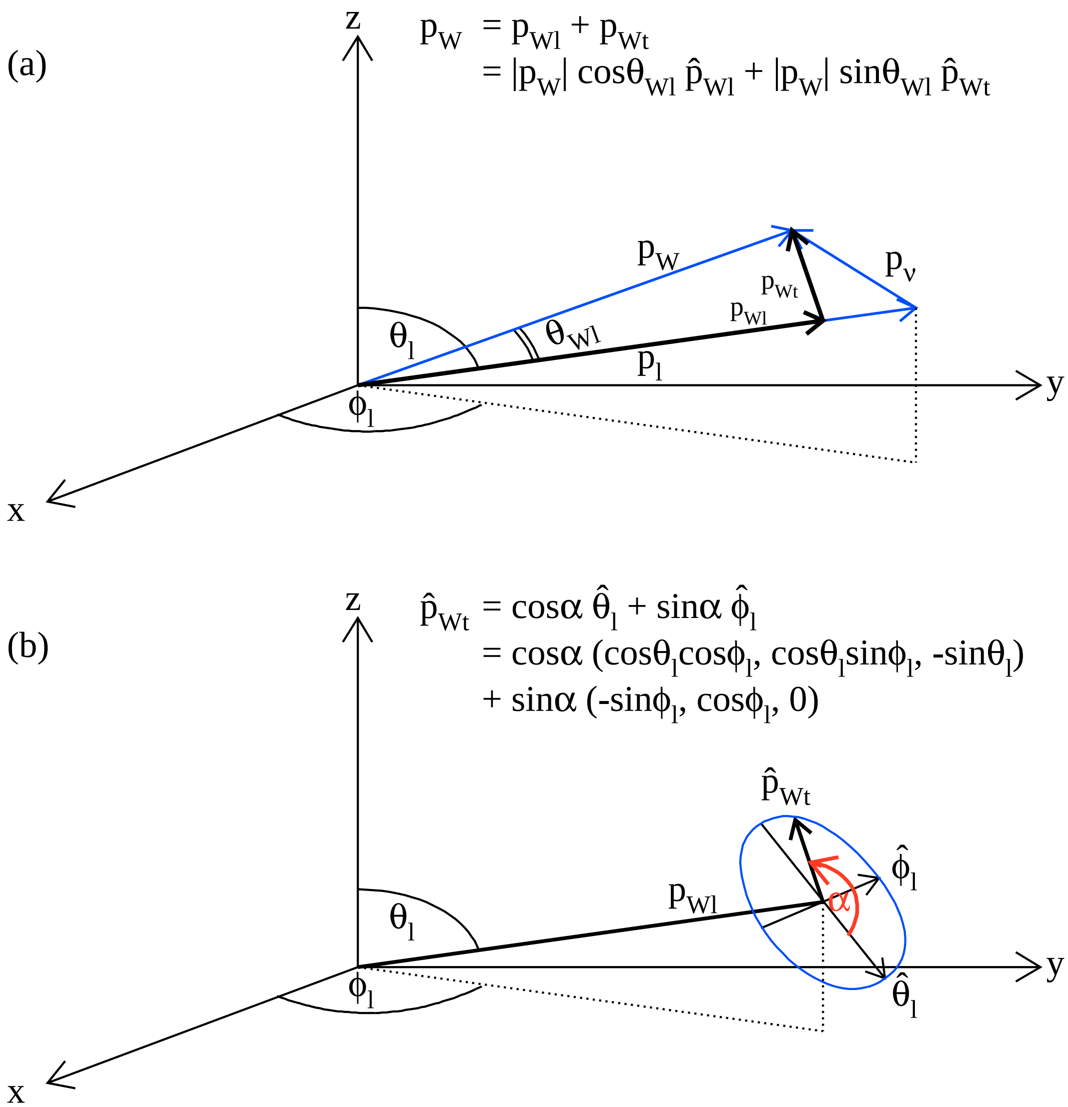

Figure 4.9: Definition of the angle α. (a) shows the components of the W momentum parallel and perpendicular to the lepton momentum. (b) shows the components of the W momentum perpendicular to the lepton with respect to the $\hat{\theta}$ and $\hat{\phi}$ directions of the lepton.

The most vulnerable part of the fit is the calculation of the starting values for the masses, angles and fitted four-vectors from the measured four-vectors. If the event is badly reconstructed, then it may be impossible to satisfy all the constraints at once. The most obvious manifestation of this is when the W momentum, as calculated by the energy conservation constraint, does not complete the vector triangle formed by the lepton and neutrino four-vectors, as illustrated in Figure 4.10.

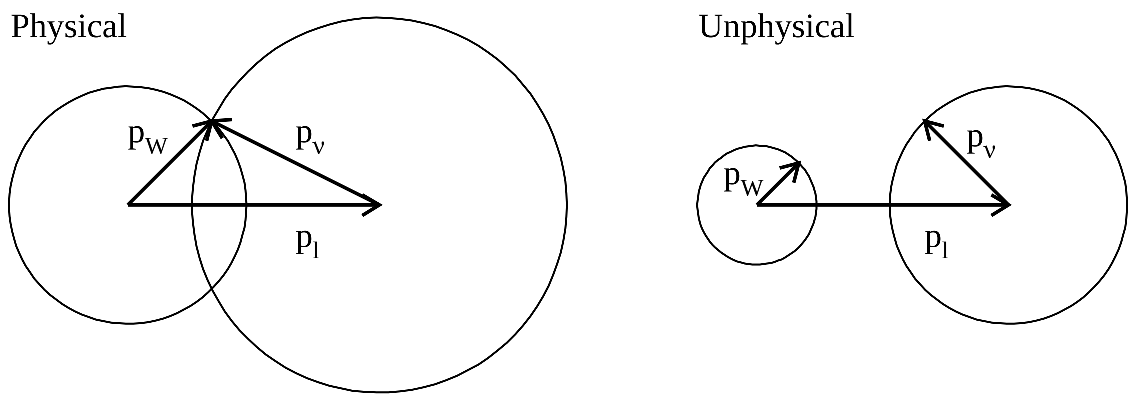

Figure 4.10: Physical and unphysical values for $\mathbf{p}_W$, $\mathbf{p}_\ell$ and $\mathbf{p}_\nu$.

This situation typically occurs when the value obtained for p_W from the conservation of energy constraint is too low. This implies that the reconstructed hadronic and leptonic invariant masses are too high, the causes of which include:

- The inclusion of energy deposits from the lepton in the jets.
- The inclusion of a FSR photon from the lepton in the jets.
- The loss of particles from the jets due to the finite detector acceptance.
- Resolution fluctuations on the jet measurements.

The first two sources are the motivation for the optimisation of the Bremsstrahlung correction routine for the electron (3.2.4), the search for FSR photons from the lepton (3.2.5) and the extended association of energy flow objects from the calorimeters to the lepton (3.2.7). The convergence rate increases by 6% on the implementation of these changes.

The third source suggests that corrections for particle losses for jets near the beam axis (developed in 4.2.3) should be applied to the measured jets before the starting values for the masses, angles and fitted four-vectors are calculated. This is done by assuming that any expected energy loss occurs entirely in the direction parallel to the beam axis. So, the z-component of the jet momentum and the jet energy are always increased by the expected energy loss. This recovers another 4%, giving a convergence rate of 88%.

The fourth source is tackled by first finding a solution to an analytical fit that applies the constraints of energy and momentum conservation and zero neutrino mass [96]. The fit operates by rescaling the four-momentum of the jets by factors α_1 and α_2. As there is only one constraint for two free parameters, there is an infinity of solutions, which is sampled by fixing the ratio $t = \alpha_2/\alpha_1$ and trying 89 values for $t = \tan\phi$ from $\phi = 1°$, $2°$, ..., $89°$. For each value of t, the equation of zero neutrino mass is a second order equation in α_1 and a χ^2_{ana} is calculated for both solutions. If the solutions are unphysical, *ie* the square root of a negative number is required, then the lepton momentum is rescaled until the solutions are physical. The χ^2_{ana} function contains contributions from:

- The difference between the rescaled and measured jet energies, where the jet energy measurement error is assumed to be $100\%\sqrt{E}$.

- The difference between the rescaled and measured lepton energy, where the lepton energy measurement error is assumed to be $0.0006E^2$.

- The Breit-Wigner probabilities for the two W resonances, including a phase space factor:

$$P_{BW} = \frac{M^2_{W1r} M^2_{W2r} (E^2_{W1r} - M^2_{W1r})}{\left(M^2_{W1r} - M^2_W + \left(\frac{M^2_{W1r}\Gamma_W}{M_W}\right)^2\right)\left(M^2_{W2r} - M^2_W + \left(\frac{M^2_{W2r}\Gamma_W}{M_W}\right)^2\right)} \tag{4.11}$$

  No arbitrary reference mass, which could lead to possible biases, is required as the mass of resonance, M_W, is taken to be the average of the rescaled masses M_{W1r} and M_{W2r} of the di-jet and the lepton-missing momentum systems respectively. The width of the Breit-Wigner is fixed and a value of 10 GeV is found to give good results.

Therefore, the χ^2_{ana} is:

$$\chi^2_{ana} = -2\ln P_{BW} + E_1(\alpha_1 - 1)^2 + E_2(\alpha_2 - 1)^2 + \frac{(\alpha_\ell - 1)^2}{0.0006E^2_\ell} \tag{4.12}$$

and the solution with the minimum value for the χ^2_{ana} is kept. This fit always finds a solution. If the starting point is still unphysical after applying the energy loss correction, then the fitted four-vectors from this analytical fit are used to calculate an improved starting point. This approach recovers an additional 4%, which raises the convergence rate to 92% for fits with one or two degrees of freedom.

The remaining 8% of events for which the fit does not converge successfully is due to problems that occur as the fit iterates towards a solution. For example, the fit variable α, which is the azimuthal angle that the component of the W momentum perpendicular to the lepton, p_{Wt}, makes with respect to the $\hat{\theta}$ direction of the lepton, means that the fit is sensitive to events in which the lepton and the W are almost parallel or anti-parallel, *ie* to the endpoints of the lepton energy spectrum. In this case, α is poorly defined as p_{Wt} is not significantly different from zero. Mathematically, this means that the first and second derivatives of the χ^2 with respect to α are very close to zero, which causes problems for MIGRAD as a zero first derivative is also the definition of a minimum and a zero second derivative creates problems in covariance matrix, which MIGRAD uses to find the direction to the minimum. A more careful treatment of the angle α when p_{Wt} is small could recover these events.

Figure 4.11 shows the measured muon energy spectrum and the fitted invariant mass distribution, for fully simulated, selected $W^+W^-\rightarrow\mu\bar{\nu}q\bar{q}$ decays, after a kinematic fit with two degrees of freedom. The shading indicates the fraction of fits that have converged successfully with a positive-definite covariance matrix and the fractions that have a forced positive-definite covariance matrix or only a diagonal approximation to the covariance matrix. As expected, the successful convergence rate is clearly lower for those events near the endpoints of the lepton energy spectrum, where the angle α is not well-defined. The fit does return a value for the W mass for over 99% of the events, but the level of confidence that should be placed in this number varies with the status of the covariance matrix. The resolution on the W mass afforded by those events that do not have positive-definite covariance matrices is correspondingly poorer.

The reason that the fit apparently fails completely for some events is due to a similar problem with the angles $\theta_1^\star$ and $\phi_1^\star$. If $\theta_1^\star$ is not significantly different from 0° or 180°, then the angle $\phi_1^\star$ is not well-defined. As $\phi_1^\star$ is unbounded and the χ^2 may well be slightly periodic in $\phi_1^\star$, MIGRAD may increase the value of $\phi_1^\star$ beyond the memory limit

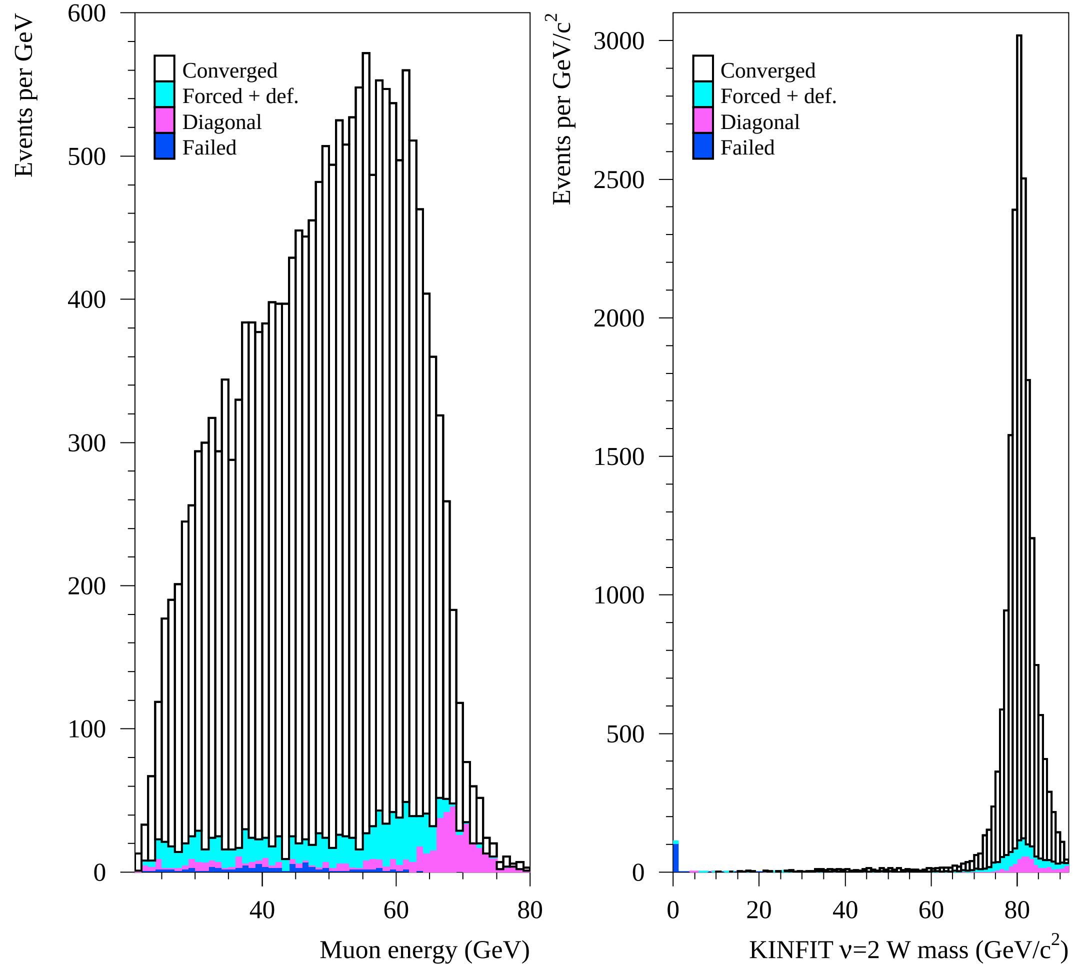

Figure 4.11: The measured muon energy spectrum and the fitted invariant mass distribution, for fully simulated, selected $W^+W^-\to\mu\bar{\nu}q\bar{q}$ decays, after a fit with two degrees of freedom

for double precision numbers. In order to avoid this, the kinematic fit is halted if $\phi_1^\star$ becomes larger than 1000 radians [97]. A more careful treatment of these events, either by redefining the direction of the z-axis or using transverse momentum components rather than spherical polar angles, could recover these events. This problem also affects the $e^+e^-\to W^+W^-\to\tau\bar{\nu}q\bar{q}$ and $e^+e^-\to W^+W^-\to q\bar{q}q\bar{q}$ channels.

Figure 4.12 shows the shape of the χ^2 function near the minimum for all nine variable parameters, where only one parameter is varied at a time, for a kinematic fit with two degrees of freedom to a simulated $e\bar{\nu}q\bar{q}$ event. Note well that the variable parameters do not correspond directly to the χ^2 variables. The shape of the χ^2 function is not very parabolic for the m_1 and m_2 parameters, indicating that these parameters are correlated with the other parameters. The shallowness of the minimum for these two parameters is also problematic for the minimisation. A better choice for these two parameters could help to improve the convergence rate.

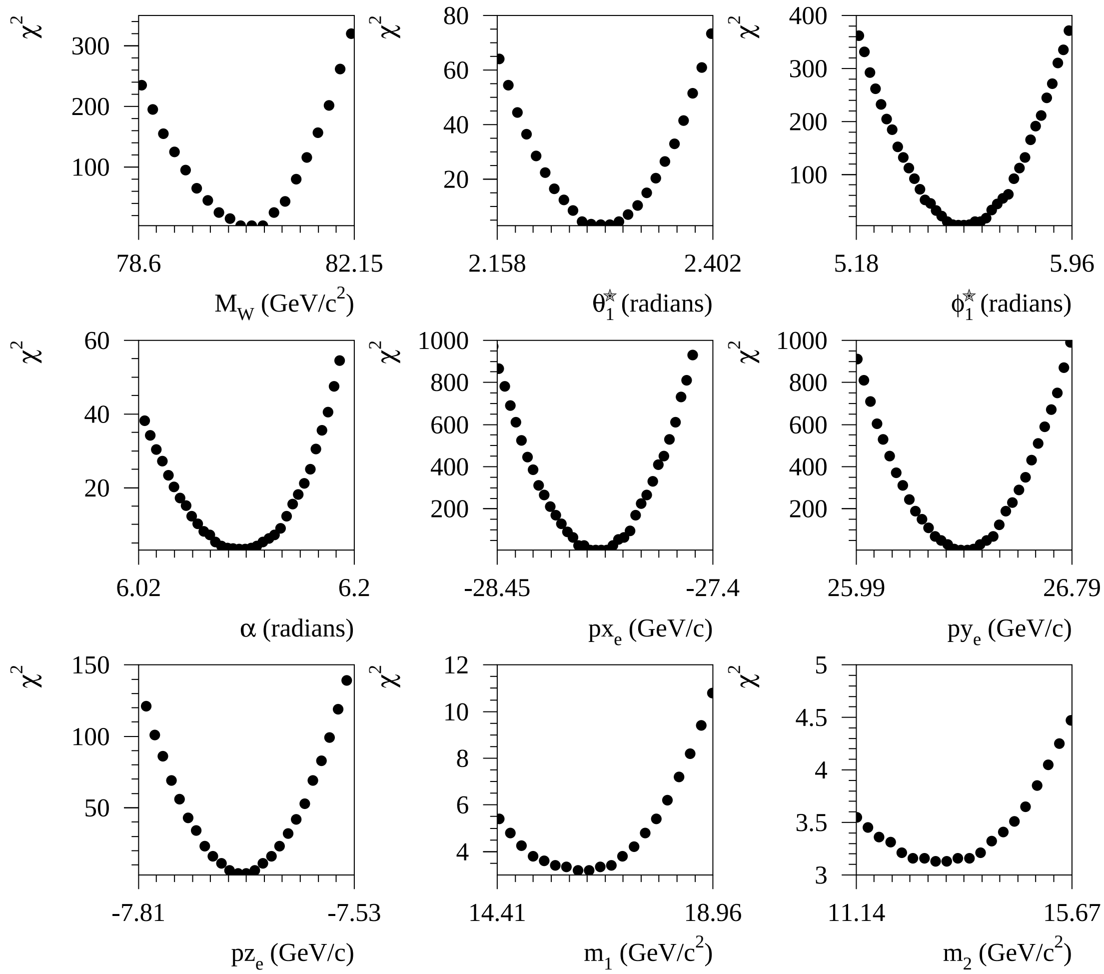

Figure 4.12: The shape of the KINFIT χ^2 function near the minimum for all nine variable parameters, where only one parameter is varied at a time, in a kinematic fit with two degrees of freedom to a simulated $e\bar{\nu}q\bar{q}$ event. The range shown for each parameter is one standard deviation on each side of the value at the minimum.

4.2.3 Parameterisation of jet and lepton corrections.

This section briefly describes the structure of the Least Squares minimisation and the variables chosen to represent the measurements. The parameterisation of the expected biases, expected resolutions and correlation matrices is then discussed in detail as this is one of the most important parts of the entire analysis since the parameterisation controls the kinematic fit and thus the fitted W mass and error.

The function to be minimised is:

$$\mathcal{S} = \Delta^{'T} V^{-1} \Delta^{'} \equiv \left(\frac{\Delta - < \Delta >}{\sigma_\Delta}\right)^T V^{-1} \left(\frac{\Delta - < \Delta >}{\sigma_\Delta}\right) \tag{4.13}$$

The variables $\Delta = x_{meas} - x_{fit}$ describe the distance between the measured, x_{meas}, and the fitted, x_{fit}, four-vectors of the particles. The expected biases, $< \Delta >$, and expected resolutions, σ_Δ, are mapped from simulation and used to transform the variables Δ to variables $\Delta^{'} = \frac{\Delta - <\Delta>}{\sigma_\Delta}$ that are distributed as Gaussians. Then a difference of one standard deviation of the fitted from the measured value, minus any expected bias, carries the same weight for each variable. This allows the value of $\mathcal{S}$ at the minimum to be interpreted as if from a χ^2 distribution with the requisite number of degrees of freedom. V is the full, average, correlation matrix for the $\Delta^{'}$ variables.

The variables x are chosen such that they are minimally correlated and are close to the quantities that are actually measured in order to have Gaussian-like properties. As the jet velocity is not assumed to be perfectly measured in this kinematic fit, the jets are described by four variables:

$$\Delta\beta, \Delta E, p_{T\theta} \text{ and } p_{T\phi} \tag{4.14}$$

which represent the difference between the measured and fitted jet velocities and energies respectively as well as the transverse momentum of the measured jet relative to the fitted jet in both θ and ϕ. The exact definition of $p_{T\theta}$ and $p_{T\phi}$ is given in Appendix B. These variables, with $\Delta\beta$ set to zero, are also used to describe the lepton in events where calorimetric energy is added to the track measurement of the lepton energy. Otherwise, the lepton is described by:

$$\Delta 1/r, \Delta \tan\lambda \text{ and } \Delta\phi_0 \tag{4.15}$$

which represent the difference between the measured and fitted lepton inverse radius of curvature, dip angle and azimuthal direction at the event vertex, as used in the track helix fit.

The expected bias, $< \Delta >$, and expected resolution, σ_Δ, on the variables are parameterised as functions of the true (before the simulation of detector effects) energy,

E_{True}, and the true polar angle, $\cos\theta_{True}$, of the particle concerned. Therefore, at each iteration of the fit, the expected bias and expected resolution are recalculated, using the fitted energies and polar angles from the previous iteration as the best estimates for the true ones. This avoids the serious biases that can arise from a parameterisation in terms of the measured energies and measured polar angles, as discussed in 4.1.4 for the first kinematic fit used in the $\sqrt{s} = 172$ GeV analysis.

Studies of $Z/\gamma \to q\bar{q}$ decays at $\sqrt{s} = 91$ GeV reveal discrepancies between the simulated jet energy and the measured jet energy in data. However, thanks to improvements in the simulation for the 1997 data, the largest discrepancy is 1.5% in the overlap between the barrel and the end-cap segments of the calorimeters. This discrepancy is mainly the result of the difficulty of accurately simulating the effects of the large amount of inactive material (cables, cooling pipes etc.) in this region [98].

Contrary to the approach taken for the $\sqrt{s} = 172$ GeV W mass measurement (see 7.1.3), the discrepancy is parameterised as a function of $|\cos\theta|$ and used to correct the simulated jet energies so that the simulation and the data resemble each other more closely. The more appropriate ratio of the jet energies, rather than the hemisphere energies, defines the discrepancy in order to model the $|\cos\theta|$ behaviour more accurately. The correction is applied to the simulated jets before the kinematic fit and therefore the correction is also applied to the simulated jets before the parameterisation of the fit variables is undertaken.

The expected bias and expected resolution are parameterised for each variable using 400,000 CC03 WW events fully simulated using KORALW. The lepton and jet variables are parameterised separately for the $e\bar{\nu}q\bar{q}$ and $\mu\bar{\nu}q\bar{q}$ channels in case of any residual effects from Bremsstrahlung or FSR photons. The leptons that are defined solely by the tracking detectors are also parameterised separately from the leptons that have calorimetric energy added. The parameterisation procedure for the variable ΔE for jets in $e\bar{\nu}q\bar{q}$ events is taken as an example.

The first step is to histogram the value of ΔE for both jets in each selected $e\bar{\nu}q\bar{q}$ event. The allowed kinematic range in the true particle energy and polar angle is divided into 5 and 20 bins respectively. This gives 100 one-dimensional histograms, some of which are shown in Figure 4.13. The bin ranges are chosen so that the histograms can be adequately described by a Gaussian distribution. Therefore, the binning is finer near the beam-axis, where the biases and resolutions change rapidly. The bin edges are:

$$
\begin{array}{lcllllllll}
E_{True} & : & 25, & 34, & 43, & 52, & 61, & 70\ \text{GeV}. & & \\
\cos\theta_{True} & : & -1.00, & -0.95, & -0.90, & -0.85, & -0.80, & -0.75, & -0.70, & -0.60, \\
 & & -0.40, & -0.20, & 0.00, & 0.20, & 0.40, & 0.60, & 0.70, & 0.75, \\
 & & 0.80, & 0.85, & 0.90, & 0.95, & 1.00. & & &
\end{array}
$$

Each histogram is fitted with a Gaussian function. The mean and width of the fitted Gaussian are taken to be the expected bias and the expected resolution on ΔE for $e\bar{\nu}q\bar{q}$ jets with true energies and polar angles in the range covered by the bin.

The next step is to fit the dependence of the expected bias of ΔE, and likewise the expected resolution, as a function of the true energy and the true polar angle. For each range j in true energy, the dependence of the expected bias of ΔE on the true polar angle is fitted by the MIGRAD program using a power series of the form:

$$q_j(\cos\theta_{True}) = \sum_{i=0}^{N_a} a_{ij}\cos\theta^i_{True} \tag{4.16}$$

Note that if the dependence on $\cos\theta_{True}$ is symmetric (asymmetric), then only even (odd) powers of $\cos\theta_{True}$ are used. Also note that the fitted function is compared with the measured value at the mean $\cos\theta_{True}$ of the bin contents rather than at the bin centre in order to describe the variation correctly [99]. The energy dependence of the ith set of a_{i*} coefficients is then described similarly by:

$$r_i(a_{i*}) = \sum_{k=0}^{N_b} b_{ik}E^k_{True} \tag{4.17}$$

where k may be a rational number. So, the dependence of the mean of ΔE on the true energy and polar angle may be written as:

$$< \Delta E > (E_{True}, \cos\theta_{True}) = \sum_{i=0}^{N_a}\left(\sum_{k=0}^{N_b} b_{ik}E^k_{True}\right)\cos\theta^i_{True} \tag{4.18}$$

The measured and the fitted values for the expected bias and expected resolution of ΔE are shown in the second row of Figures 4.14 and 4.15 for the whole range of true energy and true polar angle. The fitted functions follow the measured values well. The first, third and fourth rows show the measured and fitted values for the expected bias and expected resolution on $\Delta\beta$, $p_{T\theta}$ and $p_{T\phi}$. The descriptions for $\Delta 1/r$, $\Delta\tan\lambda$ and $\Delta\phi_0$ for electrons, which have no calorimetric energy added, are shown in Figures 4.16 and 4.17,

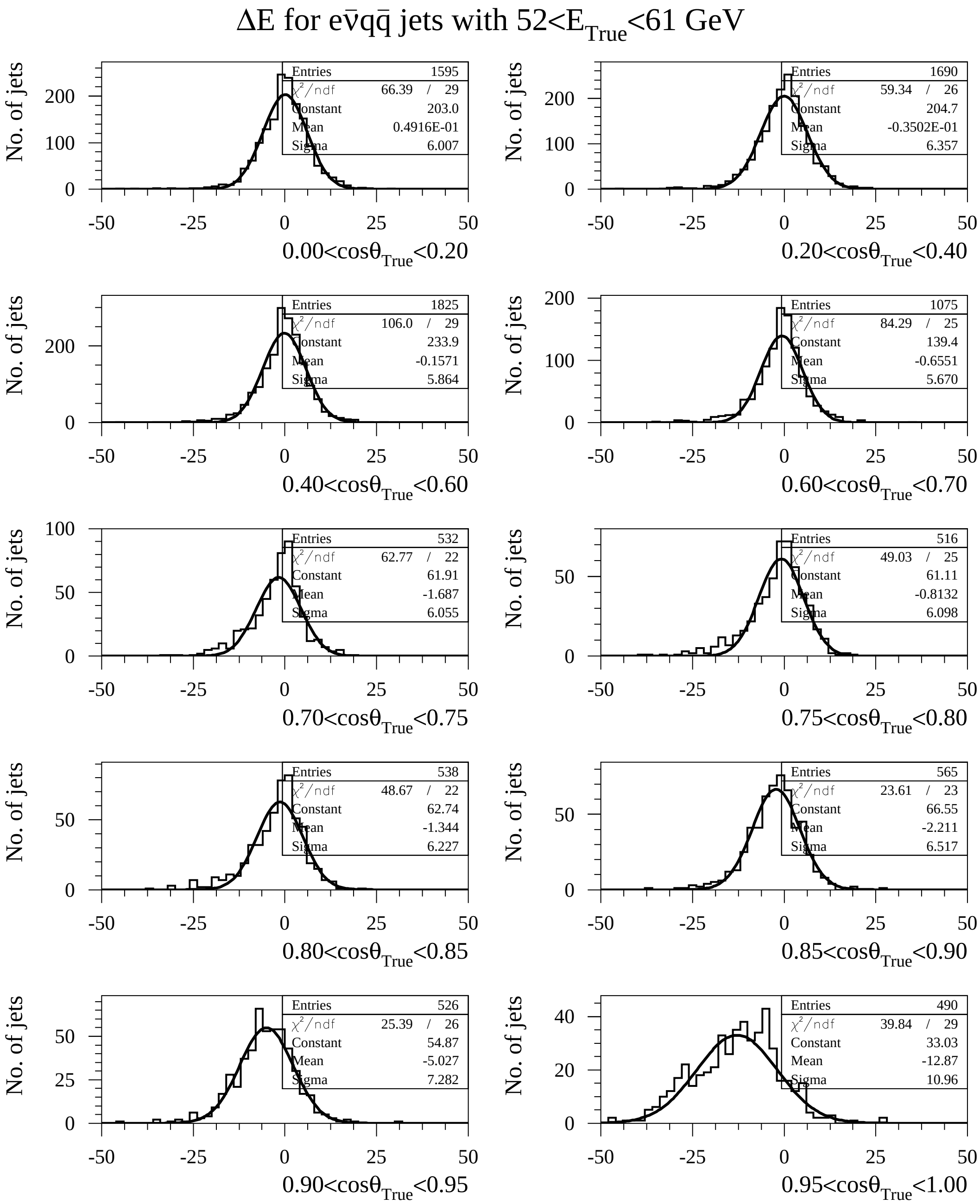

Figure 4.13: The distributions of the variable ΔE for jets in fully simulated, selected $e\bar{\nu}q\bar{q}$ events that have true energies in the range 52 to 61 GeV. The results of a Gaussian fit to each distribution are shown.

while those for ΔE, $p_{T\theta}$ and $p_{T\phi}$ for electrons, to which calorimetric energy is added, are shown in Figures 4.18 and 4.19. In this case, the binning is much broader due to the smaller amount of statistics available.

The quality of the fits is defined more quantitatively in Tables 4.2 and 4.3, which list the coefficients b_{ik} and the χ^2 for the expected biases and expected resolutions in the $e\bar{\nu}q\bar{q}$ channel. The jets and the muon in the $\mu\bar{\nu}q\bar{q}$ channel are parameterised separately, with similar results.

Note that the parameter $p_{T\phi}$ switches sign for positive and negative charges and the forward and backward hemispheres. As negatively charged leptons are emitted preferentially in the forward hemisphere and positively charged leptons in the backward hemisphere, the expected bias and resolution are calculated for negative leptons only. This is in order to avoid fitting the bias multiplied by the difference in the number of positively and negatively charged leptons in each range in polar angle. The expected bias for positive leptons is simply obtained by multiplying that for negative leptons by -1.

The expected bias and expected resolution are used to transform the variables Δ into Gaussian-like variables $\Delta' = \frac{\Delta - <\Delta>}{\sigma_\Delta}$, which are shown in Figure 4.20 for the $e\bar{\nu}q\bar{q}$ channel. The distributions are also fitted to Gaussians in the range [-5,5] in order to evaluate the quality of the parameterisations for the expected bias and expected resolution. The fitted means and widths of the Gaussians are compatible with zero and one respectively, so the parameterisations are sufficient. The χ^2 values are quite high as the tails of the distributions are above the fitted Gaussians due to poorer experimental resolution on a subset of events.

The final step is to evaluate the correlation matrices between the Δ' variables. The correlations, which are averaged over all true polar angles and true energies are small by design and are shown in Table 4.4 for the $e\bar{\nu}q\bar{q}$ channel, where no calorimetric energy is added to the electron. The only large correlation is that between $\Delta 1/r$ and $\Delta\phi_0$.

To understand the source of this correlation, consider a very high momentum particle that produces a straight track. To simplify the argument, imagine that only three coordinates are used to define the track: one in the VDET, one in the innermost layer of the TPC and one in the outermost layer of the TPC. Now suppose that the coordinate in the innermost TPC layer has a measured value for ϕ that happens to be larger than the true value of ϕ due to the finite resolution of the tracking detectors. This has two effects:

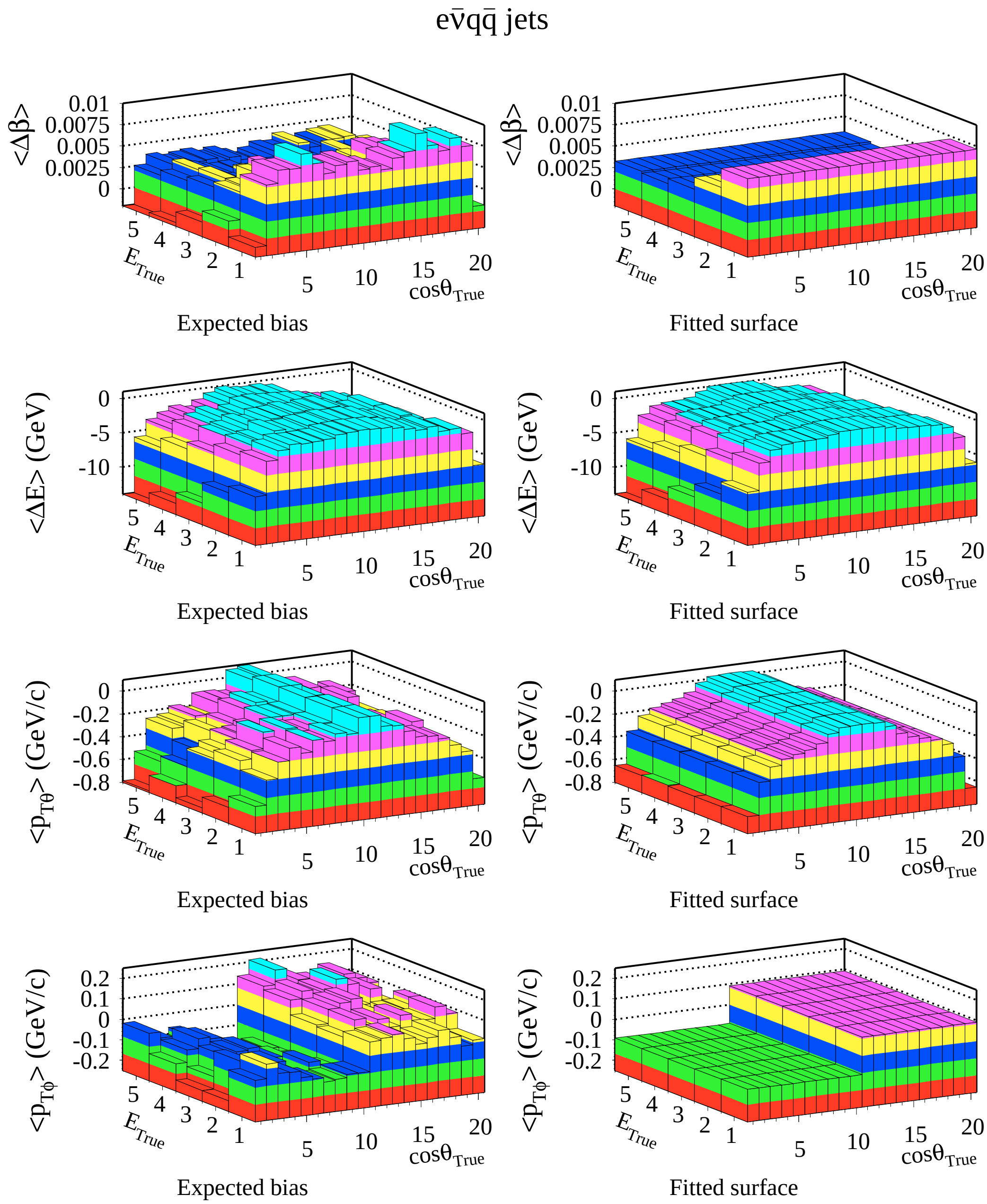

Figure 4.14: The measured and fitted values for the expected bias of $\Delta\beta$, ΔE, $p_{T\theta}$ and $p_{T\phi}$ are shown in the first, second, third and fourth rows respectively, for jets in fully simulated, selected $e\bar{\nu}q\bar{q}$ events. The binning corresponds to that given in the text.

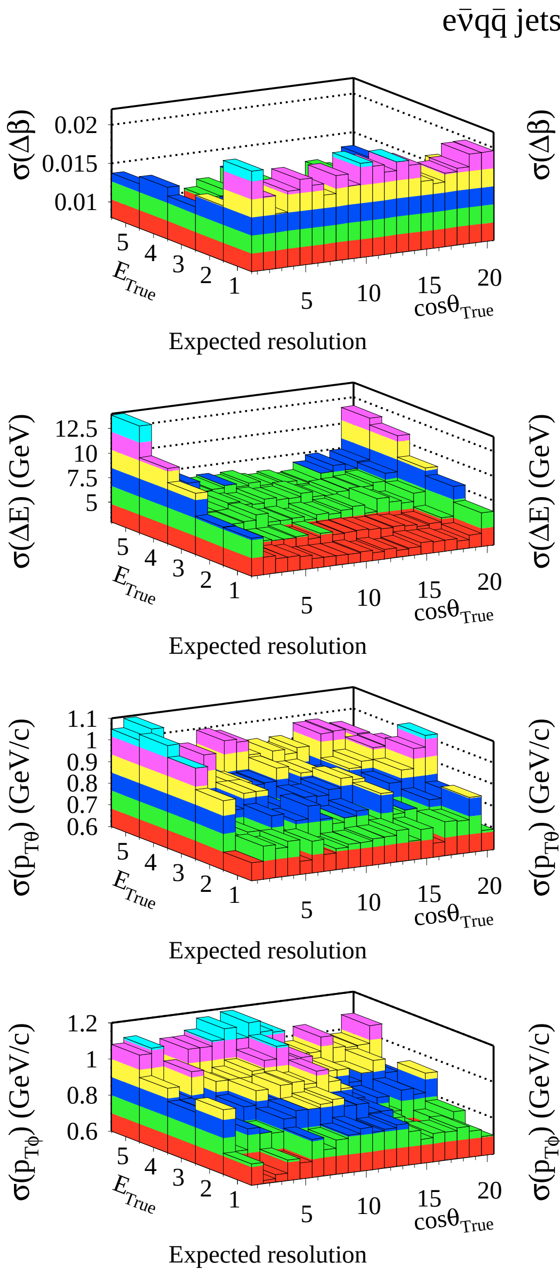

Figure 4.15: The measured and fitted values for the expected resolution of $\Delta\beta$, ΔE, $p_{T\theta}$ and $p_{T\phi}$ are shown in the first, second, third and fourth rows respectively, for jets in fully simulated, selected $e\bar{\nu}q\bar{q}$ events. The binning corresponds to that given in the text.

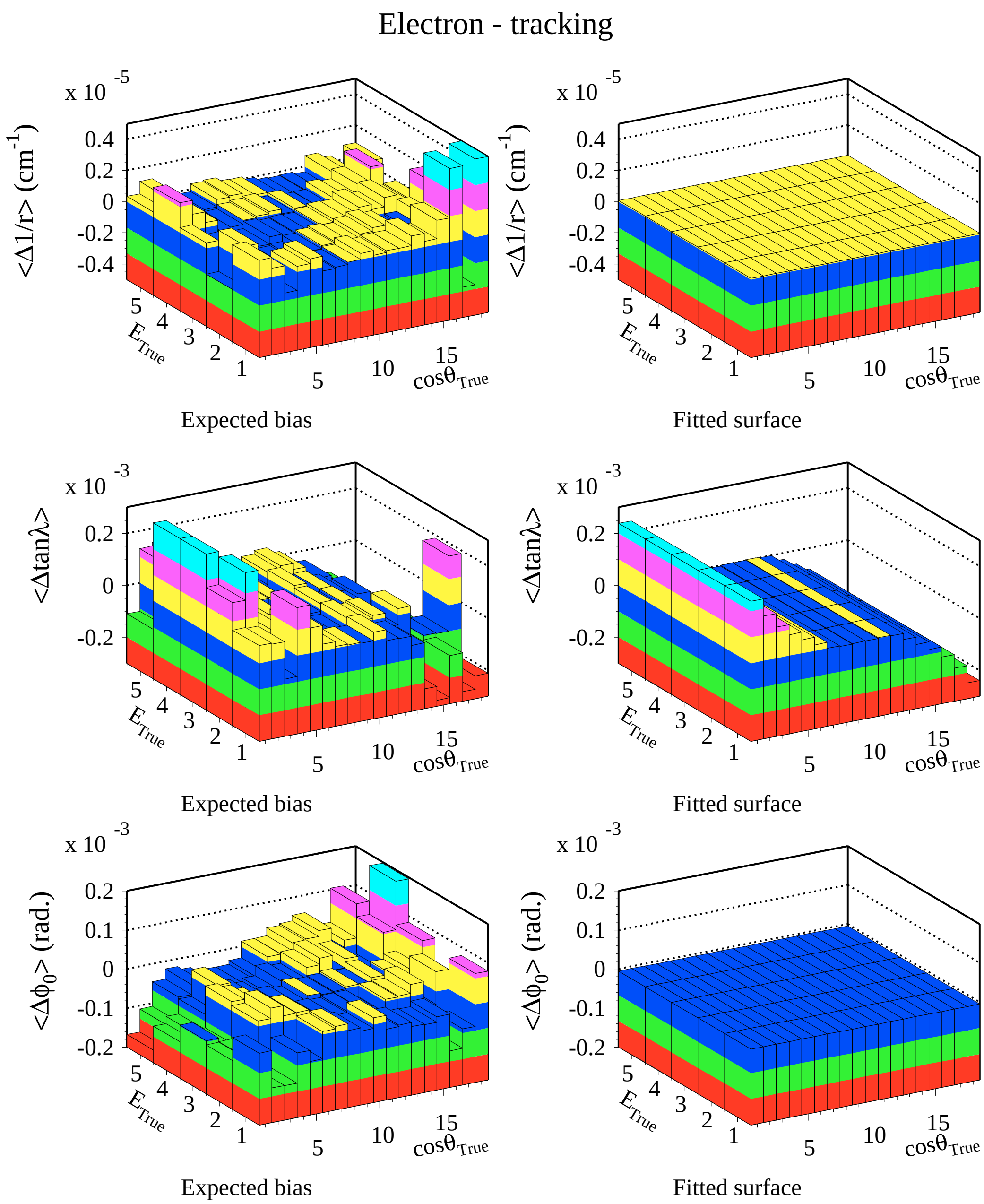

Figure 4.16: The measured and fitted values for the expected bias of $\Delta 1/r$, $\Delta \tan\lambda$ and $\Delta\phi_0$ are shown in the first, second and third rows respectively, for electrons, reconstructed using information from the tracking detectors only, in fully simulated, selected $e\bar{\nu}q\bar{q}$ events. The binning corresponds to that given in the text, minus the $\cos\theta_{True}$ bins between -1.00 and -0.95 and 0.95 and 1.00.

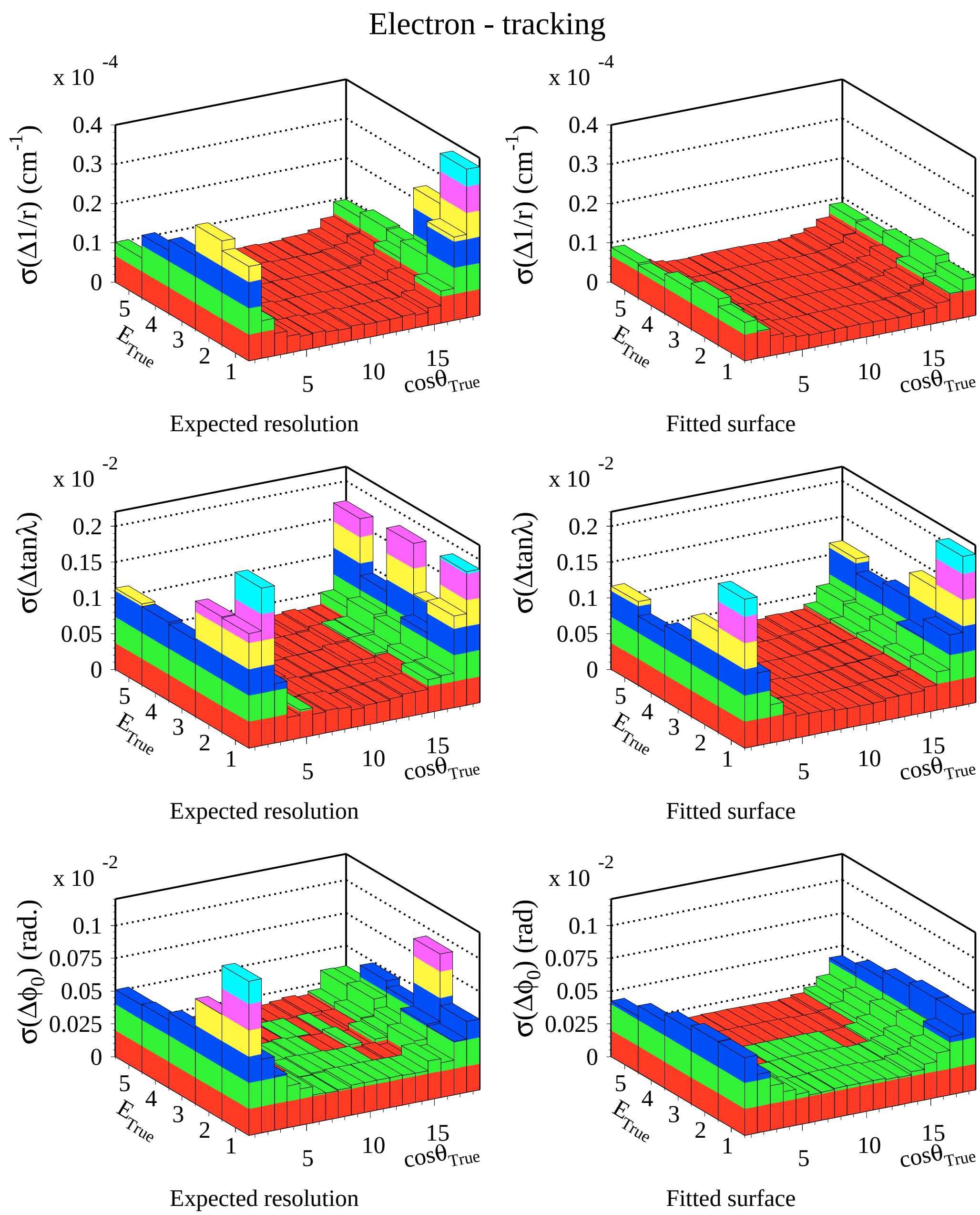

Figure 4.17: The measured and fitted values for the expected resolution of $\Delta 1/r$, $\Delta \tan\lambda$ and $\Delta\phi_0$ are shown in the first, second and third rows respectively, for electrons, reconstructed using information from the tracking detectors only, in fully simulated, selected $e\bar{\nu}q\bar{q}$ events. The binning corresponds to that given in the text, minus the $\cos\theta_{True}$ bins between -1.00 and -0.95 and 0.95 and 1.00.

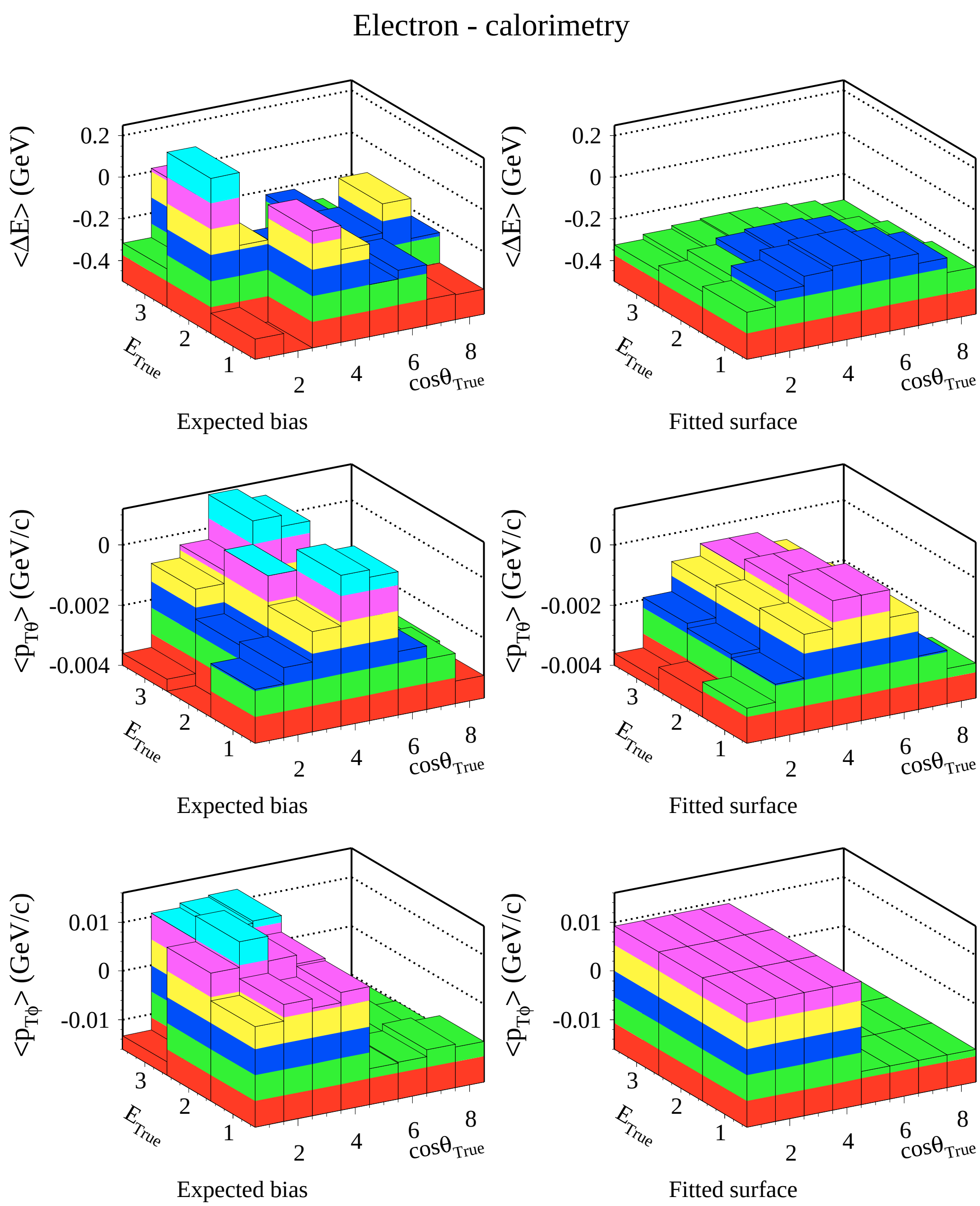

Figure 4.18: The measured and fitted values for the expected bias of ΔE, $p_{T\theta}$ and $p_{T\phi}$ are shown in the first, second and third rows respectively, for electrons that have calorimetric energy added in fully simulated, selected $e\bar{\nu}q\bar{q}$ events. Due to lower statistics, the bin ranges in E_{True} are: 25, 40, 55, 70 GeV, and in $\cos\theta_{True}$ are: -0.95, -0.7, -0.45, -0.2, 0.0, 0.2, 0.45, 0.7, 0.95.

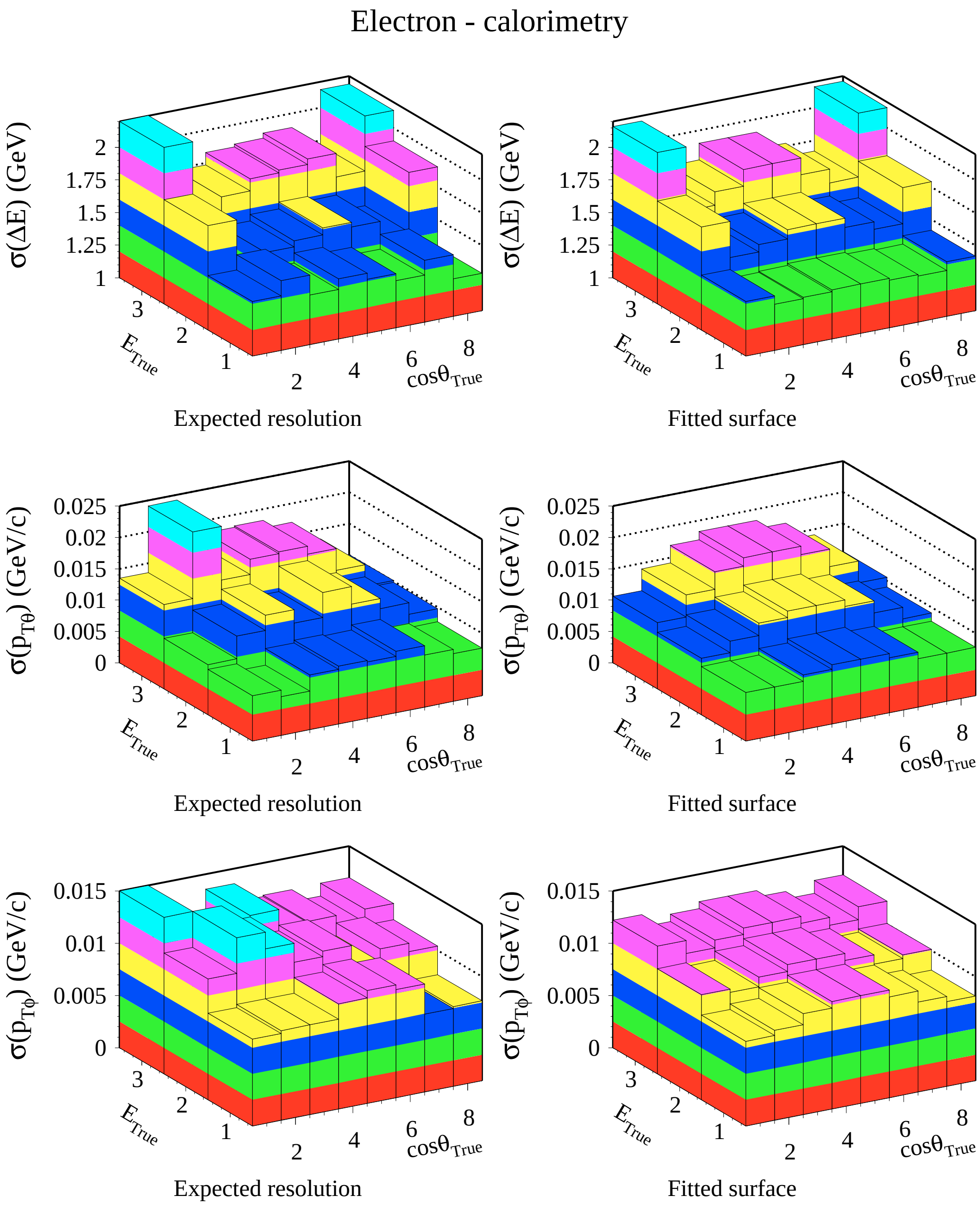

Figure 4.19: The measured and fitted values for the expected resolution of ΔE, $p_{T\theta}$ and $p_{T\phi}$ are shown in the first, second and third rows respectively, for electrons that have calorimetric energy added in fully simulated, selected $e\bar{\nu}q\bar{q}$ events. Due to lower statistics, the bin ranges in E_{True} are: 25, 40, 55, 70 GeV, and in $\cos\theta_{True}$ are: -0.95, -0.7, -0.45, -0.2, 0.0, 0.2, 0.45, 0.7, 0.95.

Variable		Coefficients of fit function							
		$\cos\theta^0$	$\cos\theta^2$	$\cos\theta^3$	$\cos\theta^4$	$\cos\theta^5$	$\cos\theta^6$	$\cos\theta^8$	$\cos\theta^{10}$
	E^0	b_{00}	b_{20}	b_{30}	b_{40}	b_{50}	b_{60}	b_{80}	b_{100}
	$E^{\frac{1}{2}}$	$b_{0\frac{1}{2}}$	$b_{2\frac{1}{2}}$	$b_{3\frac{1}{2}}$	$b_{4\frac{1}{2}}$	$b_{5\frac{1}{2}}$	$b_{6\frac{1}{2}}$	$b_{8\frac{1}{2}}$	$b_{10\frac{1}{2}}$
	E^1	b_{01}	b_{21}	b_{31}	b_{41}	b_{51}	b_{61}	b_{81}	b_{101}
χ^2/ndf	E^2	b_{02}	b_{22}	b_{32}	b_{42}	b_{52}	b_{62}	b_{82}	b_{102}
$<\Delta\beta>$	jet	0.2399E-1	-	-	-	-	-	-	-
		-0.1039E-1	-	-	-	-	-	-	-
		-0.1876E-1	-	-	-	-	-	-	-
446/96		0.9019E-2	-	-	-	-	-	-	-
$<\Delta E>$	jet	0.1573E+1	-	-	-	-	-0.7163E+1	0.2116E+2	-0.1614E+2
		-	-	-	-	-	-	-	-
		-0.1046E+1	-	-	-	-	-0.5273E+2	0.1397E+3	-0.9937E+2
231/92		-	-	-	-	-	-	-	
$<p_{T\theta}>$	jet	0.2869E-1	-	-	-	-	-0.5300E+1	0.1187E+2	-0.7473E+1
		-	-	-	-	-	-	-	-
		-	-	-	-	-	-	-	-
356/96		-	-	-	-	-	-	-	-
$<p_{T\phi}>$	jet	0.9160E-1	-	-	-	-	-	-	-
		-	-	-	-	-	-	-	-
		-	-	-	-	-	-	-	-
188/99		-	-	-	-	-	-	-	-
$<\Delta 1/r>$	e	0.7814E-7	-	-	-	-	-	-	-
		-	-	-	-	-	-	-	-
		-	-	-	-	-	-	-	-
306/89		-	-	-	-	-	-	-	-
$<\Delta\tan\lambda>$	e	-0.4349E-6	-	0.1249E-3	-	-0.4987E-3	-	-	-
		-	-	-	-	-	-	-	-
		-	-	-	-	-	-	-	-
176/87		-	-	-	-	-	-	-	-
$<\Delta\phi_0>$	e	-0.5234E-5	-	-	-	-	-	-	-
		-	-	-	-	-	-	-	-
		-	-	-	-	-	-	-	-
361/89		-	-	-	-	-	-	-	-
$<\Delta E>$	e	0.2925E-1	-0.3616E+0	-	-	-	-	-	-
		-	-	-	-	-	-	-	-
		-0.2217E+0	0.2110E+0	-	-	-	-	-	-
306/20		-	-	-	-	-	-	-	-
$<p_{T\theta}>$	e	0.1169E-2	-0.1783E-1	-	0.1936E-1	-	-	-	-
		-	-	-	-	-	-	-	-
		-0.1173E-2	0.9805E-2	-	-0.1436E-1	-	-	-	-
176/18		-	-	-	-	-	-	-	-
$<p_{T\phi}>$	e	-0.9244E-2	-	-	-	-	-	-	-
		-	-	-	-	-	-	-	-
		-	-	-	-	-	-	-	-
361/23		-	-	-	-	-	-	-	-

Table 4.2: The coefficients b_{ik} of the functions used to describe the expected biases of the variables in the $e\bar{\nu}q\bar{q}$ channel. The overall χ^2 is given for each variable, for the fitted surface with respect to the measured surface.

Variable		Coefficients of fit function					
		$\cos\theta^0$	$\cos\theta^2$	$\cos\theta^4$	$\cos\theta^6$	$\cos\theta^8$	$\cos\theta^{10}$
	E^0	b_{00}	b_{20}	b_{40}	b_{60}	b_{80}	b_{100}
	$E^{\frac{1}{2}}$	$b_{0\frac{1}{2}}$	$b_{2\frac{1}{2}}$	$b_{4\frac{1}{2}}$	$b_{6\frac{1}{2}}$	$b_{8\frac{1}{2}}$	$b_{10\frac{1}{2}}$
	E^1	b_{01}	b_{21}	b_{41}	b_{61}	b_{81}	b_{101}
χ^2/ndf	E^2	b_{02}	b_{22}	b_{42}	b_{62}	b_{82}	b_{102}
$\sigma(\Delta\beta)$ jet		0.4634E-1	-	-	-	-	-
		-0.1601E-1	-	-	-	-	-
		-0.3219E-1	-	-	-	-	-
289/96		0.1442E-1	-	-	-	-	-
$\sigma(\Delta E)$ jet		-0.9604E+0	-	-	-0.3846E+2	0.1220E+3	-0.8288E+2
		0.3172E+1	-	-	0.3436E+2	-0.1047E+3	0.7143E+2
		0.4328E+1	-	-	0.5624E+2	-0.1748E+3	0.1206E+3
199/84		-0.1343E+1	-	-	-0.3084E+2	-0.9295E+2	-0.6086E+2
$\sigma(p_{T\theta})$ jet		-0.1364E+1	-	-	-	-	-
		0.5246E+1	-	-	-	-	-
		-0.3742E+1	-	-	-	-	-
177/96		0.6657E+0	-	-	-	-	-
$\sigma(p_{T\phi})$ jet		-0.3368E+1	-	-	-	-	-
		0.1073E+2	-	-	-	-	-
		-0.7817E+1	-	-	-	-	-
381/96		0.1349E+1	-	-	-	-	-
$\sigma(\Delta 1/r)$ e		0.2124E-4	-	-	0.8084E-5	-0.7179E-3	-
		-0.4518E-4	-	-	-0.1922E-4	0.1951E-2	-
		0.3208E-4	-	-	-0.1865E-4	-0.1408E-2	-
171/78		-0.5109E-5	-	-	0.1155E-4	0.2107E-3	-
$\sigma(\Delta\tan\lambda)$ e		0.1535E-2	-	-	0.2874E-1	-0.1117E+0	0.1071E+0
		-0.3540E-2	-	-	-0.1499E-1	0.5940E-1	-0.5702E-1
		0.2765E-2	-	-	-0.2436E-1	0.9491E-1	-0.9027E-1
98/74		-0.4905E-3	-	-	0.1497E-1	-0.5658E-1	0.5241E-1
$\sigma(\Delta\phi_0)$ e		0.2625E-3	-	-	-0.1332E-1	0.4481E-1	-0.3414E-1
		0.1464E-4	-	-	0.8288E-2	-0.2954E-1	0.2405E-1
		-0.9088E-4	-	-	0.1208E-1	-0.4113E-1	0.3209E-1
111/74		0.1678E-4	-	-	-0.6880E-2	0.2400E-1	-0.1927E-1
$\sigma(\Delta E)$ e		0.7945E+0	0.1475E+1	-0.2455E+1	-	-	-
		-	-	-	-	-	-
		0.8128E+0	-0.2325E+1	0.3907E+1	-	-	-
171/18		-	-	-	-	-	-
$\sigma(p_{T\theta})$ e		-0.1825E-5	-0.2082E-2	0.1277E-1	-	-	-
		-	-	-	-	-	-
		0.1327E-1	-0.8743E-2	-0.6468E-2	-	-	-
98/18		-	-	-	-	-	-
$\sigma(p_{T\phi})$ e		0.8194E-2	-0.7058E-2	0.9130E-3	-	-	-
		-	-	-	-	-	-
		0.3066E-2	-0.6468E-3	0.7090E-2	-	-	-
111/18		-	-	-	-	-	-

Table 4.3: The coefficients b_{ik} of the functions used to describe the expected resolutions of the variables in the $e\bar{\nu}q\bar{q}$ channel. The overall χ^2 is given for each variable, for the fitted surface with respect to the measured surface.

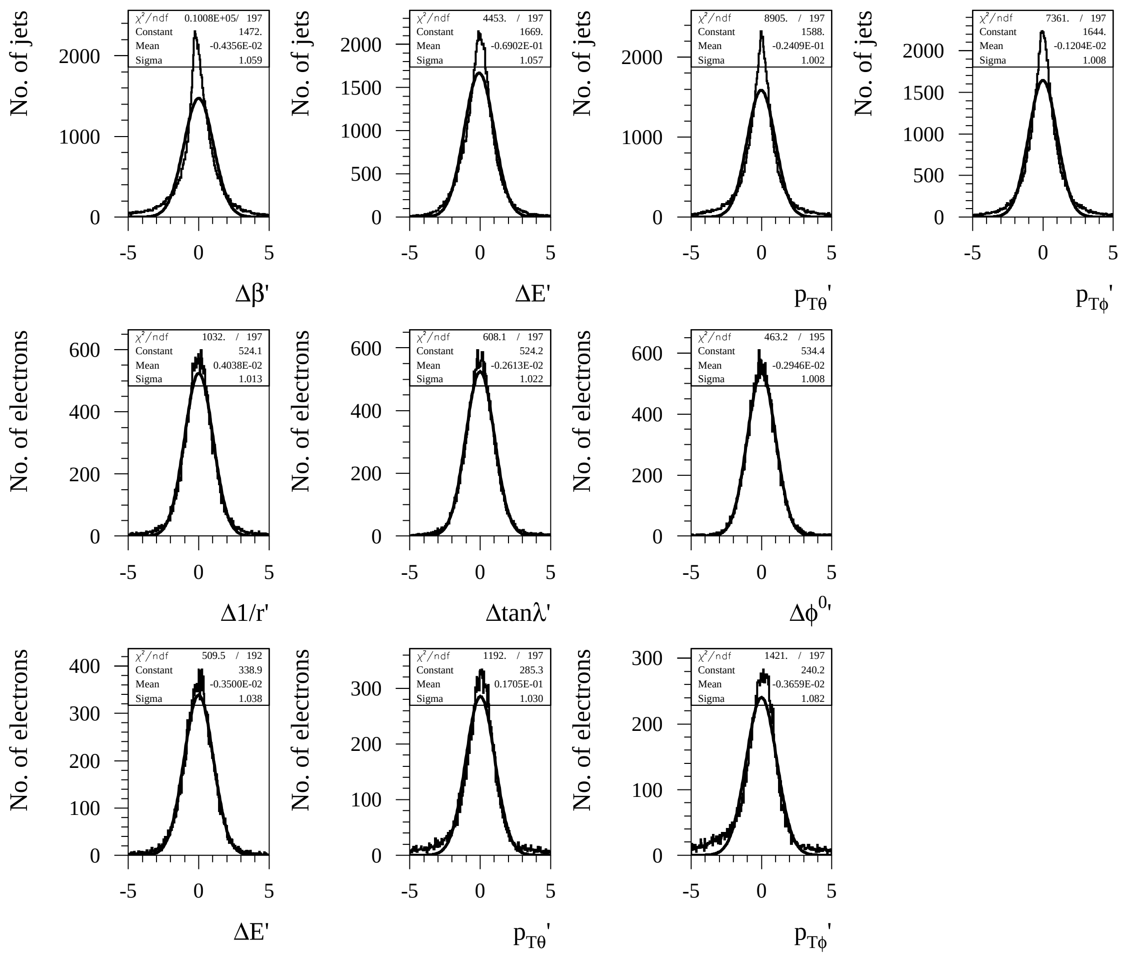

Figure 4.20: The pull distributions Δ' for fully simulated, selected $e\bar{\nu}q\bar{q}$ events.

- The reconstructed track is curved, having a measured radius of curvature that is too low and therefore a value for $1/r$ that is too large and negative. Note that $1/r$ is signed negative if the track bends clockwise with respect to the z-axis in the ALEPH coordinate system.

- The measured azimuthal direction at the event vertex, ϕ_0, is given approximately by a line that points from the VDET coordinate to the innermost TPC coordinate and is therefore too large and positive.

Hence a negative correlation between $\Delta 1/r$ and $\Delta\phi_0$ is expected [100].

Particle		jet 1				jet 2				electron		
	Variable	$\Delta\beta'$	$\Delta E'$	$p'_{T\theta}$	$p'_{T\phi}$	$\Delta\beta'$	$\Delta E'$	$p'_{T\theta}$	$p'_{T\phi}$	$\Delta 1/r'$	$\Delta \tan\lambda'$	$\Delta\phi^{0'}$
jet 1	$\Delta\beta'$	1.00	-	-0.07	0.01	-0.24	0.05	0.02	-	-	0.01	-
	$\Delta E'$	-	1.00	0.07	0.01	0.06	-	-0.02	-	-	-	-
	$p'_{T\theta}$	-	-	1.00	-	0.01	0.01	-	0.01	-	-0.01	-
	$p'_{T\phi}$	-	-	-	1.00	-	-	-	-0.02	-	-	-0.02
jet 2	$\Delta\beta'$	-	-	-	-	1.00	0.01	-0.10	-	-	-	-
	$\Delta E'$	-	-	-	-	-	1.00	0.08	0.03	-	-	-
	$p'_{T\theta}$	-	-	-	-	-	-	1.00	-	0.01	-	-
	$p'_{T\phi}$	-	-	-	-	-	-	-	1.00	-	0.01	-
electron	$\Delta 1/r'$	-	-	-	-	-	-	-	-	1.00	0.01	-0.69
	$\Delta \tan\lambda'$	-	-	-	-	-	-	-	-	-	1.00	-0.01
	$\Delta\phi^{0'}$	-	-	-	-	-	-	-	-	-	-	1.00

Table 4.4: The expected correlations between the Δ' variables in the $e\bar{\nu}q\bar{q}$ channel, where no calorimetric energy is added to the electron.

4.2.4 Performance of KINFIT.

The performance of this kinematic fit is shown in Figures 4.21 and 4.22 for selected $e\bar{\nu}q\bar{q}$ and $\mu\bar{\nu}q\bar{q}$ events from simulation, in terms of the resolution on the average event-by-event generated W mass and the pull, which is defined as the resolution divided by the event-by-event error. The $\nu = 2$ W mass estimator is required to be greater than 74 GeV/c^2 in the performance plots so that the long tail at low mass values does not obscure the results discussed in the following. The resolution on the W mass is 1.68 GeV/c^2 and 1.64 GeV/c^2 in the $e\bar{\nu}q\bar{q}$ and $\mu\bar{\nu}q\bar{q}$ channels respectively. The contribution from events with energetic ISR photons (defined as $E_\gamma \geq 500$ MeV) is denoted by the cross-hatching. As the effects of ISR are neglected by the fit, the W mass is biased upwards for these events, which skews the pull distribution away from the ideal case of a Gaussian distribution with mean zero and width one. If the events with energetic ISR photons, which is known in the simulation, are excluded, then the kinematic fit performs excellently, with a mean bias that is close to zero and a pull distribution that is compatible with the ideal case for the W mass estimator in the $\mu\bar{\nu}q\bar{q}$ channel.

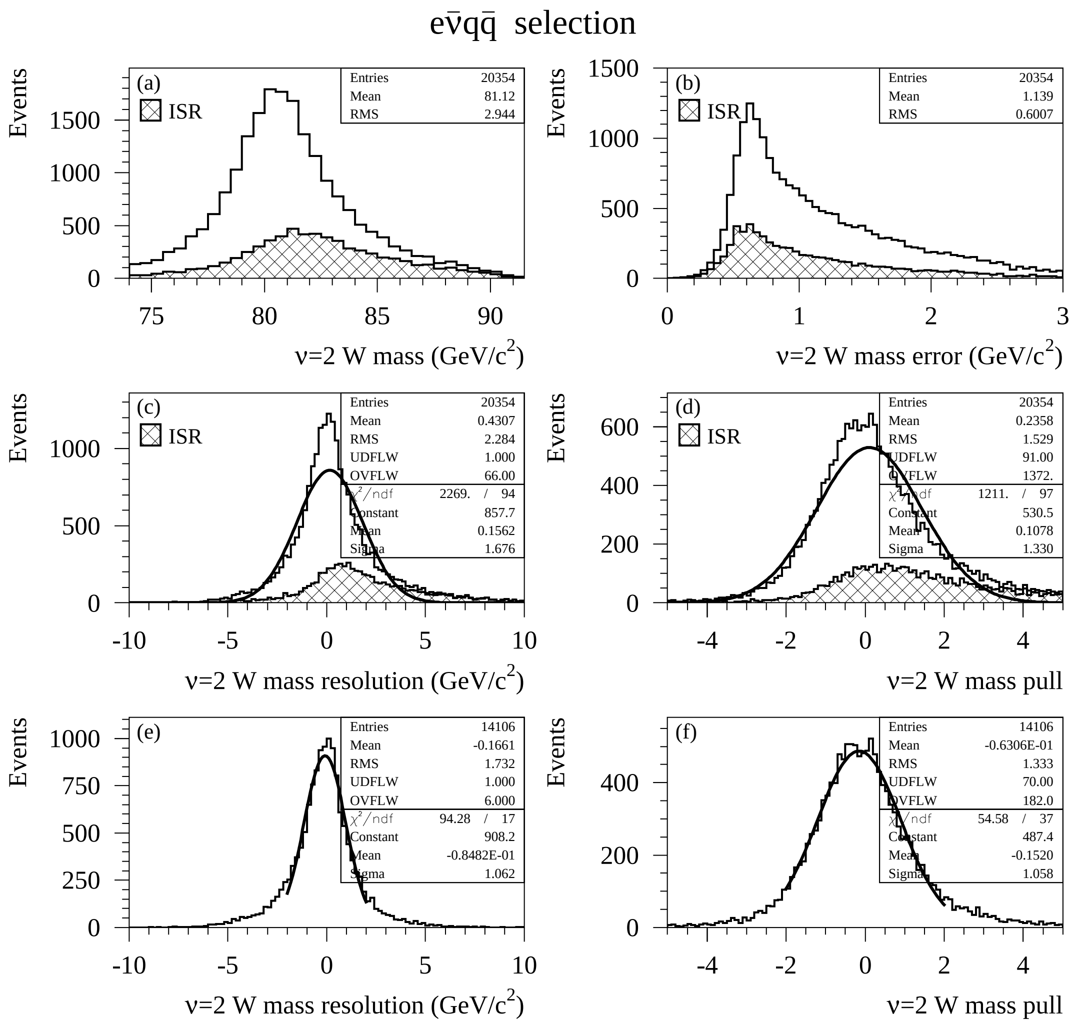

Figure 4.21: The (a) invariant mass, (b) event-by-event error, (c) resolution on the average generated W mass and (d) pull distributions for the ν=2 W mass estimator for fully simulated, selected $e\bar{\nu}q\bar{q}$ events. The contribution from events with more than 500 MeV of of energy lost to ISR is shown by the hatching. The (e) resolution and (f) pull distributions are also shown for events with less than 500 MeV of energy lost to ISR. Note that the $\nu = 2$ mass is required to be greater than 74 GeV/c^2 in all cases.

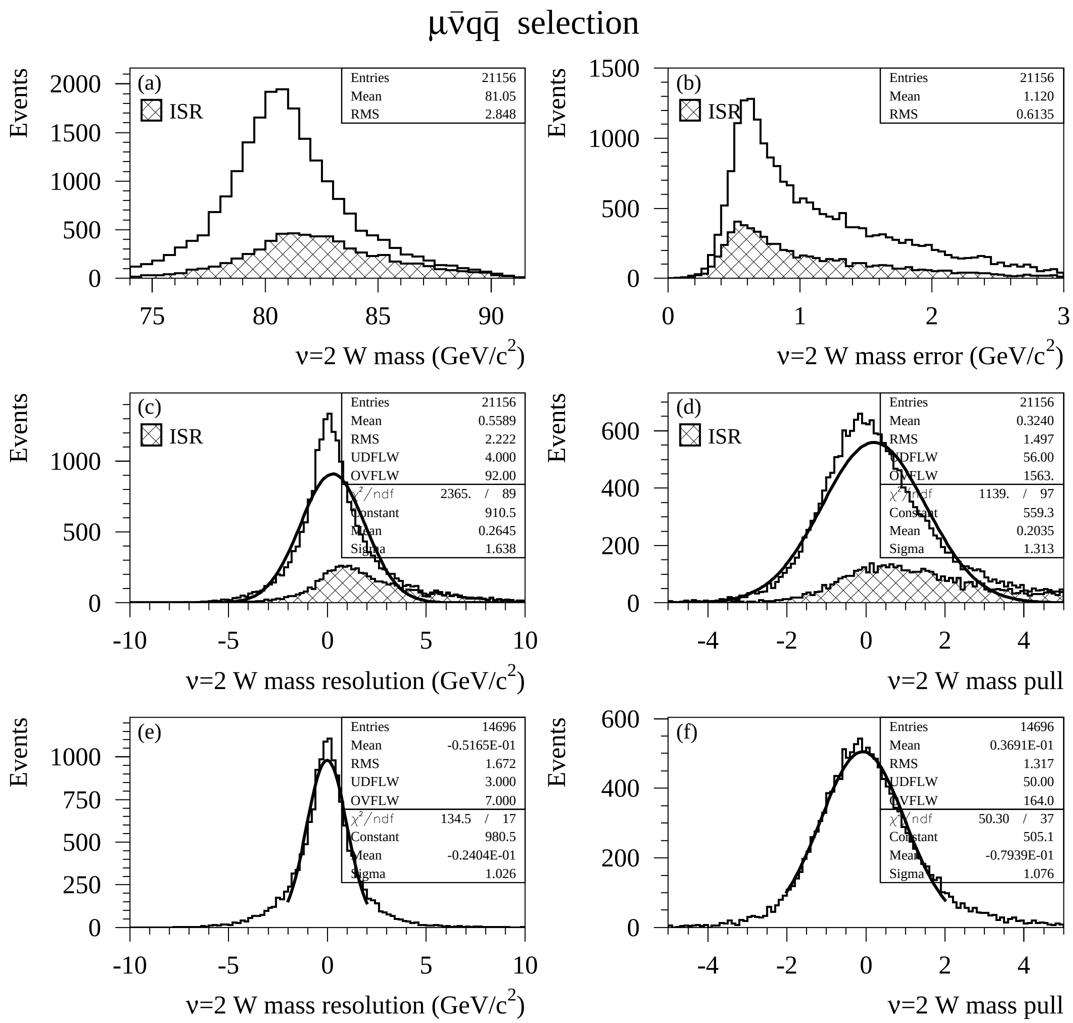

Figure 4.22: The (a) invariant mass, (b) event-by-event error, (c) resolution on the average generated W mass and (d) pull distributions for the ν=2 W mass estimator for fully simulated, selected $\mu\bar{\nu}q\bar{q}$ events. The contribution from events with more than 500 MeV of of energy lost to ISR is shown by the hatching. The (e) resolution and (f) pull distributions are also shown for events with less than 500 MeV of energy lost to ISR. Note that the $\nu = 2$ mass is required to be greater than 74 GeV/c^2 in all cases.

However, Figure 4.22(e) shows that the W mass estimator in the $e\bar{\nu}q\bar{q}$ channel now underestimates the average generated W mass by 170 MeV/c^2. Some further detective work is required to understand the source of this bias. Figure 4.23 divides the selected $e\bar{\nu}q\bar{q}$ events, which have less than 500 MeV of energy lost to ISR, into three classes:

(a) Events where the reconstructed lepton energy is within 1 GeV of the true lepton energy, which is known from simulation and includes any energy lost to FSR.

(b) Events where the reconstructed lepton energy underestimates the true lepton

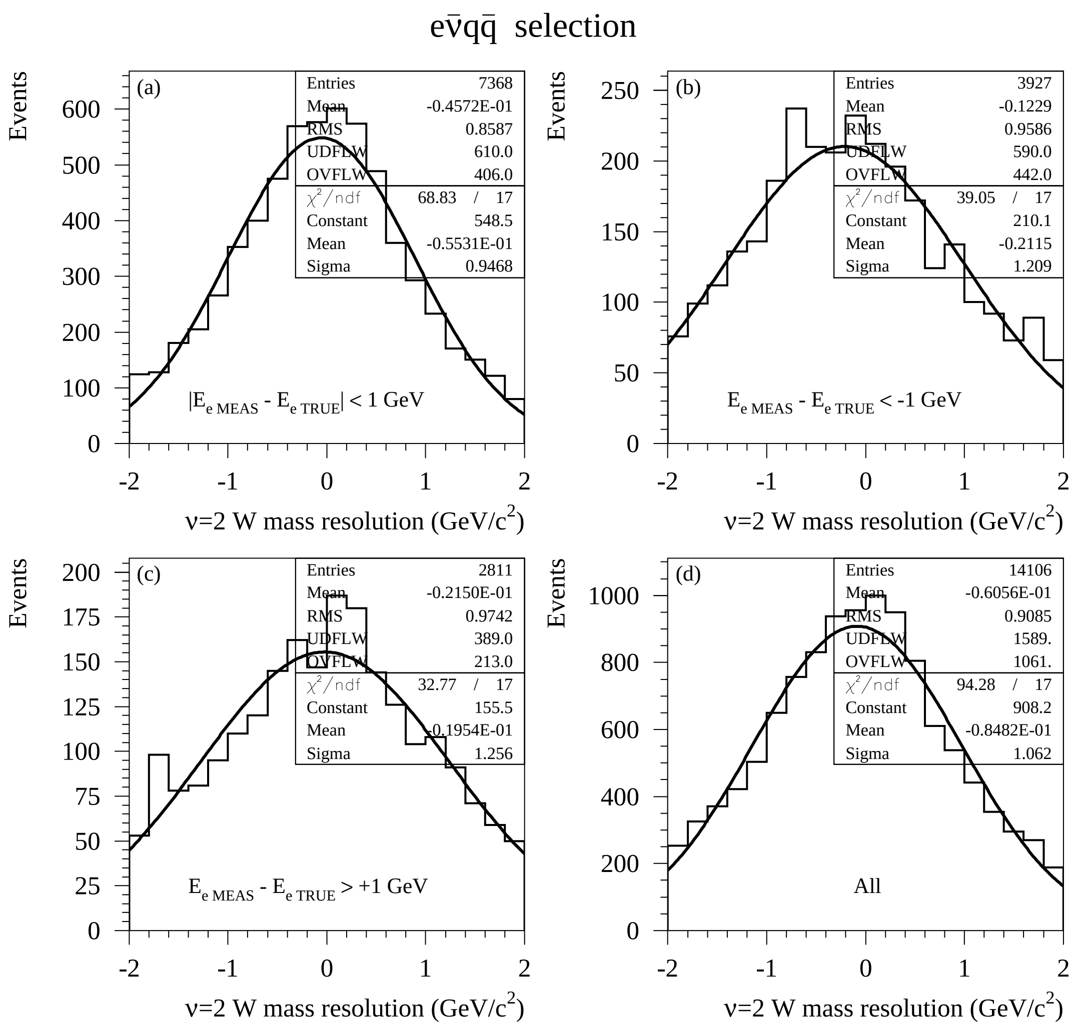

Figure 4.23: The resolution on the average generated W mass for fully simulated, selected $e\bar{\nu}q\bar{q}$ events where the reconstructed electron energy is (a) within 1 GeV of the true energy, (b) underestimated by at least 1 GeV, (c) overestimated by at least 1 GeV and (d) any of the above. Events with more than 500 MeV of energy lost to ISR are excluded. Note that the $\nu = 2$ mass is required to be greater than 74 GeV/c^2 in all cases.

energy by more than 1 GeV.

(c) Events where the reconstructed lepton energy overestimates the true lepton energy by more than 1 GeV.

It is clear that the negative bias on the W mass estimator comes from class (b), where the electron energy is underestimated due to Bremsstrahlung or FSR photons that are not recovered by the correction routine. This implies that more effort is needed to recover these photons for future analyses.

The χ^2 and $P(\chi^2 > \mathcal{S}_{min})$ for the kinematic fits with two degrees of freedom are shown in Figure 4.24 for selected $e\bar{\nu}q\bar{q}$ and $\mu\bar{\nu}q\bar{q}$ events from simulation. The χ^2 closely resembles

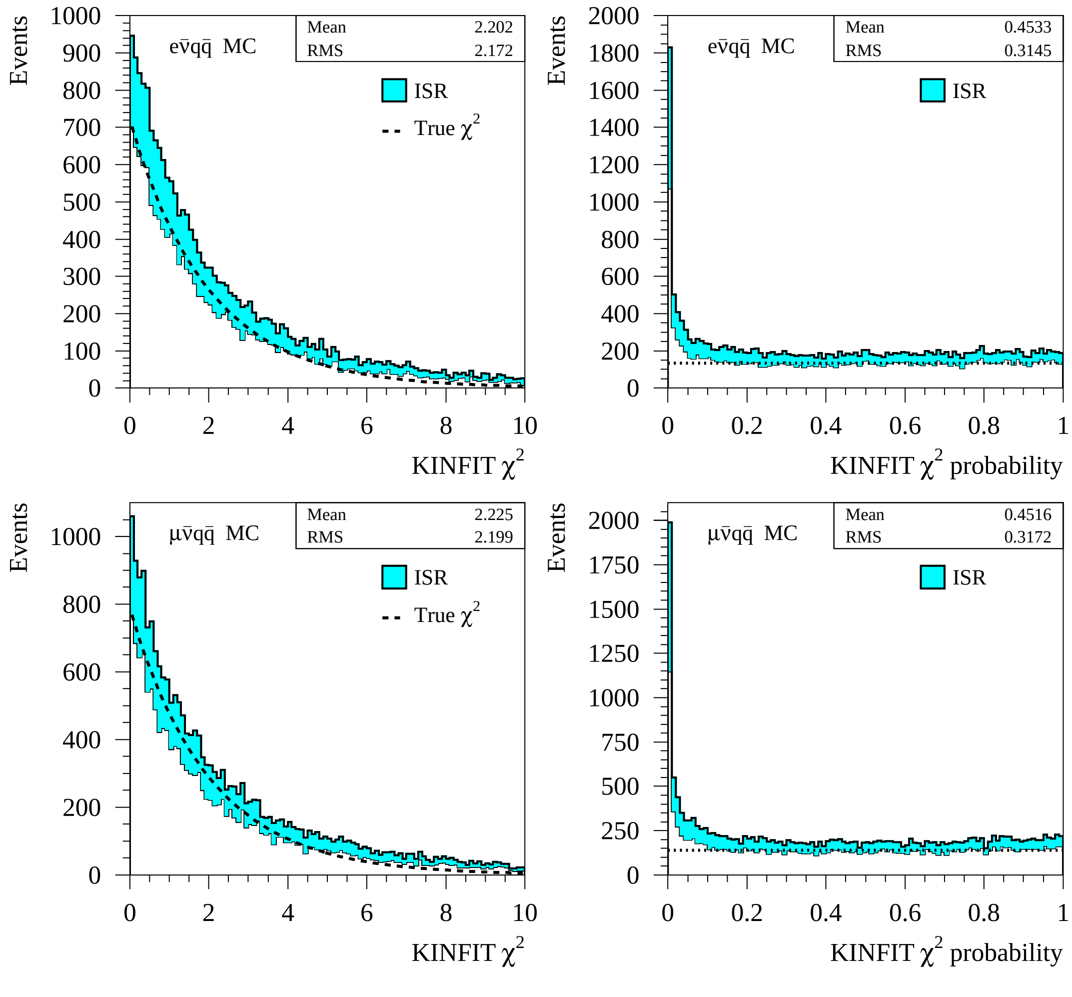

Figure 4.24: The KINFIT χ^2 and χ^2 probability distributions from a kinematic fits with two degrees of freedom for fully simulated, selected $e\bar{\nu}q\bar{q}$ and $\mu\bar{\nu}q\bar{q}$ events. The contribution from events with more than 500 MeV of energy lost to ISR is indicated by the shading.

the true χ^2 distribution below χ^2 values of 10. The excess at higher χ^2 values appears as a peak at the low end of the distribution of the probability to obtain a worse kinematic fit result. This peak implies that the assumptions made by the kinematic fit are incorrect for 5% of $e\bar{\nu}q\bar{q}$ and $\mu\bar{\nu}q\bar{q}$ events. In general, the main sources of a peak at low probabilities are:

- Events that are measured with a lower accuracy than the majority. The peak region of an experimental distribution may approximate to a Gaussian, but the tails of the distribution tend to lie above the fitted Gaussian curve. So the probability for a large deviation is underestimated when calculated from the Gaussian fitted to the majority of the data. In reality, the event could correspond to a much more probable fluctuation from a subset of data with a larger variance.

- Semileptonic WW events that do not satisfy the assumed hypotheses, which come from several sources, listed below in order of decreasing importance, that include:

  (1) Events with a high energy photon from ISR, which lowers the effective centre-of-mass energy available for WW production and boosts the WW system in a direction anti-parallel to that of the ISR photon. The current implementation of the conservation of energy and momentum constraints ignores the effects of ISR.

  (2) Gluon radiation is in direct disagreement with the treatment of the jets as independent objects. Even rather soft gluon radiation leads to jet broadening in a specific direction.

  (3) The optional equal mass constraint ignores the effect of the W width.

- Contamination from background events.

This excess of events with poor fits can be removed by requiring $P(\chi^2 > \mathcal{S}_{min})$ to exceed some minimum value. The minimum value should be chosen carefully in order to avoid losing too many events that are compatible with the assumed hypotheses but to reject most of the events for which the assumed hypotheses or error parameterisations do not apply [89]. A minimum value of 0.02 for the kinematic fit with two degrees of freedom removes most of the excess. This cut corresponds to rejecting events with a $\chi^2 \geq 7.8$ for

2 degrees of freedom. Such events have very shallow minima and even small changes to the measurements can drastically alter the values for the fitted parameters if a slightly deeper minimum can be found as a result. The original motivation for studying the fit quality came from the observation that the systematic error from the detector calibration was dominated by such poorly fitted events.

The efficiencies for the successful convergence and the $P(\chi^2 > \mathcal{S}_{min}) > 0.02$ requirements are shown in Table 4.5 for data and simulation. The efficiencies are in good agreement and, as expected, are much lower for background than for signal processes. The mass distributions for the main background processes are shown for the ν=2 kinematic fit in Figures 4.25 and 4.26 for the $e\bar{\nu}q\bar{q}$ and $\mu\bar{\nu}q\bar{q}$ channels, respectively. The contribution remaining after the χ^2 probability cut is indicated by the cross-hatching.

Process	Efficiency (%)			
	$e\bar{\nu}q\bar{q}$ channel		$\mu\bar{\nu}q\bar{q}$ channel	
	V pos. def.	$P_{\chi^2} > 0.02$	V pos. def.	$P_{\chi^2} > 0.02$
$e^+e^-\to W^+W^-\to e\bar{\nu}q\bar{q}$	75.5	67.5	0.05	0.03
$e^+e^-\to W^+W^-\to \mu\bar{\nu}q\bar{q}$	0.14	0.08	78.3	69.6
$e^+e^-\to W^+W^-\to \tau\bar{\nu}q\bar{q}$	2.67	0.66	2.82	0.68
$e^+e^-\to W^+W^-\to q\bar{q}q\bar{q}$	0.01	0.00	0.01	0.00
$e^+e^-\to W^+W^-\to \ell\nu\ell\nu$	0.13	0.00	0.07	0.00
$e^+e^-\to Z/\gamma\to q\bar{q}(\gamma)$	0.04	0.02	0.01	0.00
$e^+e^-\to Z/\gamma\to \tau^+\tau^-(\gamma)$	0.05	0.01	0.03	0.00
$e^+e^-\to ZZ$	0.26	0.15	0.33	0.14
$e^+e^-\to Ze^+e^-$	0.04	0.02	0.00	0.00
$e^+e^-\to We\nu_e$	1.42	0.83	0.07	0.05
Efficiency (%)	75.5	67.5	78.3	69.6
Purity (%)	91.0	95.4	95.4	98.7
Predicted events	108.3	92.4	106.7	91.7
Observed events	118	97	98	81

Table 4.5: Efficiencies for the requirements that the covariance matrix should be positive-definite at the minimum and that the probability to obtain a worse kinematic fit result should be greater than 0.02.

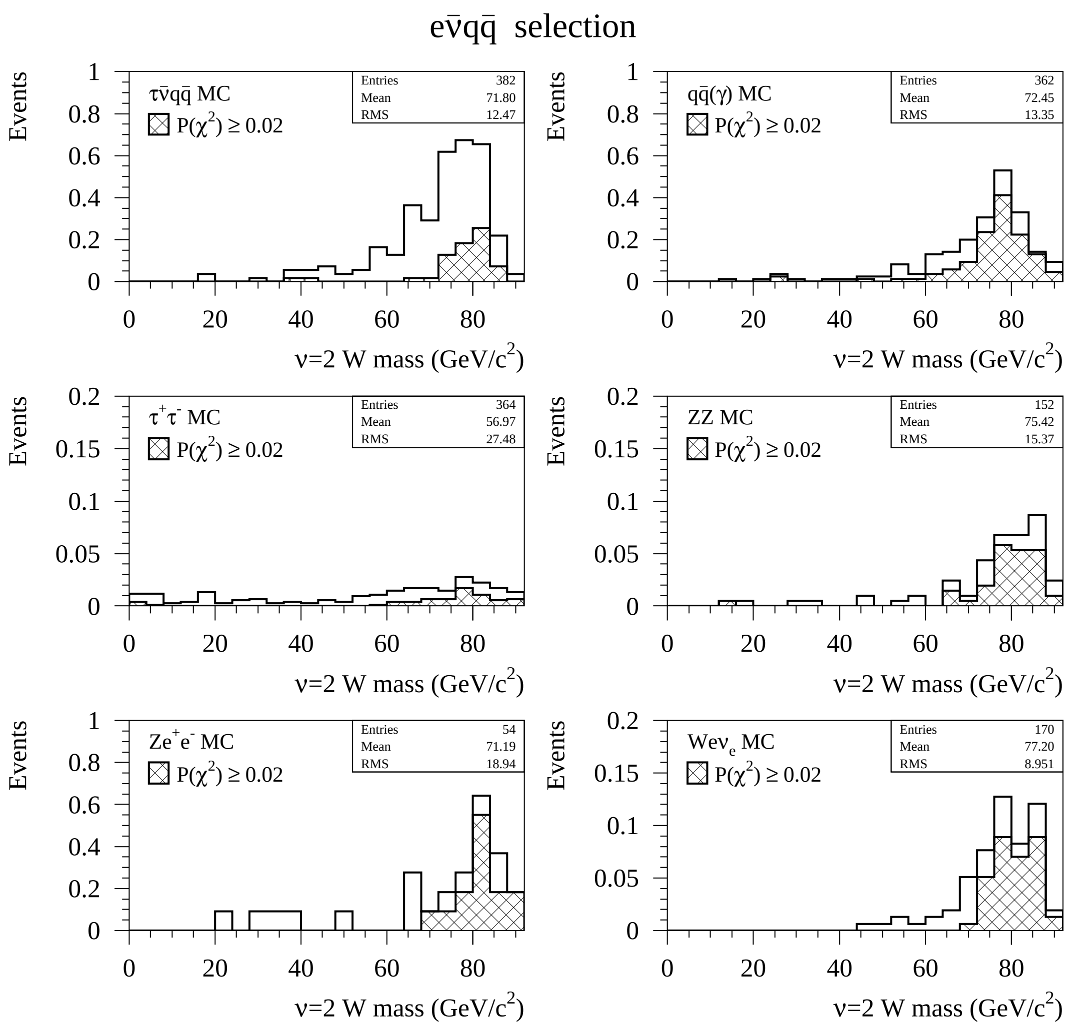

Figure 4.25: The invariant mass distributions for the simulated backgrounds to the $e\bar{\nu}q\bar{q}$ channel, after a kinematic fit with ν=2. The number of events is normalised to the luminosity of the $\sqrt{s}$ = 183 GeV data.

4.2.5 Comparisons of data and simulation.

The mass fit technique depends on the simulation being able to accurately reproduce the data distributions. Comparisons between data and simulation [101] for the measured energy, polar angle, azimuthal angle and mass of the jets and the measured energy, polar angle and azimuthal angle of the lepton are shown in Figures 4.27 and 4.28 after the $e\bar{\nu}q\bar{q}$ and $\mu\bar{\nu}q\bar{q}$ selections, respectively. The same distributions are shown for the fitted quantities, after the kinematic fit with ν=2 and successful convergence, in Figures 4.29 and 4.30. The distributions of the fitted invariant mass, event-by-event error, χ^2 and χ^2

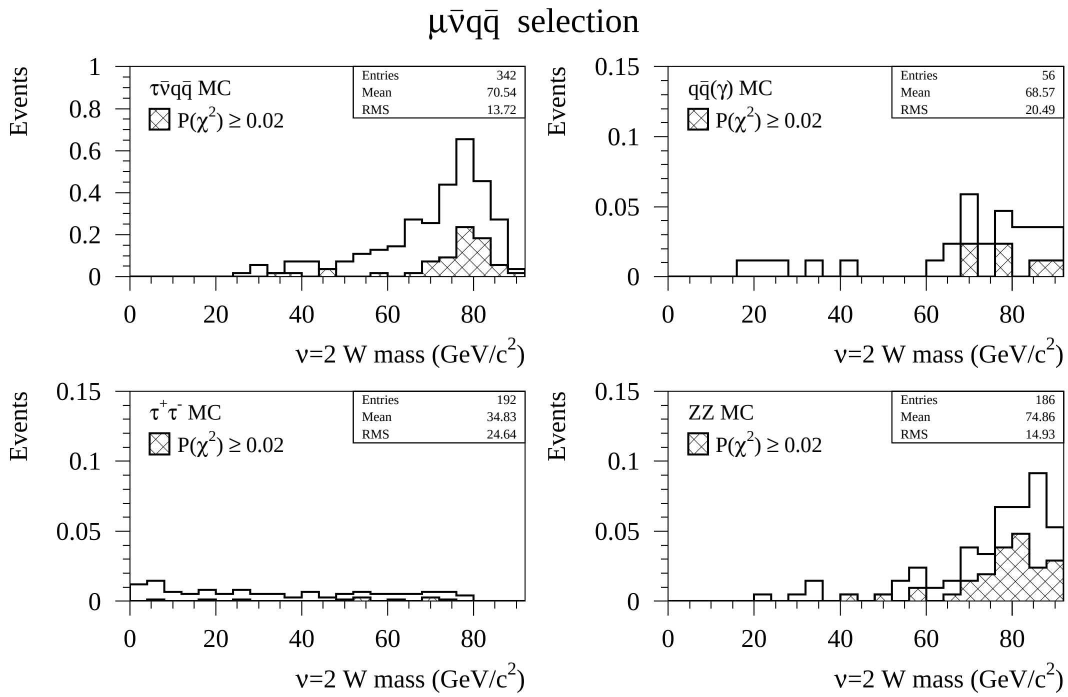

Figure 4.26: The invariant mass distributions for the simulated backgrounds to the $\mu\bar{\nu}q\bar{q}$ channel, after a kinematic fit with ν=2. The number of events is normalised to the luminosity of the $\sqrt{s}$ = 183 GeV data.

probability are compared in Figures 4.31 and 4.32. The simulation is normalised to the number of events observed in the data in all the plots.

The effects of the low statistics available are accounted for in the definition of the χ^2 shown on the plots. No statistically significant discrepancies are observed.

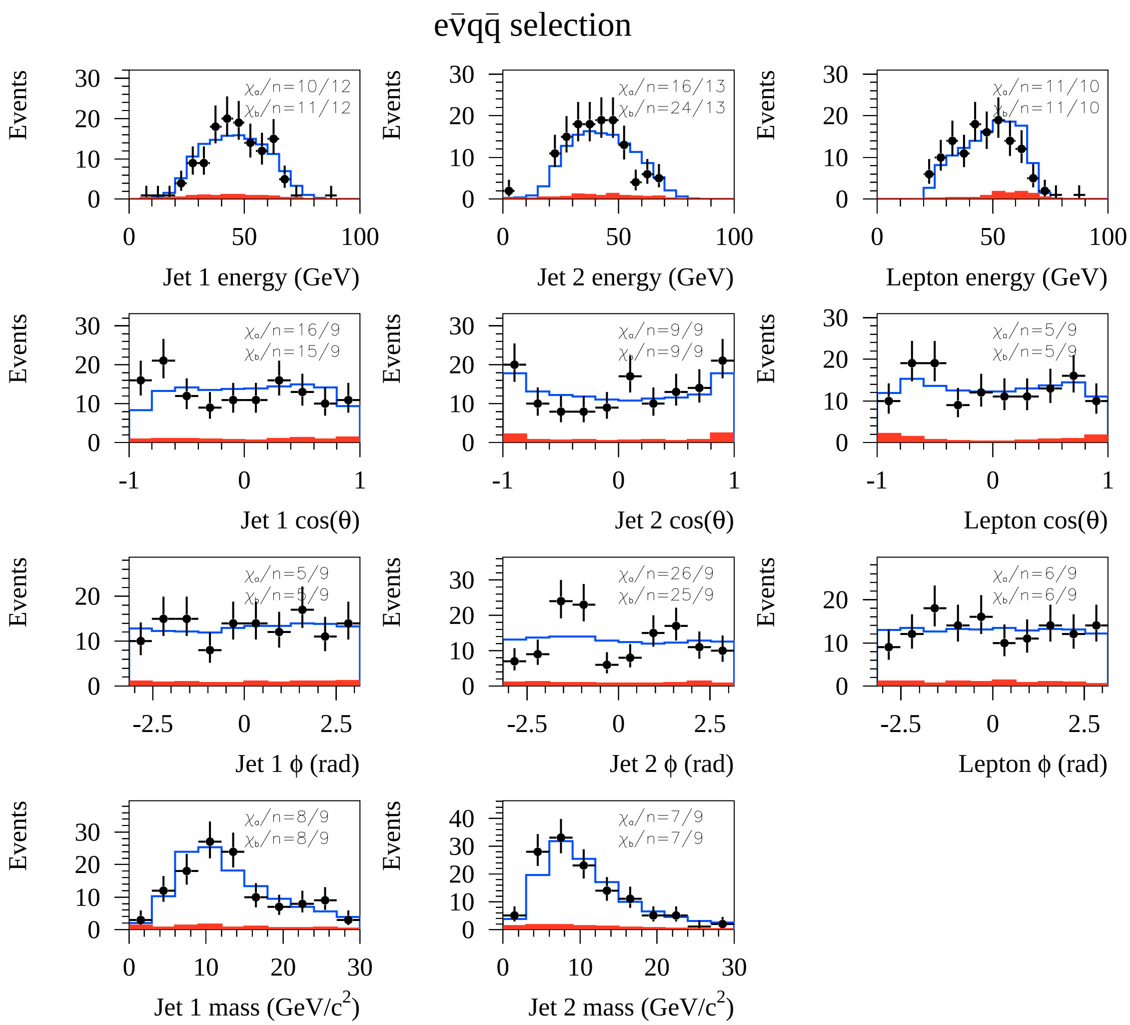

Figure 4.27: The reconstructed energy, polar angle, azimuthal angle and mass for the jets and the electron in the $e\bar{\nu}q\bar{q}$ channel. The dots represent the data, the solid line the simulation and the shading the background contribution.

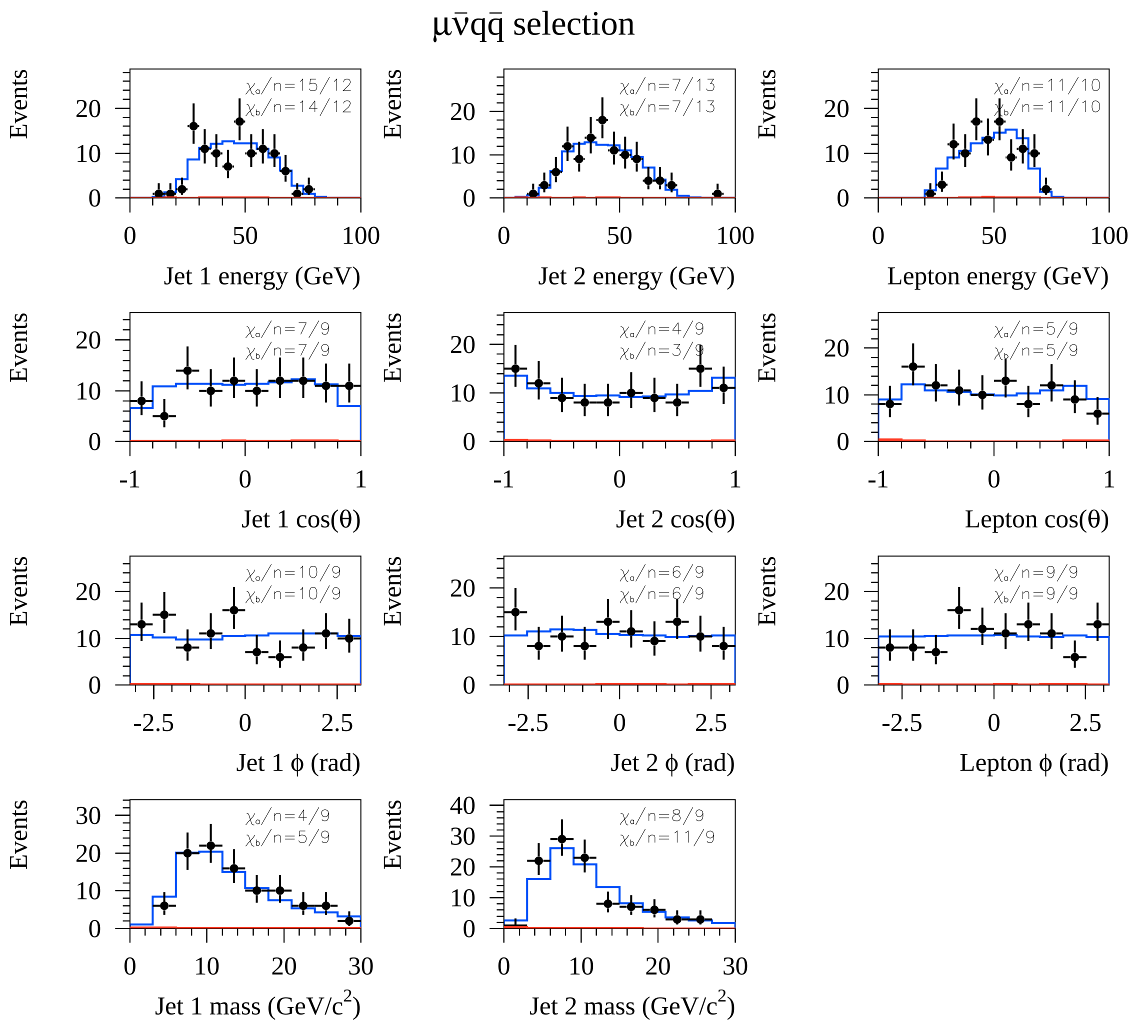

Figure 4.28: The reconstructed energy, polar angle, azimuthal angle and mass for the jets and the muon in the $\mu\bar{\nu}q\bar{q}$ channel.

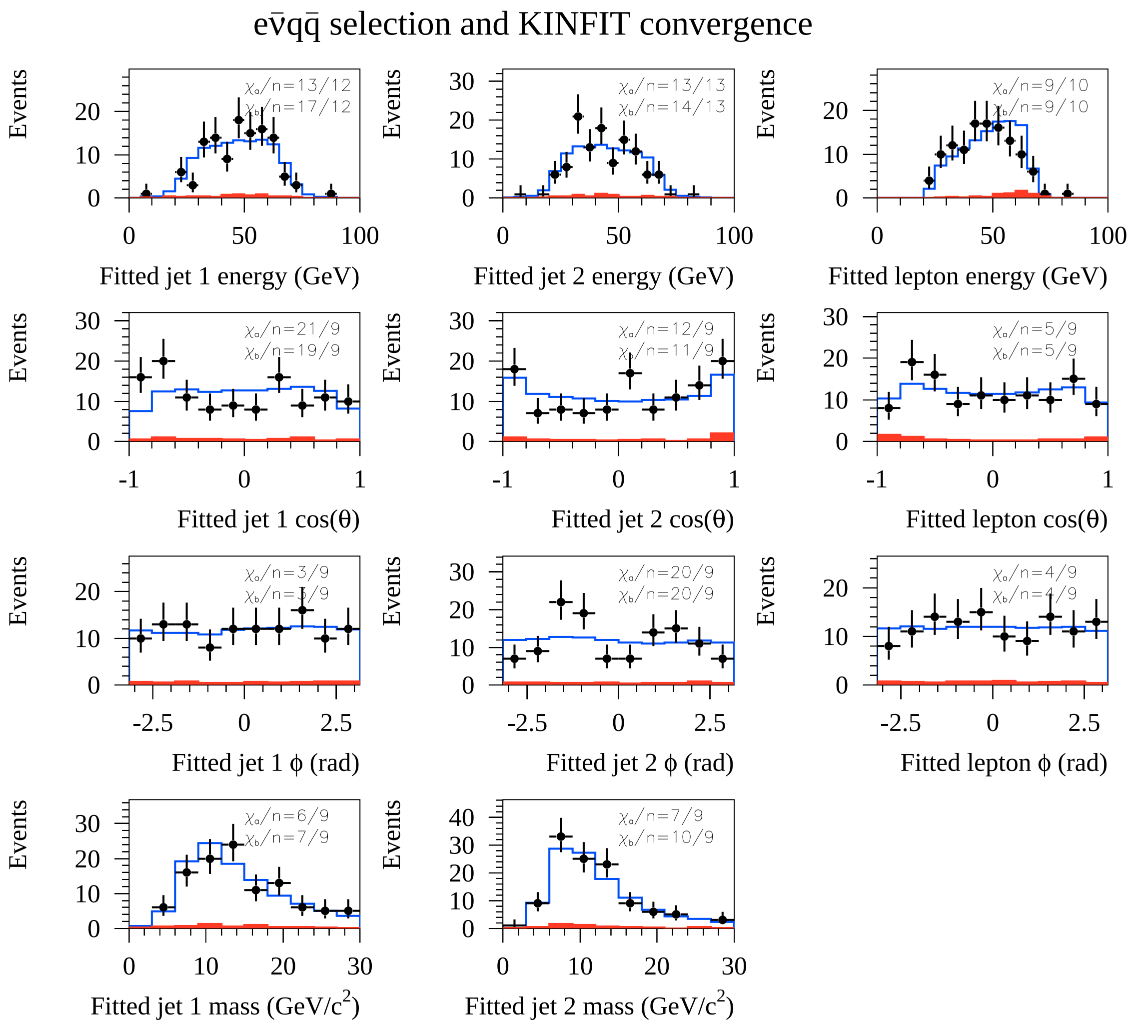

Figure 4.29: The fitted energy, polar angle, azimuthal angle and mass for the jets and the electron in the $e\bar{\nu}q\bar{q}$ channel.

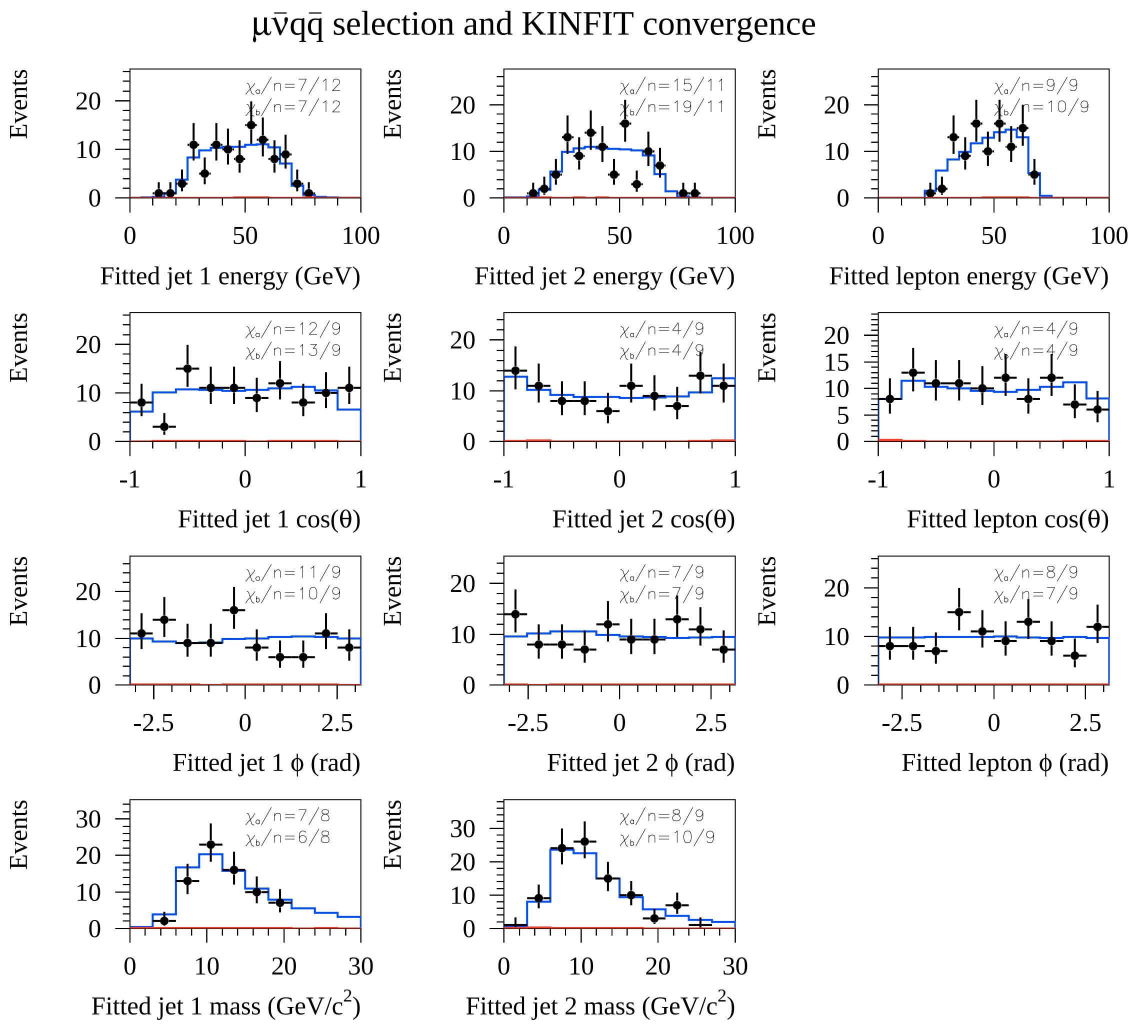

Figure 4.30: The fitted energy, mass, polar angle and azimuthal angle for the jets and the muon in the $\mu\bar{\nu}q\bar{q}$ channel.

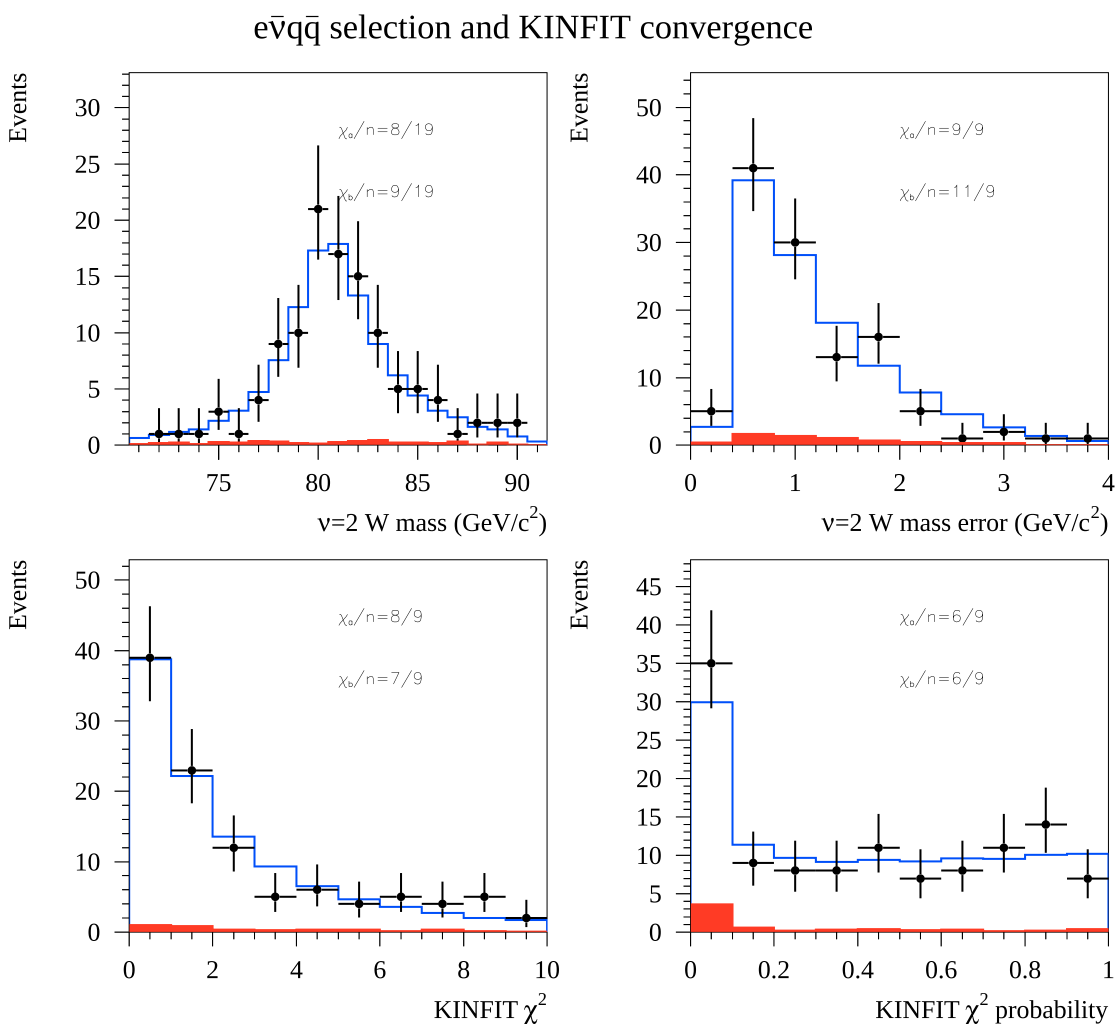

Figure 4.31: The fitted invariant mass, event-by-event error, χ^2 and χ^2 probability distributions after a kinematic fit with ν=2 in the $e\bar{\nu}q\bar{q}$ channel. A W mass of 80.35 GeV/c^2 is assumed in the simulation.

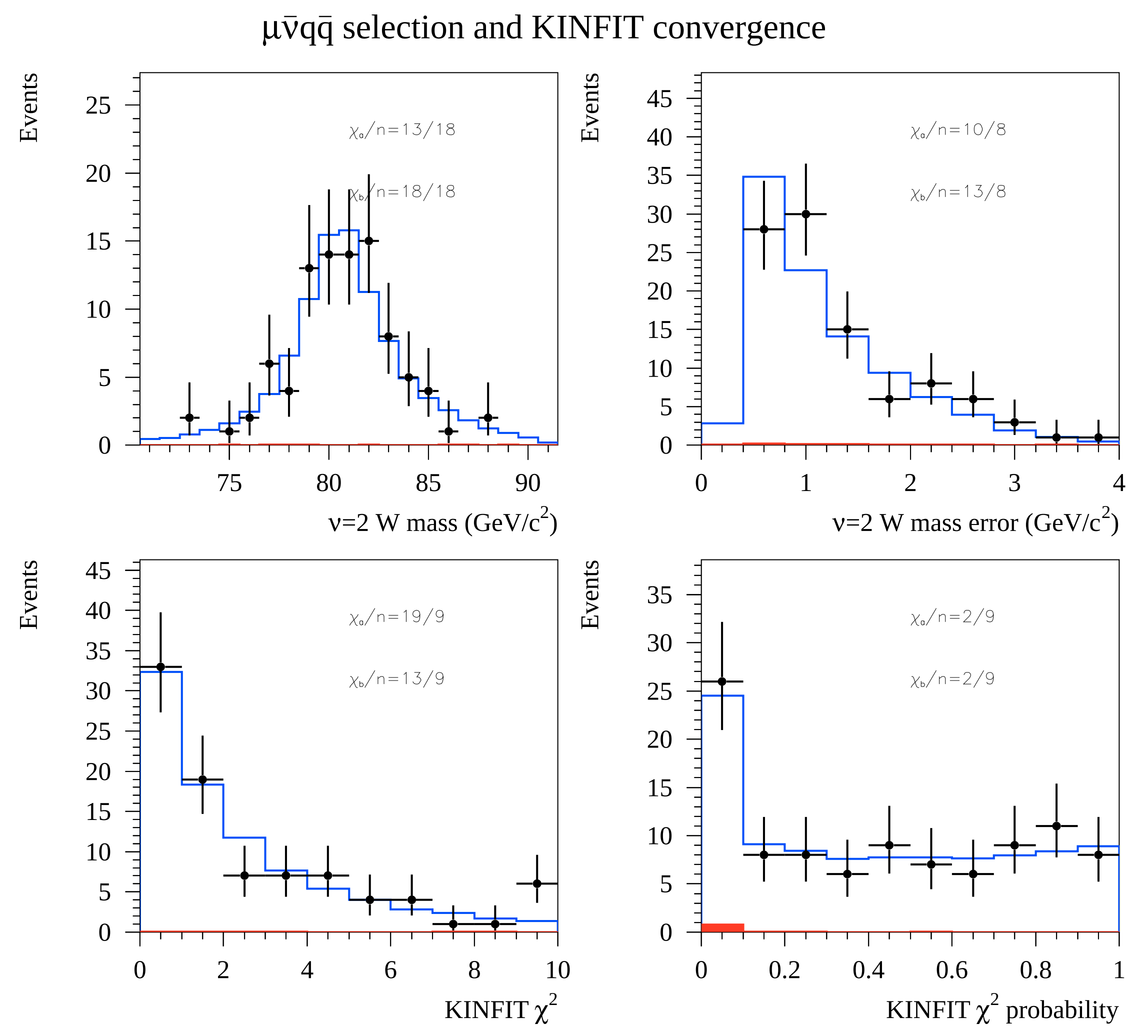

Figure 4.32: The fitted invariant mass, event-by-event error, χ^2 and χ^2 probability distributions after a kinematic fit with ν=2 in the $\mu\bar{\nu}q\bar{q}$ channel. A W mass of 80.35 GeV/c^2 is assumed in the simulation.

4.2.6 Summary.

A new kinematic fit package is adapted to the semileptonic channel, with the advantages that the undetected neutrino is treated correctly and that the parameterisation of the expected bias and expected resolution for the fit variables is in terms of the fitted energy and polar angle rather than the measured energy and polar angle. The latter technique can lead to serious biases as discussed in 4.1. The fit strategy is to impose all the constraints and then find the set of fitted four-vectors that is closest (in the least squares sense) to the measured set of four-vectors.

The initial convergence rate of the fit was effectively 0%, due to high correlations induced among the fit variables by the well-measured lepton. These correlations are eliminated by using the lepton momentum explicitly as a fit variable and the convergence rate jumps to 78%. The fit does not converge successfully if the starting point is too far from the solution as then it is difficult to impose all the constraints at once. Therefore, several strategies are used to improve the starting point. An increase of 6% is achieved by improving the event reconstruction. The implementation of the energy loss correction for jets close to the beam axis recovers another 4%, as does the prior use of an analytical fit with the constraints of energy and momentum conservation and zero neutrino mass. This gives a final convergence rate of 92%, where this number represents the events that satisfy the mathematical definition of convergence, *ie* that have a positive-definite covariance matrix at the minimum. The remaining 8% is due to problems that occur as the fit iterates towards a solution. One of the fit variables, the angle α, makes the fit very sensitive to events where the leptonic W and the lepton are nearly parallel or anti-parallel.

The KINFIT χ^2 distributions agree well with the true χ^2 for χ^2 values below 10. A peak at low values of the probability to obtain a worse kinematic fit result is observed, which is due to events that are incompatible with the assumed error parameterisation or the hypotheses of WW kinematics and no ISR. These badly-fitted events are removed by requiring that the probability to obtain a worse kinematic fit result should be larger than 0.02.

In the absence of ISR, there is no bias on the W mass from the fit and the pull distribution is ideal, indicating that the fitted event-by-event errors and the expected bias and expected error parameterisations are correct. The resolution on the average W mass from a kinematic fit with two degrees of freedom is 1.6 GeV/c^2.

After the requirements that the fit converges successfully and that the χ^2 probability is larger than 0.02, the overall efficiency of a kinematic fit with two degrees of freedom is 83%. The efficiencies of the convergence and probability cuts compare well between data and simulation. Detailed comparisons of the distributions of the fitted variables reveal no significant discrepancies.

Chapter 5

Determination of the W boson mass.

This chapter describes the extraction of the W boson mass from the reconstructed invariant mass distributions of the selected events in the $\sqrt{s}$ = 172 GeV and $\sqrt{s}$ = 183 GeV data samples.

5.1 Mass fit technique.

The mass fit technique compares the data invariant mass distribution directly with that predicted by simulation for various W mass values [93, 102]. The W mass value that gives the best fit to the data distribution is then the result for the W mass. This approach has the advantage that the best description (*ie* the simulation) of all the effects that distort the invariant mass distribution is used. The caveat to this is that the effects must be accurately simulated.

In principle, many large Monte Carlo samples could be generated at many different W mass values. However, this is unfeasible in practice due to the large amount of computation time required for a complete simulation of each interaction and the detector response. A solution to this problem is to generate a large Monte Carlo sample at one reference W mass, M_W^{ref}. The ratio of the squared matrix elements, for the process $e^+e^-\rightarrow W^+W^-\rightarrow f_1\bar{f}_2f_3\bar{f}_4$, is used to reweight each event in the sample to a new W mass, M_W:

$$w_i(M_W, \Gamma_W) = \frac{\mid \mathcal{M}(M_W, \Gamma_W, p_i^1, p_i^2, p_i^3, p_i^4) \mid^2}{\mid \mathcal{M}(M_W^{ref}, \Gamma_W^{ref}, p_i^1, p_i^2, p_i^3, p_i^4) \mid^2} \tag{5.1}$$

where p_i^j denotes the four-momentum (before the simulation of the detector response) of the outgoing fermion j in event i. Note that any FSR radiation produced by PHOTOS is recombined with the lepton four-momentum in order to define the lepton four-momentum that enters the matrix element. This is an event weight and can therefore be applied to any simulated distribution. The matrix element $\mathcal{M}$ is calculated for the CC03 diagrams, which are the lowest order diagrams for WW pair production [103]. The W width is assumed to vary with the W mass according to the Standard Model relation:

$$\begin{aligned} \Gamma_W &= 3\Gamma_\ell + \Gamma_h \\ \Gamma_\ell &= \tfrac{G_F M_W^3}{6\sqrt{2}\pi} \\ \Gamma_h &= 6\Gamma_\ell(1 + \tfrac{\alpha_s}{\pi}) \end{aligned} \tag{5.2}$$

Figure 5.1 compares the reconstructed invariant mass distribution from the sample generated with $M_W^{ref} = 80.25$ GeV/c^2 and reweighted to $M_W = 81.25$ GeV/c^2, with that from the sample generated with $M_W = 81.25$ GeV/c^2. These two distributions agree well and are very different from the unweighted distribution.

Distributions of the weights are shown in Figure 5.2 for the reference Monte Carlo sample upon reweighting to several different W masses. The weights differ increasingly from unity as the difference between the new W mass and the reference W mass increases. This implies a fractional loss in statistical power of:

$$\frac{n_{eff}}{n} = \frac{1}{n} \frac{\left(\sum_{i=1}^n w_i\right)^2}{\left(\sum_{i=1}^n w_i^2\right)} \tag{5.3}$$

where n is the number of events in the reference sample and n_{eff} is the effective number after reweighting to a new W mass value. As shown in Table 5.1, this loss is approximately 45% for a new W mass value that is 1 GeV/c^2 away from the reference W mass. Therefore, the reference Monte Carlo sample must be quite large in order to avoid detrimental statistical fluctuations from the reweighting process, which would degrade the information that is to be extracted from the data.

A binned, maximum likelihood method [76, 89] is used to determine the reweighted invariant mass distribution from simulation that gives the best fit to the data distribution.

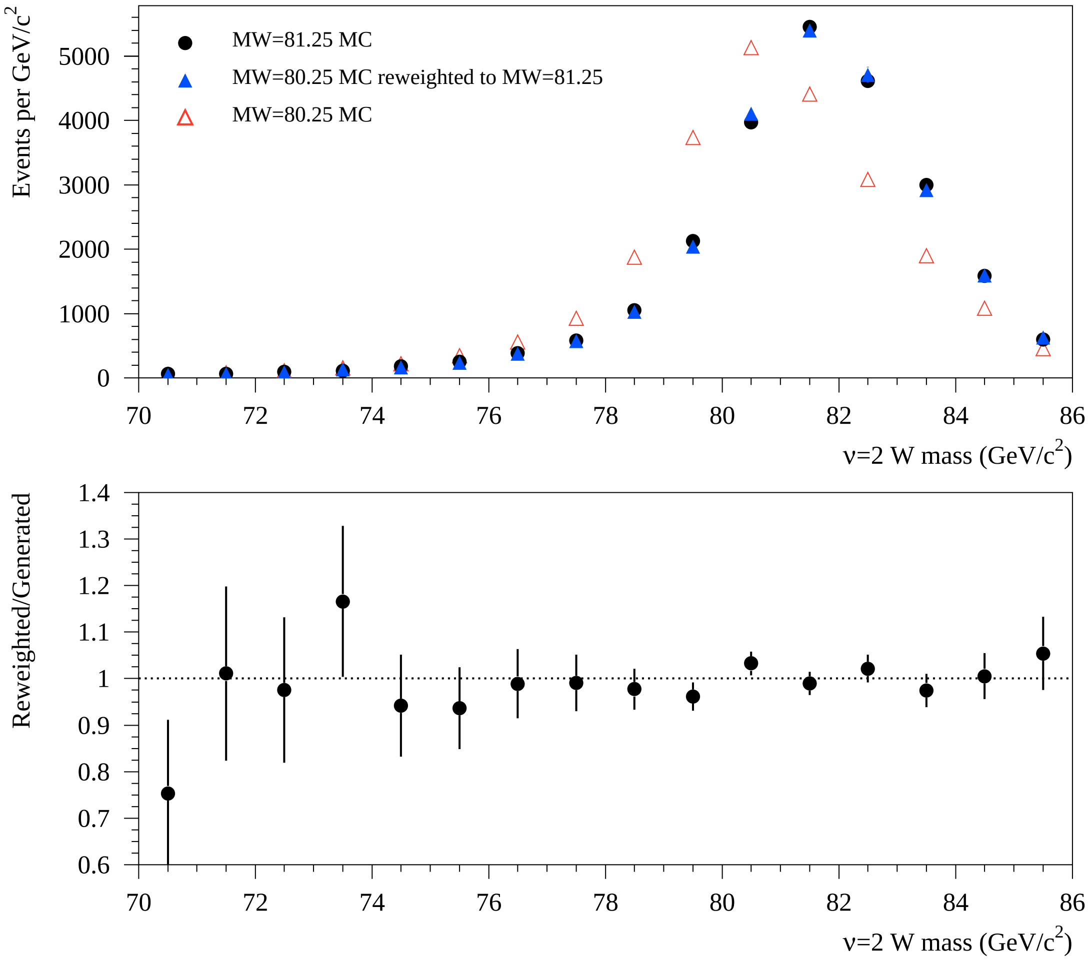

Figure 5.1: Comparison of reweighted and generated W mass distributions.

New W mass (GeV/c^2)	$\frac{n_{eff}}{n}$
79.25	0.457
79.75	0.798
80.00	0.943
80.25	1.000
80.50	0.943
80.75	0.796
81.25	0.449

Table 5.1: The effective number of events after reweighting the reference sample, which contains n events with $M_W^{ref} = 80.25$ GeV/c^2, to several new W mass values [93].

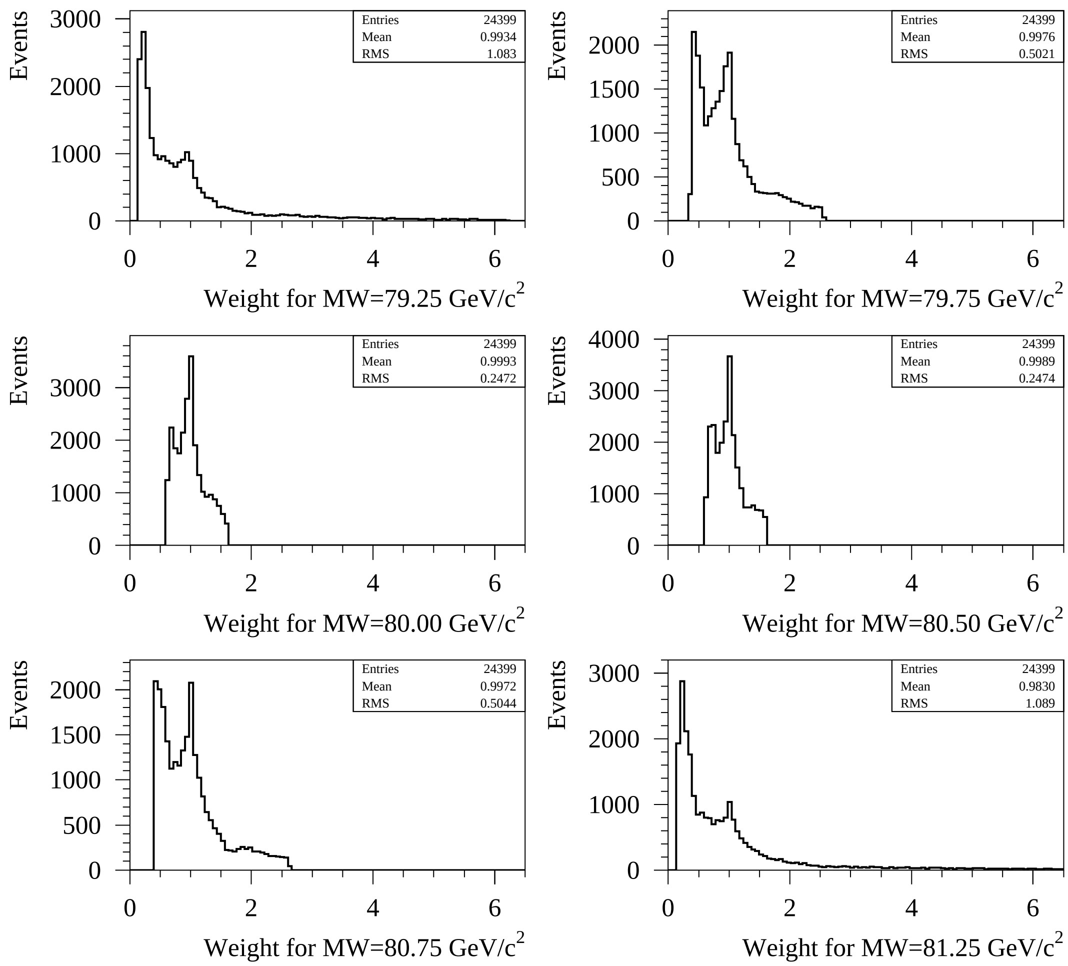

Figure 5.2: Event weight distributions when the Monte Carlo reference sample at $M_W^{ref} = 80.25$ GeV/c^2 is reweighted to $M_W = 79.25$, 79.75, 80.00, 80.50, 80.75 and 81.25 GeV/c^2 respectively.

The likelihood function, $\mathcal{L}$, is defined as the product of the probabilities y_i for all the events in the data sample:

$$\mathcal{L}(M_W) = \prod_{i=1}^{N_{evt}} y_i(m_i \mid M_W) \tag{5.4}$$

So for any specific value of M_W, $\mathcal{L}$ is the joint probability density for observing the particular set of reconstructed invariant masses m_i seen in the data. $\mathcal{L}$ is maximised as a function of M_W in order to find the value of M_W that best describes the data sample.

The probability density function $y_i(m_i \mid M_W)$ is computed from the simulation as a function of the reconstructed invariant mass m and the mass M_W to which the simulation is reweighted:

$$y_i(m_i \mid M_W) = \frac{\rho_s(M_W)N_s^i(M_W) + \rho_b(M_W)N_b^i}{\Delta m_i N_{TOT}} \tag{5.5}$$

$\rho_s(M_W)$ is the purity of the selection[1] and so $\rho_b(M_W) = 1 - \rho_s(M_W)$ is the background fraction. The purities depend on the W mass because the total WW cross section, σ_s, is a function of the W mass. Denoting the efficiency of the selection for WW events as ϵ_s and the efficiency and cross section for non-WW background processes as ϵ_b and σ_b respectively, then:

$$\rho_s(M_W) = \frac{\epsilon_s \sigma_s(M_W)}{\epsilon_s \sigma_s(M_W) + \epsilon_b \sigma_b} \tag{5.6}$$

The dependence of the WW cross section on the W mass is parameterised using GENTLE [104] as:

$$\sigma_s(M_W) = \sigma_s(M_W^{ref}) \left[1 - a(M_W - 80.25) - b(M_W - 80.25)^2\right] \tag{5.7}$$

where a=0.06341 and b=0.008033.

The weighted number of simulated WW events in the ith reconstructed mass bin is given by:

$$N_s^i(M_W) = \sum_{j=1}^{N_s^j} w_j(M_W) \tag{5.8}$$

N_b^i is the total number of non-WW background events found in the same range. The background does not depend on the W mass, so the background shape and absolute normalisation are constant throughout the likelihood fit. N_{TOT} is the weighted sum of all the simulated events:

$$N_{TOT} = \sum_{i=1}^{N_{bin}} \left(\rho_s(M_W) \sum_{j=1}^{N_s^j} w_j(M_W) + \rho_b(M_W) N_b^i \right) \tag{5.9}$$

Δm_i is the size of the ith reconstructed invariant mass bin. The individual bins are the same size for the simulation and for the data. The bin widths are computed from the amount of reference Monte Carlo available so that the statistical precision remains approximately constant over the range of the reconstructed invariant mass distribution.

[1] All selected WW events must be reweighted and are hence treated as signal.

The bins are narrower near the peak ($\sim$ 150 MeV/c^2) and broader in the tails ($\sim$ 800 MeV/c^2). The mass range used in the fit is from the kinematic limit of 86 GeV/c^2 down to 74 GeV/c^2, since the information contained in the reduced statistics below this is negligible. The final selected cross sections, the efficiency, the purity and the expected and observed number of events are shown in Table 5.2.

Process	σ_{sel} (pb)	
	$e\bar{\nu}q\bar{q}$ channel	$\mu\bar{\nu}q\bar{q}$ channel
$e^+e^-\to W^+W^-\to e\bar{\nu}q\bar{q}$	1.478	0.001
$e^+e^-\to W^+W^-\to \mu\bar{\nu}q\bar{q}$	0.001	1.569
$e^+e^-\to W^+W^-\to \tau\bar{\nu}q\bar{q}$	0.042	0.043
$e^+e^-\to W^+W^-\to q\bar{q}q\bar{q}$	0.000	0.000
$e^+e^-\to W^+W^-\to \ell\nu\ell\nu$	0.000	0.000
$e^+e^-\to Z/\gamma\to q\bar{q}(\gamma)$	0.013	0.006
$e^+e^-\to Z/\gamma\to \tau^+\tau^-(\gamma)$	0.007	0.000
$e^+e^-\to ZZ$	0.005	0.008
$e^+e^-\to Ze^+e^-$	0.000	0.000
$e^+e^-\to We\nu_e$	0.004	0.000
Total background	0.072	0.058
Efficiency (%)	79.6	85.7
Purity (%)	95.3	96.3
Predicted events	16.5	17.4
Observed events	14	20

Table 5.2: Expected cross sections after requiring the reconstructed invariant mass to lie in the range 74 to 86 GeV/c^2.

Computationally, it is more convenient to use the logarithm of the likelihood function:

$$\ell(M_W) = -2\log\mathcal{L}(M_W) = -2\sum_{i=1}^{N_{evt}} \log y_i(m_i \mid M_W) \qquad (5.10)$$

in order to avoid rounding errors from multiplying small values of y. The MIGRAD program from MINUIT [95] is used to minimise the log-likelihood as a function of the W mass.

The need to calculate the CC03 matrix element ratio for each event at every chosen value of M_W slows the minimisation down considerably. However, this lost speed can be recovered by building templates of the reconstructed mass distribution from reweighted WW events at many W mass values in advance [105]. At $\sqrt{s} = 183$ GeV, the templates are calculated at W mass intervals of 10 MeV/c^2 from 76.00 to 84.00 GeV/c^2. A linear interpolation between neighbouring templates allows the rapid calculation of the reweighted WW mass distribution for any W mass value. This trick is very useful for some of the consistency checks discussed in chapter 6.

The MINOS program from MINUIT is used to calculate the error on the fitted W mass, M_W^{fit}. Any non-parabolic behaviour of the log-likelihood function is taken into account by MINOS, which finds the change in M_W required to increase ℓ by 1.0 from the minimum value, *ie*:

$$\ell(M_W^{fit} - \sigma_{neg}) = \ell(M_W^{fit} + \sigma_{pos}) = \ell(M_W^{fit}) + 1.0 \tag{5.11}$$

The range $M_W^{fit} - \sigma_{neg} \leq M_W^{fit} \leq M_W^{fit} + \sigma_{pos}$ has the property that the probability that it contains the true value of the W mass is 68%.

5.2 W boson mass result at $\sqrt{s} = 172$ GeV.

The $e\bar{\nu}q\bar{q}$ and $\mu\bar{\nu}q\bar{q}$ events are fitted simultaneously at $\sqrt{s} = 172$ GeV. The reconstructed invariant mass distribution for the selected events in the $\sqrt{s} =$ 172 GeV data sample is shown in Figure 5.3, where the reference Monte Carlo sample is reweighted to the fit result of:

$$M_W = 80.54 \pm 0.37 \text{ GeV/c}^2$$

The error is the statistical error from a single fit to the $\sqrt{s} = 172$ GeV data sample. The parabolic shape of the log-likelihood function near the minimum is shown in Figure 5.4.

Note that a positive shift of 27 MeV/c^2 is applied here to the W mass result so that the definitions of the W and Z boson masses are consistent. The inconsistency arises from the fact that a Breit-Wigner propagator with a fixed width is used to simulate the $e^+e^- \rightarrow W^+W^- \rightarrow f_1\bar{f}_2f_3\bar{f}_4$ process, in order to conserve gauge invariance and to avoid dramatically wrong cross sections in certain regions of phase space [29]. However, when the mass of the Z^0 boson was measured at LEP1, a mass definition corresponding to a propagator with an energy dependent width was used.

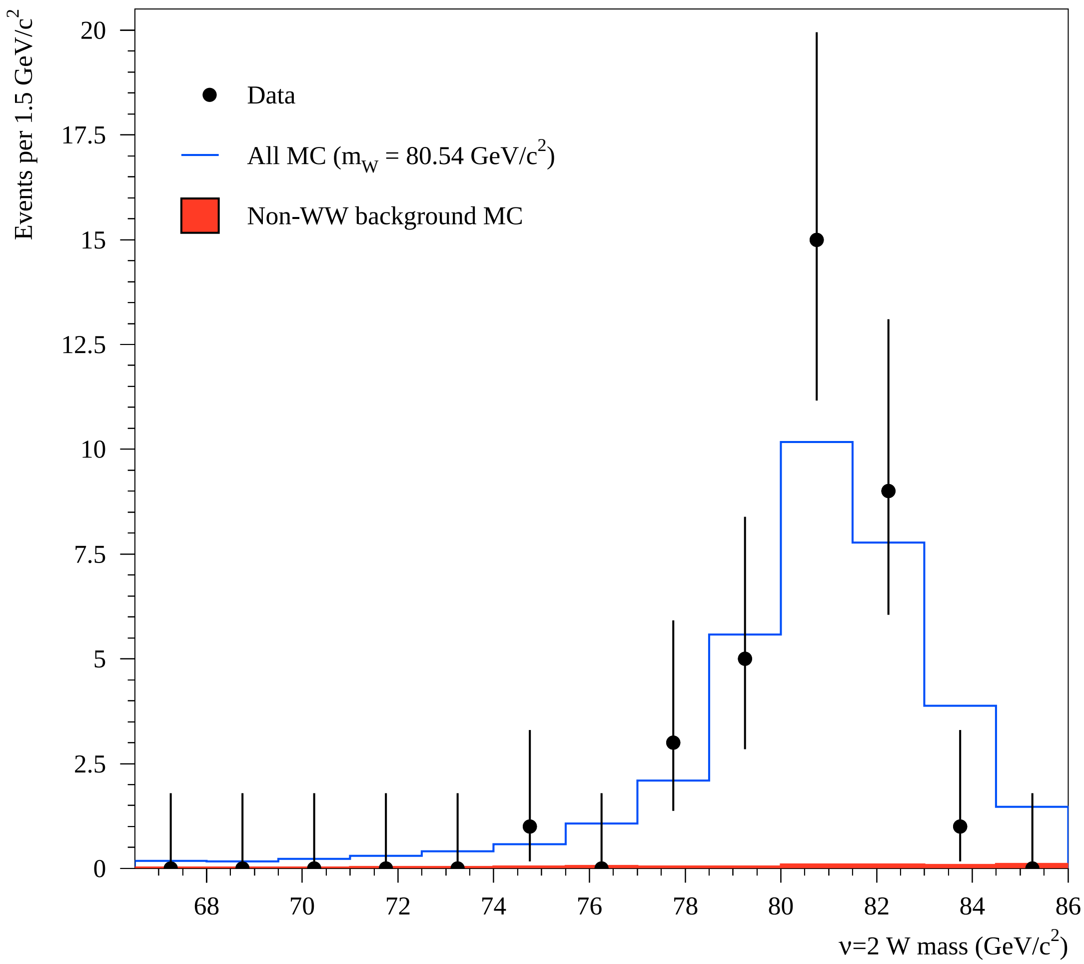

Figure 5.3: The reconstructed invariant mass distribution for the $\sqrt{s}$ = 172 GeV data and simulation [93].

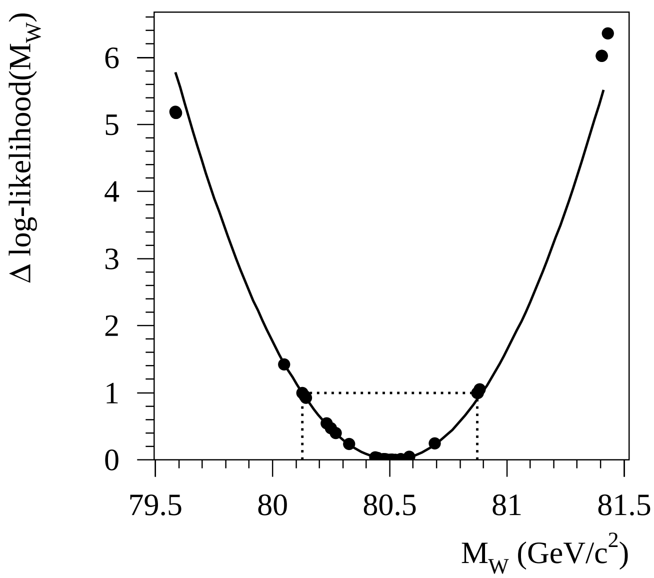

Figure 5.4: The shape of the minimum of the log-likelihood function for the $\sqrt{s} = 172$ GeV data.

5.3 Modifications to the mass fit technique at $\sqrt{s} = 183$ GeV.

The technique to extract the W mass from the reconstructed invariant mass distribution of the $\sqrt{s} = 183$ GeV data is the same as that used for the $\sqrt{s} = 172$ GeV measurement, except for three changes:

- The reconstructed mass range used to fit the W mass is expanded to 74.0-91.5 GeV/c^2, *ie* up to the kinematic limit at $\sqrt{s} = 183$ GeV. The final selected cross sections, the efficiency, the purity and the expected and observed number of events are shown in Table 5.3.

- A constant bin width of 0.5 GeV/c^2 is used instead of a variable bin width. The reason is illustrated in Figure 5.5, which shows the reconstructed invariant mass distributions from simulation with assumed W masses of 79.85 GeV/c^{2}and 80.85 GeV/c^2. The minimum number of events per bin is marked according to the variable binning procedure used at $\sqrt{s} = 172$ GeV, scaled to a reference sample of 50,000 events. This produces relatively broad bins in the peak region for the M_W=79.85 GeV/c^2 simulation and relatively narrow bins for the M_W=80.85 GeV/c^2 simulation. The effect is to emphasise undesirable statistical fluctuations in the

M_W=80.85 GeV/c^2 simulation and thus reduce the reproducibility of the fit result upon replacing the reference sample with one simulated with a different value for the W mass.

Process	σ_{sel} (pb)	
	$e\bar{\nu}q\bar{q}$ channel	$\mu\bar{\nu}q\bar{q}$ channel
$e^+e^-\rightarrow W^+W^-\rightarrow e\bar{\nu}q\bar{q}$	1.506	0.001
$e^+e^-\rightarrow W^+W^-\rightarrow \mu\bar{\nu}q\bar{q}$	0.002	1.549
$e^+e^-\rightarrow W^+W^-\rightarrow \tau\bar{\nu}q\bar{q}$	0.013	0.013
$e^+e^-\rightarrow W^+W^-\rightarrow q\bar{q}q\bar{q}$	0.000	0.000
$e^+e^-\rightarrow W^+W^-\rightarrow \ell\nu\ell\nu$	0.000	0.000
$e^+e^-\rightarrow Z/\gamma\rightarrow q\bar{q}(\gamma)$	0.018	0.001
$e^+e^-\rightarrow Z/\gamma\rightarrow \tau^+\tau^-(\gamma)$	0.001	0.000
$e^+e^-\rightarrow ZZ$	0.003	0.003
$e^+e^-\rightarrow Ze^+e^-$	0.000	0.000
$e^+e^-\rightarrow We\nu_e$	0.005	0.000
Total background	0.042	0.018
Efficiency (%)	65.6	67.7
Purity (%)	97.3	98.9
Predicted events	87.9	89.0
Observed events	93	78

Table 5.3: Expected cross sections after requiring the reconstructed invariant mass to lie in the range 74.0 to 91.5 GeV/c^2.

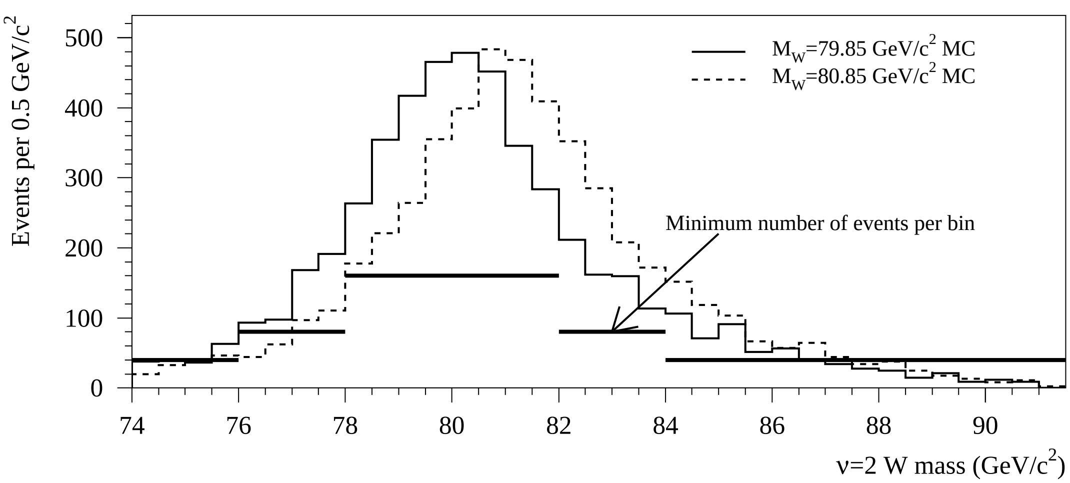

Figure 5.5: The reconstructed invariant mass distributions, after a kinematic fit with $\nu = 2$, from simulation with assumed W mass values of 79.85 GeV/c^{2}and 80.85 GeV/c^2.

- The dependence of the WW cross section at $\sqrt{s} = 183$ GeV on the W mass is parameterised from GENTLE as described in Equation 5.7 with a=0.007067 and b=0.002503.

5.4 W boson mass results at $\sqrt{s} = 183$ GeV.

The reconstructed invariant mass distributions for the selected events in the $\sqrt{s} =$ 183 GeV data sample are shown in Figures 5.6 and 5.7 for the $e\bar{\nu}q\bar{q}$ and $\mu\bar{\nu}q\bar{q}$ channels respectively, where the reference Monte Carlo sample is reweighted to the fit results of:

$$M_W^{e\bar{\nu}q\bar{q}} = 80.410 \pm 0.272 \text{ GeV/c}^2$$
$$M_W^{\mu\bar{\nu}q\bar{q}} = 80.364 \pm 0.289 \text{ GeV/c}^2$$

and the statistical errors are from a single fit to the data samples. The parabolic shape of the log-likelihood functions near the minimum are shown in Figure 5.8. Again, note that a positive shift of 27 MeV/c^2 is applied here to make the definition of the W and Z boson masses consistent.

Due to a new data calibration for the GAMPEX program, which is used to find FSR photons, the data reconstructed masses changed slightly and one additional event was selected as an $e\bar{\nu}q\bar{q}$ candidate. The final fit results for the W mass at $\sqrt{s} = 183$ GeV are [106]:

$$M_W^{e\bar{\nu}q\bar{q}} = 80.428 \pm 0.269 \text{ GeV/c}^2$$
$$M_W^{\mu\bar{\nu}q\bar{q}} = 80.370 \pm 0.287 \text{ GeV/c}^2$$

The combination of the W mass results from the $e\bar{\nu}q\bar{q}$ and $\mu\bar{\nu}q\bar{q}$ channels at $\sqrt{s} = 183$ GeV is:

$$M_W = 80.401 \pm 0.196 \text{ GeV/c}^2$$

which is more precise than the combination of all the ALEPH W mass measurements at $\sqrt{s} = 172$ GeV and at the threshold for WW pair production.

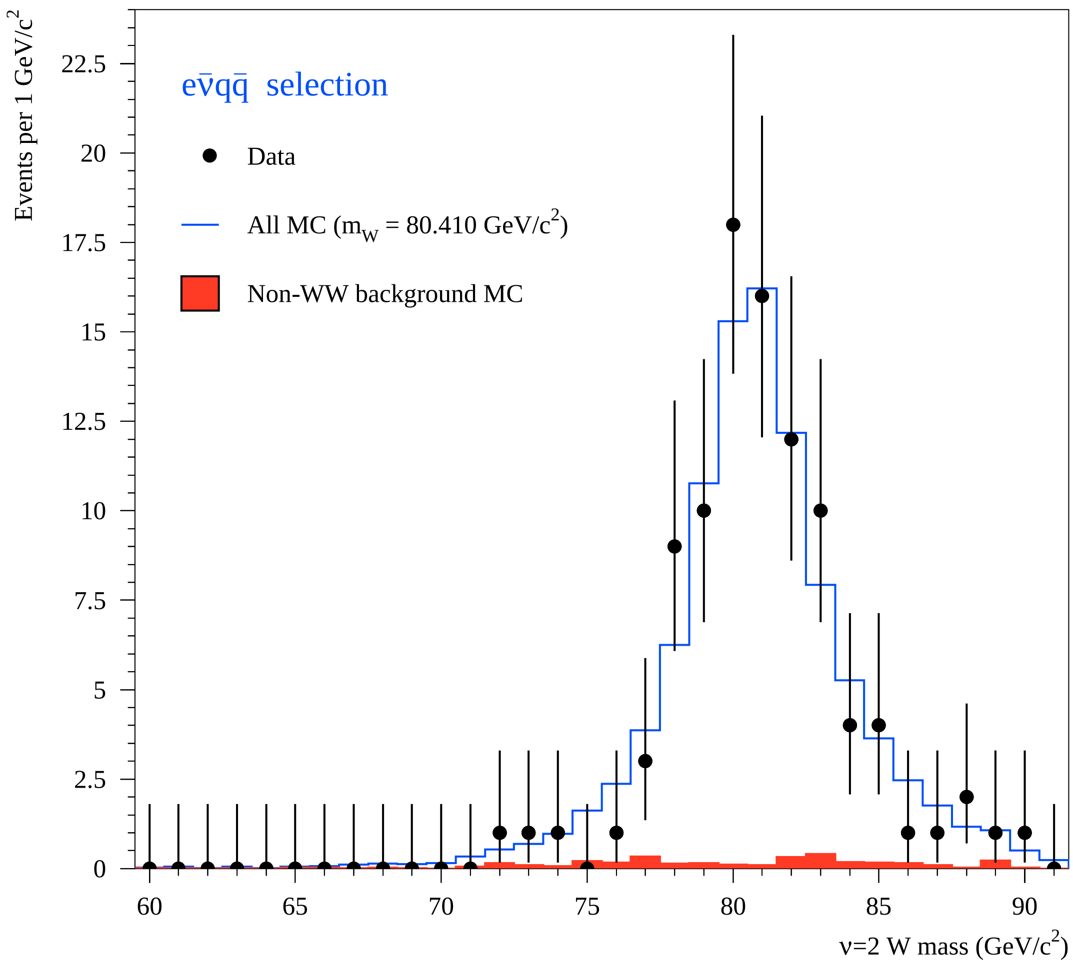

Figure 5.6: The reconstructed invariant mass distributions from the $\sqrt{s}$ = 183 GeV data and simulation for the $e\bar{\nu}q\bar{q}$ channel.

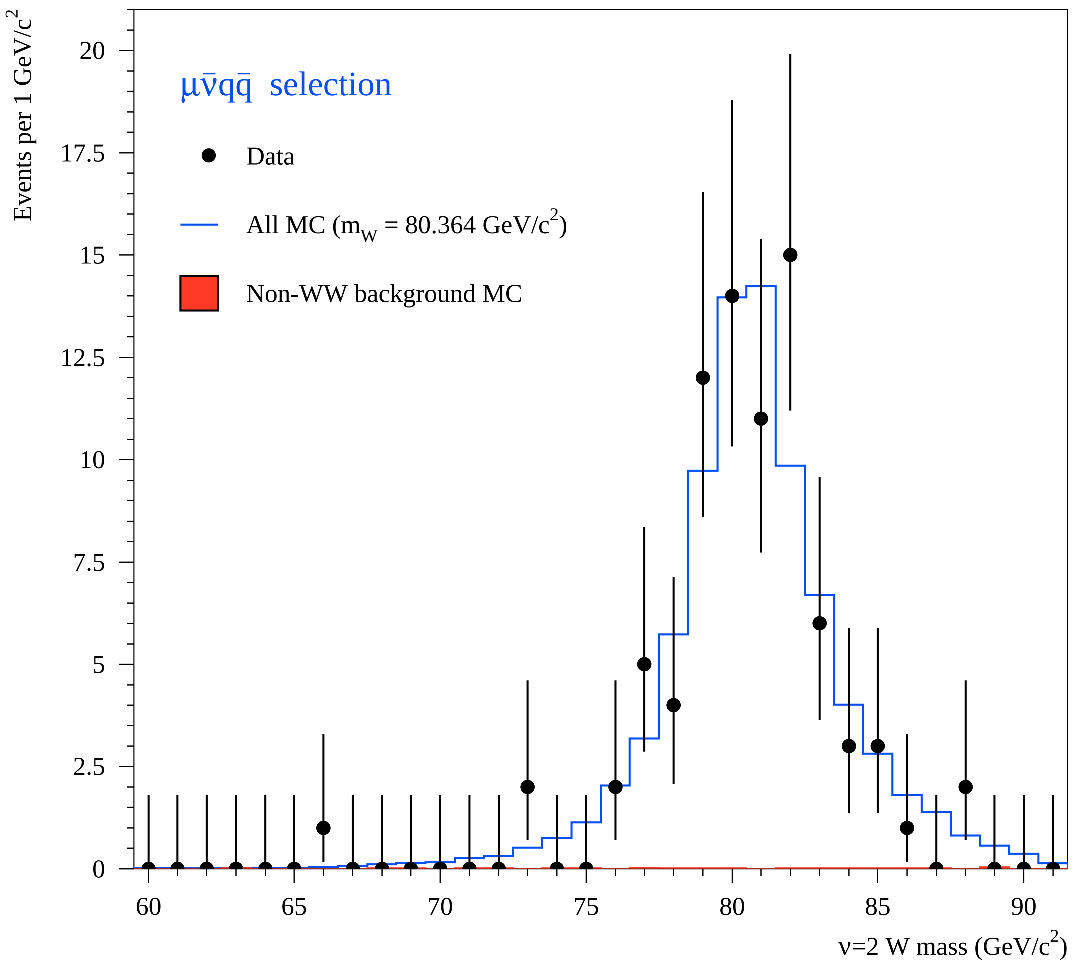

Figure 5.7: The reconstructed invariant mass distributions from the $\sqrt{s} = 183$ GeV data and simulation for the $\mu\bar{\nu}q\bar{q}$ channel.

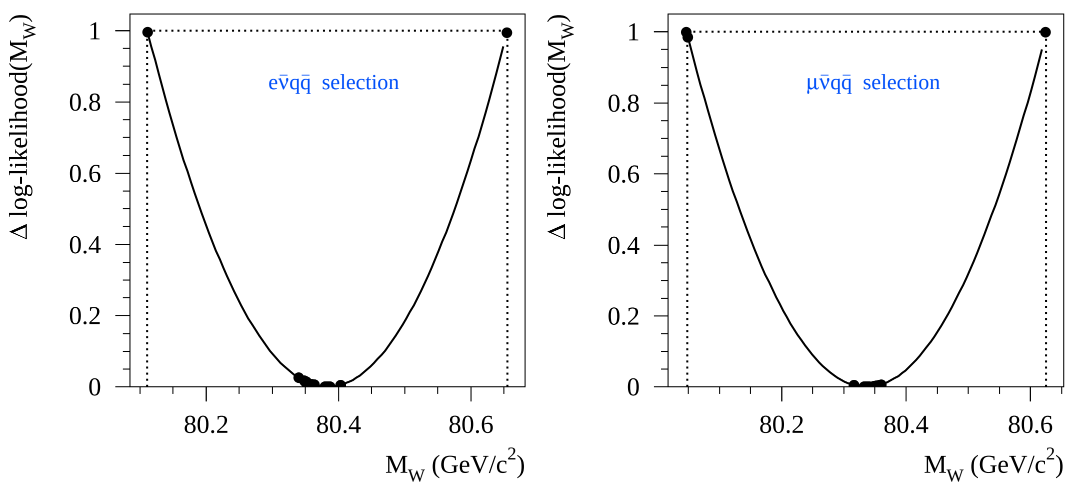

Figure 5.8: The shape of the minima of the log-likelihood functions from the $\sqrt{s}$ = 183 GeV data for the $e\bar{\nu}q\bar{q}$ and $\mu\bar{\nu}q\bar{q}$ channels.

Chapter 6

Reproducibility and stability checks.

It is essential to test that the chosen fitting procedure gives results that are reproducible and stable. These criteria are checked in this chapter for the Monte Carlo interpolation with reweighting technique.

6.1 Reproducibility checks at $\sqrt{s} = 172$ GeV.

Any fitting procedure must fulfil the following two requirements when applied to an ensemble of simulated experiments of the same sample size:

- The mean fitted mass value must be consistent with the W mass assumed in the simulation.
- The RMS spread of the fitted masses must be consistent with the mean statistical accuracy of the fit.

These criteria are checked as a function of the assumed W mass in the simulation. Seven ensembles of simulated events with W mass values of 79.25, 79.75, 80.00, 80.25, 80.50, 80.75 and 81.25 GeV/c^2 are used. A number of samples, N_s, each containing the number of events expected in the data sample, are fitted for each W mass value.

Table 6.1 shows that the mean fitted mass, M_W^{fit}, is consistent with the W mass assumed in the simulation, M_W^{gen}, over the range studied. The relationship is parameterised as shown in Figure 6.1:

$$M_W^{fit} = (80.25 \pm 0.03) + (0.945 \pm 0.044) \times (M_W^{gen} - 80.25) \tag{6.1}$$

This is compatible with the ideal case of a linear relation with a gradient of one and an offset of zero.

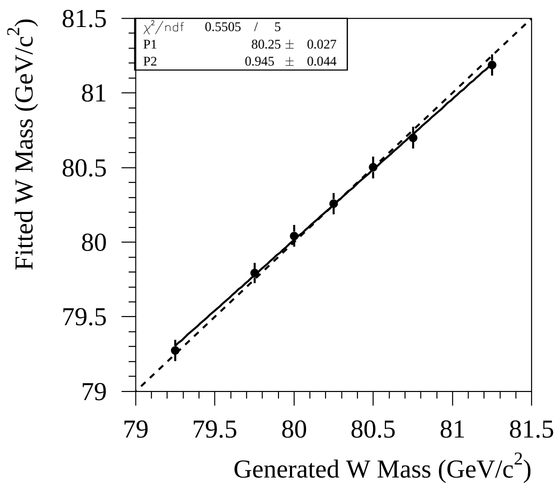

Figure 6.1: The relationship between the fitted W mass and the W mass assumed in the simulation [93].

Table 6.1 also shows that the RMS spread on the fitted mass is compatible with the mean fit error. The reliability of the fit error is further confirmed by the fact that the width of the pull distribution, where the pull is defined as $\frac{(M_W^{fit} - M_W^{gen})}{\sigma_{fit}}$, is consistent with unity as a function of the fit error [107].

M_W^{gen} (GeV/c^2)	N_s	Mean M_W^{fit} (GeV/c^2)	RMS M_W^{fit} (GeV/c^2)	Mean σ_{fit} (GeV/c^2)	RMS σ_{fit} (GeV/c^2)
79.25	64	79.338 ± 0.067	0.537	0.483 ± 0.009	0.071
79.75	141	79.843 ± 0.037	0.439	0.457 ± 0.005	0.065
80.00	68	80.068 ± 0.049	0.405	0.464 ± 0.007	0.058
80.25	503	80.237 ± 0.022	0.488	0.470 ± 0.003	0.074
80.50	71	80.490 ± 0.050	0.424	0.476 ± 0.009	0.073
80.75	137	80.723 ± 0.041	0.480	0.457 ± 0.006	0.070
81.25	281	81.209 ± 0.027	0.459	0.455 ± 0.004	0.073

Table 6.1: Results of the fits to many samples of simulated events. The errors on the mean values are also the errors on the RMS values [93].

Table 6.1 shows that the statistical fit error has a large uncertainty due to the small size of the data sample. Since the uncertainty on the mean fit error is considerably smaller than the uncertainty on the RMS of the fitted mass, the mean fit error of 0.47 GeV/c^2 is taken as the expected statistical error and is quoted as the statistical error on the W mass result from the $\sqrt{s} = 172$ GeV data.

6.2 Stability checks at $\sqrt{s} = 172$ GeV.

The stability of the fitted W mass from the data sample is checked with respect to variations in:

- The probability cuts used to identify semileptonic WW decays.
- The reconstructed mass range used in the fit.
- The bin size used to build the probability density function for the fit.

In addition to verifying the fit procedure, the first two checks also test the event modelling and the background simulation. In order to test the stability of the fit in more detail, a high statistics sample, containing approximately 1,500 selected WW events simulated with a W mass of 80.50 GeV/c^2, is also studied.

The electron and muon probability cuts are independently varied over the entire range. Figure 6.2 shows the fitted W mass for the data and the Monte Carlo samples as a function of the probability cut values. The fit result is clearly stable under these changes.

The reconstructed mass range in the fit has a lower bound of 74 GeV/c^2 and an upper bound, which is set by the kinematic limit, of 86 GeV/c^2. The lower bound is varied from 66 to 76 GeV/c^2 and Figure 6.3 illustrates that the fit result is stable.

The bin sizes used to build the probability density function for the fit are set such that each bin contains a minimum number of events. This minimum number varies over the reconstructed mass range, where m refers to the $\nu = 2$ mass of a single event:

$N_{min} \geq 200$ events for $m < 76$ and $m \geq 84$ GeV/c^2.

$N_{min} \geq 400$ events for $m \in [76, 78)$ and $m \in [82, 84)$ GeV/c^2.

$N_{min} \geq 800$ events for $m \in [78, 82)$ GeV/c^2.

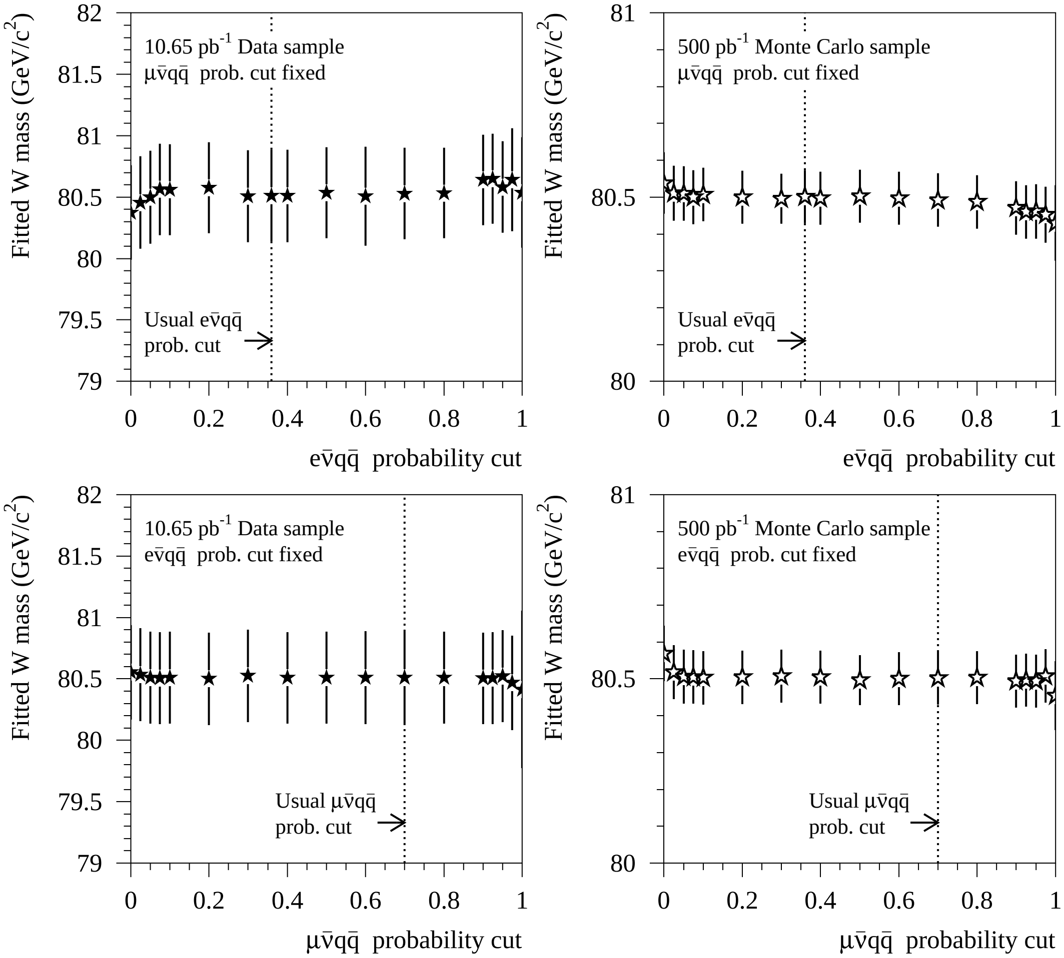

Figure 6.2: Stability of the fitted W mass as a function of the applied $e\bar{\nu}q\bar{q}$ and $\mu\bar{\nu}q\bar{q}$ probability cut for the data and the Monte Carlo samples. The uncertainties on the different points are highly correlated [93].

The above values for N_{min} are multiplied by factors of 0.5, 2.0 and 3.0 in order to check the stability of the fit. No significant variations are observed [93].

6.3 Reproducibility checks at $\sqrt{s} = 183$ GeV.

Several independent subsamples, which each contain the observed number of events in the data sample, are fitted from five ensembles of simulated events with W mass values of 79.85, 80.10, 80.35, 80.60 and 80.85 GeV/c^2. Note that the reference must be much larger than the total number of events in the fitted subsamples, otherwise statistical fluctuations in the reference sample will influence the mean of the fit results. The results for the $e\bar{\nu}q\bar{q}$ and $\mu\bar{\nu}q\bar{q}$ channels are shown in Tables 6.2 and 6.3 respectively.

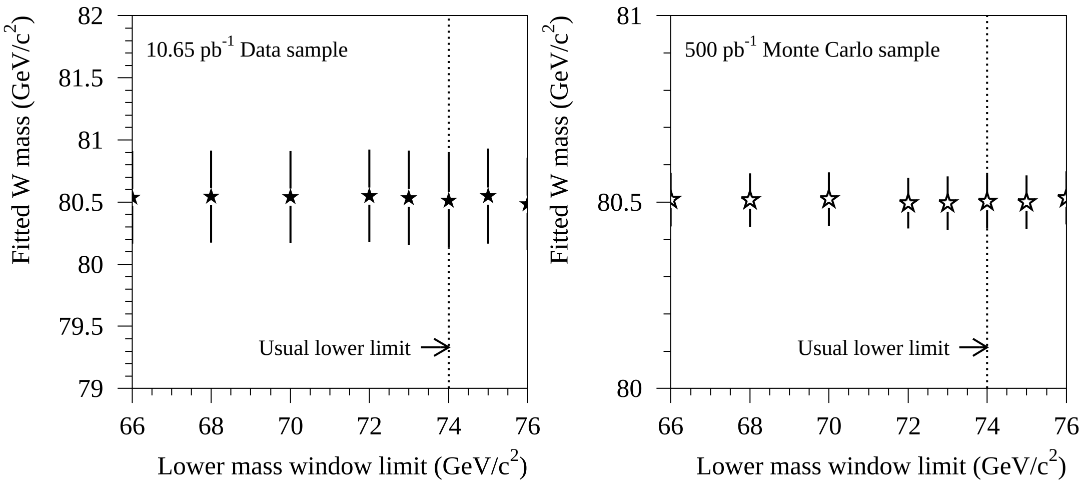

Figure 6.3: Stability of the fitted W mass for various lower mass window limits for the data and the Monte Carlo sample. The uncertainties on the different points are highly correlated [93].

M_W^{gen} (GeV/c^2)	N_s	Mean M_W^{fit} (GeV/c^2)	RMS M_W^{fit} (GeV/c^2)	Mean σ_{fit} (GeV/c^2)	RMS σ_{fit} (GeV/c^2)
79.85	25	79.810 ± 0.048	0.242	0.284 ± 0.004	0.019
80.10	25	80.198 ± 0.054	0.272	0.287 ± 0.004	0.016
80.35	25	80.350 ± 0.046	0.228	0.286 ± 0.004	0.019
80.60	25	80.698 ± 0.061	0.305	0.285 ± 0.005	0.023
80.85	25	80.822 ± 0.054	0.268	0.283 ± 0.004	0.021

Table 6.2: Results of the fits to many samples of simulated events in the $e\bar{\nu}q\bar{q}$ channel. The errors on the mean values are also the errors on the RMS values.

M_W^{gen} (GeV/c^2)	N_s	Mean M_W^{fit} (GeV/c^2)	RMS M_W^{fit} (GeV/c^2)	Mean σ_{fit} (GeV/c^2)	RMS σ_{fit} (GeV/c^2)
79.85	25	79.846 ± 0.072	0.358	0.291 ± 0.004	0.022
80.10	25	80.066 ± 0.065	0.326	0.290 ± 0.004	0.022
80.35	25	80.338 ± 0.058	0.289	0.291 ± 0.004	0.020
80.60	25	80.618 ± 0.056	0.278	0.287 ± 0.003	0.016
80.85	25	80.878 ± 0.053	0.265	0.298 ± 0.003	0.017

Table 6.3: Results of the fits to many samples of simulated events in the $\mu\bar{\nu}q\bar{q}$ channel. The errors on the mean values are also the errors on the RMS values.

The mean fitted W mass, M_W^{fit}, is consistent with the W mass assumed in the simulation, M_W^{gen}, over the range studied for both channels. The relationship is parameterised as shown in Figure 6.4:

$$e\bar{\nu}q\bar{q}: \quad M_W^{fit} = (80.368 \pm 0.023) + (1.014 \pm 0.066) \times (M_W^{gen} - 80.35) \tag{6.2}$$

$$\mu\bar{\nu}q\bar{q}: \quad M_W^{fit} = (80.349 \pm 0.027) + (1.052 \pm 0.078) \times (M_W^{gen} - 80.35) \tag{6.3}$$

which are both compatible with the ideal case of a linear relation with a gradient of one and a bias of zero from the reference mass of 80.35 GeV/c^2..

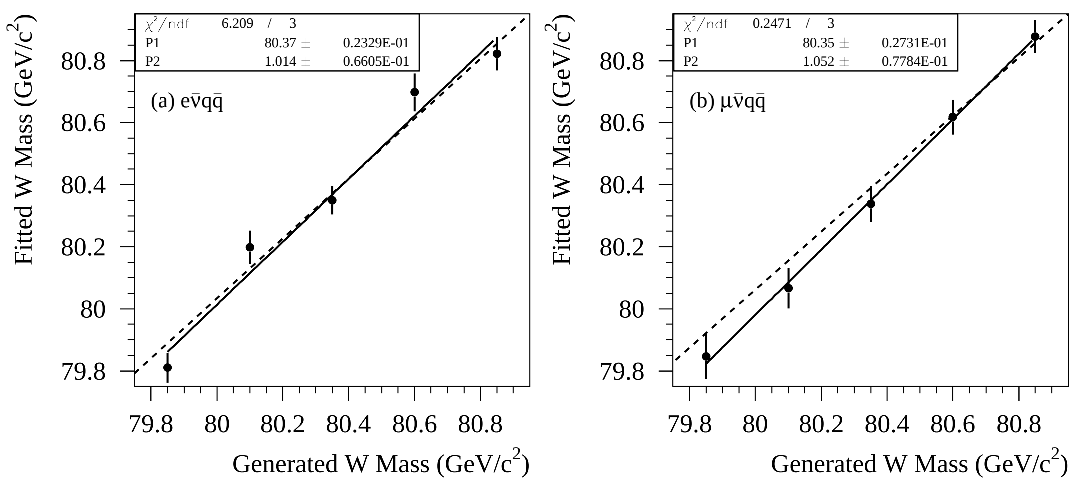

Figure 6.4: The relationship between the fitted W mass and the W mass assumed in the simulation for (a) $e\bar{\nu}q\bar{q}$ events and (b) $\mu\bar{\nu}q\bar{q}$ events.

The RMS spread on the fitted mass is also compatible with the mean fit error. The reliability of the fit error is confirmed by the fact that the width of the pull distribution, which is defined as $\frac{(M_W^{fit} - M_W^{gen})}{\sigma_{fit}}$, is consistent with unity as a function of the fit error. This is illustrated in Figure 6.5, where 3200 subsamples of the same size of the data have been randomly chosen from the sample with a W mass of 80.35 GeV/c^2. The agreement is good considering that the large number of samples means that the results are sensitive to statistical fluctuations in the reference sample.

The expected fit error in each channel is defined to be the mean fit error from Tables 6.2 and 6.3, which is $\pm$0.285 GeV/c^2 in the $e\bar{\nu}q\bar{q}$ channel and $\pm$0.291 GeV/c^2 in the $\mu\bar{\nu}q\bar{q}$ channel. Due to the increased size of the data sample, the uncertainty on the statistical fit

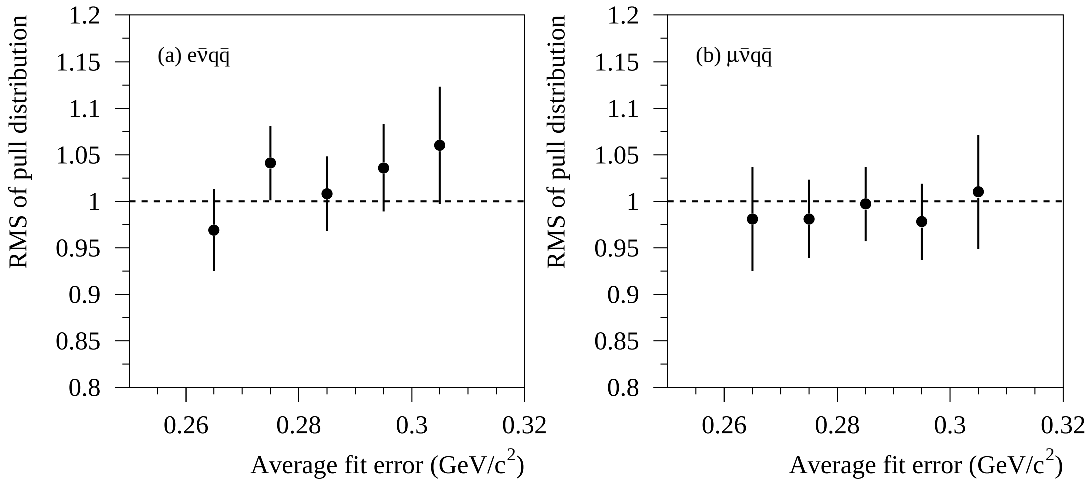

Figure 6.5: The RMS of the pull distribution as a function of the average fit error for (a) $e\bar{\nu}q\bar{q}$ events and (b) $\mu\bar{\nu}q\bar{q}$ events.

error, shown in Figure 6.6 for the $e\bar{\nu}q\bar{q}$ channel, is much smaller than at $\sqrt{s} = 172$ GeV. Therefore, as the fit error has been proven above to be reliable, the statistical error from a fit to the data sample is quoted as the statistical error on the W mass result at $\sqrt{s} = 183$ GeV.

6.4 Stability checks at $\sqrt{s} = 183$ GeV.

Figures 6.7, 6.8, 6.9 and 6.10 show that the fit results from the data sample and a high statistics sample from simulation are stable with respect to variations in:

- The probability cuts used to identify semileptonic WW decays.
- The reconstructed mass range used in the fit.
- The bin size used to build the probability density function for the fit.
- The cut on the χ^2 probability in the kinematic fit.

The high statistics sample contains approximately 2,500 selected semileptonic WW events, simulated with a W mass of 80.60 GeV/c^2.

The replacement of the CC03 matrix element with the complete 4-f matrix element from EXCALIBUR [108] produces small shifts in the fitted W masses of 10 and 0 MeV/c^2

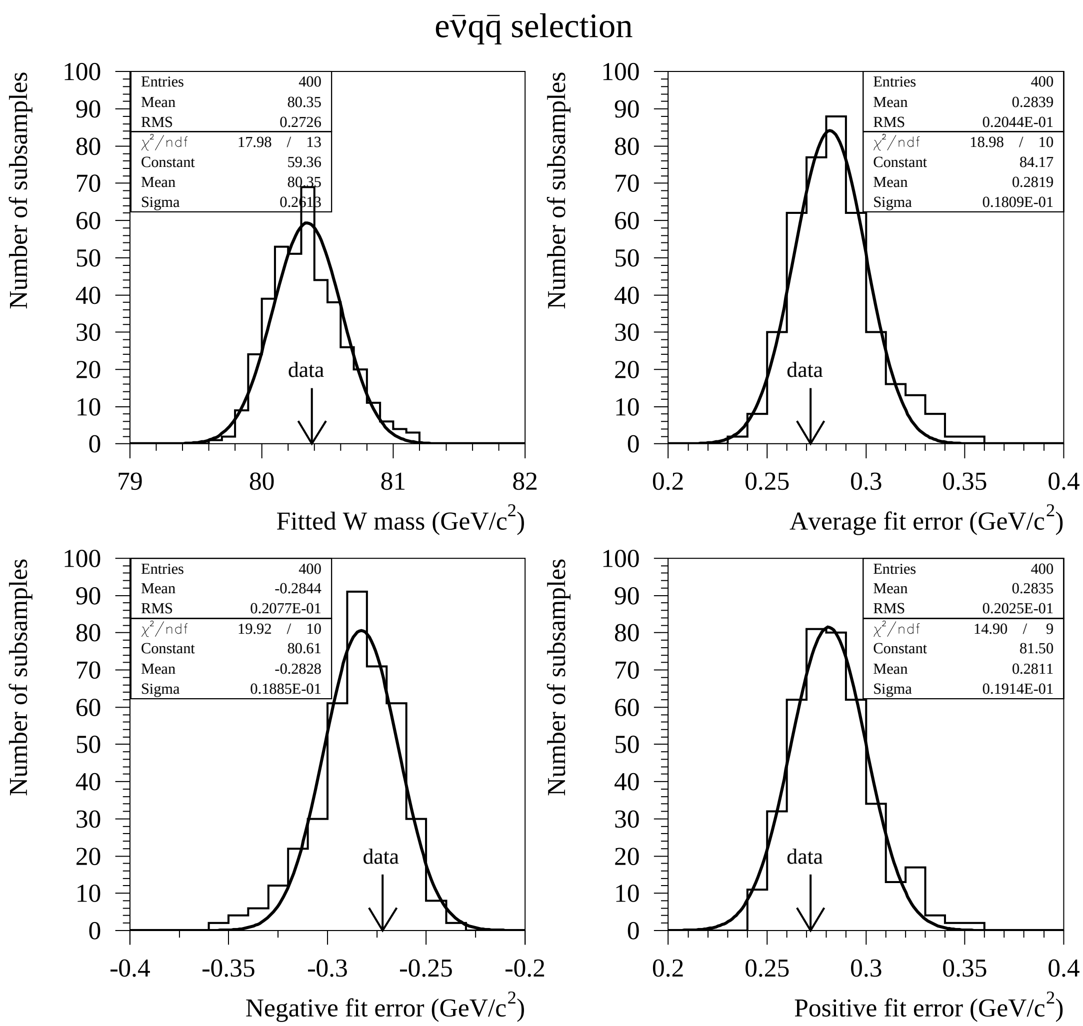

Figure 6.6: Distributions of the fitted mass, parabolic, positive and negative fit errors for 400 independent subsamples of simulated events with $M_W^{gen} = 80.35$ GeV/c^2 in the $e\bar{\nu}q\bar{q}$ channel.

for the $e\bar{\nu}q\bar{q}$ and $\mu\bar{\nu}q\bar{q}$ channels respectively. In combination with the absence of any significant bias or difference from one for the gradient of the relationship between the fitted W mass and the W mass assumed in the simulation, this implies that the CC03 matrix element is sufficient at present for an unbiased result.

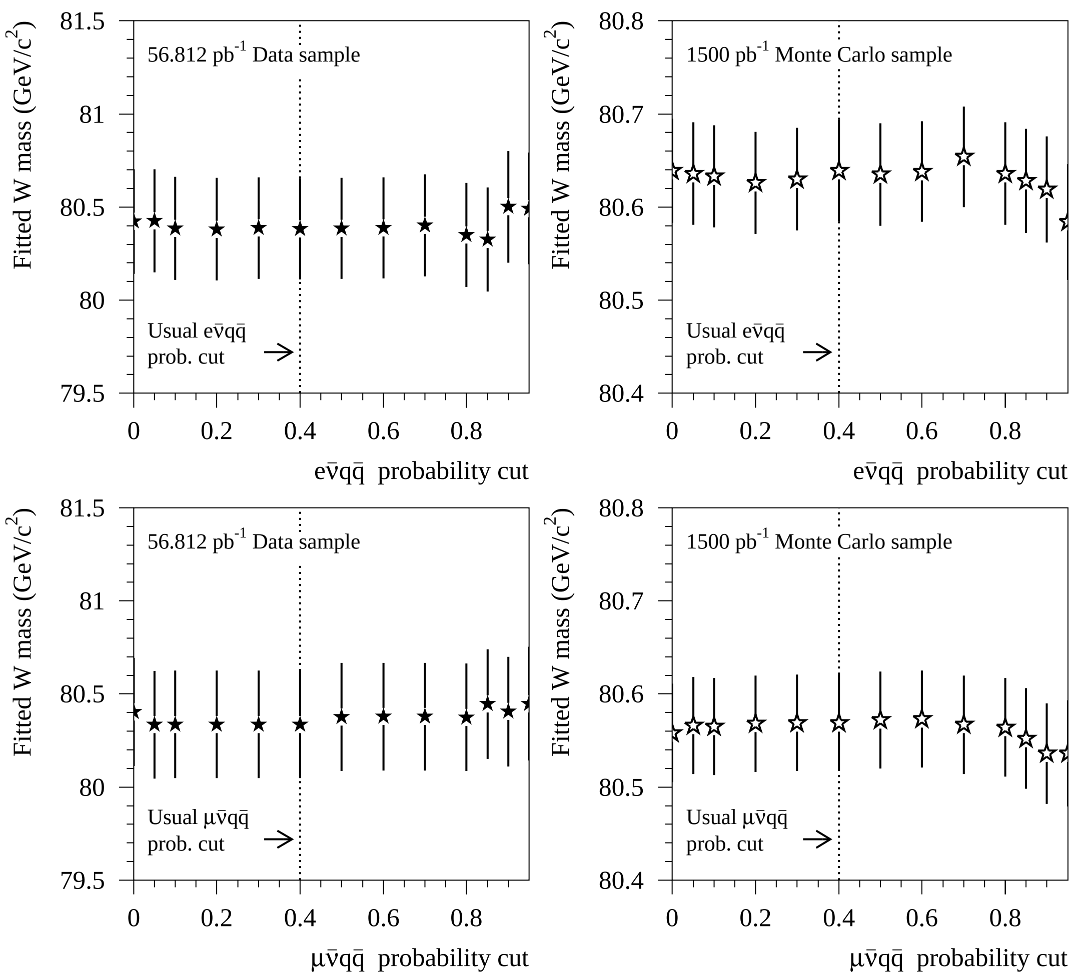

Figure 6.7: Stability of the fitted W mass as a function of the applied selection cut for $e\bar{\nu}q\bar{q}$ (top) and $\mu\bar{\nu}q\bar{q}$ (bottom) events using the data and a 1500 pb^{-1} Monte Carlo sample. The uncertainties on the different points are highly correlated.

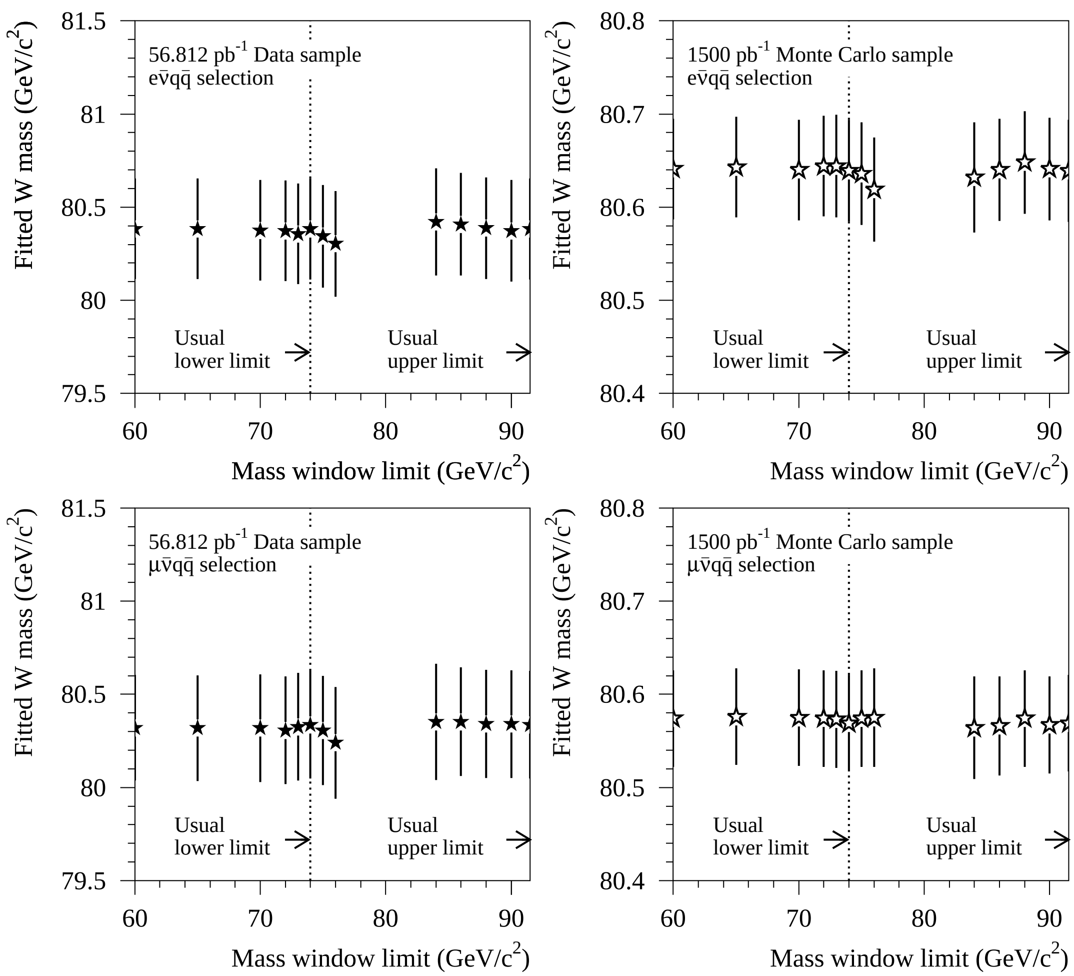

Figure 6.8: Stability of the fitted W mass for several mass windows for $e\bar{\nu}q\bar{q}$ (top) and $\mu\bar{\nu}q\bar{q}$ (bottom) events using the data and a 1500 pb^{-1} Monte Carlo sample. The uncertainties on the different points are highly correlated.

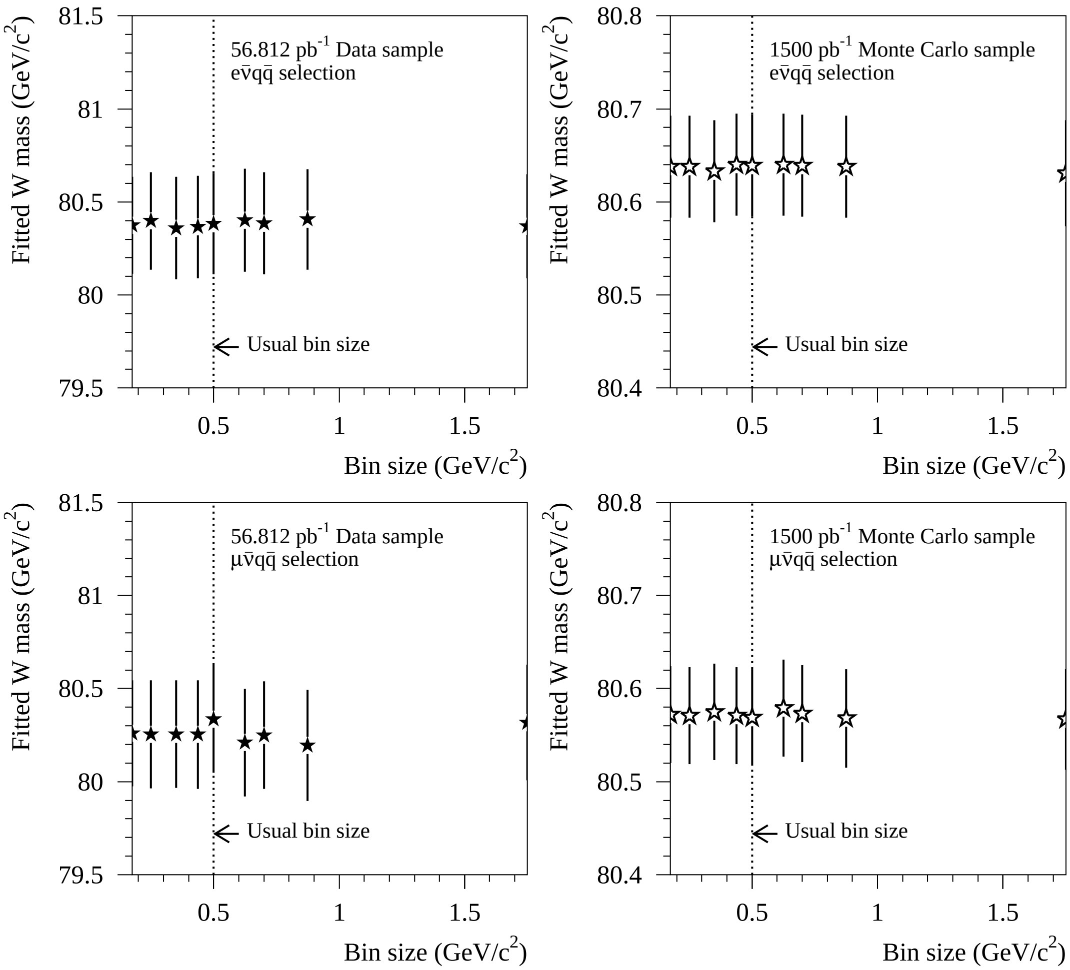

Figure 6.9: Stability of the fitted W mass as a function of the bin size for $e\bar{\nu}q\bar{q}$ (top) and $\mu\bar{\nu}q\bar{q}$ (bottom) events using the data and a 1500 pb^{-1} Monte Carlo sample. The uncertainties on the different points are highly correlated.

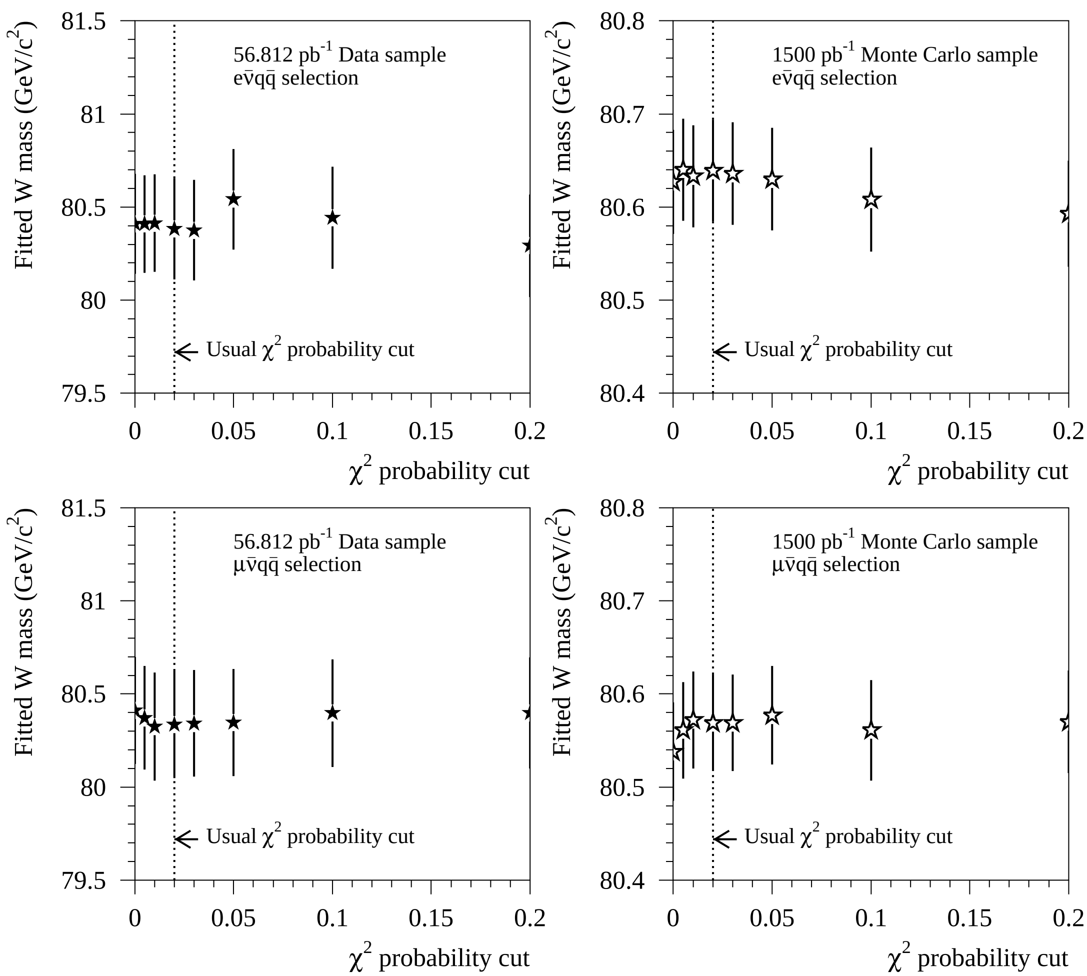

Figure 6.10: Stability of the fitted W mass as a function of the χ^2 probability cut for $e\bar{\nu}q\bar{q}$ (top) and $\mu\bar{\nu}q\bar{q}$ (bottom) events using the data and a 1500 pb^{-1} Monte Carlo sample. The uncertainties on the different points are highly correlated.

6.5 Summary.

The W mass extraction technique chosen gives a result for the W mass that is reproducible, stable and does not require any bias correction. Due to the small size of the data sample at $\sqrt{s} = 172$ GeV, the mean fit error of 0.47 GeV/c^2 from an ensemble of simulated samples is quoted as the statistical error on the W mass result. With the higher statistics at $\sqrt{s} = 183$ GeV, the fit error from the data sample is quoted as the statistical error on the W mass result.

Chapter 7

Systematics.

This chapter describes all the systematic uncertainties considered for the W boson mass measurements at $\sqrt{s} = 172$ GeV and $\sqrt{s} = 183$ GeV.

7.1 Systematics at $\sqrt{s} = 172$ GeV.

7.1.1 Monte Carlo fragmentation of the $W \rightarrow q\bar{q}$ decays.

The systematic error from this source is taken to be 10 MeV/c^2, where the mass is fitted using a Breit-Wigner function [65]. This error represents the shift in the fitted W mass on varying the main fragmentation parameters in JETSET (Λ - the QCD scale parameter that controls the parton shower, M_{min} - the invariant mass cutoff of the hadronic shower, σ - the Gaussian width of the transverse momentum distribution for the primary hadrons, B - the fragmentation parameters for light hadrons) to extreme values, which are typically four standard deviations from the measured values [109].

7.1.2 Calorimeter calibrations.

The uncertainties on the global energy calibration of the ECAL and HCAL detectors are assessed to be 1.5% and 4% respectively for the $\sqrt{s} = 172$ GeV data [110]. The effect of a possible mis-calibration on the W mass is estimated by rescaling all ECAL and HCAL energy depositions by $\pm 1.5\%$ and $\pm 4\%$ respectively for the data sample only and determining the change that this produces in the fitted W mass. Using the biggest change in both cases, the ECAL and HCAL errors are combined in quadrature to give an error of 47 MeV/c^2.

7.1.3 Jet corrections in the kinematic fit.

The jet correction factors are calculated solely from simulation. Studies of hadronic Z^0 decays at $\sqrt{s} \approx 91$ GeV show that the jet energy corrections in data differ from simulation by up to 30% in the region $|\cos\theta_T| \geq 0.95$ [111], where θ_T is the angle between the thrust axis[1] and the beam axis. This discrepancy is parameterised by the variable Δ:

$$\Delta = \frac{(E_{beam} - E_{hemi}^{sim})}{E_{beam}} - \frac{(E_{beam} - E_{hemi}^{data})}{E_{beam}} \tag{7.1}$$

where E_{hemi} is the total energy of the particles in one hemisphere of a two jet Z^0 event. Table 7.1 lists the values of Δ in different $|\cos\theta_T|$ ranges.

$\lvert\cos\theta_T\rvert$	Δ
0.00-0.65	0.01
0.65-0.75	0.015
0.75-0.80	0.01
0.80-0.90	0.04
0.90-0.95	0.04
0.95-1.00	0.09

Table 7.1: Values of the discrepancy Δ observed between 1996 Z^0 data and simulation.

So the simulation underestimates the hemisphere energy and therefore overestimates the jet energy correction factor when the thrust axis is close to the beam axis. This discrepancy is not corrected for and so a systematic error must be estimated.

Identifying the jet energy with the hemisphere energy, the jet polar angle with the thrust angle and the jet correction factor from simulation, a_i, with $\frac{E_{beam}}{E_{hemi}^{sim}}$, then equation 7.1 can be solved for $a_i^{mod} = \frac{E_{beam}}{E_{hemi}^{data}}$, where:

$$a_i^{mod} = a_i(1 - f\Delta) \tag{7.2}$$

This modified correction factor is applied to the jet energy in the data sample only. The kinematic fit is re-applied and the W mass is then extracted from the modified data mass distribution. This is done for $f = 1.0$, 0.5, 0.0, -0.5 and -1.0. A value of 1.0 for f "corrects"

[1] The thrust axis is the direction along which the sum of the magnitudes of the projected momentum components of all the particles in the event is a maximum. The plane perpendicular to the thrust axis divides an event into two hemispheres.

for the discrepancy, whereas a value of -1.0 makes the discrepancy two times worse. In order to avoid statistical fluctuations from events moving above or below the lower limit on the fitted mass range, only data events common to all the variations are used. Table 7.2 shows the fitted W masses relative to the result with f=0. The quoted systematic error is 90 MeV/c^2, which is the average of the shifts with f = ± 0.5.

f	ΔM_W (MeV/c^2)
+1.0	+154
+0.5	+88
-0.5	-97
-1.0	-69

Table 7.2: Mass shifts due to jet energy discrepancies observed between 1996 Z^0 data and simulation [93].

7.1.4 Initial State Radiation.

The KORALW event generator, which simulates the $e^+e^- \to W^+W^- \to f_1\bar{f}_2f_3\bar{f}_4$ process, features QED initial state radiation up to $\mathcal{O}(\alpha^2L^2)$, *ie* up to second order in the leading-log approximation. The effect of the missing terms on the W mass measurement is studied at generator level in [112] by degrading KORALW to $\mathcal{O}(\alpha^1L^1)$ and checking the size of the pure $\mathcal{O}(\alpha^2L^2)$ correction. A systematic error of 15 MeV/c^2 is quoted.

7.1.5 Reference Monte Carlo statistics.

A finite number of simulated events at the reference mass is used to define the probability density function for the mass fit. The statistical fluctuations present are exacerbated by the reweighting procedure. In order to estimate the systematic error from this source, the reference sample of 100,000 KORALW 4-f events is divided into smaller, statistically independent, samples of equal size. Each sample is used as the reference sample for a fit to the data distribution. The RMS of the fitted masses scales as the square root of the number of samples, N_s, that the original reference sample is divided into, *ie* $RMS = c\sqrt{N_s}$. So the systematic error from using the full reference sample is the factor c. From this method, the systematic error due to finite reference Monte Carlo statistics is 35 MeV/c^2.

7.1.6 Background contamination.

The error from this source is expected to be small because the background from other physics processes is only a small fraction of the selected semileptonic WW decays. Nevertheless, an error from a possible mismodelling of the shape of the reconstructed mass distribution of the background and an error from a wrong normalisation of the background cross section are estimated.

Background shape.

The small size of the data sample does not allow a detailed comparison of its properties with those predicted by simulation. To overcome this problem, the technique developed in [113] is used. This compares high statistics Z peak data taken during 1994 to $Z^0 \rightarrow q\bar{q}$ simulation in order to evaluate the effect of any discrepancies in the shape of the reconstructed mass distribution of the background.

The semileptonic WW decay selection described in Section 3.1 is rescaled to the LEP1 energy of $\sqrt{s}$ = 91.2 GeV. The multidimensional discrimination and the kinematic fit are not used as they are tuned to the simulation of WW decays at $\sqrt{s}$ = 172 GeV. A comparison between the shape of the di-jet mass distribution for the data and the simulation is shown in Figure 7.1. The ratio of the data to the simulation is used to correct the shape of the reconstructed mass distribution used in the fit for the W mass. The systematic error from this source is found to be negligible.

Background normalisation.

The uncertainty in the background normalisation is estimated by comparing the number of data and simulated events that have an $e\bar{\nu}q\bar{q}$ or $\mu\bar{\nu}q\bar{q}$ probability value of less than 0.1. This region is dominated by background and differences of the order of 30% are observed for both channels. To estimate the size of the systematic error, the cross sections for all the backgrounds are scaled by ± 30% in the fit for the W mass. Again, the systematic error is found to be negligible.

7.1.7 CC03 matrix element.

The KORALW generator produces all the four-fermion final states that can come from WW production and decay. Therefore, there are no large errors due to the omission of

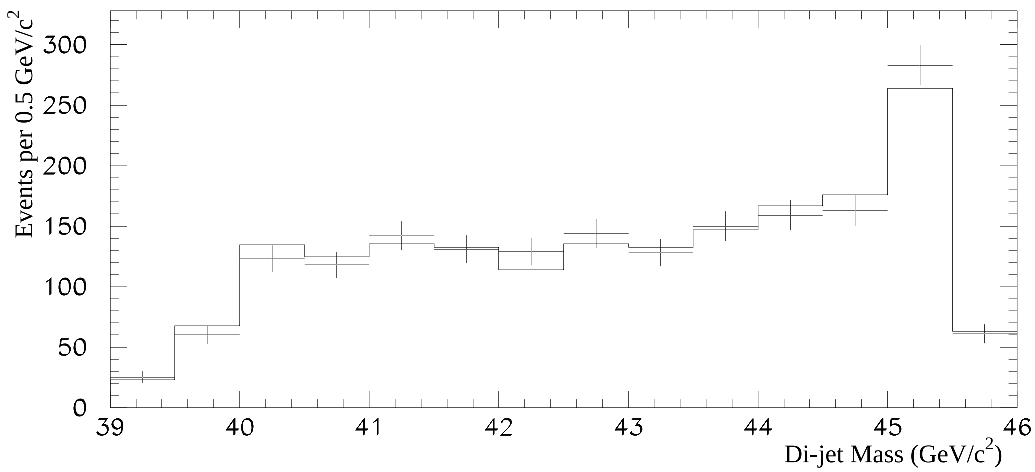

Figure 7.1: Comparison of the shapes of the di-jet mass spectra from LEP1 data and simulation, using a rescaled version of the semileptonic WW selection. The crosses are the data and the histogram is the simulation [93].

relevant Feynman diagrams from the simulation [114].

However, for simplicity, the matrix element used in the reweighting procedure corresponds only to the lowest order CC03 diagrams. The effect of this approximation is studied by using the complete four-fermion matrix element [108] to reweight the simulated WW events. The difference in the fitted W mass is 3 MeV/c^2, which is quoted as a systematic error.

7.1.8 W boson width.

The W boson width varies with the third power of the W boson mass in the fit according to Standard Model relation given in Equation 5.2. To investigate the effect of a systematic shift in the central value for the W width on the W mass, the width is varied about its central value by the known experimental error of 0.07 GeV/c^2 [115]. The difference in the fitted mass is at most 10 MeV/c^2 for all the WW decay channels and this is quoted as a systematic error.

7.1.9 LEP energy.

The relative uncertainty on the LEP beam energy, $\frac{\Delta E_{beam}}{E_{beam}}$, translates into the same relative uncertainty on the fitted W mass, $\frac{\Delta M_W}{M_W}$, since the beam energy is used explicitly by the conservation of energy constraint in the kinematic fit. Therefore the systematic error on the W mass is given by:

$$\Delta M_W = \Delta E_{beam} \frac{M_W}{E_{beam}} \quad (7.3)$$

The LEP beam energy uncertainty for the $\sqrt{s} = 172$ GeV data is 30 MeV [116], so a conservative systematic error of 30 MeV/c^2 is quoted.

7.1.10 Summary.

The systematic errors from all the sources discussed above are summarised in Table 7.3. The total systematic error on the W mass result from the $\sqrt{s} = 172$ GeV data is 113 MeV/c^2 and is dominated by the systematics from the jet corrections and the calorimeter calibration.

Source	ΔM_W (MeVc^2)
MC fragmentation $\star$	10
Calorimeter calibrations $\star$	47
Jet corrections $\star$	90
Initial State Radiation $\star$	15
Reference MC statistics	35
Background contamination	-
CC03 matrix element $\star$	3
W width $\star$	10
LEP energy $\star$	30
Total	113

Table 7.3: Summary of systematic errors on M_W. $\star$ denotes effects that are correlated between the $e(\mu)\bar{\nu}q\bar{q}$, $\tau\bar{\nu}q\bar{q}$ and $q\bar{q}q\bar{q}$ channels [93].

7.2 Systematics at $\sqrt{s} = 183$ GeV.

7.2.1 Monte Carlo fragmentation of the $W \rightarrow q\bar{q}$ decays.

A more significant effect from Monte Carlo fragmentation is found on replacing JETSET with HERWIG [53] for the hadronisation of the partons from an independent sample of 400,000 WW events generated with KORALW. The HERWIG fragmentation parameters are optimised for hadronic Z decays. The detector response is simulated more rapidly and less completely by the QUFSIM program [117].

The HERWIG and JETSET samples are used as reference samples to fit many simulated samples, which are derived from the fully simulated sample of 400,000 WW events with M_W=80.35 GeV/c^2 and each contain the number of events expected in the data sample. The average of the difference between the fitted mass with the HERWIG sample as reference and the fitted mass with the JETSET sample as reference is +27 and -10 MeV/c^2 for the $e\bar{\nu}q\bar{q}$ and $\mu\bar{\nu}q\bar{q}$ channels respectively. A systematic error of 25 MeV/c^2 is taken for both channels.

Note that no allowances are made for any discrepancies between the LEP1 data and the simulation of hadronic Z decays that result from the description of udsc-quark fragmentation by HERWIG or JETSET. Therefore, the fragmentation systematic error quoted should be considered as an upper limit.

7.2.2 Calorimeter calibrations.

The uncertainties on the global energy calibration of the ECAL and HCAL detectors are assessed to be 0.9% and 2% respectively for the $\sqrt{s}$ = 183 GeV data [110]. One way of estimating the effect of a possible mis-calibration on the W mass, which is used for the $\sqrt{s}$ = 172 GeV analysis, is to rescale all the ECAL and HCAL energy depositions by $\pm$0.9% and $\pm$2% respectively for the data sample only and then determine the change that this produces in the fitted W mass. The shifts are shown in Table 7.4, where common events (before and after the induced shift) are maintained throughout in order to suppress statistical fluctuations. This corresponds to neglecting at most 3/93 $e\bar{\nu}q\bar{q}$ events and 2/78 $\mu\bar{\nu}q\bar{q}$ events. The total systematic error is then calculated by combining in quadrature the maximum shifts in M_W for each calorimeter energy scale adjustment. This would give a systematic error of 49 MeV/c^2 and 36 MeV/c^2 for the $e\bar{\nu}q\bar{q}$ and $\mu\bar{\nu}q\bar{q}$ channels respectively.

This systematic is reduced by the complete removal from the jets of energy flow objects from the lepton and the cut on the χ^2 probability from the kinematic fit. Table 7.5 shows the size of the calorimeter calibration systematic error for several values of the χ^2 probability cut. With no χ^2 probability cut, the systematic error in the $e\bar{\nu}q\bar{q}$ channel is dominated by one badly-fitted event that has a χ^2 of 60 for 9 degrees of freedom. The reason for the large χ^2 for this event is that the measured energies of the two jets are very low at 15 GeV and 20 GeV, while the conservation of energy and the equal mass constraints force the sum of the jet energies to equal the beam energy of 91.3 GeV. The

Variation	ΔM_W (MeV/c^2)	
	$e\bar{\nu}q\bar{q}$ channel	$\mu\bar{\nu}q\bar{q}$ channel
ECAL +0.9%	+40	+26
ECAL -0.9%	-36	-8
HCAL +2.0%	-29	+25
HCAL -2.0%	+29	-25
Total	49	36

Table 7.4: Systematic shifts in the fitted W mass of the data sample from the calorimeter calibrations.

kinematic fit scales the jet energies to 53.1 GeV and 38.2 GeV under the nominal ECAL calibration. However, the jet energies scale to 23.5 GeV and 67.8 GeV under the ECAL -0.9% calibration and the fitted mass is 9 GeV/c^2 lower at 77 GeV/c^2, which affects in turn the result of the log-likelihood fit to the mass distribution.

Channel	Variation	ΔM_W (MeV/c^2)						
	P_{χ^2} cut	0.00	0.005	0.01	0.02	0.03	0.05	0.10
$e\bar{\nu}q\bar{q}$	ECAL +0.9%	+12	+27	+37	+40	+41	+40	+37
	ECAL -0.9%	-72	-29	-32	-36	-34	-37	-40
	HCAL +2.0%	-29	-29	-27	-29	-29	-30	-31
	HCAL -2.0%	+46	+29	+29	+29	+28	+25	+24
	Total	85	41	47	49	50	50	51
$\mu\bar{\nu}q\bar{q}$	ECAL +0.9%	+27	+26	+26	+26	+26	+27	+31
	ECAL -0.9%	-12	-10	-13	-8	-8	-8	-9
	HCAL +2.0%	+36	+34	+28	+25	+22	+22	+18
	HCAL -2.0%	-32	-25	-28	-25	-25	-27	-26
	Total	45	43	38	36	36	38	40

Table 7.5: Systematic shifts in the fitted W mass from the calorimeter calibrations, as a function of the χ^2 probability cut in the $e\bar{\nu}q\bar{q}$ and $\mu\bar{\nu}q\bar{q}$ channels.

In order to estimate how likely the systematic shifts found in the data are, the study is repeated using fifty simulated samples of the size of the data, which are taken from the ensemble of simulated events with a W mass value of 80.60 GeV/c^2. The results are shown in Figures 7.2 and 7.3 for the $e\bar{\nu}q\bar{q}$ and $\mu\bar{\nu}q\bar{q}$ channels respectively and imply that the shifts observed in the data sample are quite reasonable.

The shifts in the fitted mass of the samples are actually dominated by the appear-

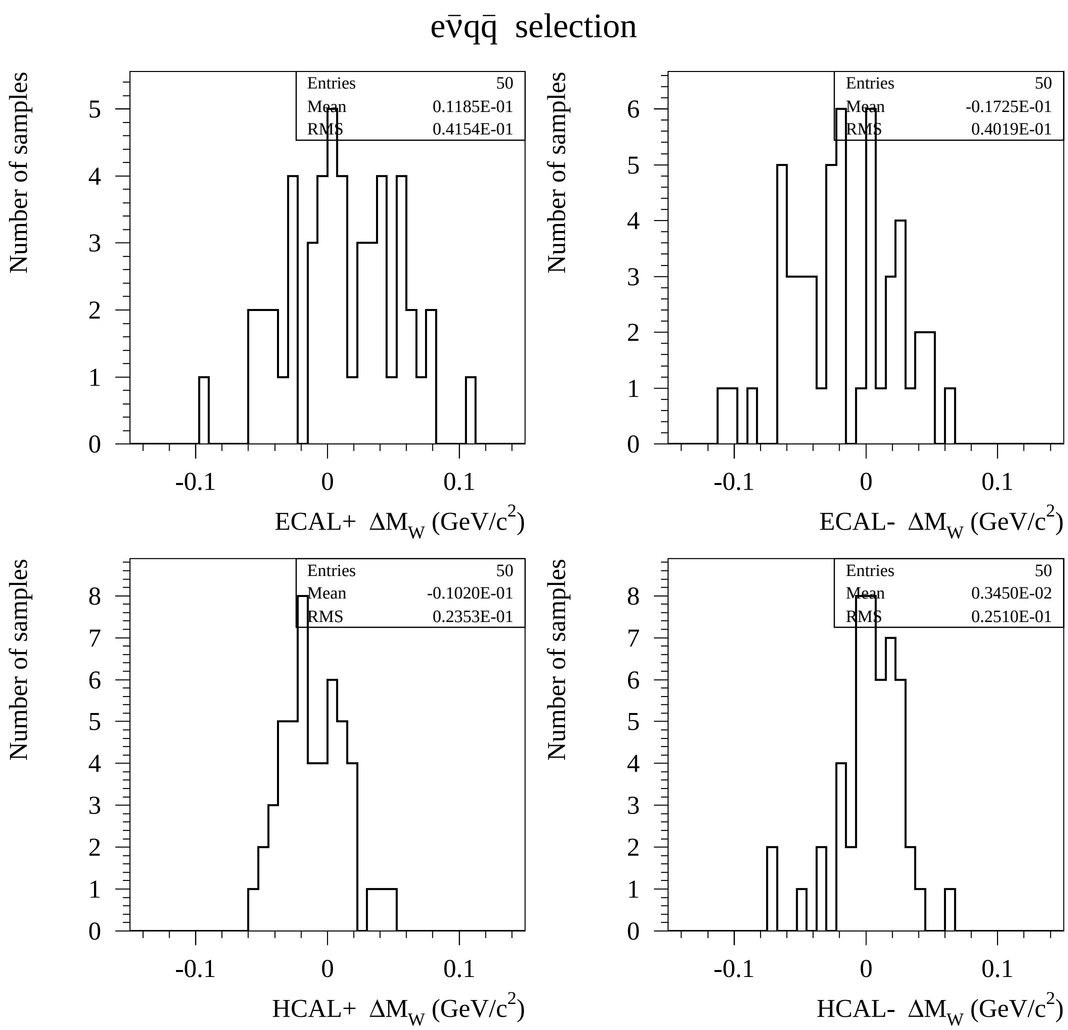

Figure 7.2: Shifts in the fitted W mass for fifty simulated WW samples, which are the same size as the data sample for the $e\bar{\nu}q\bar{q}$ channel, when the ECAL and HCAL calibrations are scaled by their global uncertainties.

ance/disappearance of energy flow objects, as illustrated by Figure 7.4. This shows the change in the event-by-event KINFIT mass produced by rescaling the calorimeter energy deposits. The diagonal is only pronounced for the ECAL variation in the $e\bar{\nu}q\bar{q}$ channel, where the large energy deposit in ECAL from Bremsstrahlung and FSR photons strongly anti-correlates the event-by-event mass shift with the calorimeter energy scale. The source of the un-intuitive horizontal and vertical bands, which form a cross in all four plots, is the effect of thresholds in the energy flow algorithm [118]. For instance, neutral hadrons are identified as an excess of calorimetric energy with respect to nearby charged tracks.

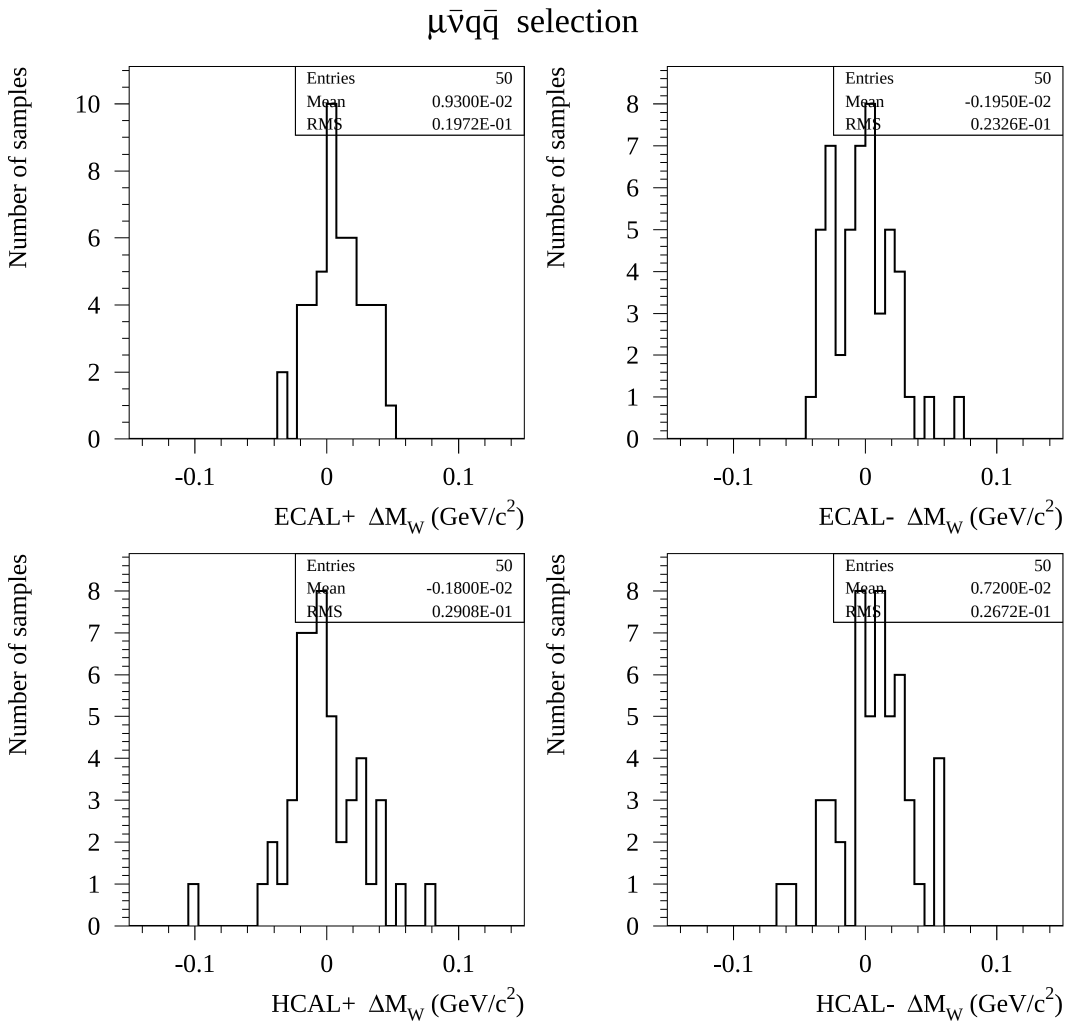

Figure 7.3: Shifts in the fitted W mass for fifty simulated WW samples, which are the same size as the data sample for the $\mu\bar{\nu}q\bar{q}$ channel, when the ECAL and HCAL calibrations are scaled by their global uncertainties.

A variation in the calorimeter calibration that causes an energy deposit to move below or above such a threshold can then change the energy flow structure of the event. This can have a much larger effect than the actual 0.9% or 2.0% variation in the energy scale.

However, the resolution on the W mass is already degraded by events that have extra/missing energy flow objects with the normal calibration. Therefore this effect is already included in the statistical error and it is incorrect to include it again in the systematic error [119]. The underlying shift is then the correct systematic error to quote and is estimated from the mean mass shifts, shown in Table 7.6, of the fifty simulated

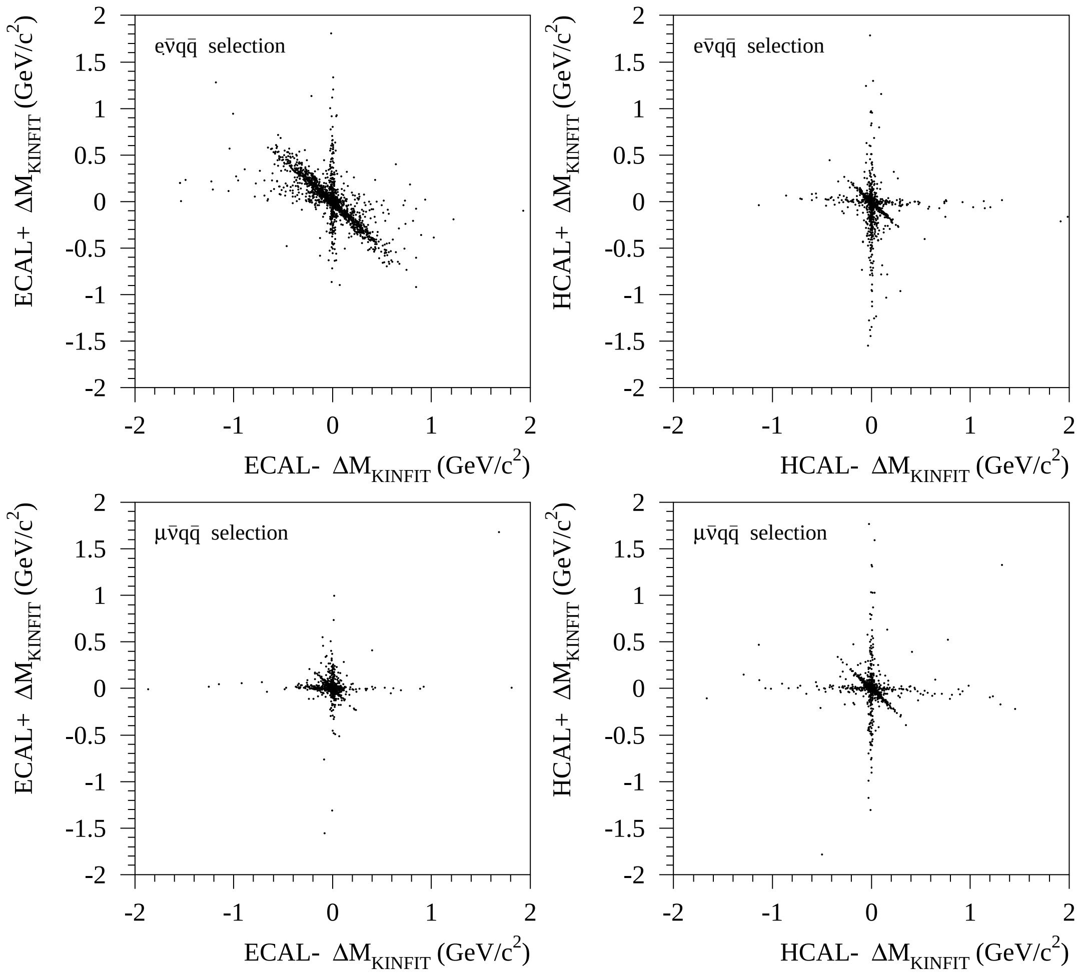

Figure 7.4: Shifts in the individual event-by-event KINFIT masses for fully simulated, selected WW events, when the ECAL and HCAL calibrations are scaled by their global uncertainties.

subsamples. Taking the largest shift for each energy scale adjustment and adding in quadrature as before gives a systematic of 20 MeV/c^2 for the $e\bar{\nu}q\bar{q}$ channel and 11 MeV/c^2 for the $\mu\bar{\nu}q\bar{q}$ channel.

7.2.3 Detector alignment.

The alignment of the VDET, ITC and TPC tracking detectors strongly influences the momentum determination of high energy charged particles and thus the W boson mass measurement in the semileptonic channel. As a case in point, the original alignment for the $\sqrt{s} = 183$ GeV data suffered from a deformation to the VDET. After the removal of this deformation and realignment of the detectors, the fitted W boson mass values

Variation	ΔM_W (MeV/c^2)	
	$e\bar{\nu}q\bar{q}$ channel	$\mu\bar{\nu}q\bar{q}$ channel
ECAL +0.9%	+12	+9
ECAL -0.9%	-17	-2
HCAL +2.0%	-10	-2
HCAL -2.0%	+3	+7
Total	20	11

Table 7.6: The mean systematic shifts of the fitted W mass for fifty simulated samples, of the same size as the data, from the calorimeter calibrations.

changed by approximately -80 MeV/c^2 and +30 MeV/c^2 in the $e\bar{\nu}q\bar{q}$ and $\mu\bar{\nu}q\bar{q}$ channels respectively. Therefore, it is important to estimate a systematic error to account for any possible misalignments that remain.

The detector alignment fits the charged particle tracks from $Z/\gamma \rightarrow \mu^+\mu^-$ decays, which are collected in a dedicated run at $\sqrt{s} = 91$ GeV before data-taking at high energies commences, to a single helix. The aim is to make the fitted muon momentum equal the beam energy by varying the alignment of the TPC, ITCand VDET. Any distortions left are then corrected by equalising the measured momentum of the μ^+ and the μ^-. These sagitta corrections are parameterised as a function of $\cos\theta$ and momentum. The corrections are largest at high $\cos\theta$ [120].

The difference between the fitted W mass with and without the sagitta correction is used to estimate the systematic error from the detector alignment. Considering only the common events in the data samples with and without the sagitta correction, the fitted W mass shifts by -24 MeV/c^2 and -77 MeV/c^2 in the $e\bar{\nu}q\bar{q}$ and $\mu\bar{\nu}q\bar{q}$ channels respectively. Considering all events, the changes are -71 MeV/c^2 and -23 MeV/c^2 in the $e\bar{\nu}q\bar{q}$ and $\mu\bar{\nu}q\bar{q}$ channels respectively [121].

In order to study the effect of the sagitta correction alone, the study is repeated using fifty simulated samples of the size of the data. Figure 7.5 shows the shifts in the fitted W mass, where the RMS is about 7 MeV/c^2 in the $e\bar{\nu}q\bar{q}$ and $\mu\bar{\nu}q\bar{q}$ channels. A systematic error of 10 MeV/c^2 is quoted for both channels.

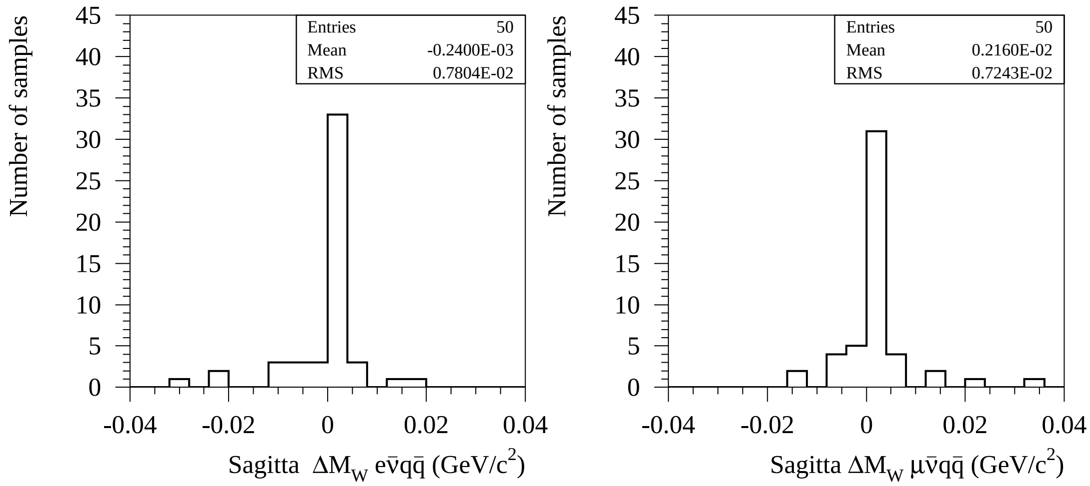

Figure 7.5: Shifts in the fitted W mass for fifty simulated WW samples, which are the same size as the data samples, when the sagitta correction is applied to the simulation.

7.2.4 Jet corrections before the kinematic fit.

Due to the improvements in the simulation, the largest discrepancy between the simulated jet energy and the measured jet energy in data, found from studies of hadronic Z decays [98], is only 1.5% instead of 30%. Nevertheless, the discrepancy is parameterised as a function of polar angle and used to correct the simulated jet energies. To estimate the systematic error, two modified parameterisations are evaluated that accommodate the $\pm 1\sigma$ errors, scaled by the χ^2 per degree of freedom of the original fit. The shifts in the fitted W mass, when the modified parameterisations are used to correct the simulated jet energies, are shown in Table 7.7. The largest shift of 5 MeV/c^2 is taken as a systematic error for both channels.

Variation	ΔM_W (MeV/c^2)	
	$e\bar{\nu}q\bar{q}$ channel	$\mu\bar{\nu}q\bar{q}$ channel
Jet corrections $+1\sigma$	-4	+2
Jet corrections -1σ	-1	+5
Total	4	5

Table 7.7: Systematic shifts in the fitted W mass from the jet corrections.

7.2.5 Initial State Radiation.

KORALW, the main event generator used to simulate the $e^+e^-\to W^+W^-\to f_1\bar{f}_2f_3\bar{f}_4$ process, features QED initial state radiation up to $\mathcal{O}(\alpha^2L^2)$, *ie* up to second order in the leading log approximation. The effect of the missing terms on the W mass measurement is estimated by weighting each event in a specially generated KORALW sample according to the ratio of the first to second order squared matrix elements: $\mathcal{O}(\alpha^1L^1)/\mathcal{O}(\alpha^2L^2)$. The difference between the fitted mass from the unweighted sample and the fitted mass from the weighted sample is 5 MeV/c^2 and 1 MeV/c^2 for the $e\bar{\nu}q\bar{q}$ and $\mu\bar{\nu}q\bar{q}$ channels respectively. A conservative systematic error of 5 MeV/c^2 is taken for both channels.

7.2.6 Reference Monte Carlo statistics.

A finite number of simulated events is used to define the probability density function for the mass fit. The statistical fluctuations present are exacerbated by the reweighting procedure. The systematic error from this source is evaluated by a more precise method than that for $\sqrt{s}=172$ GeV. Since the Monte Carlo events are used in bins, the total uncertainty is calculated by combining the statistical uncertainty from each bin, taking into account both the efficiencies after all analysis steps and the effective number of events after reweighting. The systematic error from this method is 15 MeV/c^2 for the $e\bar{\nu}q\bar{q}$ channel and 13 MeV/c^2 for the $\mu\bar{\nu}q\bar{q}$ channel, reflecting the higher efficiency and therefore available statistics for the $\mu\bar{\nu}q\bar{q}$ channel.

7.2.7 Background contamination.

The error from this source is evaluated in the same way as at $\sqrt{s}=172$ GeV. The systematic error for the $e\bar{\nu}q\bar{q}$ channel is 6 MeV/c^2, whilst that for the $\mu\bar{\nu}q\bar{q}$ channel is negligible.

7.2.8 LEP energy.

The LEP beam energies are calculated every 15 minutes and more frequently if significant shifts are observed in the RF frequency of the accelerating cavities. The instantaneous value recorded nearest in time to each selected data event is used in this analysis. The relative uncertainty on the LEP beam energy translates into the same relative uncertainty on the fitted W mass, since the beam energies are used explicitly by the conservation of energy constraint in the kinematic fit. The LEP beam energy uncertainty for the $\sqrt{s}$ = 183 GeV data is 24 MeV [43], which gives a systematic error of 21 MeV/c^2 on the W mass.

7.2.9 Summary.

The systematic errors from all the sources discussed above are summarised in Table 7.8. The total systematic errors on the W mass results from the $\sqrt{s}$ = 183 GeV data are 43 MeV/c^2 for the $e\bar{\nu}q\bar{q}$ channel and 39 MeV/c^2 for the $\mu\bar{\nu}q\bar{q}$ channel.

Source	ΔM_W (MeV/c^2)	
	$e\bar{\nu}q\bar{q}$ channel	$\mu\bar{\nu}q\bar{q}$ channel
MC fragmentation $\star$	25	25
Calorimeter calibrations $\star$	20	11
Alignment$\star$	10	10
Jet corrections $\star$	5	5
Initial State Radiation $\star$	5	5
Reference MC statistics	15	13
Background contamination	6	-
LEP energy $\star$	21	21
Total	43	39

Table 7.8: Summary of systematic errors on M_W. $\star$ denotes effects that are correlated between the $e\bar{\nu}q\bar{q}$, $\mu\bar{\nu}q\bar{q}$, $\tau\bar{\nu}q\bar{q}$ and $q\bar{q}q\bar{q}$ channels.

Chapter 8

Combination and interpretation.

This chapter deals with the combination of the W boson mass results presented in this thesis with other ALEPH, LEP and hadron collider results. The world average for the W boson mass is then interpreted as a test of the Standard Model.

8.1 Combination of ALEPH W mass results.

The $\sqrt{s} = 172$ GeV results for the W mass from this analysis, the $e^+e^- \rightarrow W^+W^- \rightarrow \tau\bar{\nu}q\bar{q}$ and the $e^+e^- \rightarrow W^+W^- \rightarrow q\bar{q}q\bar{q}$ [122] analyses are:

$$\begin{aligned}
M_W^{e(\mu)\bar{\nu}q\bar{q}} &= 80.54 \pm 0.47(stat.) \pm 0.11(syst.)\mathrm{GeV/c^2} \\
M_W^{\tau\bar{\nu}q\bar{q}} &= 79.56 \pm 1.08(stat.) \pm 0.23(syst.)\ \mathrm{GeV/c^2} \\
M_W^{q\bar{q}q\bar{q}} &= 81.30 \pm 0.47(stat.) \pm 0.11(syst.)\mathrm{GeV/c^2}
\end{aligned}$$

The combined W mass and correlated systematic errors are simply given by the statistically weighted means. The uncorrelated errors are weighted and combined in quadrature. Therefore, the average result for the semileptonic channel at $\sqrt{s} = 172$ GeV is:

$$M_W^{\ell\bar{\nu}q\bar{q}} = 80.38 \pm 0.43(stat.) \pm 0.13(syst.)\ \mathrm{GeV/c^2}$$

which is slightly more precise than the result from the hadronic channel. Combining the results from the fully hadronic and semileptonic channels, the average W mass from direct reconstruction of WW decays in ALEPH at $\sqrt{s} = 172$ GeV is:

$$M_W = 80.80 \pm 0.32(stat.) \pm 0.10(exp.syst.) \pm 0.03(th.syst.) \pm 0.03(LEP)\ \mathrm{GeV/c^2}$$

where the theoretical systematic is due to uncertainties in the modelling of final state interactions (colour reconnection and Bose-Einstein correlations) in the fully hadronic channel and the last systematic is from the LEP energy uncertainty.

The $\sqrt{s}=183$ GeV results for the W mass from this analysis, the $e^+e^- \rightarrow W^+W^- \rightarrow \tau\bar{\nu}q\bar{q}$ and $e^+e^- \rightarrow W^+W^- \rightarrow q\bar{q}q\bar{q}$ [106] analyses are:

$$\begin{aligned}
M_W^{e\bar{\nu}q\bar{q}} &= 80.428 \pm 0.269(stat.) \pm 0.043(syst.)\ \mathrm{GeV/c^2}\\
M_W^{\mu\bar{\nu}q\bar{q}} &= 80.370 \pm 0.287(stat.) \pm 0.039(syst.)\ \mathrm{GeV/c^2}\\
M_W^{\tau\bar{\nu}q\bar{q}} &= 79.758 \pm 0.540(stat.) \pm 0.088(syst.)\ \mathrm{GeV/c^2}\\
M_W^{q\bar{q}q\bar{q}} &= 80.461 \pm 0.177(stat.) \pm 0.075(syst.)\ \mathrm{GeV/c^2}
\end{aligned}$$

The individual results from the $e\bar{\nu}q\bar{q}$ and $\mu\bar{\nu}q\bar{q}$ channels are already more precise than the combination of all the results at $\sqrt{s}=172$ GeV. The average result for the semileptonic channel at $\sqrt{s}=183$ GeV is:

$$M_W^{\ell\bar{\nu}q\bar{q}} = 80.326 \pm 0.184(stat.) \pm 0.045(syst.)\ \mathrm{GeV/c^2}$$

and in combination with the fully hadronic channel, the average W mass from the direct reconstruction of WW decays in ALEPH at $\sqrt{s}=183$ GeV is:

$$M_W = 80.393 \pm 0.128(stat.) \pm 0.041(exp.syst.) \pm 0.028(th.syst.) \pm 0.021(LEP)\ \mathrm{GeV/c^2}$$

The experimental systematics are much reduced with respect to $\sqrt{s}=172$ GeV, with the result that the theoretical uncertainty from final state interactions in the fully hadronic channel and the uncertainty on the LEP energy begin to contribute appreciably to the total systematic error of 56 MeV/c^2.

The $\sqrt{s}=172$ GeV and $\sqrt{s}=183$ GeV results can be combined separately for the semileptonic and hadronic channels to improve the precision slightly to:

$$\begin{aligned}
M_W^{\ell\bar{\nu}q\bar{q}} &= 80.334 \pm 0.170(stat.) \pm 0.052(syst.)\ \mathrm{GeV/c^2}\\
M_W^{q\bar{q}q\bar{q}} &= 80.573 \pm 0.166(stat.) \pm 0.072(syst.)\ \mathrm{GeV/c^2}
\end{aligned}$$

Therefore, the combined W mass from the direct reconstruction of WW decays in ALEPH at $\sqrt{s}=172$ GeV and $\sqrt{s}=183$ GeV is:

$$M_W = 80.451 \pm 0.119(stat.) \pm 0.045(exp.syst.) \pm 0.024(th.syst.) \pm 0.022(LEP)\ \mathrm{GeV/c^2}$$

These results are consistent with the ALEPH result from the combined study of the WW cross section at threshold [123] and at $\sqrt{s}=172$ GeV [124]:

$$M_W = 80.20 \pm 0.33(stat.) \pm 0.09(syst.) \pm 0.03(LEP)\ \mathrm{GeV/c^2}$$

The combination of the cross section and the direct reconstruction measurements gives the most precise ALEPH W mass value of:

$$M_W = 80.423 \pm 0.112(stat.) \pm 0.054(syst.)\ \mathrm{GeV/c^2}$$

which is dominated by the $\sqrt{s} = 183$ GeV results. The total error on the W mass from ALEPH alone is 124 MeV/c^2.

8.2 Combination with other LEP experiments.

The published W mass results from the direct reconstruction of semileptonic and fully hadronic WW decays at $\sqrt{s} = 172$ GeV are shown in Figure 8.1 for all four LEP collaborations [122, 125, 126, 127]. All the results are consistent. The manifestation of Bose-Einstein and colour reconnection effects in fully hadronic WW decays may systematically shift the W mass measured in this channel [30]. No significant difference is observed between the LEP averages for the semileptonic and fully hadronic W mass results. Therefore, the final LEP average of all the direct reconstruction results at $\sqrt{s} = 172$ GeV is [128]:

$$M_W = 80.53 \pm 0.18\ \mathrm{GeV/c^2}$$

The preliminary W mass results, at the time of the International Conference on High Energy Physics in July 1998, from the direct reconstruction of semileptonic and fully hadronic WW decays at $\sqrt{s} = 183$ GeV are shown in Figure 8.2 for all four LEP collaborations [129, 130, 131, 132]. All the results are consistent. Note that the ALEPH results differ slightly from those quoted in this thesis only because the final alignment of the ALEPH detector was not available at that time. No significant difference is observed between the LEP averages for the semileptonic and fully hadronic W mass results. Therefore, the preliminary LEP average of all the direct reconstruction results at $\sqrt{s} = 183$ GeV is [133]:

$$M_W = 80.32 \pm 0.10\ \mathrm{GeV/c^2}$$

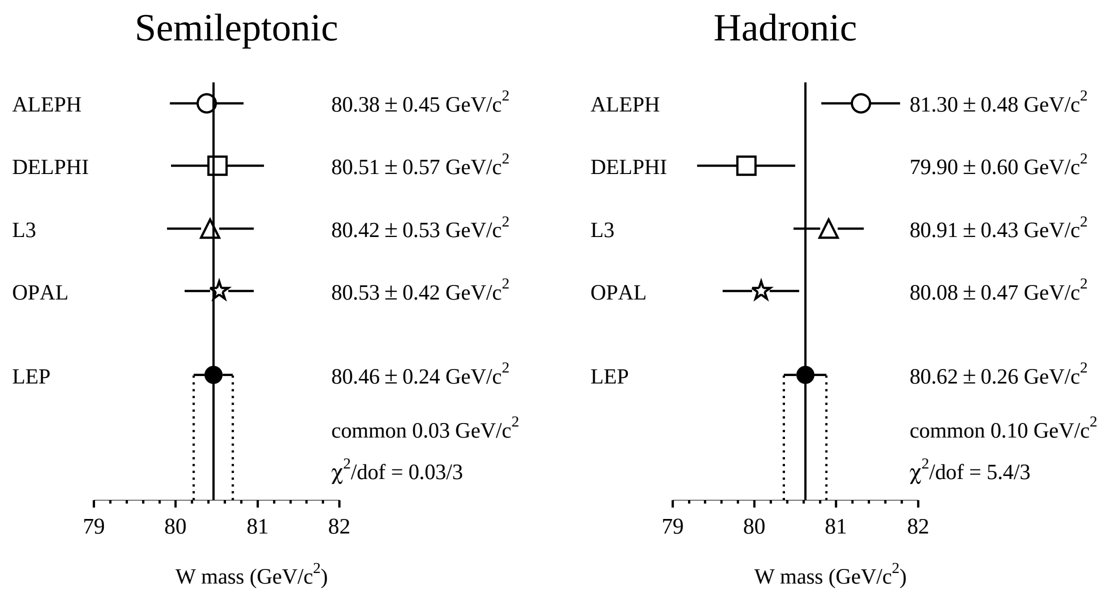

Figure 8.1: LEP Collaboration W mass measurements from direct reconstruction of semileptonic and fully hadronic WW decays at $\sqrt{s} = 172$ GeV.

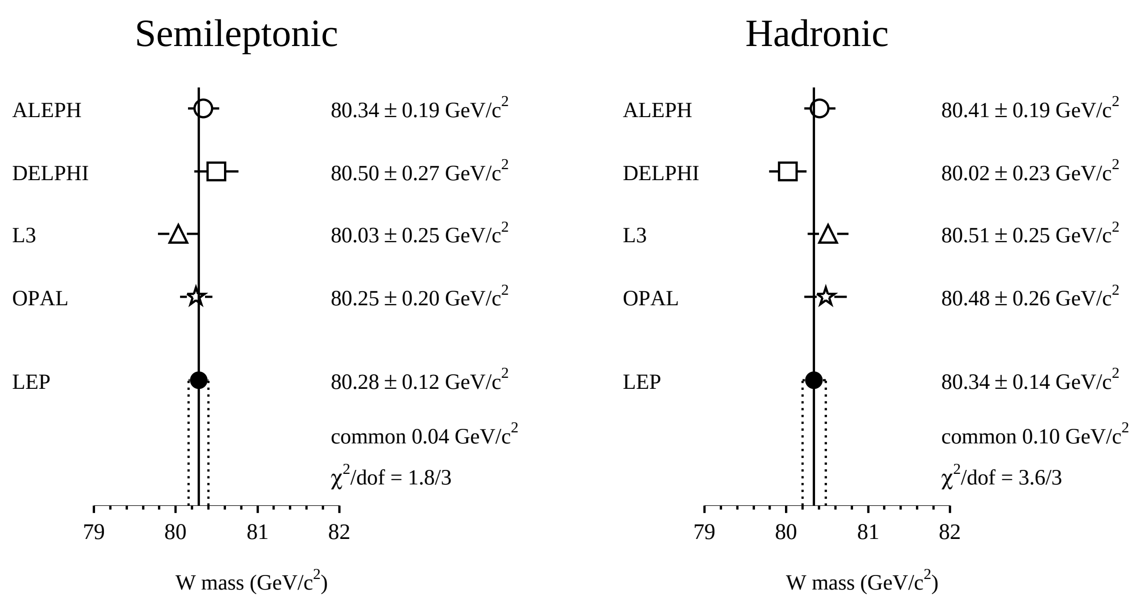

Figure 8.2: LEP Collaboration W mass measurements from direct reconstruction of semileptonic and fully hadronic WW decays at $\sqrt{s} = 183$ GeV.

The combination of all the LEP results on the W boson mass, from the cross section measurement at $\sqrt{s}$ = 161 GeVand by direct reconstruction at $\sqrt{s}$ = 172 GeV and $\sqrt{s}$ = 183 GeV, gives a preliminary LEP average of:

$$M_W = 80.37 \pm 0.09 \text{ GeV/c}^2$$

8.3 Interpretation of the World average for the W boson mass.

All the measurements of the W mass, at the time of the International Conference on High Energy Physics in July 1998 [134], are shown in Figure 8.3. The LEP2 results are consistent with those from the $p\bar{p}$ collider experiments and are of equal precision. Combining all of the direct measurements of the W boson mass, the world average is:

$$M_W = 80.39 \pm 0.06 \text{ GeV/c}^2$$

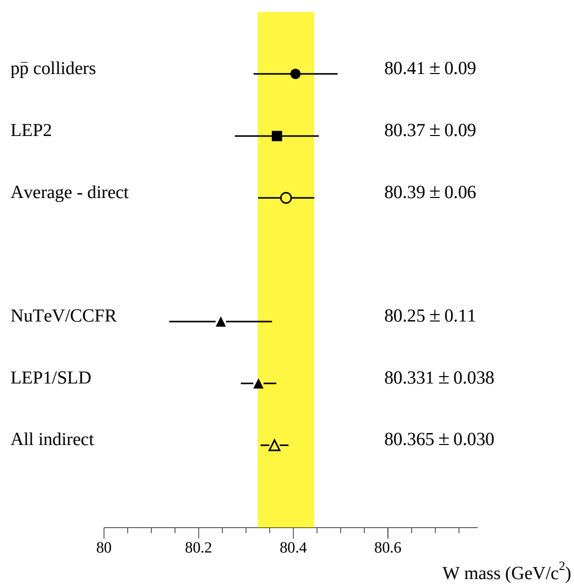

Figure 8.3: Status of W mass measurements at the Vancouver International Conference on High Energy Physics in July 1998 [134].

This direct measurement is consistent with the very precise indirect W mass determination from a global fit to all other high precision electroweak data [134]. It is also consistent with the prediction from νN scattering at NuTeV and CCFR [135]. Figure 8.4

shows the overlap between the direct and indirect measurements of the W boson and top quark masses. This is a critical test of the Standard Model and the direct and indirect measurements are in good agreement. The Standard Model prediction for the relationship between the W mass and the top quark mass is also shown for several values of the Higgs boson mass. The data indicates a slight preference for a light Higgs boson mass.

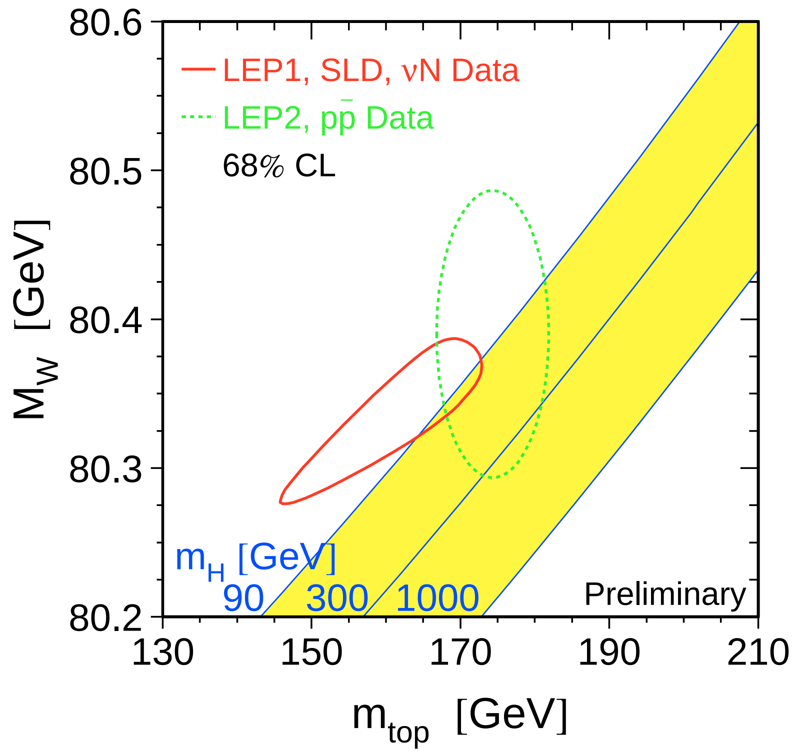

Figure 8.4: Direct and indirect measurements of M_W and m_{top}, compared with the Standard Model for several values of m_H (68% probability contours) [133].

The excellent internal consistency of all the experimental data with the Standard Model is shown by Figure 8.5. The χ^2 per degree of freedom is 16.4/15 and no measurement deviates from the Standard Model by more than two standard deviations. The χ^2 of this fit can be plotted as a function of the Higgs boson mass, as illustrated by Figure 8.6. This favours a low value for the Higgs boson mass of:

$$M_H = \left(84 \begin{array}{c} +91 \\ -51 \end{array} \right) \text{ GeV/c}^2$$

leading to a one-sided 95% confidence level bound for the Higgs boson mass of $M_H <$ 280 GeV/c^2. Note that the direct search results are not used in the definition of this

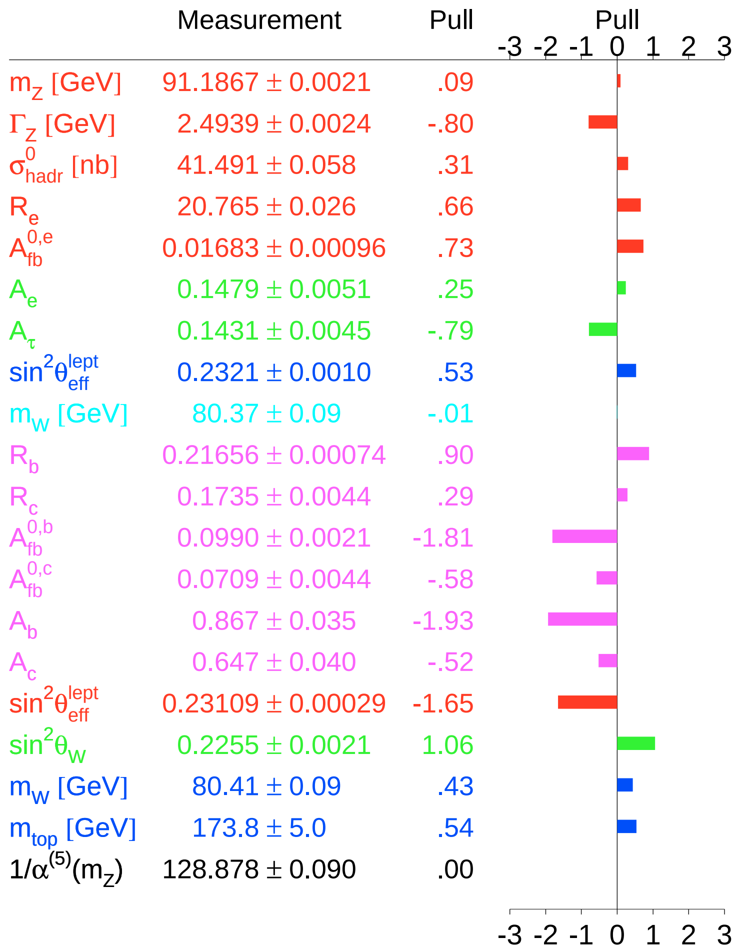

Figure 8.5: Pulls of the electroweak parameters with respect to the global fit including the direct determinations of M_W and M_{top}. The pull is defined as the difference of the measurement to the Standard Model prediction divided by the measurement error [134].

bound. A caveat is that the central value of the preferred Higgs mass moves upwards by over 50 GeV/c^2 if one of the results, namely the value for $\sin^2\theta^{lept}_{eff}$ from the measurement of A_{LR} at SLD, is excluded from the electroweak fit. A more precise determination of the W boson mass will reduce this sensitivity to the difference between the LEP and SLD measurements of $\sin^2\theta^{lept}_{eff}$.

Figure 8.7 shows the range of predictions for the W boson mass in the Standard Model and the Minimal Supersymmetric Standard Model, where it is assumed that no direct discovery of supersymmetric particles is made at LEP2. Precise determinations of the W boson mass and the top quark mass could eventually be decisive for the separation between the models.

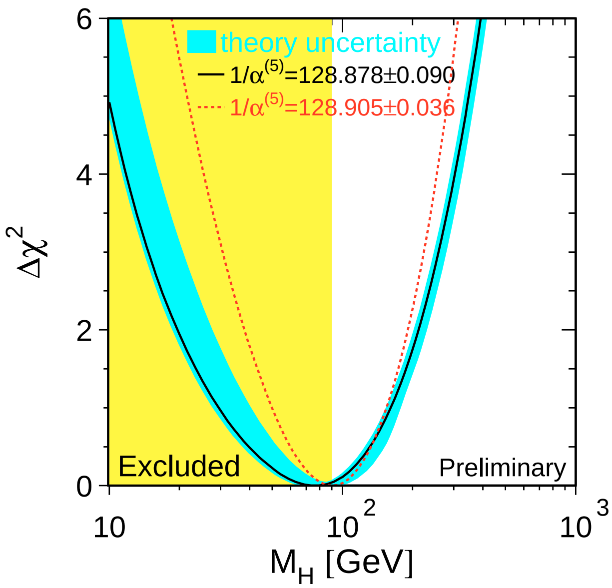

Figure 8.6: Dependence of the χ^2 of the global electroweak fit on the Higgs boson mass [134]. The width of the band represents an estimate of the theoretical uncertainty due to missing higher order corrections. The vertical band shows the 95% confidence level exclusion limit from the direct search [17].

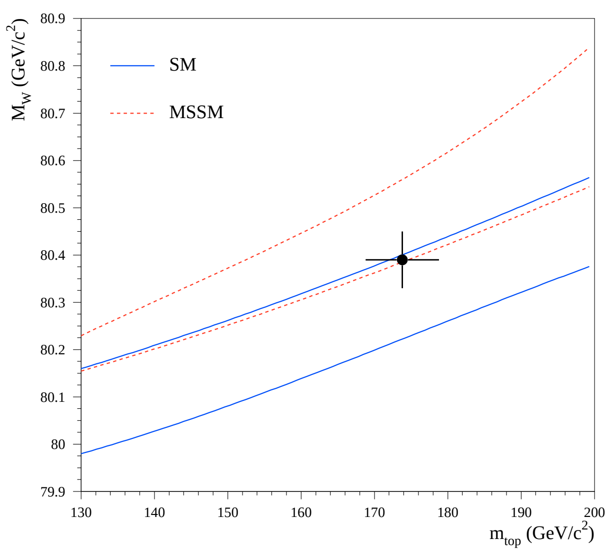

Figure 8.7: Predictions for the W boson mass as a function of the top quark mass in the Standard Model (area between solid lines) and in the MSSM (area between the dashed lines). The point is the world average for the masses of the W boson and top quark [23].

Chapter 9

Conclusions.

This thesis presents the first measurements of the W boson mass by the direct reconstruction of the W decay products in $e^+e^-\rightarrow W^+W^-\rightarrow e\bar{\nu}q\bar{q}$ and $e^+e^-\rightarrow W^+W^-\rightarrow \mu\bar{\nu}q\bar{q}$ events, using the ALEPH detector at the LEP collider. This required the development of an efficient selection, a kinematic fit specific to the semileptonic channel in order to treat the undetected neutrino correctly and an unbiased method to extract the W boson mass from the chosen distribution.

The selection exploits the characteristic presence of a high energy, isolated lepton and a large amount of missing momentum, due to an undetected neutrino, to select semileptonic WW decays with high efficiency and purity. At $\sqrt{s} = 172$ GeV, the efficiency and purity are 83% and 91% in the $e\bar{\nu}q\bar{q}$ channel and 89% and 93% in the $\mu\bar{\nu}q\bar{q}$ channel. From the integrated luminosity of 10.65 pb^{-1}of data, 14 and 20 events are selected in the $e\bar{\nu}q\bar{q}$ and $\mu\bar{\nu}q\bar{q}$ channels, respectively, in agreement with the corresponding expectations of 18.0 and 18.5 from simulation. At $\sqrt{s} = 183$ GeV, the efficiency and purity are 82% and 90% in the $e\bar{\nu}q\bar{q}$ channel and 85% and 95% in the $\mu\bar{\nu}q\bar{q}$ channel. From the integrated luminosity of 56.81 pb^{-1} of data, 130 and 105 events are selected in the $e\bar{\nu}q\bar{q}$ and $\mu\bar{\nu}q\bar{q}$ channels, respectively, in agreement with the corresponding expectations of 119.6 and 116.4 from simulation.

The accurate reconstruction of the lepton energy is very important to the W mass measurement and a search is performed to recover energy lost due to Bremsstrahlung and Final State Radiation. This retrieves 71% of Bremsstrahlung photons and 60% of FSR photons with energies over 5 GeV. Care must be taken to remove all the energy flow objects associated to the lepton before the reconstruction of the two jets of hadrons.

The kinematic fit improves the reconstruction of the four-vectors for the two jets and the lepton and thus the resolution on the W boson mass, typically by a factor of four. The measurements are corrected for any biases introduced by the finite acceptance of the detector and are then varied according to their experimental resolutions in order to satisfy the physical constraints of energy and momentum conservation. An extra constraint, which requires the di-jet invariant mass to equal that of the lepton-missing momentum system, is used to sharpen the resolution on the W boson mass further.

The correct treatment of the unmeasured neutrino requires a kinematic fit specifically tailored to the semileptonic channel. The bias correction and resolution functions for the jets have to be parameterised specifically for the semileptonic channel, in order to take advantage of the better jet definition. Most importantly, the functions must be parameterised in terms of the true particle energy and polar angle rather than the measured values in order to avoid serious biases.

These requirements are met by the kinematic fit developed for the $\sqrt{s} = 183$ GeV analysis. The fit converges successfully for 92% of the selected semileptonic WW decays and provides one estimator per event for the W boson mass, with a resolution of 1.6 GeV/c^2. Future work could recuperate much of the remaining 8%. The degree of uniformity of the χ^2 probability distribution is a sensitive test that the momenta and angles are not biased and that their resolutions are correctly estimated. The χ^2 probability distribution is flat, except for a peak at very low probabilities from events that are either badly-measured, lose a lot of energy to ISR or are from background processes. These events are removed by requiring the χ^2 probability to be larger than 2%, which reduces the overall efficiency of the kinematic fit for semileptonic WW decays to 83%. Future work could recover some of these events by improving event reconstruction and allowing for the possibility of ISR.

The W boson mass fit technique is based on a direct comparison of the data invariant mass distribution with simulated distributions for various W mass values, which are obtained by reweighting a large reference sample fully simulated at one W mass value. By construction this technique does not require any bias correction, but does depend on the accurate reproduction of the data distributions by the simulation. This assumption is checked by comparing the reconstructed and fitted kinematic quantities for the jets and the lepton. No significant discrepancies are found, though such studies must be extended with the higher statistics available in future years. The fit technique gives a value for the W boson mass that is reproducible and stable.

The result for the W mass from direct reconstruction of 34 semileptonic WW candidates at $\sqrt{s} = 172$ GeV is:

$$M_W = 80.54 \pm 0.47(stat.) \pm 0.11(syst.)\ \mathrm{GeV/c^2}$$

The $e\bar{\nu}q\bar{q}$ and $\mu\bar{\nu}q\bar{q}$ channels are studied separately with the higher statistics at $\sqrt{s} = 183$ GeV. The results from the direct reconstruction of 94 $e\bar{\nu}q\bar{q}$ and 78 $\mu\bar{\nu}q\bar{q}$ candidates are:

$$M_W^{e\bar{\nu}q\bar{q}} = 80.428 \pm 0.269(stat.) \pm 0.043(syst.)\ \mathrm{GeV/c^2}$$
$$M_W^{\mu\bar{\nu}q\bar{q}} = 80.370 \pm 0.287(stat.) \pm 0.039(syst.)\ \mathrm{GeV/c^2}$$

which combine to give:

$$M_W = 80.401 \pm 0.196(stat.) \pm 0.041(syst.)\ \mathrm{GeV/c^2}$$

The $\sqrt{s} = 172$ GeV result contributes at the level of 14.8% to a weighted average of:

$$M_W = 80.422 \pm 0.181(stat.) \pm 0.040(syst.)\ \mathrm{GeV/c^2}$$

This thesis gives a measurement of the W boson mass with a precision of 185 MeV/c^2. The result is also the official ALEPH result and is consistent with other measurements at ALEPH, LEP and the Tevatron. The combination of the semileptonic and fully hadronic W boson mass results from all four LEP experiments gives a value for the W boson mass with an error of 90 MeV/c^2, equal to that from the Tevatron. As the data analysed so far represents just 13% of the expected LEP2 data set, future measurements of the W boson mass at LEP2 should reduce this uncertainty by a factor of three. This allows a crucial, new test of the consistency of the Standard Model, which is also sensitive to the mass of the Higgs boson.

Appendix A

Relativistic kinematics of WW events.

This appendix derives the relativistic transformations between the four-vectors (q_1, q_2, q_3, q_4) of the four fermions and the twelve masses and angles (M_{W1}, M_{W2}, m_1, m_2, m_3, m_4, θ, ϕ, $\theta_1^\star$, $\phi_1^\star$, $\theta_2^\star$, $\phi_2^\star$) utilised by KINFIT to describe a $e^+e^- \rightarrow W^+W^- \rightarrow f_1\bar{f}_2f_3\bar{f}_4$ decay, assuming the conservation of energy and momentum.

Forward direction.

The four-vectors of the hadronic W and the leptonic W are $p_{W1} = q_1 + q_2$ and $p_{W2} = q_3 + q_4$ respectively. Then the masses M_{W1}, M_{W2}, m_1, m_2, m_3 and m_4 are easily defined as the invariant masses of p_{W1}, p_{W2}, q_1, q_2, q_3 and q_4 respectively.

The angles θ and ϕ are the polar and azimuthal angles of p_{W1} with respect to the direction of the e^- beam. The angles $\theta_1^\star$ and $\phi_1^\star$ of q_1 in the rest frame of the hadronic W and the angles $\theta_2^\star$ and $\phi_2^\star$ of q_3 in the rest frame of the leptonic W are obtained in two steps.

The first step is to boost the decay products q_1 and q_3 into the rest frame of the relevant W according to the general relativistic transformation equations, which are given below for a W boson moving in a direction $\hat{\mathbf{n}}$:

$$\begin{array}{rcllll} \mathbf{q}' & = & \mathbf{q} & - & (1-\gamma)\hat{\mathbf{n}}(\hat{\mathbf{n}}.\mathbf{q}) & - \;\beta\gamma E\hat{\mathbf{n}} \\ E' & = & \gamma E & - & \beta\gamma(\hat{\mathbf{n}}.\mathbf{q}) & \end{array} \tag{A.1}$$

Noting that $\beta = p_W/E_W$ and $\gamma = E_W/M_W$, equations A.1 simplify to the following for $q_1^{'}$ and $q_3^{'}$:

$$\begin{array}{lclcl} \mathbf{q}^{'} & = & \mathbf{q} & - & \mathbf{p}_W \frac{(E+E^{'})}{(E_W+M_W)} \\ E^{'} & = & \frac{E_W}{M_W} E & - & \frac{\mathbf{p_W} \cdot \mathbf{q}}{M_W} \end{array} \tag{A.2}$$

The second step is to rotate the rest frame of each W, so that the z-axis of the new frame is parallel to the direction of flight of the W in the laboratory frame. This is illustrated in Figure A.1 and $q_1^{''}$ and $q_3^{''}$ are given by:

$$\begin{array}{lclclcl} q_x^{''} & = & \cos\theta\cos\phi q_x^{'} & + & \cos\theta\sin\phi q_y^{'} & - & \sin\theta q_z^{'} \\ q_y^{''} & = & \sin\phi q_x^{'} & + & \cos\phi q_y^{'} & & \\ q_z^{''} & = & \sin\theta\cos\phi q_x^{'} & + & \sin\theta\sin\phi q_y^{'} & - & \cos\theta q_z^{'} \\ E^{''} & = & E^{'} & & & & \end{array} \tag{A.3}$$

The angles $\theta_1^{\star}$ and $\phi_1^{\star}$ are the polar and azimuthal angles of $q_1^{''}$ and the angles $\theta_2^{\star}$ and $\phi_2^{\star}$ are the polar and azimuthal angles of $q_2^{''}$ with respect to the z-axis.

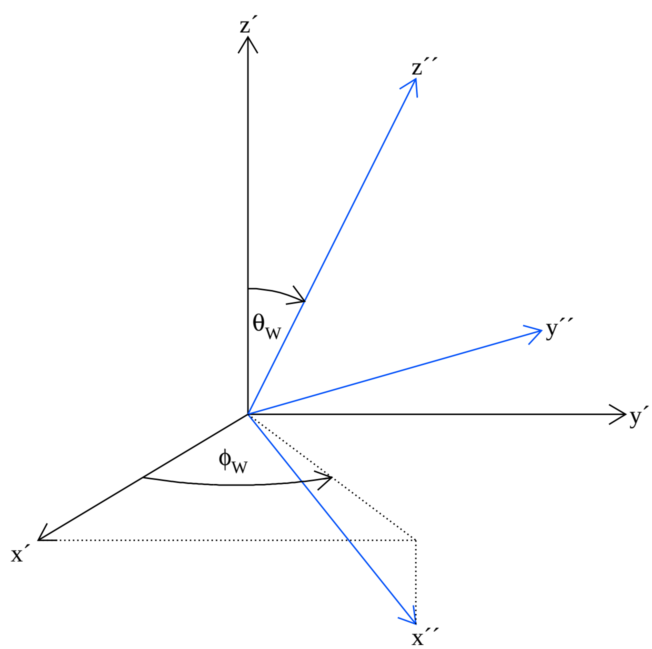

Figure A.1: Rotation from the rest frame of the W to the frame where the z$^{''}$-axis is parallel to the flight direction of the W in the laboratory frame.

Backward direction.

In reverse, the four-vectors $(q_1^{''}, q_2^{''}, q_3^{''}, q_4^{''})$ are defined from the masses and angles as:

$$\begin{aligned}
q_{x1}^{''} &= p_W \sin\theta_1^\star \cos\phi_1^\star \\
q_{y1}^{''} &= p_W \sin\theta_1^\star \sin\phi_1^\star \\
q_{z1}^{''} &= p_W \cos\theta_1^\star \\
E_1^{''} &= \sqrt{p_W^2 + m_1^2}
\end{aligned}$$

$$\begin{aligned}
q_{x2}^{''} &= p_W \sin(\pi - \theta_1^\star)\cos(\pi + \phi_1^\star) \\
q_{y2}^{''} &= p_W \sin(\pi - \theta_1^\star)\sin(\pi + \phi_1^\star) \\
q_{z2}^{''} &= p_W \cos(\pi - \theta_1^\star) \\
E_2^{''} &= \sqrt{p_W^2 + m_2^2}
\end{aligned}$$

$$\begin{aligned}
q_{x3}^{''} &= p_W \sin\theta_2^\star \cos\phi_2^\star \\
q_{y3}^{''} &= p_W \sin\theta_2^\star \sin\phi_2^\star \\
q_{z3}^{''} &= p_W \cos\theta_2^\star \\
E_3^{''} &= \sqrt{p_W^2 + m_3^2}
\end{aligned}$$

$$\begin{aligned}
q_{x4}^{''} &= p_W \sin(\pi - \theta_2^\star)\cos(\pi + \phi_2^\star) \\
q_{y4}^{''} &= p_W \sin(\pi - \theta_2^\star)\sin(\pi + \phi_2^\star) \\
q_{z4}^{''} &= p_W \cos(\pi - \theta_2^\star) \\
E_4^{''} &= \sqrt{p_W^2 + m_4^2}
\end{aligned} \tag{A.4}$$

where p_W is defined from conservation of energy as:

$$p_W = \frac{1}{2\sqrt{s}}\sqrt{s^2 + M_{W1}^4 + M_{W2}^4 - 2sM_{W1}^2 - 2sM_{W2}^2 - 2M_{W1}^2 M_{W2}^2} \tag{A.5}$$

The four-vectors $(q_1^{''}, q_2^{''}, q_3^{''}, q_4^{''})$ are then rotated back to the laboratory frame by the inverse of A.4, where θ and ϕ are replaced by $\pi - \theta$ and $\pi + \phi$ in order to obtain $q_3^{'}$ and $q_4^{'}$:

$$\begin{aligned}
q_x^{'} &= \cos\theta\cos\phi q_x^{''} - \sin\phi q_y^{''} + \sin\theta\cos\phi q_z^{''} \\
q_y^{'} &= \cos\theta\sin\phi q_x^{''} + \cos\phi q_y^{''} + \sin\theta\sin\phi q_z^{''} \\
q_z^{'} &= -\sin\theta q_x^{''} + \cos\theta q_z^{''} \\
E^{'} &= E^{''}
\end{aligned} \tag{A.6}$$

And finally the four-vectors are boosted back to the laboratory frame by the inverse of A.2 to obtain values for (q_1, q_2, q_3, q_4) that satisfy the constraints of energy and momentum conservation:

$$\begin{aligned} \mathbf{q} &= \mathbf{q}^{'} &&+ \mathbf{p}_W \tfrac{(E+E^{'})}{(E_W+M_W)} \\ E &= \tfrac{E_W}{M_W} E^{'} &&+ \tfrac{p_W . q^{'}}{M_W} \end{aligned} \tag{A.7}$$

Appendix B

Definition of $p_{T\theta}$ and $p_{T\phi}$.

$p_{T\theta}$ and $p_{T\phi}$ define the magnitude and the direction of the transverse momentum of the measured particle with respect to the fitted particle. Denoting the momentum vector of the measured particle as $\mathbf{p}_m$ and that of the fitted particle as $\mathbf{p}_f$, then:

$$\begin{aligned} p_{T\theta} &= \mid \mathbf{p}_m \mid \sin\theta_{fm} \cos\phi_{fm} \\ p_{T\phi} &= \mid \mathbf{p}_m \mid \sin\theta_{fm} \sin\phi_{fm} \end{aligned} \tag{B.1}$$

The angle θ_{fm} is simply the angle between the fitted and measured jets:

$$\cos\theta_{fm} = \hat{\mathbf{p}}_m . \hat{\mathbf{p}}_f \tag{B.2}$$

The angle ϕ_{fm} is the azimuthal angle of the transverse momentum of the fitted jet with respect to the measured jet, around the measured jet. ϕ_{fm} is always defined for an anti-clockwise rotation around $\mathbf{p}_m$. This is illustrated in Figure B.1 and $\cos\phi_{fm}$ is defined mathematically as:

$$\begin{aligned} \cos\phi_{fm} &= \hat{\mathbf{q}}_1 . \hat{\mathbf{q}}_2 \\ \mathbf{q}_1 &= (\mathbf{p}_m \wedge \mathbf{p}_f) \wedge \mathbf{p}_m \\ \mathbf{q}_2 &= (\hat{\mathbf{z}} \wedge \mathbf{p}_m) \wedge \mathbf{p}_m \end{aligned} \tag{B.3}$$

The vector $\mathbf{q}_1$ is perpendicular to $\mathbf{p}_m$ in the plane containing $\mathbf{p}_m$ and $\mathbf{p}_f$, points towards $\mathbf{p}_f$ and has magnitude $p_m^2 p_f \mid \sin\theta_{fm} \mid$. The vector $\mathbf{q}_2$ is perpendicular to $\mathbf{p}_m$ in the plane containing $\mathbf{p}_m$ and the z-axis, points away from the z-axis if the angle between $\mathbf{p}_m$ and the z-axis, θ_m, is less than 90° and towards the z-axis if θ_m is greater than 90° and has magnitude $p_m^2 \mid \sin\theta_m \mid$.

$\sin\phi_{fm}$ is positive if $\mathbf{q}_1 \wedge \mathbf{q}_2$ points along $\mathbf{p}_m$ and negative otherwise. $\sin\phi_{fm}$ is zero if the transverse momentum of the measured jet with respect to the fitted jet is completely in the plane containing the measured jet and the z-axis. Note that if $\mathbf{p}_m$ is closer to the beam axis than $\mathbf{p}_f$, then $p_{T\theta}$ points towards $\mathbf{p}_f$.

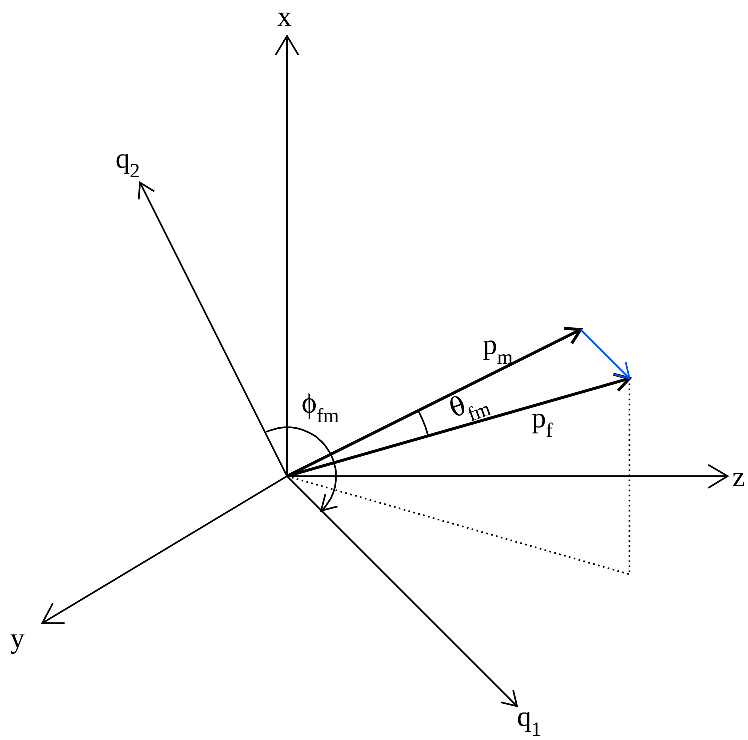

Figure B.1: Definition of θ_{fm} and ϕ_{fm}.

Bibliography

[1] D. Griffiths. "Introduction to Elementary Particles". John Wiley & Sons (1987).

[2] I.J.R. Aitchison and A.J.G. Hey. "Gauge Theories in Particle Physics". Adam Hilger (1989).

[3] F. Halzen and A.D. Martin. "Quarks & Leptons". John Wiley & Sons (1984).

[4] V.D. Barger and R.J.N. Phillips. "Collider Physics". Addison-Wesley (1987).

[5] M. Kaku. "Quantum Field Theory". Oxford University Press (1993).

[6] P.A.M Dirac. "The Quantum Theory of the Emission and Absorption of Radiation". Proc. Roy. Soc. A**114** (1927) 243; "The Quantum Theory of Dispersion". Proc. Roy. Soc. A**114** (1927) 710.

[7] S. Tomonaga. "On a Relativistically Invariant Formulation of the Quantum Theory of Wave Fields". Prog. Theor. Phys. **1** (1946) 27; "On Infinite Field Reactions in Quantum Field Theory". Phys. Rev. **74** (1948) 224.

[8] J. Schwinger. "Quantum Electrodynamics. II. Vacuum Polarization and Self-Energy". Phys. Rev. **75** (1949) 651; "Quantum Electrodynamics. III. The Electromagnetic Properties of the Electron - Radiative corrections to scattering". Phys. Rev. **76** (1949) 790.

[9] R.P. Feynman. "The Theory of Positrons". Phys. Rev. **76** (1949) 749, 769.

[10] G. 't Hooft. "Renormalization of Massless Yang-Mills Fields". Nucl. Phys. **33** (1971) 173; "Renormalizable Lagrangians for Massive Yang-Mills Fields". Nucl. Phys. **35** (1971) 167.

[11] T. Sjöstrand. "High-Energy Physics event generation with PYTHIA 5.7 and JETSET 7.4". Comp. Phys. Commun. **82** (1994) 74.

[12] S. Glashow. "Partial Symmetries of Weak Interactions". Nucl. Phys. **22** (1961) 579.

[13] A. Salam. "Elementary Particle Theory". Ed. N. Svaratholm, Stockholm: Almquist and Forlag (1968) 367.

[14] S. Weinberg. "A Model of Leptons". Phys. Rev. Lett. **19** (1967) 1264.

[15] P.W. Higgs. "Broken Symmetries, Massless Particles and Gauge Fields". Phys. Lett. **12** (1964) 132; "Spontaneous Symmetry Breakdown without Massless Bosons". Phys. Rev. **145** (1966) 1156.

[16] S. Glashow. “Blessed is the weak”. New Scientist 11 October 1997.

[17] P. M^{c}Namara. “Standard Model Higgs at LEP”. Presentation given in parallel session 10 at the 29th International Conference on High Energy Physics, July 1998, Vancouver, Canada.

[18] R.P. Feynman, F.B. Morinigo and W.G. Wagner. “Feynman Lectures on Gravitation”. Ed. B. Hatfield, Addison Wesley (1995) 29.

[19] C. Caso et al. “Review of Particle Physics”. Eur. Phys. J. C**3** (1998) 337.

[20] M. Kobayashi and K. Maskawa. “CP-Violation in the Renormalizable Theory of the Weak Interaction”. Prog. Theor. Phys. **49** (1973) 652.

[21] R.D. Peccei. “Summary and outlook”. In Proceedings of the 29th International Conference on High Energy Physics, July 1998, Vancouver, Canada hep-ph/9811309.

[22] C. Caso et al. “Review of Particle Physics”. Eur. Phys. J. C**3** (1998) 1.

[23] W. Hollik. “Standard Model Theory”. In Proceedings of the 29th International Conference on High Energy Physics, July 1998, Vancouver, Canada hep-ph/9811313.

[24] G. Arnison et al. (UA1 Collaboration). “Experimental observation of isolated large transverse energy electrons with associated missing energy at $\sqrt{s}$=540 GeV”. Phys. Lett. B**122** (1983) 103.

[25] M. Banner et al. (UA2 Collaboration). “Observation of single isolated electrons of high transverse momentum in events with missing energy at the CERN $p\bar{p}$ collider”. Phys. Lett. B**122** (1983) 476.

[26] G. Arnison et al. (UA1 Collaboration). “Experimental observation of lepton pairs of invariant mass around 95 GeV/c^2 at the CERN SPS collider”. Phys. Lett. B**126** (1983) 398.

[27] P. Bagnaia et al. (UA2 Collaboration). “Evidence for $Z^0 \to e^+e^-$ at the CERN $p\bar{p}$ collider”. Phys. Lett. B**129** (1983) 130.

[28] J. Alitti et al. (UA2 Collaboration). “An improved determination of the ratio of the W and Z masses at the CERN $p\bar{p}$ collider”. Phys. Lett. B**276** (1992) 354.

[29] W. Beenakker and F.A. Berends. “WW cross-sections and distributions”. In Physics at LEP2, G. Altarelli, T. Sjöstrand and F. Zwirner (editors), CERN 96-01 (1996), vol. 1, 79.

[30] Z. Kunst and W.J. Stirling. “Determination of the mass of the W boson”. In Physics at LEP2, G. Altarelli, T. Sjöstrand and F. Zwirner (editors), CERN 96-01 (1996), vol. 1, 162.

[31] The LEP Collaborations ALEPH, DELPHI, L3, OPAL, the LEP Electroweak Working Group and the SLD Heavy Flavour and Electroweak Groups. “A Combination of Preliminary Electroweak Measurements and Constraints on the Standard Model”. Prepared from Contributions of the LEP and SLD experiments to the 1998 Summer conferences. CERN-EP-99-015.

[32] N.K. Watson. "W^+W^- hadronic decay properties". In Proceedings of the 29th International Conference on High Energy Physics, July 1998, Vancouver, Canada hep-ph/9809564.

[33] R. Moller. "Bose-Einstein Correlations in WW events". Presentation given in parallel session 1 at the 29th International Conference on High Energy Physics, July 1998, Vancouver, Canada hep-ph/9809564.

[34] B. Abbott et al. (D0 Collaboration). "Measurement of the W boson mass". Phys. Rev. D**58** (1998) 092003.

[35] R. Madaras. "W boson physics at the Fermilab Tevatron collider". In Proceedings of the XVIII International Conference on Physics in Collision, June 1998, Frascati, Italy hep-ex/9808021.

[36] S. Keller and J. Womersley. "Measuring the mass of the W at LHC". FERMILAB-CONF 96/422-T (1996).

[37] G. Daskalakis et al. "Study of $e^+e^- \to W^+W^- \to \ell\bar{\nu}q\bar{q}$ at 500 GeV". In Proceedings of the Joint ECFA/DESY study: Physics and Detectors for a Linear Collider, February to November 1996, Hamburg, Germany hep-ph/9709256.

[38] V. Barger, M.S. Berger, J.F. Gunion and T. Han. "Precision W-boson and top-quark mass determinations at a muon collider". Phys. Rev. D**56** (1997) 1714.

[39] R. Palmer, A. Sessler, A. Tollestrup and J. Gallardo for the Muon Collider Collaboration. "Muon Collider Overview: Progress and Future Plans". In Proceedings of EPAC98, June 1998, Stockholm, Sweden physics/9807006.

[40] S. Myers and E. Picasso. "The design, construction and commissioning of the CERN Large Electron Positron collider" . Contemporary Physics **31** (1990) 387.

[41] M. Lamont. "LEP performance in 1997". In Proceedings of the VIII LEP Performance Workshop, January 1998, Chamonix, France.

[42] The LEP Energy Working Group. "Calibration of centre-of-mass energies at LEP1 for precise measurement of Z properties". CERN-EP-98-040. To be published in Eur. Phys. J. C .

[43] LEP energy working group. "LEP energy calibration above the W threshold". Contribution to the 29th International Conference on High Energy Physics, July 1998, Vancouver, Canada, ICHEP98 352.

[44] M. Placidi. "Beam energy measurements at LEP2". In Physics at LEP2, G. Altarelli, T. Sjöstrand and F. Zwirner (editors), CERN 96-01 (1996), vol. 1, 59.

[45] M. Hildreth and B. Dehning. "The LEP Spectrometer Project". CERN SL seminar 7 May 1998.

[46] R. Barate et al. (ALEPH Collaboration). "Determination of the LEP centre-of-mass energy from $Z\gamma$ events". Contribution to the 29th International Conference on High Energy Physics, July 1998, Vancouver, Canada, ICHEP98 1038.

[47] R. Fernow. "Introduction to experimental particle physics". Cambridge University Press (1986).

[48] D. Decamp et al. (ALEPH Collaboration). "ALEPH: a detector for electron-positron annihilations at LEP". Nucl. Inst. and Meth. A**294** (1990) 121.

[49] D. Buskulic et al. (ALEPH Collaboration). "Performances of the ALEPH detector at LEP". Nucl. Inst. and Meth. A**346** (1994) 461.

[50] ALEPH Collaboration. "The ALEPH handbook 1995". Vol. 1 and 2 are available from the ALEPH Secretariat at CERN.

[51] D. Creanza et al. (ALEPH Collaboration). "Construction and Performance of the new ALEPH Vertex Detector". In Proceedings of the 5th International Conference on Advanced Technology and Particle Physics, October 1996, Como, Italy.

[52] E. Lançon. "ALEPH Status Report". Presentation at CERN LEPC meeting, November 1998.

[53] G. Marchesini et al. "HERWIG: A Monte Carlo event generator for simulating hadron emission reactions with interfering gluons Version 5.1 - April 1991". Comp. Phys. Commun. **67** (1992) 465.

[54] Application Software Group, Computing and Networks Division, CERN. "GEANT: Detector Description and Simulation Tool". CERN Program Library Long Writeup W5013.

[55] M. Skrzypek, S.Jadach, W. Placzek and Z. Wąs. "Monte Carlo program KORALW-1.02 for W pair production at LEP2/NLC energies with Yennie-Frautschi-Suura exponentiation". Comp. Phys. Commun. **94** (1996) 216.

[56] MINAMI-TATEYA group. "GRACE Manual: Automatic generation of tree amplitudes in Standard Models: Version 1.0". KEK report 92-19 (1993).

[57] M. Skrzypek, S. Jadach, M. Martinez, W. Placzek and Z. Wąs. "Initial state QED corrections to W pair production at LEP-2/NLC: Monte Carlo versus semianalytical approach". Phys. Lett. B**372** (1996) 289.

[58] E. Barberio and Z. Wąs. "A universal Monte Carlo for QED radiative corrections. Version 2.0". Comp. Phys. Commun. **79** (1994) 291.

[59] V.S. Fadin, V.A. Khoze, A.D. Martin and A. Chapovskii. "Coulomb effects in W^+W^- production". Phys. Rev. D**52** (1995) 1377.

[60] S. Jadach, B.F.L. Ward and Z. Wąs. "The Monte Carlo program KORALZ, version 4.0, for the lepton or quark pair production at LEP/SLC energies". Comp. Phys. Commun. **79** (1994) 503.

[61] H. Anlauf et al. "Version 2.0: Monte Carlo event generation for large angle Bhabha scattering at LEP". Comp. Phys. Commun. **79** (1994) 466.

[62] D. Buskulic et al. "An experimental study of $\gamma\gamma \rightarrow$hadrons at LEP". Phys. Lett. B**313** (1993) 509.

[63] S. Dhamotharan. "Common preselection for semileptonic WW decays". Presentation at ALEPH WW semileptonic group meeting, January 1997.

[64] P. Azzurri. "A selection of $WW \rightarrow qqe\nu$ and $WW \rightarrow qq\mu\nu$ events at $\sqrt{s} = 161$ GeV". ALEPH Note 96-137 PHYSIC 96-125 (1996).

[65] A. Trabelsi. "Mesure de la masse du boson W$^{\pm}$ dans l'experience ALEPH". PhD thesis, DAPNIA, Saclay, France, 1996.

[66] P. Perret. "New $e\bar{\nu}q\bar{q}$ and $\mu\bar{\nu}q\bar{q}$ selection". Presentation at ALEPH WW semileptonic group meeting, March 1997.

[67] S. Wasserbaech. "Computerized tomography of the ALEPH detector". ALEPH Note 97-098 MCARLO 97-004 (1997).

[68] S. Wasserbaech. "Measurement of the τ lifetime with the impact parameter difference method: 1992 data". ALEPH Note 95-026 PHYSIC 95-024 (1995).

[69] R. Edgecock. Private communication.

[70] Y. L. Dokshitser. Workshop on jets at LEP and HERA. Durham, (1990).

[71] S. Catani, Y. L. Dokshitser, M. Olsson, G. Turnock and B.R. Webber. "New clustering algorithm for multi-jet cross-sections in e^+e^- annihilation". Phys. Lett. B**269** (1991) 432.

[72] N. Brown and W.J. Stirling. "Finding jets and summing soft gluons: a new algorithm". Z. Phys. C**53** (1992) 629.

[73] F. Machefert. "Mesure de la masse du boson W par la methode de reconstruction directe dans l'experience ALEPH au LEP". PhD thesis, École Polytechnique, France, 1998.

[74] J. Allison. "Multiquadric radial basis functions for representing multidimensional High-Energy Physics data". Comp. Phys. Commun. **77** (1993) 377.

[75] E. Lançon. "3D pdf fit". Presentation at ALEPH WW semileptonic group meeting, May 1997.

[76] G. Cowan. "Statistical data analysis". Oxford University Press, 1998.

[77] D. Casper. "Summary of Tracking Upgrade Features in LEP1 Reprocessing". ALEPH Note 98-086 SOFTWR 98-004 (1998).

[78] J. Carr. Private communication.

[79] P. Perret and M.N. Minard. "Studies on electron id at 183 GeV". Presentation at ALEPH WW semileptonic group meeting, September 1997.

[80] M.N. Minard. "ECAL simulation". Presentation at ALEPH WW group meeting, December 1997.

[81] F. Ligabue. "MC retuning and calibration". Presentation at ALEPH WW group meeting, December 1997.

[82] A. Venturi. "HCAL simulation tests". Available from: \http://dante.pi.infn.it:8088/ venturi/ALEPH_info/MC_HCAL_test.html.

[83] A. Bonissent et al. "On Z peak calibration data throughout LEP2 running". ALEPH Note 98-024 SOFTWR 98-001 (1998).

[84] In collaboration with M. Corden and R. Cavanaugh.

[85] A. Rougé. "On the reconstruction of Photon Energy (GAMPEX Calibration)". ALEPH Note 94-057 PHYSIC 94-051 (1994).

[86] G. Batagnani, G. Calderini, J.P. Lees and M. Maggi. "QPI0DO: Improvements in π^0 momentum resolution using the constraint of π^0 mass". ALEPH Note 93-095 SOFTWR 93-078 (1993).

[87] R. Edgecock. Private communication.

[88] A. Tilquin. "Constrained fit and Initial State Radiation in Four Jet Events at LEPII". ALEPH Note 95-129 PHYSIC 95-111 (1995).

[89] L. Lyons. *"Statistics for nuclear and particle physicists"*. Cambridge University Press, 1986.

[90] A.G. Frodesen, O. Skjeggestad and H. Tøfte. *"Probability and statistics in particle physics"*. Bergen Universitetsforlaget, 1979.

[91] A. Trabelsi. "New MATHKINE". Presentation at ALEPH WW group meeting, April 1997.

[92] T. Huehn. "Jet Reconstruction in WW $\rightarrow$Hadrons Events". ALEPH Note 96-111 PHYSIC 96-102 (1996).

[93] E. Lançon, H. Przysiezniak, A. Moutoussi, P.J. Negus, A.S. Thompson, E.J. Thomson, J.J. Ward and T.R. Edgecock. "W mass measurement in the Semileptonic Channel using a Monte Carlo Reweighting Technique". ALEPH Note 97-073 PHYSIC 96-064 (1997).

[94] A. Valassi. "KINFIT: A New Kinematic Fit package based on MINUIT". Presentation at ALEPH WW group meeting, August 1997.

[95] F. James. "MINUIT: Function Minimisation and Error Analysis". CERN Program Library Long Writeup D506 (1994).

[96] A. Blondel. Private communication.

[97] H. Przysiezniak. Private communication.

[98] M.N. Minard, F. Ligabue and E. Lançon. Private communication.

[99] G.D. Lafferty and T.R. Wyatt. "Where to Stick Your Data Points: The Treatment of Measurements Within Wide Bins". Nucl. Inst. and Meth. A**355** (1995) 541.

[100] I. Tomalin. Private communication.

[101] B. Raeven. Program kindly loaned by permission of author.

[102] G. Boix et al. "W mass measurement in the four jet channel using a MC reweighting technique". ALEPH Note 97-067 PHYSIC 97-059 (1997).

[103] M. Vreeswijk. "CC03 matrix element calculation". Available from: \http://alephwww.cern.ch/ jezeques/WmassWeiKWCC03.F, January 1997.

[104] D. Bardin, J. Biebel, D. Lehner, A. Leike, A. Olchevski and T.Riemann. "GENTLE/4fan v.2.0 - A Program for the Semi-Analytic Calculation of Predictions for the Process $e^+e^-\to 4f$". DESY Preprint **96-233** (1996).

[105] P. Perez and H. Przysiezniak. "Accelerated reweighting". Presentation at ALEPH WW semileptonic group meeting, September 1997.

[106] R. Barate et al. (ALEPH Collaboration). "Measurement of the W mass in e^+e^- collisions at 183 GeV". Phys. Lett. B**453** (1999) 121.

[107] J.J. Ward. "Statistical error on the W mass measurement at $\sqrt{s} = 172$ GeV: expected or fit errorΓ" Presentation at ALEPH WW group meeting, September 1997.

[108] F.A. Berends, R. Pittau and R. Kleiss. "EXCALIBUR: a Monte Carlo program to evaluate all four fermion processes at LEP-200 and beyond". Comp. Phys. Commun. **85** (1995) 437.

[109] R. Barate et al. (ALEPH Collaboration). "Studies of Quantum Chromodynamics with the ALEPH detector". Phys. Rept. **294** (1998) 1.

[110] F. Ligabue. \http://alephwww.cern.ch/ ligabue/syst/syst.html.

[111] M.N. Minard. Private communication.

[112] S. Jadach and K. Zalewski. "W-Mass Reconstruction from Hadronic Events in LEP2: Bose-Einstein Effect". Acta Phys. Polon B**28** (1997) 1363.

[113] I. Riu. "W Mass Background Systematic Study using Z Peak Data". ALEPH Note 97-060 PHYSIC 97-053 (1997).

[114] D. Bardin and R.Kleiss. "Event generators for WW physics". In Physics at LEP2, G. Altarelli, T. Sjöstrand and F. Zwirner (editors), CERN 96-01 (1996), vol. 2, 3.

[115] R.M. Barnett et al. Phys. Rev. D**54** (1996).

[116] The working group on the LEP energy. "LEP Energy Calibration in 1996". LEP Energy Group 97-01 (1997).

[117] /al/reference/cvs/uphy/qufsim/README.

[118] J.J. Ward, R. Tenchini and F. Ligabue. "About the detector calibration systematics". Presentation at ALEPH WW semileptonic group meeting, February 1998.

[119] R. Edgecock. Private communication.

[120] I. Tomalin. Private communication.

[121] H. Przysiezniak. "The semileptonic M_W result with reprocessed data at $\sqrt{s} = 183$ GeV". Presentation at ALEPH collaboration meeting, November 1998.

[122] R. Barate et al. (ALEPH Collaboration). "Measurement of the W mass by direct reconstruction in e^+e^- collisions at $\sqrt{s} = 172$ GeV". Phys. Lett. B**422** (1998) 384.

[123] R. Barate et al. (ALEPH Collaboration). "Measurement of the W mass in e^+e^- collisions at production threshold". Phys. Lett. B**401** (1997) 347.

[124] R. Barate et al. (ALEPH Collaboration). "Measurement of the W-pair cross section in e^+e^- collisions at 172 GeV". Phys. Lett. B**415** (1997) 435.

[125] P. Abreu et al. (DELPHI Collaboration). "Measurement of the W pair cross-section and of the W mass in e^+e^- interactions at 172 GeV". Eur. Phys. J. C**2** (1998) 581.

[126] M. Acciarri et al. (L3 Collaboration). "Measurements of Mass, Width and Gauge Couplings of the W Boson at LEP". Phys. Lett. B**413** (1997) 176.

[127] K. Ackerstaff et al. (OPAL Collaboration). "Measurement of the W boson mass and W^+W^- production and decay properties in e^+e^- collisions at $\sqrt{s} = 172$ GeV". Eur. Phys. J. C**1** (1998) 395.

[128] D. Ward. "Test of the Standard Model: W mass and WWZ Couplings". Presentation given at International Europhysics Conference on High Energy Physics, August 1997, Jerusalem, Israel. hep-ph/9711515.

[129] R. Barate et al. (ALEPH Collaboration). "Measurement of the W mass in e^+e^- collisions at 183 GeV". Contribution to the 29th International Conference on High Energy Physics, July 1998, Vancouver, Canada, ICHEP98 899.

[130] P. Abreu et al. (DELPHI Collaboration). "Measurement of the W boson mass and width in e^+e^- collisions at $\sqrt{s} = 183$ GeV". Contribution to the 29th International Conference on High Energy Physics, July 1998, Vancouver, Canada, ICHEP98 341.

[131] M. Acciarri et al. (L3 Collaboration). "Measurements of Mass and Width of the W Boson in e^+e^- interactions at LEP". Contribution to the 29th International Conference on High Energy Physics, July 1998, Vancouver, Canada, ICHEP98 502.

[132] G. Abbiendi et al. (OPAL Collaboration). "Measurement of the W boson mass from direct reconstruction". Contribution to the 29th International Conference on High Energy Physics, July 1998, Vancouver, Canada, ICHEP98 392.

[133] M. Thomson. "$\mathrm{M_W}$ from LEP: $\mathrm{M_W}$ from $W^+W^- \to q\bar{q}q\bar{q}$". Presentation given in parallel session 1 at the 29th International Conference on High Energy Physics, July 1998, Vancouver, Canada.

[134] D. Karlen. "Experimental status of the Standard Model". Presentation given in plenary session 1 at the 29th International Conference on High Energy Physics, July 1998, Vancouver, Canada.

[135] T. Bolton. "New Results from NuTeV". Presentation given in parallel session 1 at the 29th International Conference on High Energy Physics, July 1998, Vancouver, Canada.